The Sensitivity of Southern Ocean Biogeochemical Cycles to Vertical Mixing

Submitted for the degree of Doctor of Philosophy by

Elizabeth Ellison

July 2023

Imperial College London
Department of Civil and Environmental Engineering

This thesis was supervised by Dr Ali Mashayek and Dr Matthew Mazloff.

Abstract

The Southern Ocean (SO) plays a critical role in global overturning circulation and biogeochemical cycles, connecting the world's major ocean basins and facilitating the upwelling of deep waters. Understanding the physical processes occurring in the SO is crucial to understand and model our climate system. While surface-intensified turbulent mixing significantly affects biogeochemical cycles, the importance of variations in the weaker background mixing below the mixed layer is generally overlooked. Background subsurface mixing rates in the SO vary greatly in space and time. The processes known to induce ocean background turbulence are typically not represented in models, and there is great uncertainty in the parameterisation of this mixing. This thesis investigates the sensitivity of biogeochemical tracers to altered SO diapycnal mixing.

Firstly, we show that changes to SO mixing over a modest range alter Atlantic biogeochemical tracer distributions over short and long timescales. On annual to decadal timescales changes are dominated by the direct impact of changes in diapycnal mixing on tracer fluxes, while on centennial timescales they are dominated by the mixing-induced variations in the advective transport of the tracers by large-scale circulation.

Secondly, we examine changes to SO biogeochemistry on sub-decadal timescales. We show that increasing the background mixing significantly alters SO air-sea CO_2 fluxes and phytoplankton productivity. These could alter atmospheric CO_2 concentration over longer timescales.

Finally, when using our current best estimates of spatially varying SO diapycnal mixing rates, we find no reduction in the misfit between modelled and observed tracer concentrations compared to using a spatially homogeneous mixing profile.

This work demonstrates the importance of accurately representing spatiotemporally variable local and non-local SO mixing processes. It is essential to simulate biogeochemical cycles on decadal timescales and to represent the indirect impact of mixing-induced changes to circulation on biogeochemical cycles on longer timescales.

Statement of Originality

This is to certify that to the best of my knowledge, the work presented in this thesis is my own. This thesis has not been submitted for any degree or other purposes. All the assistance received and sources used have been fully acknowledged.

Copyright Declaration

The copyright of this thesis rests with the author. Unless otherwise indicated, its contents are licensed under a Creative Commons Attribution-Non Commercial 4.0 International Licence (CC BY-NC). Under this licence, you may copy and redistribute the material in any medium or format. You may also create and distribute modified versions of the work. This is on the condition that: you credit the author and do not use it, or any derivative works, for a commercial purpose. When reusing or sharing this work, ensure you make the licence terms clear to others by naming the licence and linking to the licence text. Where a work has been adapted, you should indicate that the work has been changed and describe those changes. Please seek permission from the copyright holder for uses of this work that are not included in this licence or permitted under UK Copyright Law.

Acknowledgements

I would like to thank my supervisor, Ali for his time and guidance through this PhD, and for making the whole PhD so enjoyable. I feel incredibly lucky to have had all the opportunities I have as a result of his support and encouragement.

I would also like to thank Matt for all his help and advice with this work. His help with B-SOSE and his knowledge of the SO has helped me hugely in writing this PhD. I would also like to thank Laura for her valuable contribution to the work in the Chapter 2, and for sharing with us a spatially variable mixing map used in Chapters 5 and 6. I am grateful to my Thesis examiners, Alberto and Heather, for making the Viva and enjoyable and as relaxing as possible experience and for the suggestions they have made to further improve this work.

I am very fortunate to have met such a great group of people during my time at Imperial, both through the CDT and in the fluids department. I am especially thankful to Lois and Nick, without whom I think my PhD experience would not have been as much fun.

I am incredibly grateful to friends who have made living in London such a memorable and exciting time of my life. I would like to thank all my family for their support, especially my parents, who have always encouraged me to follow my interests and say yes to every opportunity. Finally, I am incredibly grateful to Guy for being there for me every day of this PhD and for constantly reassuring me that doing a PhD was not a totally crazy decision.

Contents

Abstract **3**

Statement of Originality **4**

Copyright Declaration **4**

Acknowledgements **5**

List of Tables **11**

List of Figures **12**

1 Introduction **15**

1.1 Motivation 15

1.2 Diapycnal Mixing 16

1.3 The Global Meridional Overturning Circulation 17

1.3.1 The MOC and Diapycnal Mixing 18

1.4 The Importance of the Southern Ocean for the MOC 20

1.4.1 Southern Ocean Circulation 20

1.4.2 Diapycnal Mixing in the Southern Ocean 21

1.5 The Role of the Southern Ocean in Controlling Global Biogeochemical Cycles . . 24

1.6 Representing Diapycnal Mixing in Models 25

1.6.1 The Sensitivity of the Meridional Overturning Circulation to Diapycnal Mixing 26

1.6.2 The Sensitivity of the Meridional Overturning Circulation to Southern Ocean Diapycnal Mixing 27

1.7 The Impact of Diapycnal Mixing on Biogeochemical Tracer Distributions 28

1.7.1 The Direct Impact of Mixing on Tracers 28

1.7.2 The Indirect Impact of Mixing on Tracers 29

1.8 The Impact of Southern Ocean Diapycnal Mixing on Biogeochemistry 30

1.9 Aims and Objectives 31

1.10 Thesis Outline 31

1.11 Publications 32

2 Multi-time Scale Control of Southern Ocean Diapycnal Mixing Over Atlantic Tracer Budgets 34

2.1 Abstract 34

2.2 Introduction 35

2.3 Methods 37

2.3.1 The Physical Model 37

2.3.2 The Biogeochemical Model 38

2.3.3 Experiment Design 39

2.3.4 Model Verification 43

2.4 Results: 45

2.4.1 Sensitivity of Atlantic Circulation to Southern Ocean Mixing 45

2.4.2 Sensitivity of C & N Distribution to Southern Ocean Mixing Over a Range of Temporal Scales . . . 46

2.4.3 Long-Term Equilibrated Changes . . . 55

2.4.4 Climatic Implications . . . 56

2.5 Discussion . . . 58

2.6 Acknowledgements . . . 62

3 The Biogeochemical Southern Ocean State Estimate (B-SOSE) 63

3.1 Abstract . . . 63

3.2 Model Description . . . 63

3.3 The Physical Model Set Up . . . 65

3.4 The Biogeochemical Framework . . . 66

3.5 SO Frontal Definitions . . . 71

3.6 Diapycnal Mixing in B-SOSE . . . 71

3.6.1 Experimental Design . . . 74

4 Enhanced Southern Ocean Biomass with Increased Background Diapycnal Mixing 76

4.1 Abstract . . . 76

4.2 Introduction . . . 77

4.3 Methods . . . 79

4.4 Results . . . 79

4.4.1 Changes to Phytoplankton Primary Productivity . . . 79

4.4.2 Changes to Phytoplankton Types . . . 82

4.4.3 Changes to Nutrient Concentrations and Availability 83
4.4.4 Changes to Mixed Layer Depth 86
4.4.5 Changes to Surface Iron Supply 88
4.4.6 Changes to Light Limitation 90
4.4.7 Changes to Export 93
4.5 Discussion 94

5 Hypersensitivity of Southern Ocean Air-Sea Carbon Fluxes to Background Turbulent Diapycnal Mixing 97

5.1 Abstract 97
5.2 Introduction 98
5.3 Methods 100
5.4 Results 100
5.4.1 Carbon Fluxes 100
5.4.2 Changes to Surface Ocean pCO_2 105
5.4.3 Temporal and Seasonal Variability of Changes in pCO_2 109
5.4.4 Contribution of Altered Phytoplankton Productivity to Altered Carbon Fluxes 117
5.5 Discussion 117

6 Can Biogeochemical Tracer Observations Constrain SO Diapycnal Mixing Rates? 120

6.1 Abstract 120
6.2 Introduction 121
6.3 Methods 123

6.3.1 Data Sources . . . 123

6.3.2 Data Coverage . . . 124

6.3.3 Comparison of B-SOSE Outputs to Observational Data Profiles . . . 126

6.4 Results . . . 127

6.4.1 Does a Spatially Variable Mixing Map Improve the Model Output Fit to Observations? . . . 127

6.4.2 Comparison to pCO_2 Observational Data . . . 132

6.4.3 Can Observations of Vertical Gradients be used to Constrain Mixing Rates 135

6.5 Discussion . . . 140

7 Conclusion **145**

7.1 Summary of Contributions . . . 145

7.2 Future Directions . . . 148

7.3 Thesis Implications . . . 151

References **154**

List of Tables

2.1 Diffusivity profiles used for experimental runs 41

2.2 Changes in steady state atmospheric $p\mathrm{CO}_2$ 57

3.1 Ocean and Biogeochemical Model Parameters from Swierczek et al. (2021) and Verdy and Mazloff (2017). 66

3.2 Nutrient half saturation constants for small and large phytoplankton for NO_3, PO_4 and Fe. 67

6.1 Ocean physical and biogeochemical observations used to assess model-observations misfits. 124

List of Figures

1.1 A schematic of the global Meridional Overturning Circulation 19

1.2 A schematic of Southern Ocean processes 22

2.1 A schematic of the Atlantic Ocean circulation 36

2.2 Profiles of turbulent diffusivity in the Atlantic 40

2.3 Model outputs of Atlantic Circulation 42

2.4 A comparison of the model output of biogeochemical tracer distributions to observations 44

2.5 Changes in nutrient distributions over time 47

2.6 Changes in carbon distributions over time 48

2.7 Changes in a passive tracer distribution over time 51

2.8 Mean of absolute change in nutrient, carbon and passive tracer concentration over time 53

2.9 Equilibrated changes to nutrient and carbon distributions 57

2.10 A summary of the processes altering tracer distributions in the Southern Ocean 61

3.1 A schematic of the biogeochemical model in B-SOSE 69

3.2 The location of SO fronts 72

3.3 Diapycnal mixing in B-SOSE 73

4.1 Phytoplankton productivity and changes to phytoplankton productivity 80

4.2 Phytoplankton types and changes in phytoplankton types 82

4.3 Changes in nutrient concentrations and nutrient availability 84

4.4 Changes in Mixed Layer Depth 87

4.5 Changes to the mixed layer depth and ferrocline depths 89

4.6 Mechanisms behind the changes in light availability 92

4.7 Changes in carbon export 94

5.1 SO carbon fluxes and changes to carbon fluxes 102

5.2 Changes to surface ocean partial pressure 104

5.3 The correlation between high vertical gradients and a strong sensitivity to background mixing in month one 107

5.4 The correlation between high vertical gradients and a strong sensitivity to background mixing over 6 years 108

5.5 Seaonality of changes in carbon fluxes 110

5.6 Seasonal changes in the surface ocean partial pressure 111

5.7 Seasonal changes to the vertical profiles of temperature and DIC 112

5.8 Temporal trends in the driving mechanisms of changes to surface ocean partial pressure 114

5.9 The contribution of biological productivity to changes in carbon fluxes 116

6.1 The temporal and spatial availability of biogeochemical observation 125

6.2 The cost function of B-SOSE model outputs 128

6.3 The mean root mean squared error between model output and observations of biogeochemical and physical tracers 129

6.4 The misfit between model and observed biogeochemical and physical tracer concentrations 131

6.5 Comparison of modelled pCO_2 to observations from Surface Ocean CO_2 Atlas (SOCAT) between 2012 and 2018 133

6.6 The vertical gradients of biogeochemical tracers 136

6.7 The vertical gradients of physical tracers 137

6.8 The mean of the difference in absolute vertical gradients of modelled tracers and observations 139

Chapter 1

Introduction

1.1 Motivation

The oceans play a crucial role in regulating the Earth's climate, storing 50 times more carbon than the atmosphere (Prentice et al., 2001). The Southern Ocean (SO), defined as south of 30°S, is a unique oceanographic region due to being unbound by continents and is a critical component of global ocean circulation. It links the deep waters of the Atlantic, Indian and Pacific ocean basins with the ocean surface, and up to 80% of the world's deep waters first surface within the SO (Watson & Naveira Garabato, 2006; DeVries & Primeau, 2011; L. D. Talley, 2013; Lumpkin & Speer, 2007). The SO is, therefore, a crucial link between waters formed in different ocean basins, allowing inter-basin exchanges of heat, carbon, nutrients and other tracers (L. D. Talley, 2013). Carbon predominately enters the ocean via two major pathways, the biological carbon pump or the solubility (physical) carbon pump (Volk & Hoffert, 1985). Physical and biogeochemical processes that occur in the SO are key to controlling global ocean carbon storage, biological productivity, the exchange of CO_2 between the atmosphere and the deep ocean, and the response of the ocean and atmosphere to climate change (Sarmiento et al., 2004; Marshall & Speer, 2012; Klocker, 2018; Gruber et al., 2019). It is therefore vital that we understand the governing mechanisms which drive physical and biogeochemical processes in the SO.

Diapycnal mixing is a key process which drives large-scale ocean circulation and the transport

of tracers globally, but is of such a small scale, well below the resolution of general circulation models, that it has generally been poorly represented in climate models. We are beginning to understand the huge temporal and spatial variability in the strength of diapycnal mixing globally (Whalen et al., 2012). Field campaigns have now repeatedly demonstrated the importance of the SO as a hot spot for this mixing (Naveira Garabato et al., 2004; Watson et al., 2013). This thesis employs a range of models and observational data to investigate the role of diapycnal mixing in the SO on global biogeochemical cycles over a range of timescales.

1.2 Diapycnal Mixing

In this thesis, diapycnal mixing refers to small-scale turbulent mixing which acts across density surfaces and occurs at sub-grid scales, therefore requiring parameterisation. References to mixing throughout this thesis can be assumed to mean diapycnal mixing. As well as acting on density, diapycnal mixing is key to the distribution and transport of physical and biogeochemical tracers including heat, dissolved gases, carbon and nutrients (Sarmiento & Toggweiler, 1984; Law et al., 2003; Friedrich et al., 2011; Whalen et al., 2020).

The input of mechanical energy required for diapycnal mixing in the ocean is provided by a range of highly temporally and spatially variable physical processes. In the upper ocean, diapycnal mixing is generated by convection, winds and Langmuir turbulence. This strong surface mixing leads to the weak stratification of the mixed layer. In the ocean interior, diapycnal mixing is caused primarily by the breaking of internal waves, with a small portion due to shear-driven mixing (Whalen et al., 2020, and references within). Internal waves can be driven by winds, or by tidal and geostrophic flows interacting with rough bottom topography. Tidal currents interact with rough topography generating waves known as internal tides, which either break at their generation site, known as near-field mixing, or propagate over greater distances causing far-field mixing. Surface wind stress excites inertial motions in the surface mixed layer which can radiate downward in propagating near internal waves (Alford, 2020). Double diffusive processes can also cause vertical diapycnal mixing in the ocean. This mixing occurs due to differences in

the molecular diffusivities of heat and salt and can allow the temperature or salinity-induced stratification to become unstable while the overall density stratification is stable. When the potential energy stored in the stratification of the unstable component is released, it drives double-diffusive mixing.

During wave-breaking events, diapycnal mixing can be quantified as the rate at which turbulent kinetic energy is either lost to dissipation or used to work against the ocean density gradients as a buoyancy flux, resulting in diapycnal mixing across density surfaces. When considering diapycnal mixing acting on a water mass, buoyancy can be defined as

$$b = -(\frac{g}{\rho_0})(\rho - \rho_0),$$

where ρ_0 is a reference density, and $\mathrm{N}^2 = \delta_z b$ is the buoyancy frequency squared. The diapycnal buoyancy flux (F) is then approximated as

$$F \approx -\kappa N^2 \approx \Gamma\epsilon,$$

where $\mathcal{K}$ is the rate of turbulent diffusivity ultimately needed to model vertical mixing of tracers, ϵ is the rate at which turbulent kinetic energy is dissipated and lost during wave breaking events, and Γ is the turbulent flux coefficient, often taken to be a constant value of 0.2 (Osborn, 1980).

1.3 The Global Meridional Overturning Circulation

The Global Meridional Overturning Circulation (MOC) is the Earth's large-scale ocean circulation which transports nutrients, heat and other tracers between latitudes, and between the depths of the ocean to the surface ocean where they make contact with the atmosphere. The MOC is composed of two cells, an upper and a lower cell separated in density space (Marshall & Speer, 2012) (Fig.1.1).

The upper cell begins in the Atlantic, where dense waters sink due to surface cooling and brine rejection from sea ice formation (Fig.1.1). These North Atlantic Deep Waters (NADW)

then travel southward towards the SO. Once in the SO, NADW of the upper cell is upwelled to the surface, forming Lower Circumpolar Deep Waters (LCDW). The majority of LCDW (75%) experience buoyancy loss due to further cooling, and travel south, eventually sinking as very dense Antarctic Bottom Waters (AABW). A small proportion of LCDW flows northward, feeding into the upper cell and sinking again as NADW (Sloyan & Rintoul, 2001; Marinov, Gnanadesikan, et al., 2008; Marshall & Speer, 2012; L. D. Talley, 2013; Silvester et al., 2014; Ruan et al., 2017).

The zonal pressure gradient sustained by deep SO topography allows the northward flow of the AABW which sink around Antarctica, forming the lower cell of the MOC (Marshall & Radko, 2003; Ito & Marshall, 2008; Tamsitt et al., 2017). These cold abyssal waters move northward at depth along topographic ridges and canyons, filling the basins of the Indian and Pacific oceans. The abyssal waters mix with the warmer overlying Circumpolar Deep Waters (CDW), reducing their density and allowing the upwelling of abyssal waters along topography to mid-depths (Watson & Naveira Garabato, 2006; Naveira Garabato et al., 2019; Ito & Marshall, 2008; De Lavergne et al., 2016). When the Indian and Pacific deep waters reach the SO and upwell, they are less dense than the LCDW originating in the Atlantic so tend to upwell slightly further north as Upper Circumpolar Deep Waters (UCDW). Here they experience buoyancy gain due to surface warming and freshwater precipitation, and form the northward-flowing Antarctic Intermediate Water (AAIW) and South Antarctic Mode Water (SAMW), as part of the upper cell (Marshall & Speer, 2012; Ruan et al., 2017). These waters eventually return to the SO as North Atlantic Deep Waters (NADW), completing the upper MOC cell (L. D. Talley, 2013).

1.3.1 The MOC and Diapycnal Mixing

The dense waters which sink in the Atlantic and the SO as NADW and AABW must eventually return to the surface of the ocean to enable global circulation at all depths and prevent deep waters from stagnating. Where these dense waters return to the ocean surface has been historically poorly understood. A key process in maintaining the stratification of the deep ocean is the transformation of dense abyssal bottom waters of the lower cell into lower-density deep

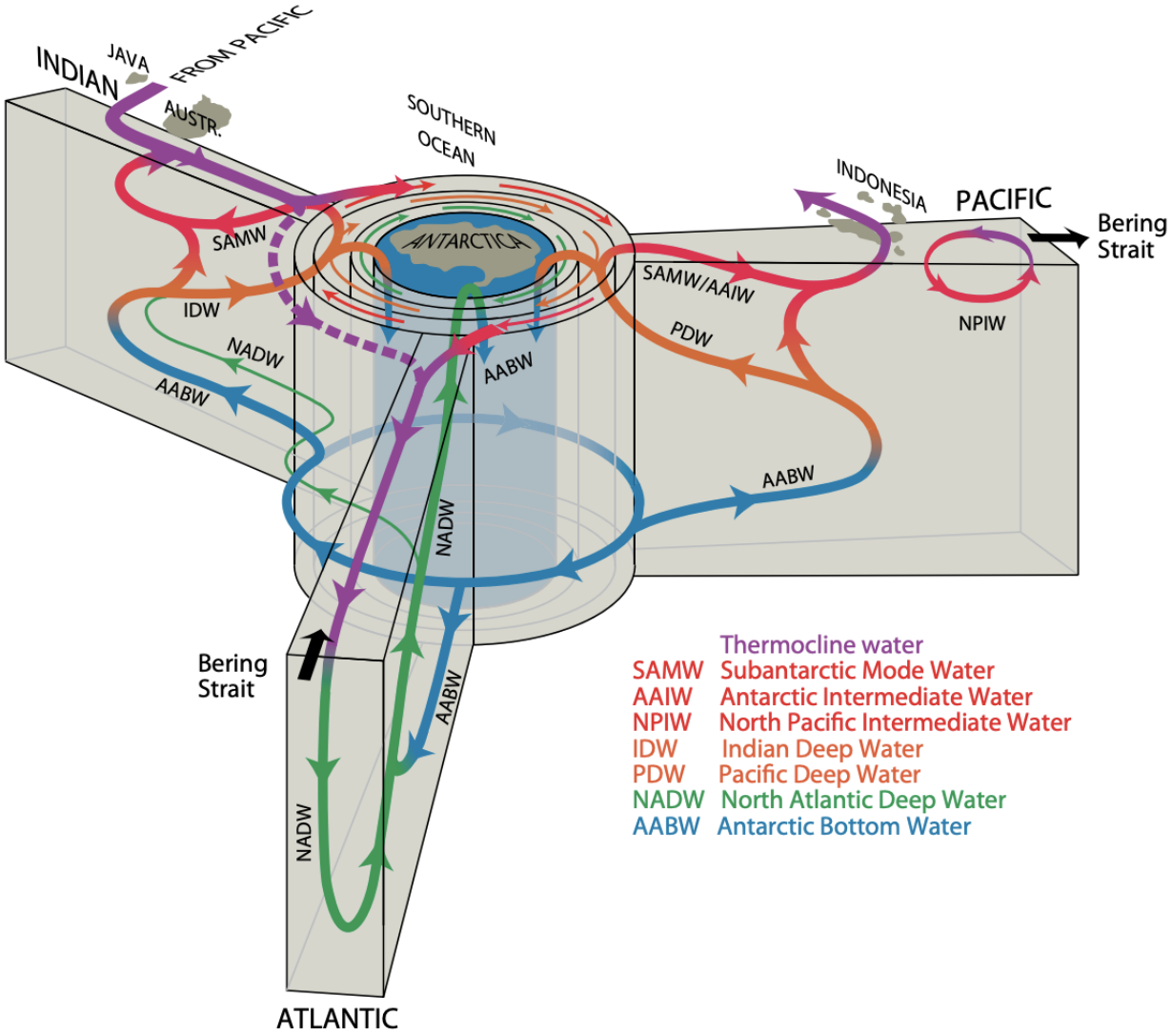


Figure 1.1: A schematic of the global Meridional Overturning Circulation (MOC) from a Southern Ocean perspective. Figure from L. D. Talley (2013).

waters. This is driven by turbulent vertical mixing causing an irreversible transformation of the density of abyssal waters (Polzin et al., 1997; W. Munk & Wunsch, 1998; Waterhouse et al., 2014). This makes diapycnal mixing key in closing the MOC (W. H. Munk, 1966; W. Munk & Wunsch, 1998; Law et al., 2003; Wunsch & Ferrari, 2004; Watson & Naveira Garabato, 2006; Marshall & Speer, 2012; L. D. Talley, 2013; De Lavergne et al., 2016).

W. H. Munk (1966) initially hypothesised that the 25 Sverdrups (Sv, 1×10^6 m^3 s^{-1}) of bottom waters sinking at the ocean poles must be balanced by an equivalent level of upwelling. This meant that a uniform diapycnal diffusivity rate of $\approx 10^{-4}m^2$ s^{-1} was required in the ocean interior. However, observations of diapycnal mixing rates in the pycnocline and the abyssal ocean, obtained via tracer release experiments and full-depth microstructure data revealed mixing rates an order of magnitude smaller, with most areas of the ocean experiencing mixing of $\mathcal{O}(10^{-5})m^2$ s^{-1} in the ocean interior (Ledwell et al., 1993, 2000; Polzin et al., 1997). This presented a paradox; if mixing does not produce the energy to raise the dense waters, how is deep water formation balanced? Subsequent work has shown that mixing rates are elevated along topography and close to the sea floor, and at ocean boundaries, indicating that vertical mixing in the ocean is highly localised (W. Munk & Wunsch, 1998; L. D. Talley et al., 2003; L. D. Talley, 2013; Waterhouse et al., 2014; Ferrari, 2014). The spatial variations in diapycnal mixing rates mean that upwelling in the deep ocean does not occur uniformly, opposing traditional views of circulation. The SO is now known as one of the largest and most important regions of mixing Passage (Naveira Garabato et al., 2004).

1.4 The Importance of the Southern Ocean for the MOC

1.4.1 Southern Ocean Circulation

Within the latitudes of the Drake Passage, strong westerly winds face no continental barriers to their flow. Wind-driven currents, coupled with the Coriolis rotation of the earth cause the transport of waters to the north. This water mass divergence is balanced by the Ekman

upwelling of CDW, composed of younger LCDW and older UCDW from around 2000 m deep to the SO Polar Front (PF) (Fig.1.2). Ekman upwelling provides an adiabatic upwelling route to the ocean surface with minimal diapycnal mixing, meaning that diapycnal mixing only needs to provide the energy to raise dense waters to the depths at which wind-driven Ekman upwelling occurs (Gnanadesikan, 1999; Marshall & Speer, 2012).

The Ekman transport causes a north-to-south gradient in sea surface height, with higher sea levels further north. This meridional pressure gradient causes a strong, deep-reaching geostrophic flow all around Antarctica, known as the Antarctic Circumpolar Current (ACC) (St. Laurent et al., 2012). Within the ACC, the most intense density gradients between water masses induce geostrophic flows, known as jets, which are regions of the most intense ACC flows (St. Laurent et al., 2012). Jets are deep-reaching and persistent physical and chemical fronts which divide the SO into distinct physical and biogeochemical zones, forming boundaries between water masses (Orsi et al., 1995; Chapman et al., 2020). The interaction of the strong ACC currents with topography creates highly energetic regions which are hot spots of eddy kinetic activity (Dufour et al., 2013; Thompson & Sallée, 2012). In the upper ocean, eddies work against the mean wind-induced northward zonal circulation to flatten isopycnals, reducing the strength of the MOC (Speer et al., 2002).

1.4.2 Diapycnal Mixing in the Southern Ocean

While the role of mixing by mesoscale eddies has been understood to be key in setting patterns of SO circulation, the role of small-scale turbulence and diapycnal mixing has been less understood until recently due to a shortage of observations (Saenko, 2008; Naveira Garabato et al., 2004). Natural and man-made tracer release experiments, inverse estimates and fine structure measurement studies have all revealed that high rates of diapycnal mixing occur within the SO (P. W. e. a. Boyd, 2000; Naveira Garabato et al., 2004; D. C. Bakker et al., 2005; Thompson et al., 2007; Watson et al., 2013; Naveira Garabato et al., 2019; Ledwell et al., 2011). Within the SO internal waves formed by strong winds, and by strong ACC bottom currents and tides interacting with bottom topography break, dissipating energy to small-scale turbulence, elevating

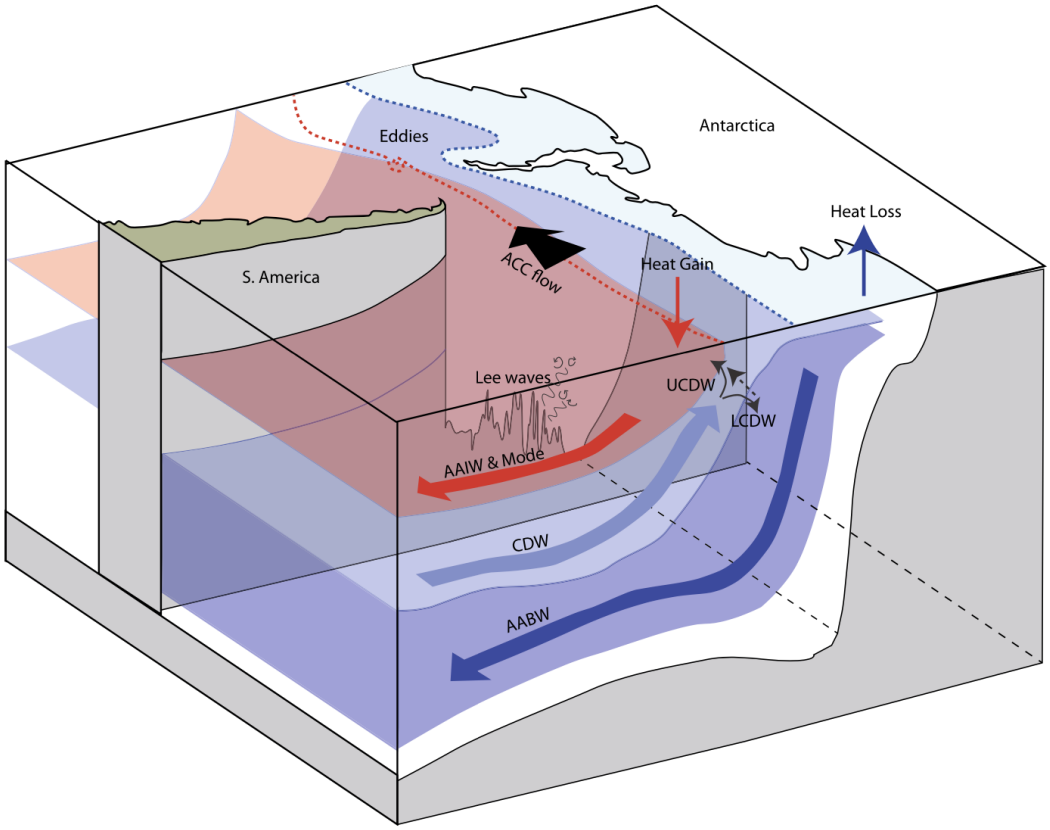


Figure 1.2: A schematic of Southern Ocean processes. The Antarctic Circumpolar Current (ACC) flowing eastward (black arrow), Circumpolar Deep Water (CDW) upwelling at about the same latitude as the ACC (light blue arrow), and the upper and lower cells of the meridional overturning circulation. Near the surface, Upper Circumpolar Deep Water (UCDW) advects northward and contributes to Antarctic Intermediate Water and mode water formation. Lower Circumpolar Deep Water (LCDW) loses heat near Antarctica and sinks to form Antarctic Bottom Water (AABW). Figure from Gille et al. (2022)

the rates of diapycnal mixing. Over abyssal ridges, mountains and rises, elevated mixing rates can extend up through the water column (Watson & Naveira Garabato, 2006; Silvester et al., 2014; Ferrari, 2014; Naveira Garabato et al., 2004; Nikurashin & Ferrari, 2013). Observations have revealed strong regional variations in diapycnal mixing rates, with values ranging from 10^{-5} m^2 s^{-1} to as high as 10^{-3} m^2 s^{-1} in energetic regions with rough bottom topography (Naveira Garabato et al., 2004; Thompson et al., 2007; Ledwell et al., 2011; Whalen et al., 2012; Watson et al., 2013; Naveira Garabato et al., 2019; St. Laurent et al., 2012; Mashayek, Ferrari, et al., 2017).

Bottom intensified mixing actually results in buoyancy losses associated with downwelling in most of the ocean, with buoyancy gain and upwelling of abyssal waters occurring within just a thin bottom boundary layer (Ferrari et al., 2016). This suggests that AABW upwelling is confined to the actively mixing turbulent boundary layers directly over rough topography (Ferrari et al., 2016; De Lavergne et al., 2016), where the upward mixing is so intense that it is able to overcome the weaker interior diapycnal sinking (Ferrari et al., 2016). This confined upwelling facilitates the transfer of water in the lower cell to mid-depths (Watson & Naveira Garabato, 2006; Marshall & Speer, 2012; Mashayek, Ferrari, et al., 2017) of around 2000 m, where waters are then lifted to the SO surface adiabatically (Marshall & Speer, 2012; Ferrari et al., 2016; Ruan et al., 2017). Therefore the ventilation of the densest waters in the world is largely diapycnally driven (Naveira Garabato et al., 2004; Watson & Naveira Garabato, 2006; Ito & Marshall, 2008; Badin et al., 2013). A significant proportion of global bottom water upwelling occurs within the SO (Naveira Garabato et al., 2004). Diapycnal mixing in the ACC is key to global and regional circulation, controlling the rates that water sinking at high latitudes can return to the surface (Garabato et al., 2007) and determining the deep ocean stratification through a balance between upwelling of dense waters and downward diffusion of light waters (Ferrari, 2014).

1.5 The Role of the Southern Ocean in Controlling Global Biogeochemical Cycles

The SO is a key region for global biogeochemical cycles and is a key regulator of the global climate (Sarmiento & Toggweiler, 1984). Waters south of 35°S absorb around 1 Pg C yr^{-1}, which is around 40% of the global annual ocean uptake of carbon (Gruber et al., 2009; Khatiwala et al., 2009; Takahashi et al., 2009, 2012; Wanninkhof et al., 2013; Rödenbeck et al., 2013; Landschützer et al., 2015). The disproportionate importance of the SO in controlling the global climate system is largely due to SO circulation.

Organic Matter (OM) fixed by photosynthetic phytoplankton sinks out of the euphotic zone and is remineralised within the water column, releasing nutrients and Dissolved Inorganic Carbon (DIC) to abyssal and deep ocean waters (Gnanadesikan et al., 2001; Marinov, Gnanadesikan, et al., 2008). Upwelling in the SO means that the SO connects the vast reservoir of remineralised nutrients and carbon stored within the deep ocean interior with the surface mixed layer (Lumpkin & Speer, 2007; Palter et al., 2010; Marshall & Speer, 2012; L. D. Talley, 2013; C. M. Moore et al., 2013). Here, carbon that has been isolated from the atmosphere for centuries is exchanged with the atmosphere, leading to the outgassing of naturally occurring carbon, while the upwelled nutrients can be utilised by phytoplankton leading to biological draw down, removing carbon from the atmosphere.

Nutrients upwelling in the SO are not fully utilised by phytoplankton due to the short residence time in the surface ocean, low temperatures, low light levels (Fauchereau et al., 2011) and low iron (Fe) concentrations (Martin, 1990; C. M. Moore et al., 2013). This makes the SO the world's largest High Nutrient Low Chlorophyll (HNLC) zone (J. K. Moore et al., 2004). The high surface nutrient concentrations in the SO are a sign of low biological efficiency, meaning nutrients are not used by phytoplankton to fix carbon into biomass.

When CDW upwell in the SO, there is a divergence known as the SO biogeochemical divide, where waters can join either the upper or the lower cell (Marinov et al., 2006). The nutrients

which upwell south of this divide and into the lower cell sink with the AABW without being incorporated into OM, and are known as preformed nutrients (Lauderdale et al., 2013). AABW ventilate such a large volume of deep waters and have such a high preformed nutrient concentration that they are the largest source of preformed nutrients to the deep ocean (Toggweiler et al., 2006; Marinov et al., 2006; Marinov, Follows, et al., 2008; Afkar, 2012). Nutrients which upwell north of this divide into waters of the upper cell are also not fully utilised by phytoplankton. They are entrained and subducted into SAMW and advected and mixed across the ACC (Sarmiento et al., 2004). From there they supply the global thermocline with nutrients, accounting for around 75% of the biological production north of 30°S (Sarmiento et al., 2004; Dutkiewicz et al., 2005; Marinov et al., 2006). Nutrients then re-enter the deep ocean via the biological carbon pump, eventually returning to the surface of the SO, completing the MOC.

1.6 Representing Diapycnal Mixing in Models

Ocean circulation models do not resolve the processes responsible for diapycnal mixing as they occur on scales much smaller than the resolution of Earth System Models (ESM), and so are parameterised in terms of a turbulent effective diffusivity, $\mathcal{K}$ (Large et al., 1994). Diapycnal mixing is difficult to accurately parameterise, due to the intermittency of the wide range of generating mechanisms (J. MacKinnon et al., 2013). To allow for the separation of the primarily wind-driven mixing above the thermocline and primarily tidally driven mixing below it, the parameterisation of diapycnal mixing in ESM is often made up of two components;

1. Surface mixed layer mixing from storms and other surface winds, as well as convective instabilities (Gaspar et al., 1990; Large et al., 1994; Fox-Kemper et al., 2022).

2. Background turbulence, representative of otherwise unparameterised processes, including the breaking of internal waves (Jayne & St. Laurent, 2001; Simmons et al., 2004; Wunsch & Ferrari, 2004; J. A. MacKinnon et al., 2017). The 'background' mixing in the ocean interior is typically several orders of magnitude smaller than that in the surface mixed layers.

Though diapycnal mixing is highly temporally and spatially variable due to its generating mechanisms, it is often parameterised as either a single constant value between 10^{-4} m^2s^{-1} and 10^{-5} m^2s^{-1}, a horizontally homogeneous value that varies as a function of depth or bottom roughness, or a temporally fixed spatially variable pattern as a function of stability (F. Bryan, 1987). Current best estimates of SO diapycnal mixing are based on 'static' maps, produced with numerous limiting assumptions, approximating to the contributions from topographically generated lee waves (Nikurashin & Vallis, 2011; Shakespeare, 2020), wind-induced near-inertial waves (Alford, 2020), and internal tides (Lavergne et al., 2020). These maps have formed the basis of our representation of such processes in ESM (A. Melet et al., 2014; A. V. Melet et al., 2022).

1.6.1 The Sensitivity of the Meridional Overturning Circulation to Diapycnal Mixing

The strength of the MOC and the magnitude of global heat transport are both sensitive to the parameterisation of $\mathcal{K}$. Altering $\mathcal{K}$ changes the vertical profile and horizontal distribution of temperature and salinity throughout the ocean, altering the density and stratification (A. Melet et al., 2016; Hieronymus et al., 2019; A. Melet et al., 2014; Tatebe et al., 2018). In simple ocean circulation models, as $\mathcal{K}$ increases, both the meridionally integrated zonal mass transport and the zonally integrated meridional mass transport increase, strengthening the MOC, while the thermocline becomes more diffuse (Gnanadesikan et al., 2003; Marinov, Follows, et al., 2008; Nikurashin & Vallis, 2011, 2012). Using a spatially variable mixing rate has been shown to influence the magnitude and vertical structure of the MOC, the deep ocean stratification, the thermocline depth, the bottom water circulation strength in the north Pacific, the horizontal circulation via vorticity dynamics, water mass properties and the depth and intensity of the ACC (Saenko & Merryfield, 2005; Simmons et al., 2004; Saenko, 2006; Oka & Niwa, 2013; A. Melet et al., 2016; Jayne, 2009; Saenko et al., 2012; A. Melet et al., 2014; Hieronymus et al., 2019). Including a representation of near field tidal mixing, far-field tidal mixing and eddy dissipation generated mixing all improve the fit of model outputs the observations of the MOC

(Simmons et al., 2004; Saenko & Merryfield, 2005; Jayne, 2009; Saenko et al., 2012; Oka & Niwa, 2013).

Many physical and biogeochemical properties are not influenced as strongly by the horizontally averaged mixing rates, but depend on details of the horizontal distribution (Simmons et al., 2004; Friedrich et al., 2011) and the vertical structure (Saenko et al., 2012), impacting circulation patterns, heat transport, stratification and the climate response to atmospheric CO_2. (Friedrich et al., 2011; Saenko, 2006). The heat transport of the ocean is potentially even more sensitive to the spatial distribution of mixing than the circulation (Saenko, 2006; Jayne, 2009). Alterations to ocean mixing can also impact air temperatures, atmospheric circulation and precipitation (A. Melet et al., 2016; Hieronymus et al., 2019; Zhu et al., 2020), indicating the importance of representative parameterisation of mixing in climate-scale models.

1.6.2 The Sensitivity of the Meridional Overturning Circulation to Southern Ocean Diapycnal Mixing

Theoretical studies have highlighted that diapycnal mixing rates in the SO are not of leading order importance for regulating the global MOC, secondary to the role of SO winds, eddies, and surface buoyancy forcing (Schmittner et al., 2005; Nikurashin & Vallis, 2012). Larger increases in the strength of the MOC are associated with slight increases in diapycnal mixing in the global pycnocline, rather than with a larger magnitude increase of diapycnal mixing in just the SO (Gnanadesikan et al., 2001). The rate of diapycnal mixing in the SO, and the representation of bottom intensified mixing are both still critical in driving the MOC (Gnanadesikan et al., 2004; Matsumoto et al., 2004; Palter et al., 2010). Isopycnal slopes in the SO are key in determining the depth of the global pycnocline (Gnanadesikan, 1999; Nikurashin & Vallis, 2011). Diapycnal mixing in the SO also plays a key role in controlling SO water mass transformations (Whalen et al., 2012; Sun et al., 2018), which can lead to significant alterations in the MOC. The representation of bottom enhanced mixing in the SO is known to enhance the transformation of AABW and LCDW to UCDW (Saenko, 2008), with these transformations especially important in driving the Pacific MOC (Tatebe et al., 2018). High rates of mixing and strong winds in

the SO are required to accurately simulate the observed C_{14} concentrations in the surface and deep ocean, whilst also achieving the desired strength of the ACC (Palter et al., 2010).

1.7 The Impact of Diapycnal Mixing on Biogeochemical Tracer Distributions

Ocean biogeochemistry is strongly controlled by ocean physics and circulation (Gnanadesikan et al., 2001). A generalised tracer equation is given by

$$\frac{\delta C}{\delta T} = -\frac{\delta C}{\delta x}u + \frac{\delta}{\delta x}(\kappa\frac{\delta C}{\delta x}),$$

where C is the concentration of any tracer per unit volume, u is the velocity and $\mathcal{K}$ is the diffusivity of the tracer. The first term on the right-hand side represents tracer advection, while the second term represents diffusive diapycnal tracer transport. This means that diapycnal mixing allows the diffusive movement of tracers across density layers, independent of the bulk advective tracer transport which control the MOC (Groeskamp et al., 2019).

Therefore diapycnal mixing can alter tracer distributions in two ways; directly via modified diapycnal mixing, and indirectly via altering tracer distributions via advection due to changes in the MOC (Doney et al., 2004; Gnanadesikan et al., 2004; L. Talley et al., 2016; Matsumoto et al., 2004).

1.7.1 The Direct Impact of Mixing on Tracers

An increased strength of diapycnal mixing increases the down gradient flux of a tracer. Schmittner et al. (2005) revealed a large sensitivity of chlorophyll concentration to the vertical mixing scheme, especially in low latitudes. This work also revealed the sensitivity of the nutracline depth to the strength of vertical diffusion. Gnanadesikan et al. (2001) reported a doubling of new production in response to an increase of vertical diffusivity in the upper 2000 m of the water

column due to an increase in convection and in vertical diffusive and advective fluxes. These works demonstrate the importance of the diapycnal mixing rate on biogeochemical cycles.

1.7.2 The Indirect Impact of Mixing on Tracers

The global rate of deep ocean heat and carbon uptake is determined by the large-scale overturning circulation, controlled to first order by vertical diffusivity parameters in the ocean component of climate models (K. Bryan & Lewis, 1980; Gnanadesikan et al., 2003; Wunsch & Ferrari, 2004; Ross et al., 2012). Strengthened diapycnal mixing strengthens the MOC, and results in younger SO deep waters (Marinov, Gnanadesikan, et al., 2008; Friedrich et al., 2011), increased convection and upwelling of deep waters into the SO and increased deep ocean ventilation via the AABW (Marinov, Follows, et al., 2008). This increases the advective transport of tracers including nutrients to the surface waters. Higher ventilation of intermediate waters in the SO reduces ocean carbon storage through the biological and solubility carbon pumps due to inefficient biological activity in the SO, causing the global preformed nutrient pool to increase, reducing the organic carbon pool (Marinov, Gnanadesikan, et al., 2008; Marinov & Gnanadesikan, 2011; Gnanadesikan et al., 2004; Lauderdale et al., 2013). Stronger diapycnal mixing can also deepen the global pycnocline, warming the upper ocean, altering the solubility of gases (Friedrich et al., 2011; Watson & Naveira Garabato, 2006; Ferrari et al., 2014) and decreasing the saturated carbon reservoir (Lauderdale et al., 2013). Using spatially variable mixing rates to represent topographically enhanced diapycnal mixing also has a significant impact on deep ocean ventilation and ocean biogeochemistry including primary productivity and the extent of oxygen minimum zones (Dutreuil et al., 2009; Friedrich et al., 2011).

Variations in deep ocean carbon storage due to increased vertical mixing and changes in the strength of the MOC are known to emanate primarily from the SO via changes to the strength of AABW convection relative to the strength of NADW formation (Marinov, Gnanadesikan, et al., 2008). CDW is composed of both the younger LCDW and the older carbon and nutrient-rich UCDW. The relative amounts of these different CDW components in the upwelling waters can alter the upwelled ocean carbon and nutrient content and heat supply to the SO (Tamsitt

et al., 2017), meaning the relative strength of the upper to lower MOC cell can alter air-sea carbon partitioning (Toggweiler et al., 2006).

1.8 The Impact of Southern Ocean Diapycnal Mixing on Biogeochemistry

The importance of background diapycnal mixing rates for biogeochemical tracer distributions has largely been assumed to be due to the role of mixing rates in the underlying dynamics of the MOC. SO diapycnal mixing is not a leading order control on the strength of the MOC, with SO winds instead playing a key role in setting its strength (Nikurashin & Vallis, 2011, 2012). Therefore, most studies (as mentioned in the previous paragraph) have assessed global changes in background diapycnal mixing rates on circulation and biogeochemistry, rather than focusing on changes associated with altered mixing rates in the SO.

However, in the SO interior, diapycnal mixing allows for further vertical transport of waters and tracers, likely to be of key importance for ocean biogeochemistry (Watson et al., 2013; Garabato et al., 2007; Mashayek, Ferrari, et al., 2017). The long residence time of tracers near mixing hot spots allows the tracer to experience above background levels of diapycnal diffusivity (Mashayek, Ferrari, et al., 2017). Changes in SO mixing rates alter the distribution of C_{14} and oxygen more than they alter the pycnocline structure or the strength of the MOC (Gnanadesikan et al., 2004), this is likely to apply to other key tracers of ocean biogeochemistry. Despite this, the sensitivity of ocean biogeochemical tracer distributions to vertical background mixing in the SO remains largely unquantified. Understanding the response of biogeochemical tracers to altered diapycnal mixing in the SO on a range of timescales is key to demonstrating the importance of correctly parameterising SO diapycnal mixing. A better understanding of the governing mechanisms of the SO climate system is essential for an accurate representation of the response of the climate to increasing atmospheric greenhouse gases.

1.9 Aims and Objectives

This PhD aims to:

- *Examine the sensitivity of biogeochemical cycles and tracer distributions to diapycnal mixing rates in the SO below the mixed layer on both long and short timescales due to altered advection and direct tracer mixing.*

  This will be achieved through the use of a zonally averaged model of the Atlantic Ocean with a simple biochemical model.

- *Demonstrate the sensitivity of biogeochemical tracer distributions to diapycnal mixing rates on short timescales and understand the mechanisms behind the sensitivity of SO carbon fluxes and SO biological productivity to alter diapycnal mixing rates on short timescales.*

  This will be achieved through the use of an ocean state estimate of the SO, which includes a biogeochemical model and assimilates a host of in-situ and remote sensing data. The model will be run for 6 years with a range of diapycnal mixing parameterisations.

- *Investigate whether biogeochemical tracer observations can be used to constrain SO diapycnal mixing rates.*

  This will be achieved by comparing model outputs with biogeochemical cycles with observational data of biogeochemical tracer distributions. We will compare if model outputs for spatially variable diapycnal mixing maps have an improved fit to data compared with models with constant diapycnal mixing parameterisations.

1.10 Thesis Outline

Firstly in Chapter 2, using an idealised model of the Atlantic MOC, we show that altering the SO vertical mixing rate alters biogeochemical tracer distributions throughout the Atlantic

over short and long timescales. On centennial timescales, alterations are dominated by the mixing-induced variations in the advective transport of the tracers by the Atlantic MOC. On annual to decadal timescales, they are dominated by the direct impact of changes in diapycnal mixing on tracer fluxes.

This work is then extended in subsequent chapters using an eddy-resolving biogeochemical-ocean model of the SO that assimilates an extensive array of observations, run using three different background diapycnal mixing parameterisations, as detailed in Chapter 3. In Chapter 4 we demonstrate that increased mixing enhances SO biomass by altering key biogeochemical and physical parameters. An increased surface supply of Fe is responsible for biomass increases in most areas, although changes in surface water temperature and nitrate availability are key to altered biological productivity in some areas. In Chapter 5 we show that higher diapycnal mixing causes a significant reduction in annual mean SO carbon uptake. The changes to SO carbon fluxes with altered mixing show spatial and seasonal variability due to the different vertical structures of DIC and temperature.

Finally, in Chapter 6 SO physical and biogeochemical tracer observations are compared to the B-SOSE solution for a high mixing, low mixing and a spatially variable mixing map. Biogeochemical tracer distributions are generally best modelled using a low mixing parameterisation, with no significant reduction in the cost function to observations when using a spatially variable map. This suggests that more work is needed to construct SO mixing maps that capture the temporal and spatial variability observed in the SO.

1.11 Publications

Published;

E. Ellison, L. Cimoli, A. Mashayek, "Multi-timescale control of Southern Ocean diapycnal mixing over Atlantic tracer budgets", Climate dynamics 2022. DOI:10.1007/s00382-022-06428-5.

In Review; Revised version submitted on 23/06/23 after minor corrections;

E. Ellison, A. Mashayek, M. Mazloff, "Hypersensitivity of Southern Ocean air-sea carbon fluxes to background turbulent diapycnal mixing", JGR Oceans. DOI:10.22541/essoar.167768107.74708518/v1

Near to submission;

E. Ellison, M. Mazloff, A. Mashayek, "Enhanced Southern Ocean biomass with increased Diapycnal mixing".

Chapter 2

Multi-time Scale Control of Southern Ocean Diapycnal Mixing Over Atlantic Tracer Budgets

The work in this chapter is published as E. Ellison, L. Cimoli, A. Mashayek (2022) "Multi-timescale control of Southern Ocean diapycnal mixing over Atlantic tracer budgets", Climate Dynamics, 60 (9), 3039–3050.

2.1 Abstract

Oceanic diapycnal mixing helps sustain the ocean density stratification and its Meridional Overturning Circulation (MOC) and is key to global tracer distributions. The Southern Ocean (SO) is a key region for the connection of the upper and lower branches of the MOC, and is where nutrient and carbon rich deep waters resurface. The SO is also rife with localized intense diapycnal mixing due to breaking of internal waves induced by the interaction of energetic eddies and currents with rough topography. SO diapycnal mixing is believed to be of secondary importance for the meridional overturning circulation (MOC). Here we show that changes to SO mixing can cause significant alterations to global biogeochemical tracer distributions over short and long timescales. While such alterations are dominated by the direct impact of changes in

diapycnal mixing on tracer fluxes on annual to decadal timescales, on centennial timescales they are dominated by the mixing-induced variations in the advective transport of the tracers by the global MOC. On long time scales, significant changes in the partitioning of carbon between the atmosphere and the ocean occur as a result of alterations to SO diapycnal mixing.

2.2 Introduction

The Meridional Overturning Circulation (MOC) transports biogeochemical tracers including carbon and nutrients meridionally and vertically between the surface and the deep ocean. The MOC moves tracers around via advection, while tracers may also experience material changes due to turbulent mixing processes with their surroundings (Groeskamp et al., 2019). Therefore the effects of altered diapycnal mixing in the SO can be broadly split into two categories; local direct effects due to mixing acting directly on tracers, and remote indirect effects from changes to the larger-scale flow and tracer advection. In this chapter, we consider the relative importance of both of these responses to altered diapycnal mixing on biogeochemical tracers on a range of timescales, from decadal to millennial.

The buoyancy forcing experienced by deep water masses that upwell in the SO are key in setting the future fate of water masses and the tracers they contain (Fig.2.1). As Circumpolar Deep Waters (CDW) upwell, they can enter into a region with fresh water and heat inputs, leading to positive buoyancy forcing and are transported northward into Antarctic Intermediate Water (AAIW) and South Antarctic Mode Water (SAMW) as part of the upper MOC cell (Marshall & Speer, 2012; Ruan et al., 2017) (Fig.2.1 Red Circulation). Conversely, Lower Circumpolar Deep Waters (LCDW) upwell into a region of negative buoyancy forcing due to air-sea fluxes and sea-ice export near the cold continent, principally in the Ross and Weddell seas (Marinov, Gnanadesikan, et al., 2008; Marshall & Speer, 2012). These waters sink to form Antarctic Bottom Water (AABW), subducting huge quantities of carbon and preformed nutrients (Sloyan & Rintoul, 2001; Silvester et al., 2014; Marinov et al., 2006; Ruan et al., 2017; Marshall & Speer, 2012) (Fig.2.1 blue circulation and grey nutrient rich regions).

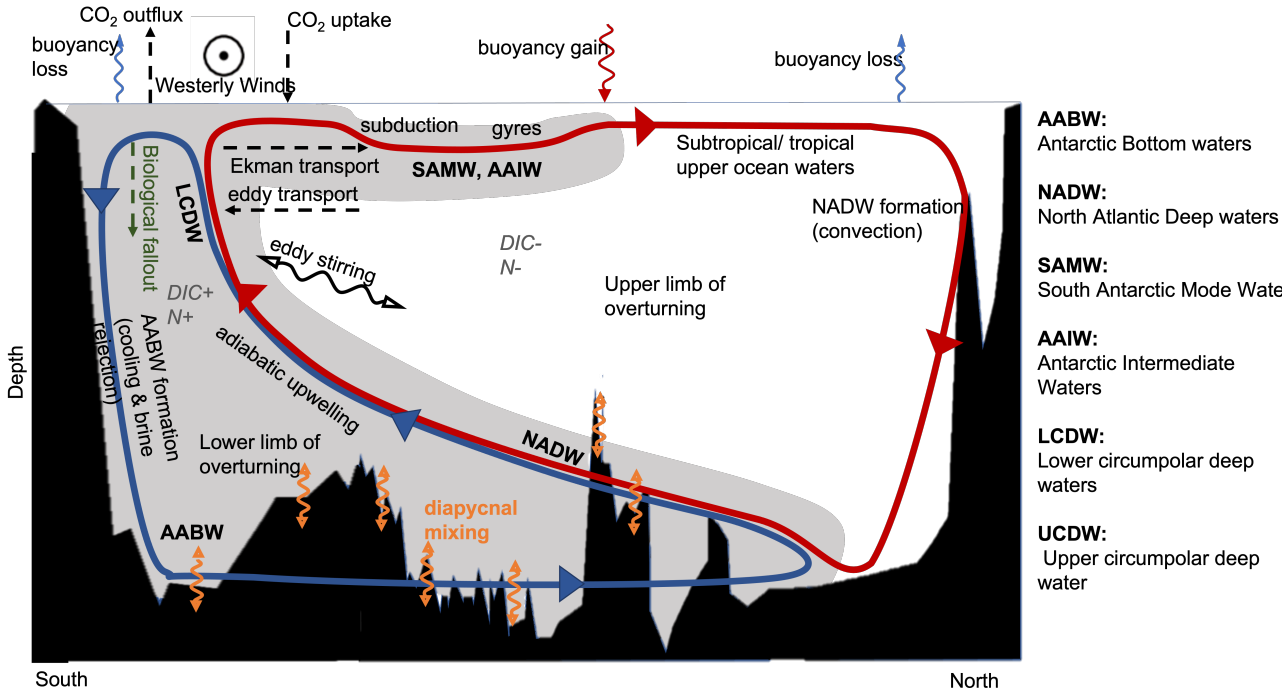


Figure 2.1: A schematic of the Atlantic Ocean circulation with an emphasis on the SO dynamics, water masses, and tracers. The upper cell is represented in red, while the lower cell is represented in blue. Diapycnal mixing occurs over rough topography. Regions in grey have high concentrations of nutrients and carbon. Adapted from Lauderdale et al. (2013) and L. D. Talley (2013).

Diapycnal mixing allows water mass transformations to occur at depth, with these transformations generally directed from denser to lighter layers of the Antarctic Circumpolar Currents (ACC) (Garabato et al., 2007). Observations suggest that deep SO waters and the tracers they contain flow over complex topography, and can short-circuit between the two cells of the MOC (Garabato et al., 2007), providing an alternative return path for the lower limb of the MOC (Watson et al., 2013; Ruan et al., 2017). It is also likely that some UCDW and LCDW are converted to denser AABW by topographic mixing in the ACC, short-circuiting from the upper to the lower branch of circulation (Garabato et al., 2007; Badin et al., 2013). This suggests that the traditional view of two entirely separate overturning cells is not appropriate, and the impact of higher mixing rates in the SO and short-circuiting on biogeochemical tracers should also be considered.

Limited work has assessed the sensitivity of biogeochemical tracer distributions to SO diapycnal mixing rates (Gnanadesikan et al., 2001, 2004). These works have failed to investigate whether changes to tracer distributions are due to direct impacts of mixing acting on tracers, rather than

centennial to millennial time scale changes to the MOC. In this chapter, we examine (i) the role of diapycnal mixing in the SO on Atlantic tracer budgets over varying timescales, using an idealised single-basin model, and (ii) whether these changes are due to altered tracer diffusion or changes to the ocean circulation.

We find that the strength of the Atlantic MOC is sensitive to the parameterised SO diapycnal mixing rates. The altered mixing also causes changes in tracer distributions and in the air-sea partitioning of carbon. We show that diapycnal mixing in the SO is crucial in setting the distribution of tracers on a range of timescales through two mechanisms. On centennial timescales, circulation and tracer advection changes dominate, especially when looking at distribution changes on a global scale, whereas changes to tracer diffusion dominate over annual to decadal timescales, especially within the SO region.

2.3 Methods

This work uses the zonally-averaged model of the Atlantic Meridional Overturning Circulation (AMOC) by Nikurashin and Vallis (2012) (hereafter NV12), extended in Watson et al. (2015) to include a simple biogeochemical model based on that introduced in Ito and Follows (2005). The model, and similar ones, have been used extensively over the past decade to study various aspects of the role of the MOC in the climate system from both dynamical and biogeochemical perspectives (Mashayek et al., 2013; Stewart et al., 2014; Ferrari et al., 2014; Watson et al., 2015; Jansen & Nadeau, 2016). Thus, we simply provide a brief phenomenological description of the model here and refer the reader to the original works for more details.

2.3.1 The Physical Model

In the NV12 model, the Atlantic Ocean is split into three key areas: a SO circumpolar channel, a NADW formation zone, and the ocean mid-latitude basin that connects the two. While NV12 employed a constant vertical diffusivity ($\mathcal{K}$) value throughout the water column in all

three zones, here we consider vertically variable mixing and distinguish between the mixing in the North Atlantic and mid-latitude basin from that in the SO. Here, we study the sensitivity of tracer distributions to variations in SO diapycnal mixing.

2.3.2 The Biogeochemical Model

The simple biogeochemical component that was added to NV12 in (Watson et al., 2015) allows for the representation of the coupled evolution of Nutrients (N) and Carbon (C), where N represents the ultimate limiting nutrient phosphate. Organic material is parameterised to sink downward, measured in units of phosphate, with the biological export time scale set to 360 days. A well-mixed atmospheric box is coupled to the ocean carbon cycle such that the partitioning of C between the atmosphere and the ocean is explicitly calculated in the model. The model conserves the total amount of C in the atmosphere and the ocean; if C is gained in the ocean, it must be lost in the atmosphere.

The biogeochemical tracers (C, N) are transported by advection and diffusion and have sources and sinks via biological activity (F_p) of uptake and remineralisation. The concentration of C is able to change via surface fluxes driven by $p\mathrm{CO}_2$ differences to account for air-sea gas transfer. More explicitly, the equations for C and N are;

$$\partial_t N + J(\psi, N) = \partial_z(\mathcal{K}\partial_z N) + \partial_z F_p, \tag{2.1}$$

$$\partial_t C + J(\psi, C) = \partial_z(\mathcal{K}\partial_z C) + R\partial_z F_p + C_{flux}\|_{z=0}, \tag{2.2}$$

$$C_{flux} = -(k_w \times k_H) \times (pCO_2a - pCO_2o) \times (1 - \text{ice cover}), \tag{2.3}$$

where ψ is the meridional overturning streamfunction representing the AMOC (Fig.2.1, Fig.2.3a, b), k_w is the air sea CO_2 exchange constant, k_H is the fugacity of CO_2, $p\mathrm{CO}_2$a is the partial pressure of CO_2 in the atmosphere, and $p\mathrm{CO}_2$o is the partial pressure of CO_2 in the surface ocean, all as in (Watson et al., 2015). The second term on the left represents advection of N and C by the AMOC, the first term on the right represents turbulence diapycnal mixing, and the final term represents biological activity (Ito & Follows, 2005). Biological activity in surface

waters removes both N and C at the ratio set by R, with N and C both released by respiration as organic matter sinks.

2.3.3 Experiment Design

Our goal is to explore the sensitivity of the AMOC and tracer budgets to SO mixing. In all experiments (soon to be introduced), the mixing in the mid-latitude basin will be fixed to an average of estimates of the diapycnal mixing ($\mathcal{K}$) based on the tidal mixing estimates of Lavergne et al. (2020) and the lee wave mixing estimates of Nikurashin and Ferrari (2013) combined (Fig.2.2a), with the resultant profile shown by the blue curve in Fig.2.2c ($\mathcal{K}_B$). Unlike NV12, here $\mathcal{K}_B$ varies with depth, showing high mixing rates in bottom waters up to a depth of around 2500 m. These high mixing rates at mid-depths are representative of the high mixing rates experienced over the Mid-Atlantic ridge due to tidally generated bottom currents interacting with rough topography causing the breaking of internal waves. All surface forcings are kept constant in all experiments and are as prescribed in NV21 (Nikurashin & Vallis, 2012). In the SO, we consider three paradigms:

1. the Low mixing scenario of $\mathcal{K}_\mathcal{L} = 10^{-5}$ m^2/s,
2. the High mixing scenario of $\mathcal{K}_\mathcal{H} = 10^{-4}$ m^2/s,
3. the Realistic mixing scenario motivated by Fig.2.2b, referred to as $\mathcal{K}_R$. The estimated global zonally-averaged diapycnal mixing in the SO is a combination of internal tides (Lavergne et al., 2020), lee waves (Nikurashin & Ferrari, 2013), and mixed-layer mixing from the observation constrained Southern Ocean Estate Estimate (Verdy & Mazloff, 2017) (Fig.2.2b).

It should be noted that 10^{-5} m^2 s^{-1} and 10^{-4} m^2 s^{-1} are canonical values in physical oceanography, respectively representing the background mixing in the ocean and the mixing required for closure of the MOC (W. H. Munk, 1966; W. Munk & Wunsch, 1998; Waterhouse et al., 2014; Ferrari et al., 2014). The sharp transition between the mixing profiles across the interface

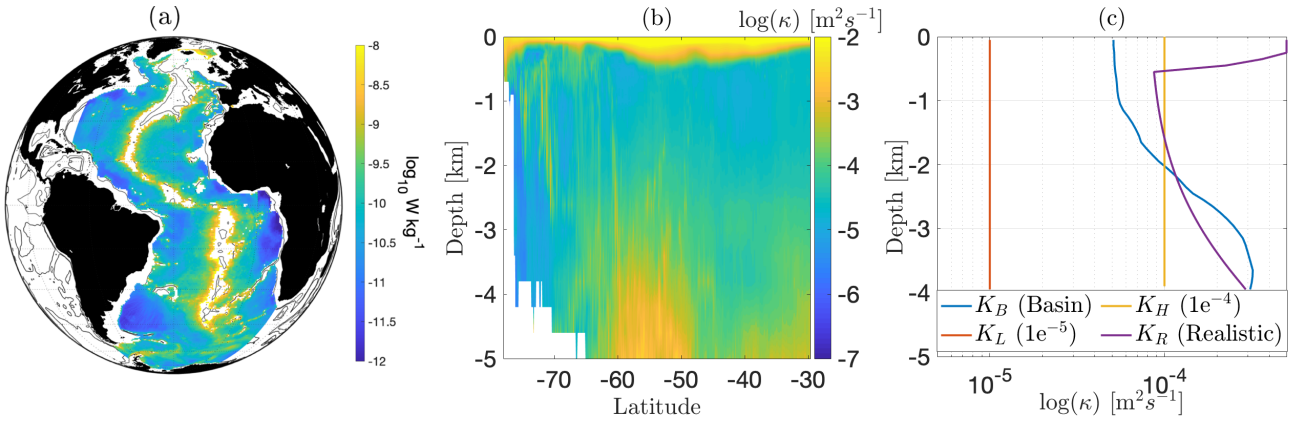


Figure 2.2: a) Turbulent diffusivity in the deep Atlantic basin (3000 m) based on the tidal mixing estimate of Lavergne et al. (2020) and lee-wave mixing estimate of Nikurashin and Ferrari (2013). b) Zonally-averaged diapycnal mixing in the SO from a combination of the interior mixing shown in panel a) and wind-induced surface mixing based on the Southern Ocean State Estimate (SOSE; Verdy and Mazloff (2017)). c) Basin-averaged diffusivities employed in the model: $\mathcal{K}_B$ is prescribed in the mid-latitude basin (and held the same in all experiments) whereas $\mathcal{K}_R$, $\mathcal{K}_L$, and $\mathcal{K}_H$ are employed in the SO for various perturbations. $\mathcal{K}_B$ is averaged over the mid-latitude basin (32°S to 48°N) based on the estimate in panel *a*. $\mathcal{K}_R$ is the SO-averaged diffusivity based on the estimate in panel *b*. $\mathcal{K}_L$ and $\mathcal{K}_H$ are the two canonical values representing the lower and upper bounds of ocean interior mixing.

of the SO channel and the mid-latitude basin reflects the difference in turbulence regimes in the two regions in the real world. While tidal mixing is dominant in the mid-latitude basin to the north, lee waves excited by the interaction of the ACC and its overlying eddies with rough topography dominate interior mixing in the SO (e.g. see Fig.1 in Nikurashin and Ferrari (2013) and Fig.2.2b here).

Hereafter we will use $\mathcal{K}_R$, $\mathcal{K}_L$, and $\mathcal{K}_H$ to name the experiments. While in some cases the same SO diffusivity will be applied to density, N, and C, in others we will apply a mixing profile to biogeochemical or passive tracers that is different from that applied to density. This will distinguish between the direct impact of mixing on tracers from the indirect effect on tracers because of the changes to the AMOC induced by the mixing of density. Thus, in naming experiments we will use superscripts 't' and 'ρ' to refer to tracer and density mixing. For example, an experiment named $[\mathcal{K}_H^t, \mathcal{K}_L^\rho]$ refers to one in which high SO mixing acts on tracers while low SO mixing acts on density, whereas $\mathcal{K}_L$ simply refers to an experiment in which low SO mixing is applied to both tracers and density. Experiments $\mathcal{K}_L$, $\mathcal{K}_H$, and $\mathcal{K}_R$ used the corresponding diffusivity profile for both buoyancy and tracers. Experiment $[K_H^t, K_L^\rho]$ used the

Experiment	Profile used; Southern Ocean		Profile used; Atlantic Basin and NADW	
	Buoyancy	Tracers (C, N or Passive)	Buoyancy	Tracers (C, N or Passive)
K_L (control)	K_L	K_L	K_B	K_B
K_H	K_H	K_H	K_B	K_B
K_R	K_R	K_R	K_B	K_B
$[K_H^t, K_L^\rho]$	K_L	K_H	K_B	K_B
$[K_L^t, K_H^\rho]$	K_H	K_L	K_B	K_B

Table 2.1: $\mathcal{K}$ profile (as shown in Fig.2.2c) used for buoyancy and tracer diffusivity in the SO channel and in the Atlantic Basin and NADW formation region for each experimental run.

$\mathcal{K}_L$ profile for SO buoyancy but the $\mathcal{K}_H$ profile for SO tracer diapycnal mixing, meaning the circulation is the same as in experiment $\mathcal{K}_L$, and therefore showing changes caused by tracer diffusion. $[K_L^t, K_H^\rho]$ used the $\mathcal{K}_H$ profile for SO buoyancy, meaning the circulation is the same as in the $\mathcal{K}_H$ experiment, but uses the $\mathcal{K}_L$ profile for SO tracer diapycnal mixing. A summary of $\mathcal{K}$ profiles used in each experiment is shown in table 2.1.

The $\mathcal{K}_L$ experiment, hereafter referred to as the 'control', is run until an equilibrated overturning circulation is achieved (4000 years) and then extended until the ocean biogeochemistry reaches an equilibrated state as well (another 4000 years). C and N are initialised with uniform concentrations of 2.2e^{-3} mol N m^{-3} and 2.2 mol C m^{-3} respectively, as in Watson et al. (2015). The atmospheric carbon concentration is set to 278 parts per million (ppm), representative of the pre-industrial level (Ito & Follows, 2005). Starting from this equilibrated $\mathcal{K}_L$ solution, we run a host of configurations varying the SO density and tracer diffusivities as shown in table 2.1. Each run is 4000 years long so a new equilibrium is achieved. In this work, we examine changes to both transient model solutions and the equilibrated changes for each experiment.

At t=0, passive tracers were injected at a distribution specified by K_L equilibrium solution for nutrients (Fig.2.4a). These passive tracers were advected and mixed, but had no additional source or sink terms. The tracers were injected at the same initial distribution in K_H, $[Kt_H, Kb_L]$, $[Kt_L, Kb_H]$ and K_R with the resulting distributions then compared to K_L.

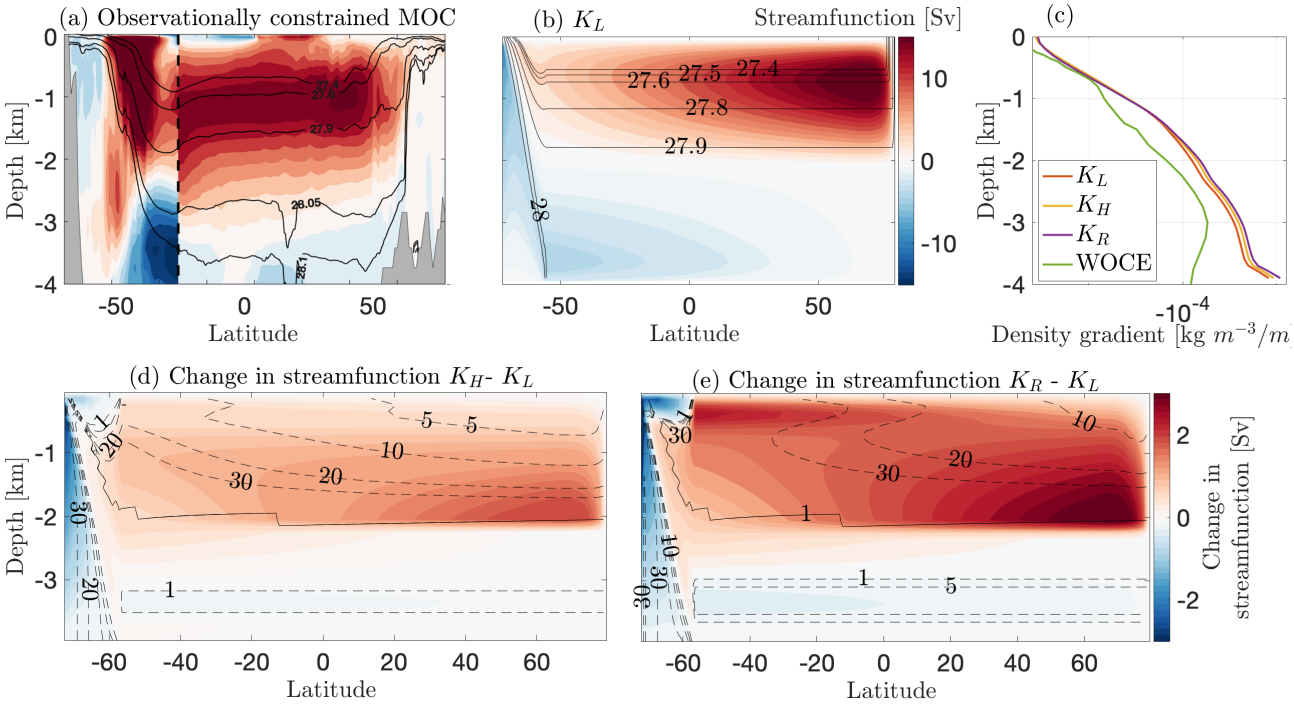


Figure 2.3: a) Zonally-averaged Atlantic Meridional Overturning Circulation (AMOC) streamfunction (ψ in Eq. 2.1 and Eq.2.2) from a climatologically-constrained ocean estimate (ECCO;(Forget, Campin, et al., 2015)). Each Sverdrup (Sv)=10^6 m^3s^{-1}. The streamfunction is calculated in the Atlantic basin up to 32°S and globally between 70-32°S. Neutral density contours are in black. b) The overturning streamfunction for the control case ($\mathcal{K}_L$) with density contours overlain (black lines). c) Vertical gradient of neutral density (Jackett & McDougall, 1997) in the model mid-latitude basin for $\mathcal{K}_L$ (red), $\mathcal{K}_H$ (yellow), and $\mathcal{K}_R$ (purple), compared to density gradient from World Ocean Circulation Experiment (WOCE (Gouretski & Koltermann, 2004)) climatology averaged between 48°N to 32°S in the Atlantic basin (green). d) Change in overturning circulation between $\mathcal{K}_H$ and $\mathcal{K}_L$ experiments. Dashed lines indicate percentage change in overturning streamfunction from $\mathcal{K}_L$. e) Similar to d but for the difference between $\mathcal{K}_R$ and $\mathcal{K}_L$.

2.3.4 Model Verification

We first verify that the model solution of circulation is comparable to oceanic observations. The model solution for circulation and density of the control case are compared to the circulation inferred from a climatologically-constrained ocean state estimate (ECCO; Forget, Campin, et al. (2015)) (Fig.2.3a-c). In the control run ($\mathcal{K}_L$), the upper cell extends to ∼2000 m deep with a maximum strength of 17 Sv (Sv=10^6 m^3s^{-1}) while the lower cell transport is about 4 Sv (Fig.2.3b), both well within the range of inverse models (Lumpkin & Speer, 2007; L. D. Talley, 2013) and ocean state estimates (Forget, Campin, et al., 2015; Cessi, 2019). Figure 2.3c compares the model stratification in the Atlantic (for experiments $\mathcal{K}_L, \mathcal{K}_H, \mathcal{K}_R$) with the Atlantic World Ocean Circulation Experiment climatology (WOCE; Gouretski and Koltermann (2004)). Since the Atlantic mid-latitude basin diffusivity is fixed at $\mathcal{K}_B$ for all experiments, unsurprisingly the model stratification is similar in all three experiments. This implies the secondary influence of the SO mixing on the mid-latitude basin stratification, consistent with theoretical arguments (Nikurashin & Vallis, 2012). The model stratification is in reasonable agreement with climatology in the upper 3 km given its idealised nature. This agreement suffices for our purposes since our primary focus is on the upper AMOC cell and the southward flowing limb of the upper cell (or in other words, on isopycnals that outcrop in both polar regions). The disagreement in stratification in the abyssal ocean has implications on millennial timescales on which the single-basin nature of our analysis most likely introduces larger errors and perhaps even causes the disagreement in the first place. Nevertheless, for our primary messages and the timescales of concern, the model stratification and the AMOC rate of overturning cells are adequate.

The distribution of C and N produced by the model are also qualitatively similar to observations and reproduce many of the key features (Fig.2.4). The surface waters are nutrient-depleted due to phytoplankton productivity, even if the model lacks the upper ocean gyre-induced circulation and thus does not capture the observed deeper nutrient and CO_2 minimum. As mentioned before, this study focuses on the inter-hemispheric isopycnals that outcrop in both the northern and southern high latitudes and lay below the upper ocean gyre circulation. As waters circulate

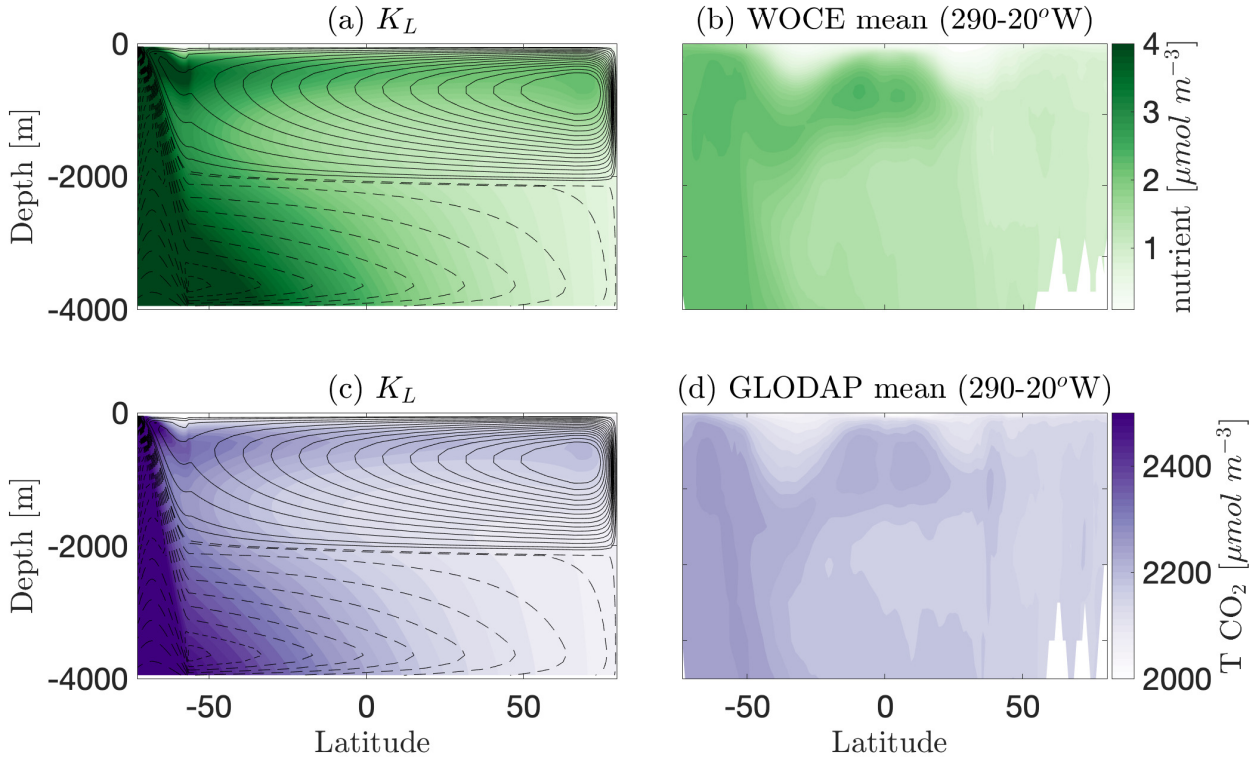


Figure 2.4: a) The concentration of N from experiment $\mathcal{K}_L$. b) the climatological zonally-integrated phosphate in the Atlantic basin from WOCE (Gouretski & Koltermann, 2004). The concentration of C from experiment $\mathcal{K}_L$ in (c) is also compared to the climatological zonally-integrated C from the Global Ocean Data Analysis Project (GLODAP Olsen et al. (2020)) in (d).

and organic matter sinks, the N and C concentrations in old deep waters are enhanced (Fig.2.1). The short residence time of these waters in the surface SO means that biota are unable to utilise all of the nutrients (Ito & Follows, 2005). Therefore, AABW and AAIW have high preformed N content. The concentration of nutrients in AAIW are rapidly depleted as waters travel north due to productivity. Regions with high (low) N levels also have high (low) C concentrations, as photosynthesis takes in both, and remineralisation releases both.

2.4 Results:

2.4.1 Sensitivity of Atlantic Circulation to Southern Ocean Mixing

On long timescales, SO diapycnal mixing rates are significant controls on overturning circulation rates, altering the mass transport of waters (Fig.2.3 d,e). Altered SO mixing causes up to a 30% change in the strength of circulation after 4000 years. Increasing SO mixing to $\mathcal{K}_H$ and $\mathcal{K}_R$ increases AMOC strength by ∼3 Sv in the upper branch and by ∼2 Sv in the deep branch. The maximum transport is increased from 16.9 Sv in $\mathcal{K}_L$, to 17.8 Sv in $\mathcal{K}_H$, and to 18.8 Sv in $\mathcal{K}_R$. The upper cell is also deepened with enhanced mixing, as the increased downward mixing of buoyant surface waters in the SO deepens the pycnocline, altering the structure of the AMOC. These changes to circulation are effective on timescales of equilibration of the circulation (centennial to millennial).

Changes in circulation can be better understood by having examined the controlling equations for each of the three oceanic regions (the SO channel, the NADW formation zone and the mid-latitude basin) ;

$$\psi_1 = \bar{\psi} + \psi^* = (\frac{\tau_0}{\rho_0 f_1} - k_e \frac{h}{ls}) L_x, \tag{2.4}$$

$$\psi_2 = \psi_3 - \psi_1, \tag{2.5}$$

$$\psi_3 = \frac{\Delta b h^2}{f_3}, \tag{2.6}$$

where $\psi_1, \bar{\psi}$ and ψ^* are scales for the residual, wind-driven and eddy induced transport in the

SO channel; ψ_2 is the mixing driven upwelling in the ocean basin and ψ_3 is the scale for deep water formation; f_1 and f_3 are the latitude-dependent Coriolis parameter; ρ_0 is the reference density; Δb is the buoyancy range for isopycnals shared between the SO channel and the NADW formation region; h is a depth scale for mid-depth stratification, l_s is the meridional extent of the circumpolar channel, meaning $\frac{h}{l_s}$ sets the slope of the zonally averaged isopycnals in the SO channel; τ_0 is the SO wind stress; K_e is the eddy diffusivity (i.e. along-isopycnal stirring); L_x and L_y are the zonal and meridional extents of the ocean basin.

Increased downward mixing of buoyant surface waters in the SO channel deepens the ocean pycnocline, h, altering the slope of SO isopycnals and changing the structure of the AMOC. Deeper stratification results in increased formation of NADW (Eq.2.6). The strengthened NADW formation is balanced by increased upwelling in the SO (Eq.2.5). The decreased upper cell strength observed in the upper waters of the SO channel is due to a more localised effect of altered isopycnal slopes (Eq. 2.4). The increased isopycnal slope gradient strengthens ψ^*, a counter-clockwise circulation. The strength of the wind-driven clockwise circulation ($\bar{\psi}$) remains constant. The enhanced anti-clockwise circulation increases the flow along the surface to the south, where waters experience strongly negative buoyancy forcing and sink, strengthening the lower cell.

2.4.2 Sensitivity of C & N Distribution to Southern Ocean Mixing Over a Range of Temporal Scales

Sensitivity of C & N Distribution to Southern Ocean Mixing Over Decadal Timescales

The N, C and passive tracer distribution anomalies between each simulation and the control simulation ($\mathcal{K}_L$) over the first 100 years are shown (Fig.2.5,2.6 & 2.7). The first row of Figure 2.5, 2.6 and 2.7 shows the change for $\mathcal{K}_H$, when both $\mathcal{K}^t$ (which acts on N, C and the passive tracer) and $\mathcal{K}^\rho$ get enhanced. The net change is due to two contributions: Firstly the indirect impact caused by alterations to the density field (higher $\mathcal{K}^\rho$) changing the AMOC, and secondly the direct impact of enhanced $\mathcal{K}^t$ directly on the tracer gradient. The indirect impact is isolated

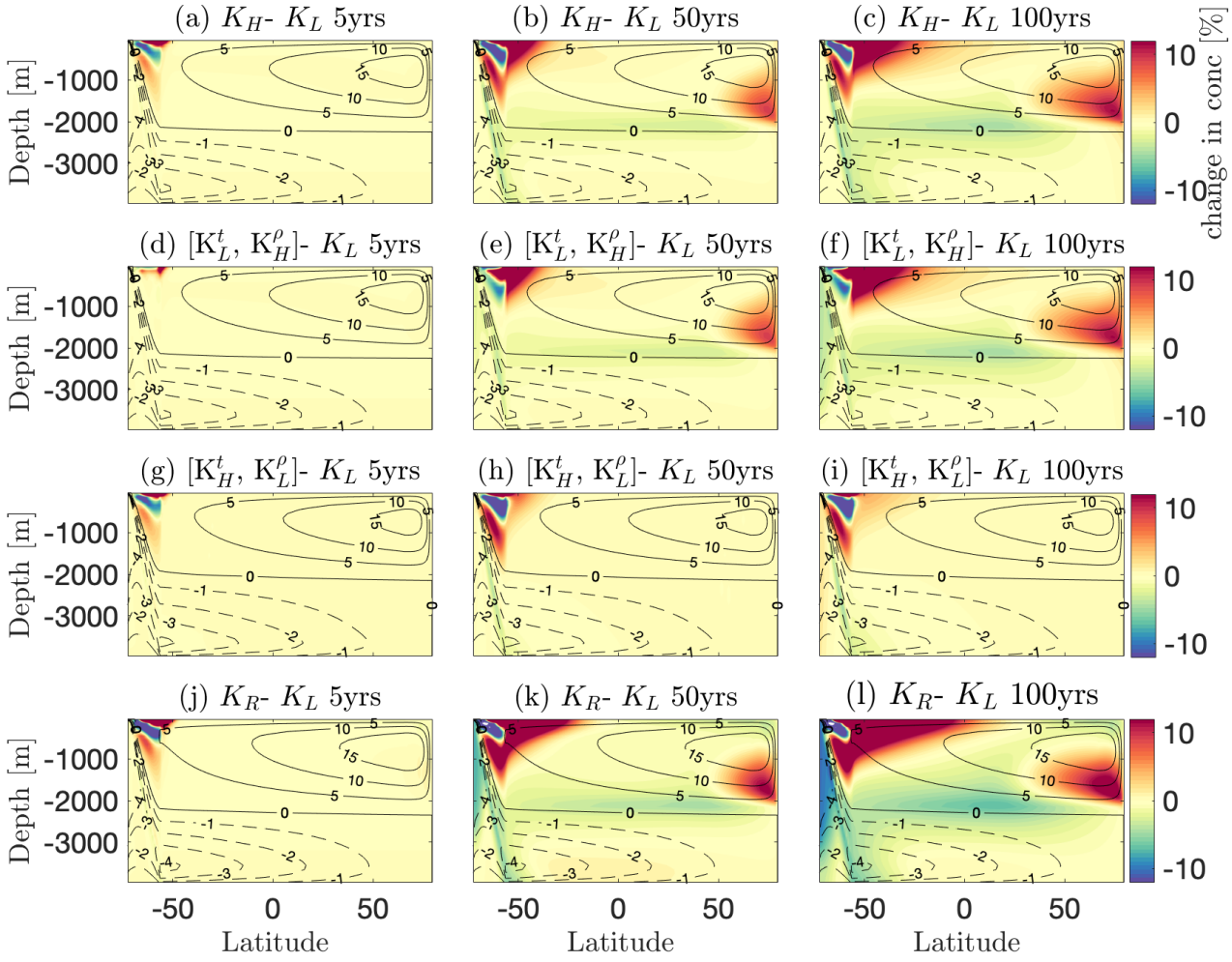


Figure 2.5: Change in N concentration at t=5, 50 and 100 years from the N concentration for the $\mathcal{K}_L$ experiment in steady-state, as was shown in Fig.2.4a. First Row: change between $\mathcal{K}_H$ and $\mathcal{K}_L$ experiments. Second Row: between $[\mathcal{K}_L^t, \mathcal{K}_H^\rho]$ and $\mathcal{K}_L$ experiments. Third row: between $[\mathcal{K}_L^t, \mathcal{K}_H^\rho]$ and $\mathcal{K}_L$ experiments. Fourth row: between $\mathcal{K}_R$ and $\mathcal{K}_L$ experiments. Red/blue implies increased/decreased tracer concentration. Black overlain lines indicate zonally averaged residual overturning circulation for each experiment, with labels indicating streamfunction in Sv.

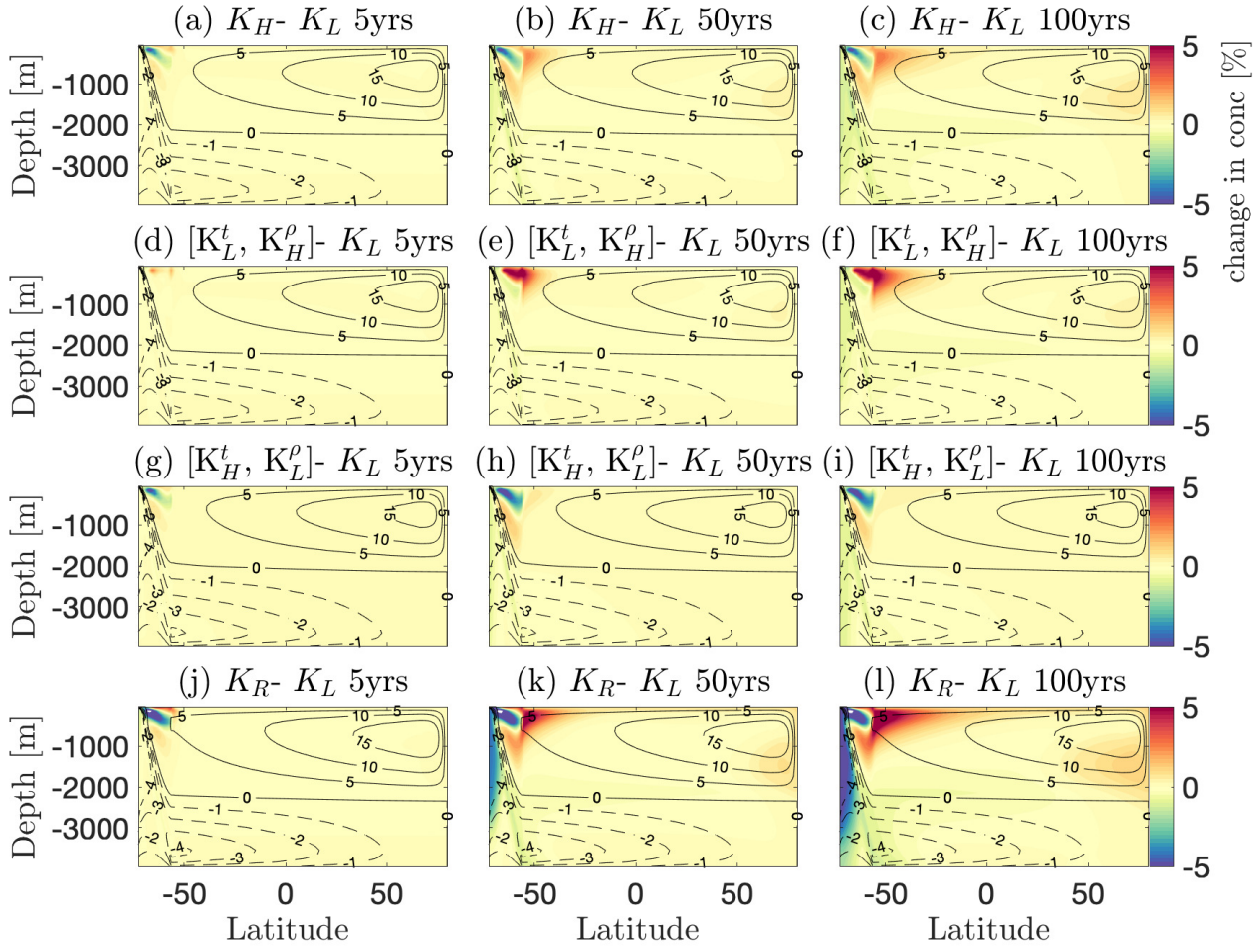


Figure 2.6: Change in C concentration at t=5, 50 and 100 years from the C concentration for the $\mathcal{K}_L$ experiment in steady-state, as was shown in Fig.2.4c. First Row: change between $\mathcal{K}_H$ and $\mathcal{K}_L$ experiments. Second Row: between $[\mathcal{K}^t_L, \mathcal{K}^\rho_H]$ and $\mathcal{K}_L$ experiments. Third row: between $[\mathcal{K}^t_L, \mathcal{K}^\rho_H]$ and $\mathcal{K}_L$ experiments. Fourth row: between $\mathcal{K}_R$ and $\mathcal{K}_L$ experiments. Red/blue implies increased/decreased tracer concentration. Black overlain lines indicate zonally averaged residual overturning circulation for each experiment, with labels indicating streamfunction in Sv.

in the second rows of Figure 2.5, 2.6 and 2.7, where $\mathcal{K}^t$ is unchanged from the control but $\mathcal{K}^\rho$ is enhanced. The anomaly is the largest in the Atlantic basin, reflecting the changes in the AMOC. The direct impact is isolated in the third row where $\mathcal{K}^\rho$ is unchanged from the control, but $\mathcal{K}^t$ is enhanced. This anomaly is SO-focused and evolves much faster than the former signal in the second row. Very minimal changes are seen north of the SO channel. The last row bears similarity to the first row as it too captures the impact of enhanced mixing on both C, N, passive tracers and density using a more realistic mixing profile, $\mathcal{K}_R$, than the simple $\mathcal{K}_H = 10^{-4}$ m^2 s^{-1}. The SO changes are more dramatic in $\mathcal{K}_R$, due to the large surface turbulent mixing, representative of SO storm tracks.

At 5 years, the same patterns of change are seen in C and N concentration, though the percentage changes to C are not as high (Fig.2.6 & 2.5, Column 1). Changes to tracer distributions are observable in the SO upper cell region for all experiments, although the changes in $[K_L^t, K_H^\rho]$ (second row) are minimal. Tracer distributions in the basin are unchanged from $\mathcal{K}_L$ for all experiments. The changes in tracer distributions of $\mathcal{K}_H$, $\mathcal{K}_R$ and $[K_H^t, K_L^\rho]$ are very similar, suggesting it is the changes to diffusion experienced by the tracer which dominates in the first few years. Higher tracer diffusion in $\mathcal{K}_H$, $[K_H^t, K_L^\rho]$, and $\mathcal{K}_R$ act to disperse the tracer more rapidly from tracer rich regions such as the AAIW and lower cell waters. Tracers are lost from the SO upper AAIW waters into the more tracer-depleted regions above and below this tracer rich region. The changes are the greatest in $\mathcal{K}_R$, showing the importance of the enhanced surface water mixing rates in this profile.

By 50 years the changes are greater and occur over a wider area than at 5 years (Fig.2.6 & 2.5, column 2). Change within the SO in experiments $\mathcal{K}_H$, $[K_H^t, K_L^\rho]$ and $\mathcal{K}_R$ (those with enhanced $\mathcal{K}^t$) are fairly similar to each other. Tracers continue to be mixed out of the high nutrient band of AAIW maintained by biology, causing an increase in nutrients above and below. Enhanced mixing acting across tracer gradients also causes tracers to be lost from the nutrient and carbon-rich sinking AABW. In $[K_L^t, K_H^\rho]$ and $[K_H]$, increased tracer concentrations begin to occur in the southern surface and northern mid-depth waters of the basin. This is due to the enhanced strength of the MOC moving more nutrient-rich waters north into the Atlantic basin. Under a higher mixing scenario, the upper cell deepens, and the very nutrient-rich waters of the lower

cell extend less far up, hence a decrease in nutrient concentration occurs at the depth of the interface between the two cells in the basin (Fig.2.3 d & e). $[K_H^t, K_L^\rho]$ has very limited changes north of the SO. The changes in $\mathcal{K}_H$ and $\mathcal{K}_R$ have elements from $[K_H^t, K_L^\rho]$ and $[K_L^t, K_H^\rho]$. The SO of $\mathcal{K}_H$ closely resembles that of $[K_H^t, K_L^\rho]$, whereas the basin of $\mathcal{K}_H$ resembles $[K_L^t, K_H^\rho]$, suggesting that changes to the diapycnal mixing profile experienced by tracers dominate in the channel, whilst changing the mixing profile experienced by buoyancy dominates the changes to tracer distribution in the basin.

The patterns for changes in N and C concentration seen at 50 years continue up to 100 years but increase in magnitude and spread spatially (Fig.2.6 & 2.5 column 3). Changes seen in $\mathcal{K}_R$ are of a greater magnitude than the changes seen in $\mathcal{K}_H$. Changes in $[K_H^t, K_L^\rho]$ continue to be confined to the SO.

While the changes in the distribution of C and N follow a very similar pattern, the percentage magnitude of the observed changes is greater for N than for C. The decrease in N concentration seen at the interface of the upper and lower cell of the Atlantic basin does not occur for C concentrations.

For passive tracers, the features maintained by biology rather than by circulation are lost over time and the passive tracer becomes more evenly dispersed (Fig.2.7 a-c). Changes to passive tracer distribution mirror the changes seen for biogeochemical tracers in each experiment at 5 years. This suggests that 5 years is too short a time for biological feedback to take place. By 50 years, the changes to passive tracer distributions are different to those seen for N and C due to biological processes and feedback further altering the tracer distributions.

Sensitivity of C & N Distribution to Southern Ocean Mixing Over Decadal to Millennial Timescales

To further quantify the changes to SO and mid-latitude basin N, C and passive tracer inventories by mixing perturbations, we calculated the mean absolute changes between various experiments and the control run ($\mathcal{K}_L$). The results are shown in Figure 2.8 for changes to N,

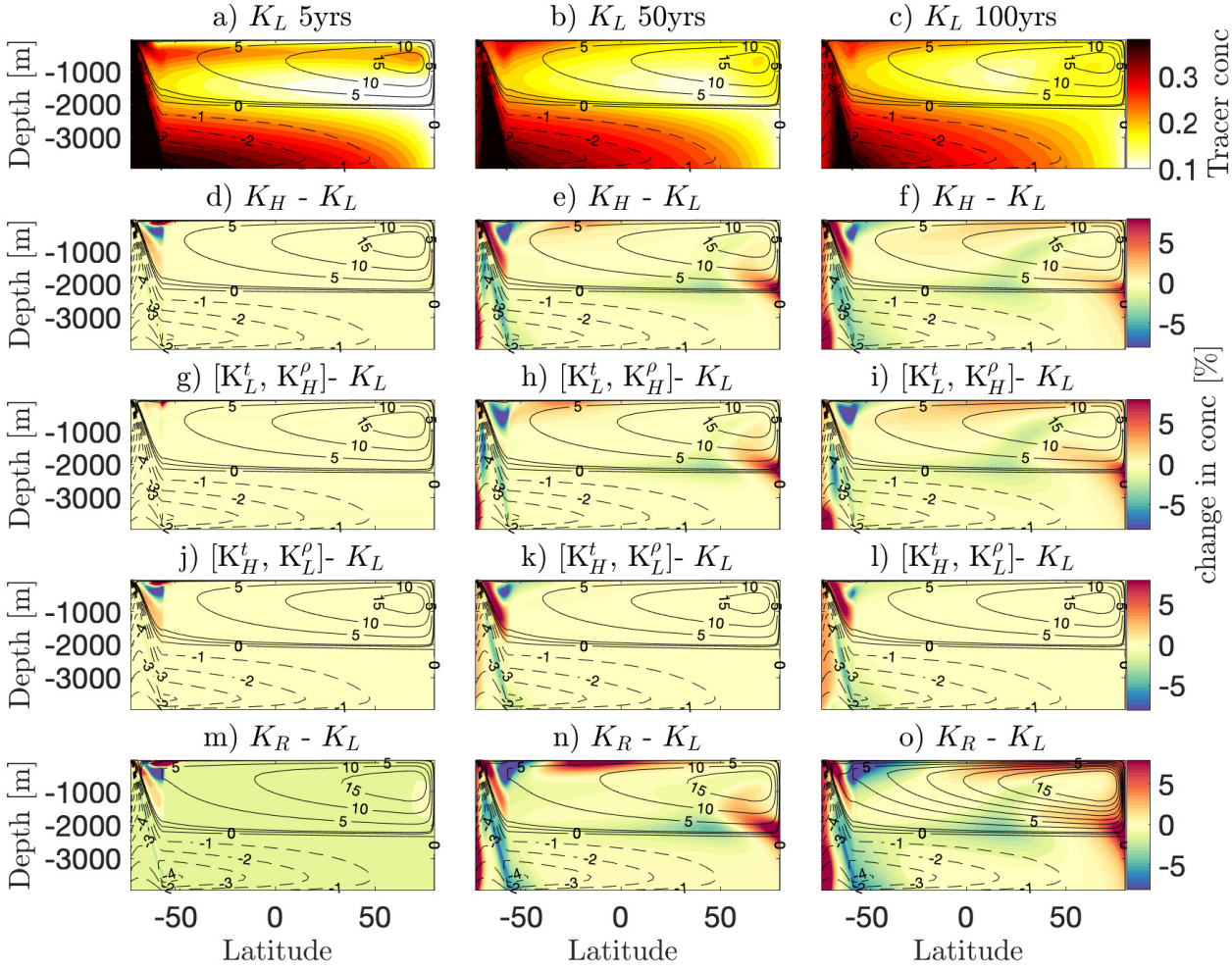


Figure 2.7: Change in passive tracer concentration at t=5, 50 and 100 years from the passive tracer concentration for the $\mathcal{K}_L$ experiment in steady-state (First row). Second row: change between $\mathcal{K}_H$ and $\mathcal{K}_L$ experiments. Third row: between $[\mathcal{K}_L^t, \mathcal{K}_H^\rho]$ and $\mathcal{K}_L$ experiments. Fourth row: between $[\mathcal{K}_L^t, \mathcal{K}_H^\rho]$ and $\mathcal{K}_L$ experiments. Fifth row: between $\mathcal{K}_R$ and $\mathcal{K}_L$ experiments. Red/blue implies increased/decreased tracer concentration. Black overlain lines indicate zonally averaged residual overturning circulation for each experiment, with labels indicating streamfunction in Sv.

C and a passive tracer. Changes are broken down by region into; the SO only (blue lines), the mid-latitude Atlantic basin only (black lines), the surface waters of the SO and the basin (red lines) and finally the waters of the entire SO and Atlantic (green lines). Since the results based on $\mathcal{K}_R$ are similar to those experiments with $\mathcal{K}_H$ in this analysis, we do not include the former.

The mean difference in N & C concentrations between various experiments and the control run ($\mathcal{K}_L$) increase over the 4000 years of experiments in all regions of the SO and the Atlantic (Fig.2.8a,b) with the mean changes reaching a constant value at around 4000 years as a new steady state solution is reached. Between 0 and 5 years, the changes to N and C are similar and only occur in the SO and SO & basin surface waters in experiments where $\mathcal{K}^t$ is enhanced (solid and dotted red and blue lines). For C the SO & Basin surface regions show the same magnitude of change as the SO region only. For N, the SO & Basin surface region shows a greater mean change than the SO. The experiments $[\mathcal{K}^t_H]$ and $[\mathcal{K}^t_H, \mathcal{K}^\rho_L]$ both show the same changes in tracer distributions, while tracers in the $[\mathcal{K}^t_L, \mathcal{K}^\rho_H]$ experiment show no alteration to their distribution compared to the control run (dashed red and blue lines). This demonstrates that all changes observed in $\mathcal{K}_L$ (solid lines) are due to altered $\mathcal{K}^t$. At 5 years, enhanced $\mathcal{K}^\rho$ beings to alter N and C distributions in just the SO, and SO & Basin surface waters. The impact of enhanced $\mathcal{K}^\rho$ on tracers becomes greater than the impact of enhanced $\mathcal{K}^t$, at around 50 years in surface waters (red dashed vs dotted lines), and at around 200 years in the SO (blue dashed vs dotted lines).

For C, it takes around 75 years for the mean difference in C concentration in the Atlantic basin to change by 0.1% (black lines), the same magnitude of change in the SO and surface waters in the first year (Fig.2.8.a). This change in C concentrations in the basin is driven by the enhanced $\mathcal{K}^\rho$ altering circulation (dashed lines), with a very small contribution from alterations to SO $\mathcal{K}^t$. It takes over 100 years for the enhanced $\mathcal{K}^t$ in the SO to have an impact on the distribution of C in the Atlantic basin of only 0.1%. Even on millennial timescales, the change to C concentrations in the Atlantic basin due to altered SO tracer mixing are less than 1%. For C, after 200 years, in all regions the greatest changes are driven by alterations to $\mathcal{K}^\rho$, altering the structure of the MOC and the advection of C. The percentage change in C concentrations in $\mathcal{K}^t_H$ strongly resemble those in $[\mathcal{K}^t_L, \mathcal{K}^\rho_H]$ (dashed lines are similar to solid lines). For C, the

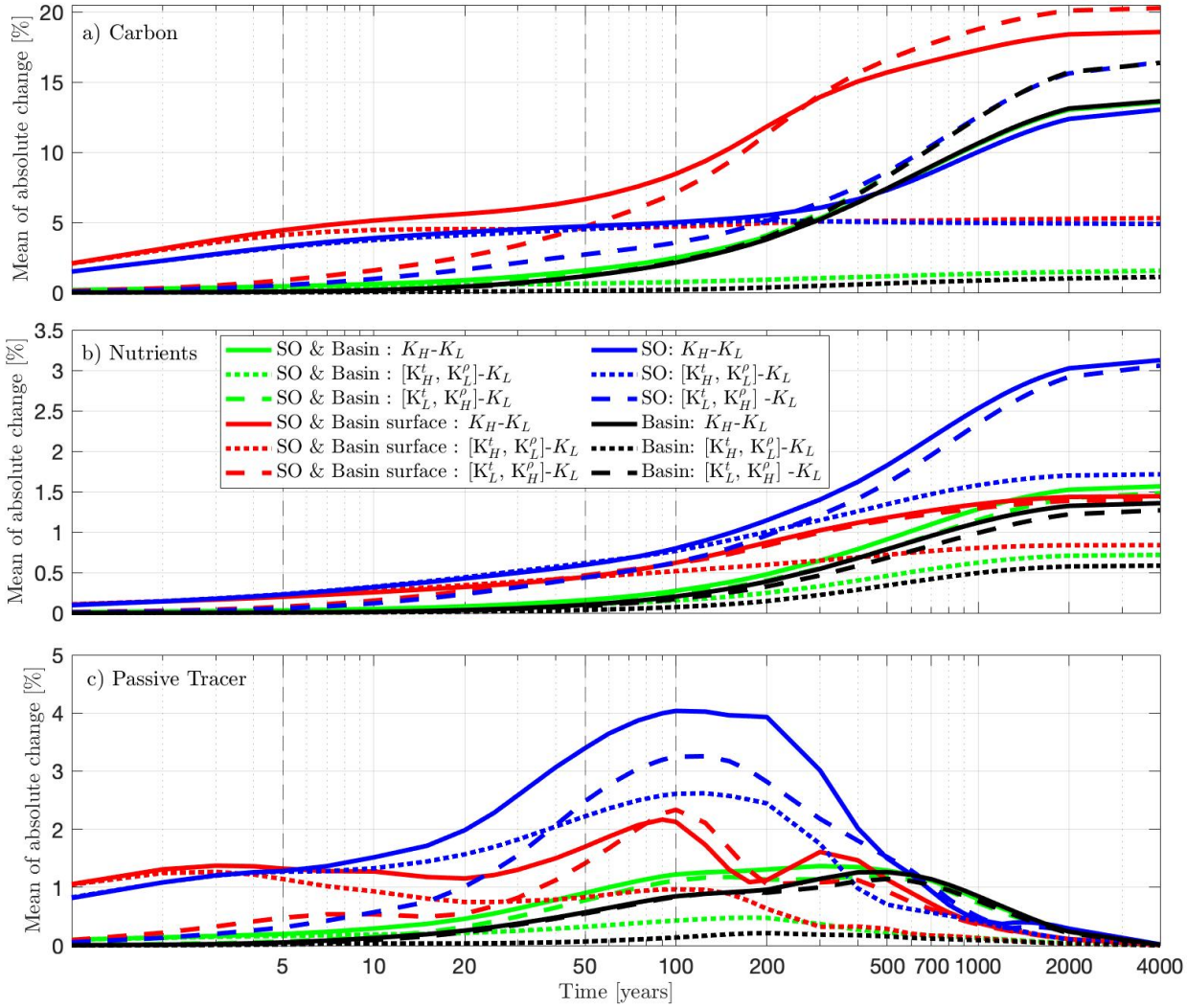


Figure 2.8: a) Mean of absolute change in integrated carbon concentration. b) Mean of absolute change in integrated nutrient concentration. c) Mean of absolute change in integrated passive tracer concentration. Panels a)-c) show results for various inventories: the entire ocean (SO + mid latitude basin) in green, the surface ocean (top 200 m of SO + mid latitude basin) in red, only the mid-latitude basin (full depth) in black, and only the SO (full depth) in blue. Solid lines denote the difference between $\mathcal{K}_H$ and $\mathcal{K}_L$ experiments, dotted lines represent differences between $[\mathcal{K}^t_H, \mathcal{K}^\rho_L]$ and $\mathcal{K}_L$ experiments, and dashed lines denote differences between $[\mathcal{K}^t_L, \mathcal{K}^\rho_H]$ and $\mathcal{K}_L$ experiments. Vertical dashed lines indicate the time slices considered in Fig.2.5.

SO is the region with the most highly altered concentrations in all experiments. Surface waters experienced higher mean C concentration changes than the full water column basin waters, but a lower mean change than the full water column SO waters.

The percentage changes to N were greater than those to C in all regions and in all experiments by almost a factor of 10 (Fig.2.8b). Changes to N concentrations in the basin also take around 75 years to change by a similar magnitude as the changes to SO waters in just one year, with changes in the basin again driven by enhanced SO $\mathcal{K}^{\rho}$ rather than enhanced $\mathcal{K}^{t}$ (black dashed lines). In the SO & Basin surface waters, changes to $\mathcal{K}^{\rho}$ dominate over changes to $\mathcal{K}^{t}$ by about 50 years, with advection driven changes dominating throughout the SO by 200 years. From about 100 years in the SO and also the SO & Basin surface waters, and about 500 years in the Atlantic Basin, the percentage change in N concentration due to enhanced $\mathcal{K}^{t}$ plateaus. Meanwhile changes due to altered $\mathcal{K}^{\rho}$ continue to increase.

Key differences exist between the changes in N and for C. For N, the surface waters of the SO & basin (red lines) are the region showing the greatest changes in concentration at all times. For C the greatest changes are in the full water column SO waters (blue lines Fig.2.8a). While for changes to C concentrations in $\mathcal{K}^{t}_{H}$ always resulted in a higher mean change than $[\mathcal{K}^{t}_{H}, \mathcal{K}^{\rho}_{L}]$ or $[\mathcal{K}^{t}_{L}, \mathcal{K}^{\rho}_{H}]$, this is not the case for N. In the SO & Basin surface waters after 200 years, and in the SO and the Basin waters after 300 years, the mean change in N in $[\mathcal{K}^{t}_{L}, \mathcal{K}^{\rho}_{H}]$ is greater than in $[\mathcal{K}^{t}_{H}, \mathcal{K}^{\rho}_{L}]$. This suggests that while for C, the impact of enhanced $\mathcal{K}^{\rho}$ and $\mathcal{K}^{t}$ are additive, this is not the case for N.

Similar trends are seen for changes to passive tracer distributions as for biogeochemical tracer distributions. The distribution of passive tracers in the surface waters of the SO and Basin show the highest initial changes in distribution in response to altered $\mathcal{K}^{t}$. In the Atlantic basin, changes are driven by enhanced SO $\mathcal{K}^{\rho}$. Enhanced SO $\mathcal{K}^{t}$ has a minimal impact on the passive tracer distributions in the Atlantic. While the mean change in passive tracer concentration in the surface waters peaks at around 50 years, the percentage change then begins to decrease with time after around 100 years. However, at around 200 years, the mean percentage change in $\mathcal{K}^{t}_{H}$ increases, and remains constant in $[\mathcal{K}^{t}_{L}, \mathcal{K}^{\rho}_{H}]$. After 200 years the mean change in surface

water passive tracer distribution in $[\mathcal{K}_H^t, \mathcal{K}_L^\rho]$ is greater than the sum of the mean change in the other two experiments. It takes about 500 years for the passive tracer in the Atlantic basin to begin to become evenly dispersed in all mixing scenarios, reducing the difference between experiments.

The biggest difference between the behaviour of passive tracers to biogeochemical tracers is that over time, the distribution of passive tracers becomes uniform in all experiments, meaning differences between experiments become small. For the passive tracer, the largest mean % change occurs at 50 years in the SO region in $\mathcal{K}_H$, as a result of enhanced $\mathcal{K}^\rho$ and $\mathcal{K}^t$. The peak in tracer distribution changes is reached much sooner for the passive tracer than for either biogeochemical tracers. For N, it is the SO and Basin surface waters which show the largest changes, peaking at a mean change of 20% 2000 years into the experiment due to enhanced $\mathcal{K}^t$ only. For C the greatest change is seen in the SO waters 2000 years into the experiment in $\mathcal{K}_H^t$, changing by around 3%.

2.4.3 Long-Term Equilibrated Changes

Mixing is spatio-temporally variable, so a steady-state solution does not necessarily describe the real world. However, it is insightful to consider the long-term equilibrated solutions of the perturbation experiments to gain an understanding of the order of magnitude importance of the changes. In Figure 2.9 we plot the changes in the steady-state C and N distributions between the various experiments and the control experiment. In all cases, the C and N concentrations are increased in surface waters. Changes to N are overall more prominent than those to C (Fig.2.9).

The steady state changes between experiment $\mathcal{K}_H$ and $\mathcal{K}_L^t$ (Fig.2.9 first column) show the same patterns for C and N. Tracers are lost from the sinking AABW and the waters which then spread north at depth to form the lower cell. Tracers are also lost from the northward flowing AAIW in the SO. Tracers are gained in the upper cell, where concentrations are increased the most in the northerly waters of the Atlantic basin. An increase in tracer concentration can also be seen in the most northerly waters of the lower cell.

In $[\mathcal{K}_H^t, \mathcal{K}_L^\rho]$, where enhanced mixing is only applied to $N\&C$, the steady state solution for tracer distributions is different to cases with altered $\mathcal{K}^\rho$ (Fig.2.9, second column), especially for N. It is also the only experiment where different patterns of change are observed for N than C. For both tracers, the change from $\mathcal{K}_L^t$ is strongest in the SO, with minimal changes observed in the Atlantic basin. $C\&N$ are lost from SO upper AAIW waters, and mixed into the more tracer depleted regions above and below. The subsequent increase in the surface N concentration is significant for the uptake of C by biological productivity, and the sinking of organic matter containing C and N as part of the biological carbon pump. N concentrations also increase in the descending AABW in the very south. There are no regions that show a strong increase in C, unlike in other experiments.

Consistent with the transient solutions, in experiments with enhanced mixing only acting on ρ (Fig.2.9, third column), the signal extends beyond the SO channel since it comes from changes to the whole AMOC. As a result, on the long-term (millennial) equilibration time scale, the indirect impact of mixing on tracers due to mixing-induced AMOC changes can overwhelm the direct impact of mixing on tracers. In all experiments with altered $\mathcal{K}^\rho$, the pattern for changes to tracer distribution is due to the transfer of tracers from the C and N rich lower cell to the upper cell of the AMOC. However, as shown in Figures 2.5 and 2.8.b, on inter-annual to decadal timescales, the direct impact is dominant and perhaps more readily relevant to short time scale climate change.

The greatest change to tracer distributions for both C and N occurs in $\mathcal{K}_R$. The alterations to tracer distributions here are very similar to those of $\mathcal{K}_H$, but with stronger changes. This highlights the conservative nature of our choice of high diffusivity in $\mathcal{K}_H$.

2.4.4 Climatic Implications

The climatic implications of the changes to N and C budgets may be encapsulated through the net change in atmospheric $p\mathrm{CO}_2$ concentrations between the various experiments and the control run in which weak mixing acts on N, C, and ρ. This is summarised in Table 2.2. All experiments have an increase in atmospheric $p\mathrm{CO}_2$ compared to $\mathcal{K}_L$. The direct impact

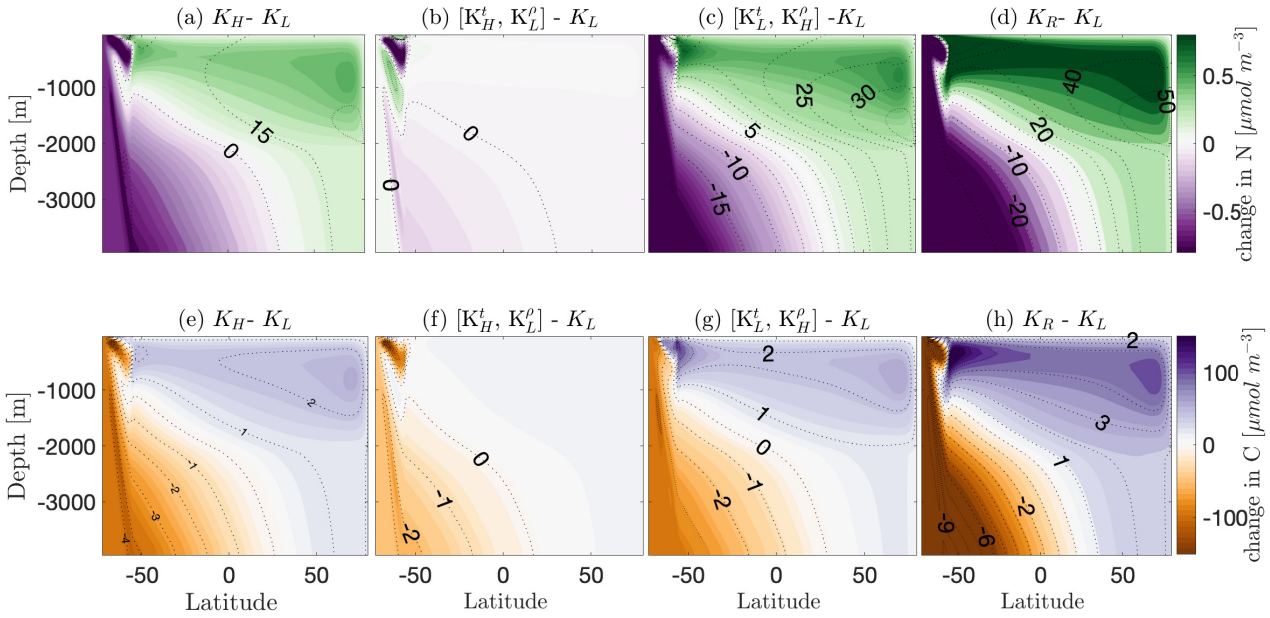


Figure 2.9: Equilibrated changes to N and C distributions. Top row: change in N concentration between $\mathcal{K}_L$ and a) $\mathcal{K}_H$, b) $\mathcal{K}^t_H$, $\mathcal{K}^\rho_L$], c) $\mathcal{K}^t_L$, $\mathcal{K}^\rho_H$], and d) $\mathcal{K}_R$. Green/purple denotes regions of increased/decreased N concentration. Black-labelled overlain lines indicate percentage changes from $\mathcal{K}_L$. Bottom row: same as above but for C, with purple/orange denoting regions of increased/decreased C concentration.

Experiment	Change in atmospheric $p\mathrm{CO}_2$ from K_L (ppm)
K_H	11.2
$[Kt_H, Kb_L]$	12.3
$[\mathcal{K}^t_L, \mathcal{K}^\rho_H]$	3.9
K_R	24.6

Table 2.2: Change in steady state atmospheric $p\mathrm{CO}_2$ from experiment $\mathcal{K}_L$

of enhanced mixing on tracers, as in $[\mathcal{K}^t_H, \mathcal{K}^\rho_L]$, causes the redistribution of C to the upper surface waters. This is potentially important for atmospheric C concentrations. These surface waters allow C to be exchanged between the atmosphere and the ocean. Therefore, enhanced $\mathcal{K}^t$ results in only a very slight increase in C content of the AMOC upper cell, but an increase in atmospheric C reservoir of 12.3ppm (Table 2.2). On the other hand, although increased $\mathcal{K}^\rho$ caused a stronger redistribution of C within the AMOC upper cell, this C was not directed to the upper surface waters. Therefore the redistribution was not as important for ocean-atmosphere fluxes of C, but caused more drastically observable changes to the C content of the upper cell. The stronger diapycnal mixing and enhanced ocean ventilation did also reduce the oceanic carbon storage causing higher atmospheric $p\mathrm{CO}_2$. Enhanced $\mathcal{K}^t$ and $\mathcal{K}^\rho$ both cause a steady state atmospheric CO_2 concentration greater than in $\mathcal{K}_L$, but the direct effect of the tracer mixing is stronger than the indirect effect of the density mixing (Table 2.2).

Of course, in the real ocean, the seasonality of mixed layer dynamics could be capable of inducing more entrainment of carbon-rich waters from below. To mimic this, our $\mathcal{K}_R$ experiment results in the greatest increase in atmospheric CO_2 content, due to the high surface mixing rates bringing carbon rich waters into contact with the atmosphere. The strong mixed layer mixing in the SO is known to raise predicted atmospheric CO_2 concentrations, and to make partitioning CO_2 into the deep ocean harder (Watson & Naveira Garabato, 2006).

2.5 Discussion

This work highlights the sensitivity of biogeochemical tracer distributions in the SO and mid-latitude ocean basins to diapycnal mixing in the SO.

Firstly, we verified that alterations to $\mathcal{K}$ in just the SO channel cause significant changes to the overturning circulation in this model configuration. Impacting the AMOC through altered SO mixing was important for this study because changes to circulation alter tracer advection (J(ψ, N) & J(ψ, C), allowing us to distinguish between alterations to tracer advection and diffusion.

Secondly, we showed that the enhanced mixing in the SO exerts a significant control on the

tracer budgets well beyond the boundaries of the SO, and on a global scale. This is in contrast to previous work showing enhanced SO diapycnal mixing only increased nutrient concentrations and production in the SO, with no changes at low latitudes (Gnanadesikan et al., 2001). However, the physical and biological set up of this model was significantly different to that used in this study. Firstly the work of Gnanadesikan et al. (2001) did not include the formation of deep-water within the SO. Secondly, the magnitude of biological production in Gnanadesikan et al. (2001) was calculated to maintain the surface nutrient distribution set by global observations, given the model transport and depth-dependence of remineralisation. We found both the direct and indirect impacts significant on their associated timescales.

Figure 2.10 summarises our key messages by showing a zoomed-in view of the zonally-averaged SO (from the model), comparing the SO-branch of the upper and lower AMOC between the low mixing control run ($\mathcal{K}_L$) and the case with a realistic SO-averaged diffusivity ($\mathcal{K}_R$). The background colour, from the control run, shows the richness of nutrients in the CDW and AABW. The arrows at mid-depths represent the interior mixing induced by the breaking of waves within the vigorous wave field of the SO, which results in diapycnal diffusion of nutrients across density surfaces.

We find that tracer responses to SO mixing manifest on two distinct timescales:

- On annual to decadal timescales due to the direct action of mixing on tracer gradients: The direct impact of enhanced mixing increases the rate of diapycnal upwelling of nutrients from high concentration AABW into the nutrient-poor water masses of the upper cell. This causes the largest changes in SO C and N budgets on decadal to centennial timescales. High rates of diapycnal mixing are known to occur across the isopycnals that separate the upper and lower cells in the SO (Silvester et al., 2014; Ferrari, 2014; Nikurashin & Ferrari, 2013). This mixing means waters can rapidly short circuit between the two cells of the MOC (Garabato et al., 2007). We have demonstrated the potential importance of this short-circuiting for tracers. The physical structure of the SO makes the site of CDW upwelling far more important in determining the fate of tracers than for tracers that upwell in other ocean regions.

The surface water tracer concentrations of the Atlantic basin begin to be modified by 50 years. This time scale corresponds to the transport and utilisation of nutrients by the northward SAMW (Palter et al., 2010) to be utilised for downstream productivity, as the resurfacing of deep nutrient rich waters at around 30°S ranges from multi-decadal to a centennial (Tamsitt et al., 2017). The advective timescale for waters subducted in NADW to reach the SO surface is of the order of a century (Tamsitt et al., 2017). Therefore, it takes around 50 years for the importance of changing $\mathcal{K}^{\rho}$ to increase to above that of changing $\mathcal{K}^{t}$. Given that between 30°S and 30°N upper ocean nutrient supply is dominated by waters originating in the SO (Palter et al., 2010), the global nutrient and carbon budgets are highly sensitive to SO mixing.

- On centennial and longer timescales due to the indirect impact of mixing through changing the isopycnal slopes in the SO. This then alters the global deep stratification and density layer slopes (Fig.2.10 coloured contours) and the inter-hemispheric AMOC. Given the global connectivity of the ocean basins through the SO, any change in SO isopycnal slopes translates to a change to the global deep stratification, thereby altering the AMOC. These indirect impacts are able to alter the tracer distributions in the Atlantic basin beyond the SO where mixing rates are altered.

We therefore consider short time scales to be those where the direct impact of vertical diffusion impacts biogeochemical tracers. Conversely, we consider long timescales to be centennial or longer, where the ocean experiences changes in its large-scale structure and circulation, which impact biogeochemical cycles globally.

Finally, we demonstrate the significance of SO diapycnal mixing on atmospheric $p\mathrm{CO}_2$ concentrations. Increased ventilation caused by stronger SO diapycnal mixing reduces ocean carbon storage, as in studies by Marinov, Gnanadesikan, et al. (2008) and Lauderdale et al. (2013). The steady state atmospheric $p\mathrm{CO}_2$ concentration was increased by $\sim$11 ppm when changed from a constant diffusivity of $\mathcal{K} = 10^{-5}$ m^{2}s^{-1} to $\mathcal{K} = 10^{-4}$ m^{2}s^{-1}. Changes were even larger, around 15 ppm when a 'realistic' mixing profile (admittedly within our idealised framework) is considered relative to a fixed diffusivity of $\mathcal{K} = 10^{-4}$ m^{2}s^{-1}. Given that glacial-interglacial cy-

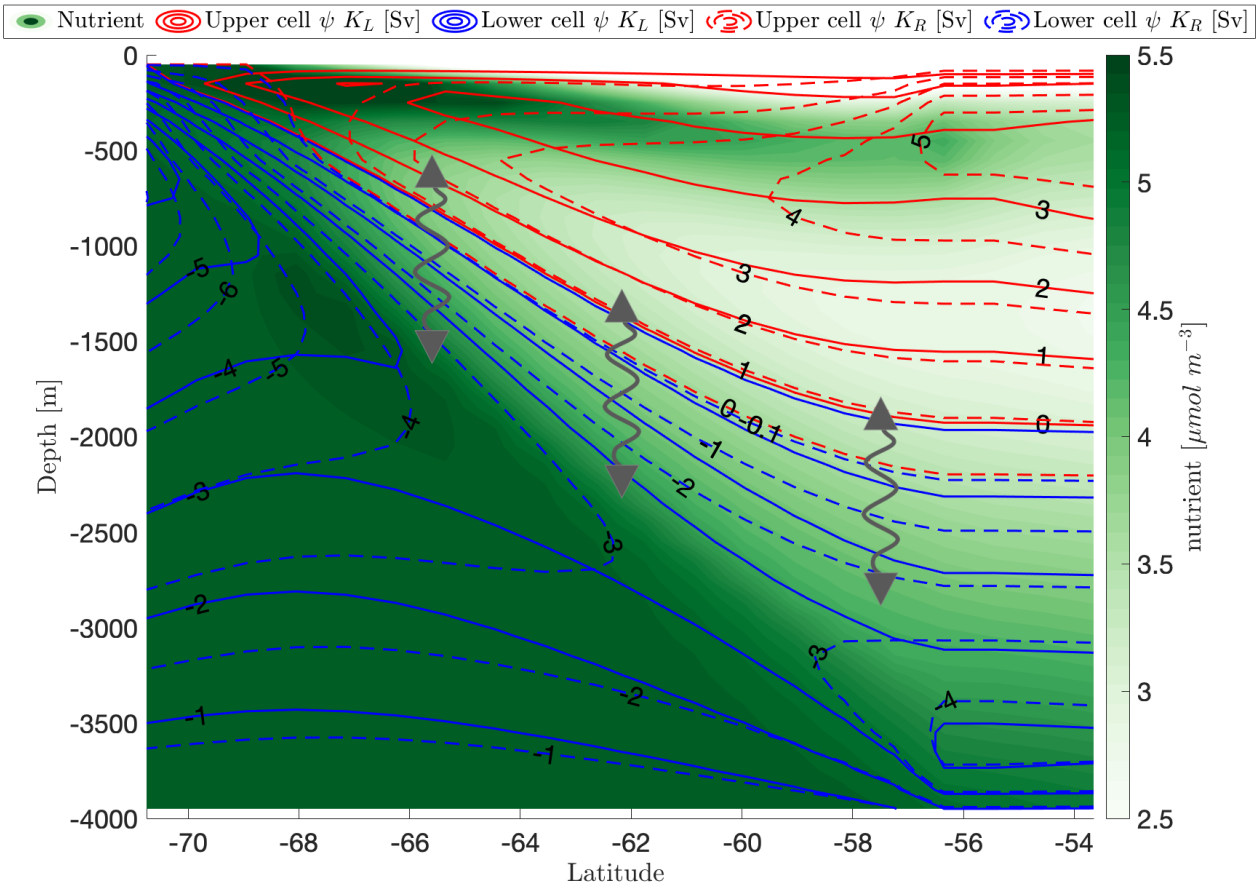


Figure 2.10: Tracer distributions in the SO are altered via two processes: firstly, through the direct impact of mixing (grey arrows) on tracer gradients, and secondly by changing the SO density stratification and thereby the global AMOC. Red and blue contours show the overturning stream functions for the upper and lower AMOC cells for the control $\mathcal{K}_L$ experiment (solid lines) vs the $\mathcal{K}_R$ experiment (dashed lines) in Sv. The background green colour represents the nutrient concentration from the equilibrated control experiment, $\mathcal{K}_L$.

cles in atmospheric pCO_2 were around 80 - 100 ppm (Sigman et al., 2010), and that present-day to pre-industrial atmospheric carbon changes are around 130 ppm, this is a significant change. This work only takes into account the Atlantic Ocean, and if similar experiments were run in a multi-basin model, we expect that similar changes would be observed in all basins, amplifying changes to atmospheric pCO_2.

The idealised nature of our model, and the mere consideration of a single ocean basin ('Atlantic'-like), implies that our results are not meant to represent the state of the real ocean. Though this work was carried out in an Atlantic only setup, it seems unlikely that the response seen is Atlantic-specific. The SO represented as a re-entrant channel in SAMBUCA is also a key feature in the Pacific and Indian Ocean circulation. We believe that the single basin configuration significantly underestimates the sensitivity of the global carbon budget to SO mixing. Though the model is highly simplistic and does not include seasonality, we expect the results obtained using this 'annual mean' configuration to hold throughout all seasons. It is possible that a slightly lower sensitivity to SO diapycnal mixing would be seen in a configuration more representative of winter, when SO winds are stronger, making the dynamics of the SO even more wind than mixing dominated. However, our primary findings should transcend the idealism of our analysis setup.

2.6 Acknowledgements

We would like to thank Maxim Nikurashin for sharing his idealised ocean model with us for use in this chapter.

Chapter 3:

The Biogeochemical Southern Ocean State Estimate

3.1 Abstract

In the subsequent chapters of this thesis, we use the outputs of the Biogeochemical Southern Ocean State Estimate (B-SOSE; Verdy and Mazloff (2017)). In this chapter, we will discuss the physical and biogeochemical components of this model relevant to the work carried out in this thesis. We will also discuss how we will use B-SOSE to investigate the sensitivity of biogeochemical cycles within this state estimate to the parameterisation of diapycnal mixing. In Chapter 4 we will examine how changes to the diapycnal mixing rate in B-SOSE impact biological productivity. In Chapter 5 we will examine how the changes to diapycnal mixing rates in B-SOSE impact on the carbon fluxes of the SO. Finally in Chapter 6 we will utilize B-SOSE to examine how changes to diapycnal mixing rates can improve or worsen the match of the state estimate to observations of biogeochemical tracers.

3.2 Model Description

B-SOSE is a state estimate of SO physics and biogeochemistry. State estimation provides a means to bring a numerical circulation model into consistency with the available observational

data. This produces a hind cast of the ocean state that fills in the gaps between incomplete observations and is dynamically consistent, with closed budgets for carbon and other biogeochemical tracers. This model generated best fit to observations provides a quantitatively useful climatology of the mean state of the SO, including biogeochemical cycles. This reduces the disparity between observations and model outputs for the physical ocean circulation and for biogeochemical cycles. The rapid increase in biogeochemical in situ observations primarily due to a large number of Biogeochemical (BGC) Argo floats deployed makes constraining the model to biogeochemical observations possible. Because B-SOSE represents the constantly evolving SO state, it is not a steady-state solution, in contrast to what one may expect from analysis of an earth system model undergoing a long spin-up process.

The state estimate is produced by solving for the model initial and boundary conditions, the so-called model 'controls', which minimize the cost function (a weighted least squares sum of model-observation misfits) between the model solution and observations by using the adjoint method. Because the adjoint method does not involve unphysical nudging terms, agreement of the solution with observations is not guaranteed but requires consistency with the model equations and closed internal budgets. This method provides the gradients of the misfit function with respect to the model controls, allowing those controls to be efficiently and systematically determined. The advantage of the adjoint method data assimilation approach is that the numerical model propagates observational information across variables using model dynamics. The observations used include physical and biogeochemical observations obtained from Argo floats, including biogeochemical parameters from the Southern Ocean Carbon and Climate Observations and Modeling project (SOCCOM) float array, satellite altimetry, satellite SST, various mooring data, and ship transect data (Verdy & Mazloff, 2017).

The B-SOSE solution provides an estimate of SO biogeochemistry, including air-sea fluxes of heat and carbon and the cycling of nutrients from a biogeochemical and carbon model. The biogeochemical model has been extensively validated against a range of biogeochemical data sets (Verdy & Mazloff, 2017), showing that B-SOSE is able to successfully reproduce the observed large-scale patterns in carbon, oxygen and nutrients distributions of the ocean.

3.3 The Physical Model Set Up

The model is run for seven years (2012 - 2018) using the adjoint method-based assimilation product, with a time step of one hour. In this work, monthly diagnostics are examined for a period of six years, from January 2013 to December 2018. The model domain extends from the equator to 78°S with 52 vertical layers of varying thickness, ranging from 4 m at the surface to around 400 m at the bottom. The zonal grid spacing is always 1/6°, but the meridional grid spacing changes as a function of latitude (δy = δx $\times$ $cos(latitude)$). Ocean physics is represented using the MIT general circulation model (MITgcm; evolved from Marshall et al. (1997)). The ocean is forced through an atmospheric boundary layer scheme where bulk formulae determine heat fluxes, freshwater (salt), and momentum (Large & Yeager, 2009). The 'first guess' atmospheric conditions are from ERA5 (Dee et al., 2011), with adjustments added that were determined by optimisation (Verdy & Mazloff, 2017) using the adjoint method. Sea-ice dynamics and thermodynamics are modelled using 0-layer thermodynamics (Fenty & Heimbach, 2013) and an implicit Line Successive Over Relaxation (LSOR) dynamical solver (Losch et al., 2010). Implicit vertical diffusivity for convection is set to 10 $m^2 s^{-1}$, and no mesoscale eddy parameterisation was implemented.

A Mixed Layer Depth (MLD) is calculated based on the first and second derivatives of model output density. For any point where the water column is deeper than three grid cells, the depth of the maximum vertical density gradient is found. Above this, the maximum second derivative of density with depth is used to find where the stratification is increasing the fastest above the pycnocline. This point is defined as the MLD.

The full set of model parameters used in this 1/6° setup are shown in table 3.1 and described in Swierczek et al. (2021); see Verdy and Mazloff (2017) for initial conditions.

Ocean Model Parameters	
Horizontal Resolution (zonal)	9-16 km
Vertical Resolution	4.2- 400 m
Time step	20 min
Ocean lateral open boundary forcing period	1 month
Atmospheric boundary forcing period	1 hour
Vertical diffusivity	**Alterd in each experient**
Lateral biharmonic diffusivity	$10^{-8}m^4$ s^{-1}
Vertical viscosity	$10^{-5}m^2$ s^{-1}
Lateral biharmonic viscosity	$10^{-8}m^4$ s^{-1}
Quadratic bottom drag coeffficient	0.002
Biogeochemical Model Parameters	
Max phytoplankton photosynthesis rate at 0°	1.3 days^{-1}

Table 3.1: Ocean and Biogeochemical Model Parameters from Swierczek et al. (2021) and Verdy and Mazloff (2017).

3.4 The Biogeochemical Framework

The original BLING model described in Galbraith et al. (2010) has been modified with the addition of nitrogen cycling and improvements in the representation of phytoplankton population dynamics and particle export (Bianchi et al., 2013; Galbraith et al., 2015). The Biogeochemistry with LIght, Nutrients and Gases (NBLING) model, described fully in Verdy and Mazloff (2017), forms the basis of the biogeochemical framework within B-SOSE. Within the NBLING biogeochemical model, biological productivity is parameterised and is influenced by light, nitrate (NO_3), phosphate (PO_4), iron (Fe) availability, and temperature. Biological activity influences the concentrations of carbon and oxygen, and organic matter is remineralisation back to inorganic nutrients. Nine prognostic tracers are simulated in NBLING: dissolved inorganic carbon (DIC), alkalinity (ALK), oxygen (O_2), NO_3, PO_4, Fe, dissolved organic nitrogen (DON), dissolved organic phosphate (DOP) and phytoplankton biomass. Tracer distributions are initialised from several sources; DIC and ALK from Global Ocean Data Analysis Project version 2 climatology (GLODAPv2 (Lauvset et al., 2016; Key et al., 2015)); oxygen, silicate, NO_3 and PO_4 from the World Ocean Atlas 2013 climatology (Garcia, Locarnini, et al., 2013; Garcia, Boyer, et al., 2013); Fe, Dissolved Organic Matter (DOM), DON are prescribed from a course resolution coupled model simulation with BLING. Aeolian Fe sources are also included

(Mahowald et al., 2005). Initial phytoplankton biomass is prescribed from a short model spin-up, and the concentration of chlorophyll is diagnosed at each time step from the total biomass and the variable chlorophyll to carbon ratio. Phytoplankton loss is expressed as a power law with a size-dependent exponent based on Dunne et al. (2005).

The partitioning of biomass into species is determined using stored ratios that are updated every time step based on growth and decay rates. We include two types of phytoplankton: large and small. Small cells represent calcifying organisms; they use calcium carbonate to form shells, while large phytoplankton represent diatom like cells.

The light saturated maximal photosynthesis rate (pc_m),

$$pc_m = pc_0 \times e^{\kappa T} \times min(\frac{NO_3}{\kappa_{NO_3} + NO_3}, \frac{PO_4}{\kappa_{PO_4} + PO_4}, \frac{Fe}{\kappa_{Fe} + Fe}), \tag{3.1}$$

is the product of the prescribed maximum photosynthesis rate (pc_0), the Epply temperature dependence ($e^{\kappa T}$) and a co-limitation term which is the minimum limitations of NO_3, PO_4 or Fe.

The nutrient limitation terms vary between 0 and 1, with a value near 0 meaning that phytoplankton growth is severely nutrient-limited. We modified the NBLING model used in Verdy and Mazloff (2017) to include size dependant nutrient limitation for phytoplankton. Nutrient half saturation constants (κ_{NO_3}, κ_{PO_4} and κ_{Fe}) vary between phytoplankton types, as shown in table 3.2. The small phytoplankton have the lowest half saturation constants, allowing for less nutrient limitation and faster growth rates in low nutrient concentrations. The Epply temperature dependence function represents the effect of temperature on uptake, synthesis and ecosystem function.

Cell type	κ_{NO_3} [mol N m^{-3}]	κ_{PO_4} [mol P m^{-3}]	κ_{Fe} [mol Fe m^{-3}]
Small phytoplankton	2×10^{-6}	1×10^{-8}	1.6×10^{-10}
Large phytoplankton	6×10^{-6}	3×10^{-8}	4.8×10^{-10}

Table 3.2: Nutrient half saturation constants for small and large phytoplankton for NO_3, PO_4 and Fe.

The carbon specific photosynthetic rate (μ), given as

$$\mu = pc_m \times (1 - e^{-irr_{MIX}/irr_\kappa}), \tag{3.2}$$

accounts for the sensitivity of phytoplankton growth to light availability. irr_{MIX} is the instantaneous irradiance field averaged across the mixed layer depth. irr_κ is the nutrient limited efficiency of algal photosystems. irr_κ is calculated as a function of the iron limitation term, to represent the importance of Fe in forming chlorophyll accessory antennae. It is the product of the light saturated maximal photosynthesis rate and the light limitation term, which varies between 1 (no light limitation) to 0 (light limited).

When short wave radiation hits the ocean, it is attenuated as a function of chlorophyll concentration, based on Manizza et al. (2005). Denser chlorophyll results in more light attenuation, a process referred to as self shading.

Phytoplankton loss by grazing is expressed as size-dependent grazing law based on Dunne et al. (2005). The small phytoplankton have a linear increase in mortality with biomass, as small zooplankton rapidly increase as growth rates increase. Large phytoplankton are grazed on by large zooplankton, which respond weakly to increases in growth rates. This produces a simple bloom dynamic, expressed by

$$\lambda_{small} = \lambda_0 \times e^{\kappa T} \times \frac{B_{small}}{B_0}, \tag{3.3}$$

$$\lambda_{large} = \lambda_0 \times e^{\kappa T} \times \frac{B_{large}}{B_0}^{1/3}. \tag{3.4}$$

B_{small} and B_{large} are small are large phytoplankton biomass, B_0 is the pivotal phytoplankton concentration at which a size class is represented to become the dominant food source, λ_0 is the mortality rate, and $e^{\kappa T}$ is the Epply temperature dependence. B_0, $e^{\kappa T}$ and λ_0 are constants determined empirically from global data sets.

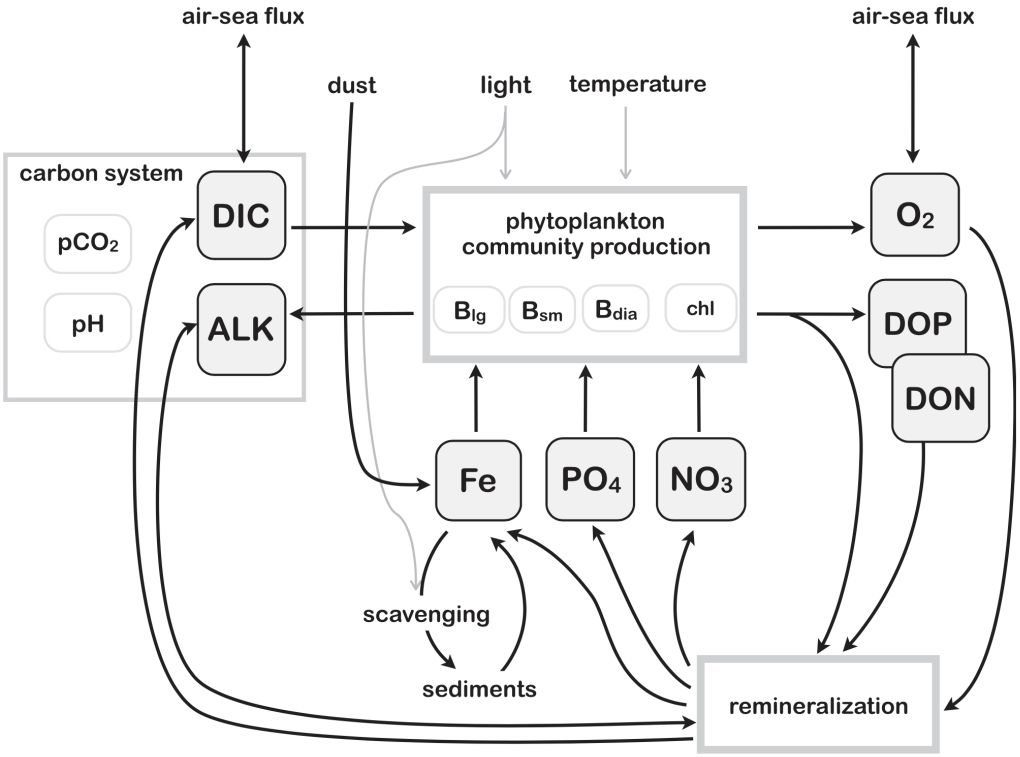


Figure 3.1: Schematic of the biogeochemical model in B-SOSE from Verdy and Mazloff (2017). There are eight prognostic variables (grey shaded boxes): dissolved inorganic carbon (DIC), alkalinity (ALK), oxygen (O_2), nitrate (NO_3), phosphate (PO_4), iron (Fe), and dissolved organic matter (composed of DON and DOP). Phytoplankton biomass, chlorophyll, pH, and pCO_2 are diagnosed from the prognostic variables. The phytoplankton community includes three types of organisms: large diatom-like cells, small calcifying cells, and diazotrophs. Phytoplankton production is limited by the availability of light and nutrients and modulated by temperature. Uptake and remineralisation of nutrients, as well as changes in oxygen and alkalinity, are calculated from the uptake and remineralisation of nitrate via stoichiometric ratios. Black arrows represent fluxes and grey arrows indicate external forcing (Verdy & Mazloff, 2017).

Phytoplankton biomass is given as;

$$B_{large} = B_{large} + B_{large}(\mu_{large} - \lambda_0 e^{\kappa T} \frac{B_{large}}{B_0}^{1/3})\Delta T, \tag{3.5}$$

$$B_{small} = B_{small} + B_{small}(\mu_{small} - \lambda_0 e^{\kappa T} \frac{B_{small}}{B_0})\Delta T. \tag{3.6}$$

Rather than refer to nutrient and light limitation as calculated in Eq 3.1 and 3.2, throughout this work nutrient and light availability are referred to. The availability term is calculated as 1 - the limitation term. Nutrient and light availability therefore also vary from 0 to 1, with 1 representing high nutrient and light availability, and an increase in nutrient or light availability representing an increase in nutrient or light supply between experiments.

Organic matter is split between three pools; one fraction is DOM, one fraction goes to the microbial loop to be instantaneously recycled (R_{ML}), and the remainder sinks as particulate organic matter (R_{POM}). The size of the R_{POM} fraction depends on phytoplankton size (Dunne et al., 2005; Galbraith et al., 2010). Net Community Production (NCP) is the net production of organic carbon from primary production after the respiration of autotrophic and heterotrophic organisms. It is equivalent to the amount of carbon fixed but not respired during primary production (in this work it consists of both the larger Particulate Organic Carbon (POC) and the smaller Dissolved Organic Carbon (DOC). As the fixed organic carbon is not respired it is available to be exported as organic matter, contributing to the biological carbon pump. Export is calculated as the integrated total NCP from the surface to 100 m for each month. Therefore export is composed of sinking and suspended POC and also DOC.

The carbonate system in the model is adapted from the MITgcm simple biogeochemical model of Dutkiewicz et al. (2006). DIC and ALK are prognostic variables and pH and the Partial Pressure of CO_2 (pCO_2) are diagnosed based on Follows et al. (2006). Oceanic surface $p\mathrm{CO}_2$ is diagnosed as a function of DIC, ALK, temperature, salinity and silica, where silica is prescribed from the 2013 World Ocean Atlas climatology (Garcia, Locarnini, et al., 2013). CO_2 and oxygen air-sea fluxes are parameterised following Wanninkhof (1992). Atmospheric $p\mathrm{CO}_2$ is prescribed

using values from the CarbonTracker product (Peters et al., 2007).

3.5 SO Frontal Definitions

We will use frontal zones as defined in Gray et al. (2018) to split the SO into five key zones, each divided by frontal jets (Fig.3.2). From north to south, these are the Subtropical Zone (STZ), the Subantarctic Zone (SAZ), the Polar Frontal Zone (PFZ), the Antarctic-Southern Zone (ASZ), and the Seasonal Ice Zone (SIZ) (Fig.3.2). The STZ is bound by the Subtropical Front (STF) to the south, with this front forming the north of the SAZ. The SAZ is between the STF and the Subantarctic Front (SAF). The PFZ is then south of the SAZ, and is the region between the SAF and the Polar Front (PF). The ASZ is bounded by the PF to the north and the seasonal ice extent to the south. The SIZ is the seasonally open water south of the 2014–2016 sea ice maximum. The definition of the frontal locations are based on potential temperatures of a certain threshold at a given depth to the Argo-based temperature and salinity climatology for 2014 – 2016 of Roemmich et al. (2009), with the spatial extent of regions remaining fixed through time. The northern edge of the SIZ is based on the mean 2014 – 2016 September 15% sea ice concentration location.

3.6 Diapycnal Mixing in B-SOSE

The parameterisation of diapycnal mixing in B-SOSE is composed of two parts:

- The GGL90 mixed layer parameterisation of Gaspar et al. (1990) is used to represent parameterised turbulence and is highly surface-enhanced (Fig.3.3d). The strength of this parameterised turbulence within the mixed layer is influenced by the wind forcing which induces strong turbulence under the seasonal atmospheric storm tracks, the stability of the upper ocean, and the vertical gradients of temperature and salinity within the mixed layer.

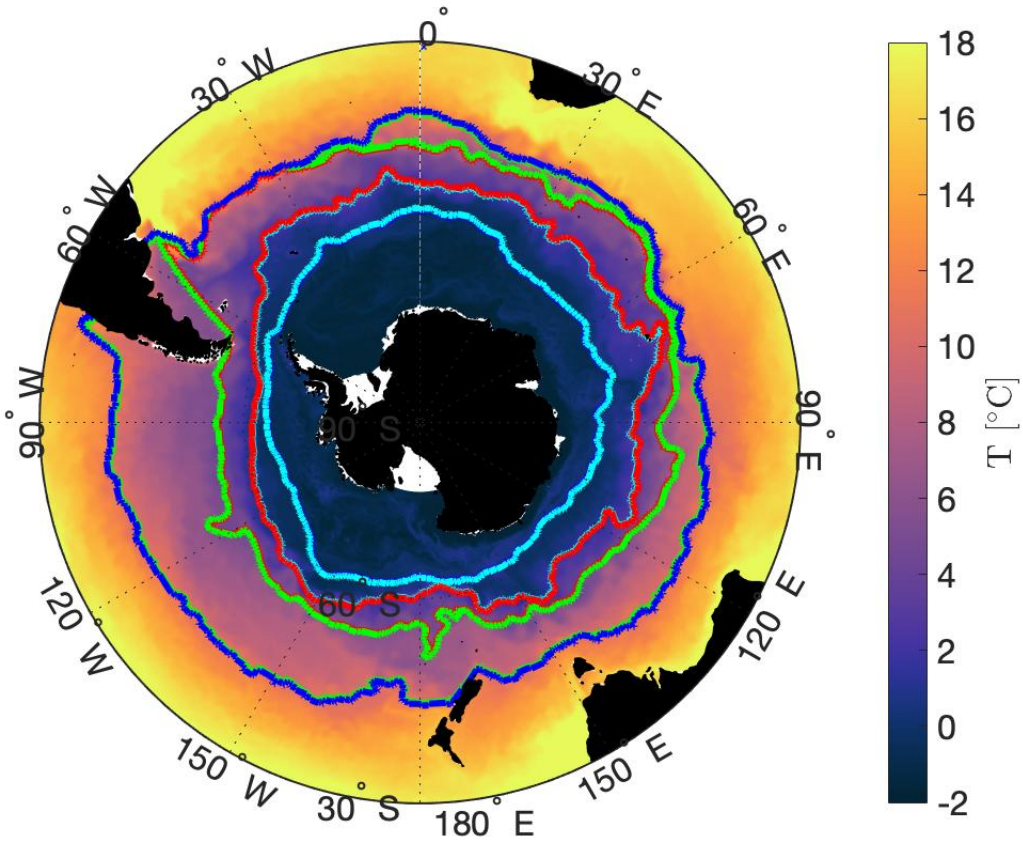


Figure 3.2: The location of SO fronts as defined by Gray et al. (2018). From north to south, they are the Subtropical Front (STF, blue), the Subantarctic Front (SAF, green), the Polar Frontal (PF, red), and the Seasonal Ice Zone extent (SIZ, Light blue). Fronts are plotted over the annual mean temperature at 100 m depth of B-SOSE.

- The background mixed layer parameterisation - this background value is the focus of the work in this thesis. In places such as under the ice or when there is no strong wind-induced turbulence, the model relies on a prescribed background value for turbulent diffusivity.

The background mixing value is added to the GGL90 mixing to achieve a total vertical diapycnal mixing value. Although background mixing values dominate over the GGL90 parameterisation in mid-depths, GGL90 is orders of magnitude larger than the background mixing value in the upper ocean (Fig.3.3).

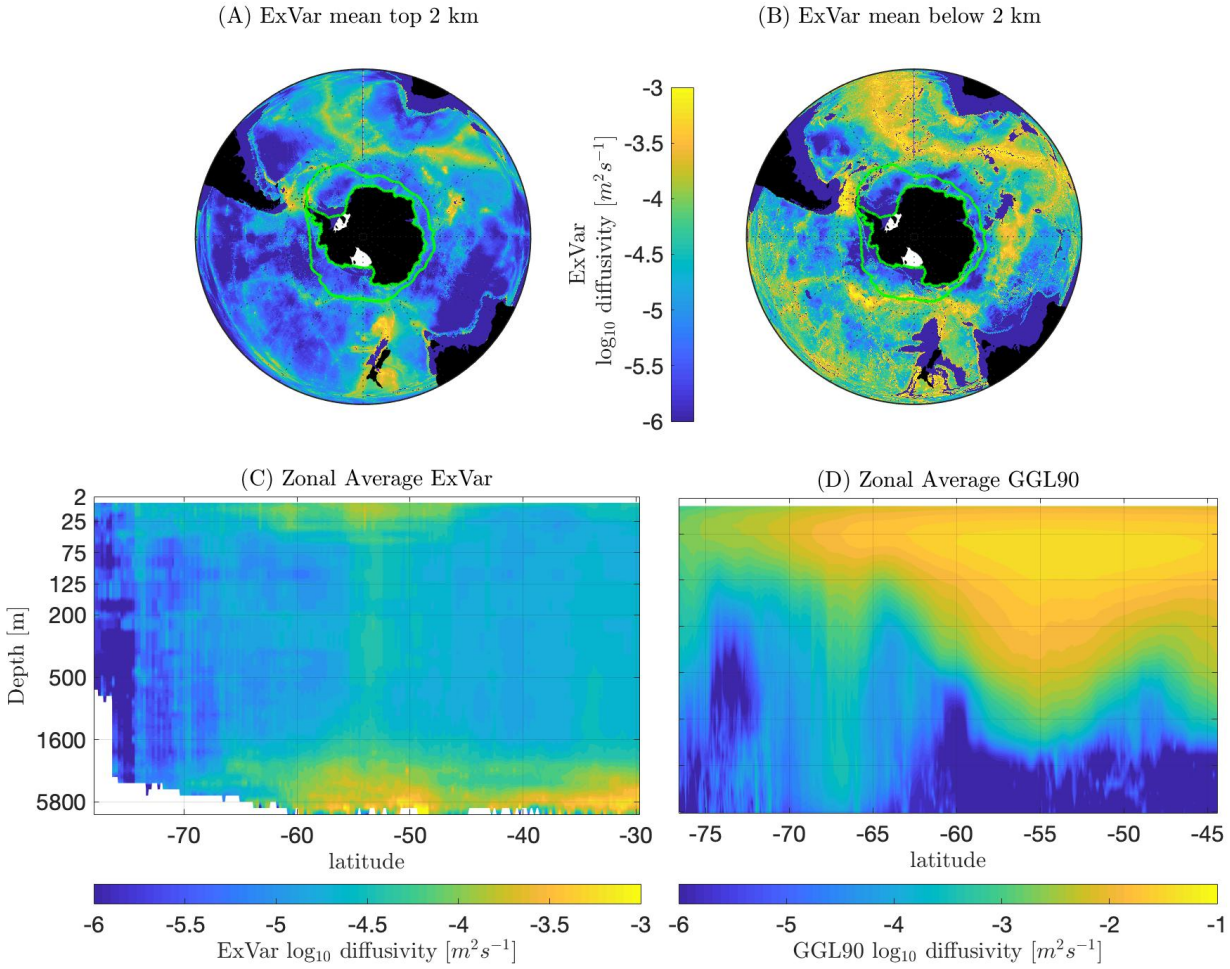


Figure 3.3: Diapycnal mixing in B-SOSE. The distribution of diapycnal mixing in the SO, constructed as the sum of contributions from tides and topographically-generated lee waves. This mixing is shown averaged in depth over the top 2 km in panel A and below 2 km depth in panel B, and zonally averaged over the SO in panel C. These maps are used in the spatially variable mixing map experiment (ExVar). For reference, a zonally-averaged map of the storm-induced mixing, as parameterised through GGL90 parameterisation in B-SOSE, is also shown in panel D. Green lines show the annual mean extent of sea ice. Note that the range of the colour bar in panel D is different from the other panels.

3.6.1 Experimental Design

In this thesis, B-SOSE is run using three parameterisations of background mixing. The three background mixing values used in experiments are:

- A spatially and temporally constant value of $10^{-4}\ m^2 s^{-1}$, we refer to this base simulation as Ex1e-4 hereafter. The high value of $10^{-4}\ m^2 s^{-1}$ for the parameterisation of diapycnal mixing can be motivated by intense Antarctic Circumpolar Current (ACC) internal wave activity (Polzin, 1999). This base simulation is not in equilibrium, as it assimilates a wide range of temporally variable data.

- The first perturbation experiment uses a spatially and temporally constant value of 10^{-5} $m^2 s^{-1}$, referred to as Ex1e-5 hereafter.

- The third experiment, ExVar, uses a spatially variable (but temporally constant) vertical diapycnal mixing map (Fig.3.3a-c). The ExVar map is constructed as the sum of contributions from tides (Lavergne et al., 2020) and topographically-generated lee waves (Nikurashin & Ferrari, 2013) and features horizontal and vertical variations over a range much broader than $10^{-5}\ m^2 s^{-1}$ to $10^{-4}\ m^2 s^{-1}$. The tidal-generated mixing estimate is composed of the contributions of local (high-mode) and long-distance propagating (low-mode) internal tides, taking into account wave-wave interactions, scattering by abyssal hills, dissipation over critical slopes, shoaling, and the propagation of the wave. When compared with the dissipation measured by microstructure profilers and parameterised mixing rates from Argo float data, there is good agreement (Lavergne et al., 2020). The lee wave generated estimate is based on the energy conversion from tidal and geostrophic motions into internal waves combined with a turbulent mixing parameterisation. This is achieved using estimates of the energy conversion into internal waves by tides and geostrophic motions combined with a parameterisation to estimate the rate of mixing generated by these waves. A water-mass transformation framework to convert mixing into water-mass transformation rates is then applied (Nikurashin & Ferrari, 2013).

The SO is a hot spot of lee wave generation (i.e. internal waves generated through the interaction of SO currents and eddies with rough topography) due to the strong ACC and the overlying energetic mesoscale eddy field. Small-scale turbulent mixing processes which are not considered in climate models can easily extend the range of variations to the background mixing beyond what was considered through this thesis (Mashayek, Salehipour, et al., 2017; Cimoli et al., 2019).

The B-SOSE's original conditions and atmospheric adjustments were obtained using $10^{-4}\ m^2 s^{-1}$ as the value for background diapycnal diffusivity (added to the GGL90 mixing). Using the same initial conditions and atmospheric state adjustments, the two additional model simulations were carried out for 2013-2018. The adjustments do result in some transient waves, but these have a negligible impact on the monthly average diagnostics we analyse in this work. In these subsequent runs, the system experiences a moderate step-function kick due to the altered background mixing, representative of the constantly changing background mixing rate of the ocean. In this thesis, we examine the short term response of tracers to the change in this background mixing rate.

The three cases together allow for evaluating the impact of the magnitude of mixing and its spatial variations on biogeochemical cycles. Our aim with these experiments is not to run a set of physically motivated mixing scenarios; rather, it is to investigate the sensitivity of some key climate parameters to the highly variable and largely unknown strength of ocean mixing.

Chapter 4:

Enhanced Southern Ocean Biomass with Increased Background Diapycnal Mixing

4.1 Abstract

Background subsurface vertical mixing rates in the Southern Ocean (SO) are known to vary by an order of magnitude temporally and spatially, due to variability in their generating mechanisms, which include winds and shear instabilities at the surface, and the interaction of tides and lee waves with rough bottom topography. There is great uncertainty in the parameterisation of this mixing in coarse resolution Earth System Models (ESM). Using a data assimilating biogeochemical-ocean model we show that SO phytoplankton productivity is highly sensitive to altering the background diapycnal mixing over short timescales. By altering key biogeochemical and physical parameters, a combination of reduced nutrient limitation and reduced light limitation causes a strong increase in productivity with higher background mixing. This leads to increased carbon export, which could alter the strength of the SO biological carbon pump and atmospheric CO_2 concentration over longer timescales, demonstrating the importance of an accurate representation of diapycnal mixing in ESM.

4.2 Introduction

The Southern Ocean (SO) plays a key role in the control of the global carbon cycle and ocean primary productivity (Sigman et al., 2010; Gruber et al., 2009; Takahashi et al., 2009), and is responsible for an estimated 30% of global annual carbon export (Schlitzer, 2002). The Biological Carbon Pump (BCP) of the SO is a key control on ocean carbon sequestration, meaning its strength and efficiency have a strong impact on atmospheric CO_2 levels (Ito & Follows, 2005; Sigman et al., 2010). As shown in Chapter 2 on centennial to millennial timescales, diapycnal mixing rates alter hydrography and circulation, with high mixing rates increasing the strength of SO ventilation, resulting in a larger supply of deep ocean nutrients to the surface of the SO (F. Bryan, 1987; Ito & Marshall, 2008; Marinov, Gnanadesikan, et al., 2008; Lauderdale et al., 2013). While these large-scale circulation patterns are important, on short timescales, sub-mesoscale processes such as diapycnal mixing also have a strong effect on the distribution of biogeochemical tracers on timescales well matched with phytoplankton growth rates (Mahadevan, 2016), influencing biological productivity, which is the focus of this chatper.

The SO is classified as a High Nutrient Low Chlorophyll (HNLC) zone, where phytoplankton productivity is limited by micronutrients, especially by iron (Fe) (Martin, 1990; P. W. Boyd, 2002), temperature and light (Mitchell et al., 1991; Fauchereau et al., 2011). Seasonal cycles and spatial variability in phytoplankton productivity are dominated by the interactions between light, temperature, and nutrient availability (mainly Fe). The major processes which supply SO surface waters with Fe are the winter entrainment of Fe-rich waters due to buoyancy loss driven convection and mixed layer deepening (Tagliabue, Sallée, et al., 2014) and vertical mixing across the base of the mixed layer (especially during storms) (Tagliabue, Sallée, et al., 2014; Llort et al., 2019). Ekman upwelling/ downwelling (Tagliabue, Williams, et al., 2014) and iceberg calving and melting can also be important sources of Fe to surface waters.

Subsurface diapycnal mixing is key in setting the vertical gradients and distributions of physical and biogeochemical tracers. Diapycnal mixing rates alter the vertical gradients and transport of biogeochemical tracers, affecting the concentrations of nutrients in the mixed layer. These

tracers often have strong vertical gradients in their distribution due to depth-varying sources and sinks (Freilich & Mahadevan, 2019). Diapycnal mixing also contributes to the water column temperature profiles, stratification, and Mixed Layer Depth (MLD). A deep mixed layer can result in surface waters being supplied with more nutrient-rich waters via entrainment and vertical mixing (Tagliabue, Sallée, et al., 2014). A deepening of the MLD can therefore cause an increase in Fe and other micronutrient supply, but a decrease in the average available light to phytoplankton in the mixed layer (P. W. Boyd et al., 2008; Sallée et al., 2010; Fauchereau et al., 2011).

Changes in the availability of light, nutrients, and temperature due to altered diapycnal mixing can alter the makeup of the phytoplankton community, causing different phytoplankton functional types to be favoured within the water column (Krumhardt et al., 2022). The phytoplankton species present, water temperature, and phytoplankton productivity and remineralisation rates can all alter the magnitude of biological export and the efficiency of the BCP (Henson et al., 2019). Alterations to the MLD can also impact the efficiency of carbon export into the ocean via the BCP (Dove et al., 2021).

The range of physical and biogeochemical factors affected by altered SO background diapycnal mixing makes it hard to predict how SO productivity will respond to altered background diapycnal mixing. Idealised models have suggested that enhanced mixing in the SO plays an important role in controlling mixed layer Fe supply and productivity (Nicholson et al., 2016, 2019) and that the impact of altered MLD on SO productivity and export is highly non-monotonic due to balancing effects of Fe and light limitation (Llort et al., 2019; Fauchereau et al., 2011). However, these works did not consider the associated changes in nutraclines, sea - ice cover, water temperatures or phytoplankton types.

Given that background mixing values are orders of magnitude smaller than storms and wind-induced mixing processes in the surface ocean, one would not expect to see significant sensitivity of biomass to altered background mixing values, especially on short timescales, where the mean large-scale dynamics remains mostly unchanged. Here, we show that SO productivity is sensitive to altered background mixing, with strong regional and seasonal variations to this

sensitivity.

4.3 Methods

In this chapter we use B-SOSE, as described in Chapter 3, to investigate how alterations to SO background mixing impacts biological productivity. We use the experimental runs of Ex1e-4 and Ex1e-5 as discussed in Chapter 3 to examine and explain the biologically significant changes to Fe, NO_3, light availability, and surface temperatures observed with increased background diapycnal mixing. The changes in productivity are examined on a seasonal and annual basis.

4.4 Results

4.4.1 Changes to Phytoplankton Primary Productivity

B-SOSE water column integrated Net Primary Production (NPP) is spatially and temporally variable due to varying light and nutrient availability, as well as temperature (Fig.4.1a&b). The annual mean water column integrated NPP (Fig.4.1a) is greatest at latitudes around 55°S, following the Polar Front (PF) (Fig.4.1a red line), with high NPP also found in the Argentine Basin and off the tip of Africa. This agrees with prior observations of phytoplankton blooms in the seasonal ice zone, shallow coastal and shelf waters, near fronts and over large bathymetry. In these regions, high productivity is attributed to the input of Fe from ice melt, sedimentary inputs or upwelling due to mesoscale processes on ocean fronts (Sokolov & Rintoul, 2007). Annual mean NPP south of the PF is low due to a combination of the low temperatures, seasonal ice cover, low light availability and low input of Fe. North of 40°S the NPP is also fairly low due to nutrient limitation, mainly that of nitrate (NO_3). In January (Austral summer), high NPP is found at latitudes as low as 70°S, and as far north as 40°S. Throughout autumn, the NPP at all latitudes gradually decreases towards a winter minimum, as light irradiance and temperatures decrease and MLD deepen (Fig.4.4a). Ice cover extends

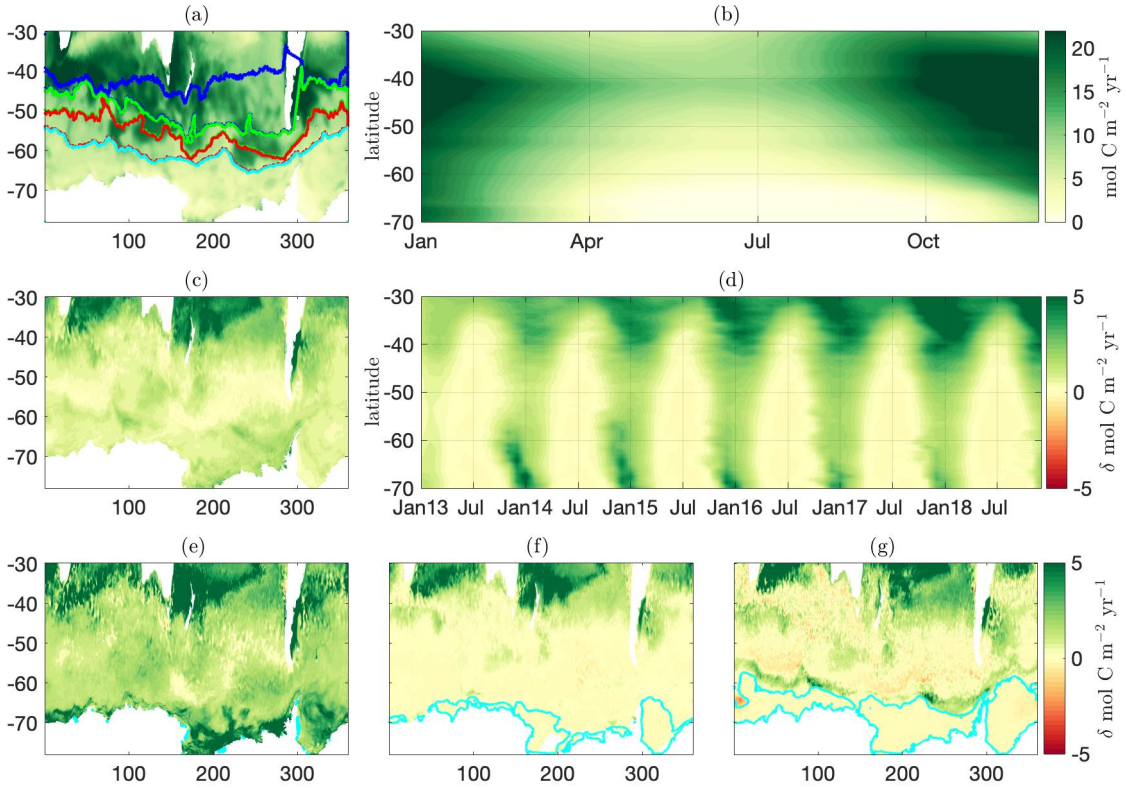


Figure 4.1: a) Six year (2013-2018) mean water column integrated net primary productivity (NPP) in Ex1e-5 for all phytoplankton groups. SO fronts are as depicted in Gray et al. (2018), and from north to south are the Subtropical Front (STF, blue), the Subantarctic Front (SAF, green), the Polar Frontal (PF, red), and the Seasonal Ice Zone extent (SIZ, Light blue). b) Seasonal cycle of zonal average integrated productivity for Ex1e-5 (2013-2018). c) Change (Ex1e-4 - Ex1e-5) in six year mean integrated productivity (2013-2018). d) Change (Ex1e-4 - Ex1e-5) in zonal average integrated productivity over the six years of the experiment. Change in mean integrated productivity for (e) January (f) May (g) September, with the blue line showing sea ice extent in each of those months.

northward throughout winter, and a greater region of the SO becomes ice-covered, where NPP is very low. The lowest average integrated NPP occurs in June (Austral winter). NPP increases again in August as temperatures warm, light irradiance and temperatures once again increase and the MLD shallows; this combines with a rich nutrient supply from wintertime deep water entrainment and mixing. December and January have the highest integrated NPP over all latitudes.

Water column integrated NPP changes with altered background mixing (Fig.4.1c-g). Higher NPP occurs with the enhanced mixing of Ex1e-4 in almost all regions of the SO in all seasons. In an annual mean sense, regions with the greatest increase in NPP in Ex1e-4 include the Argentine Basin and north of the Subtropical Front (STF). There are no regions with a mean decrease in NPP in Ex1e-4 over the six years. Regions with the lowest increase in annual mean integrated NPP almost coincide with regions along the PF, which have high annual mean productivity in Ex1e-5 (Fig.4.1c). The greatest increases in integrated NPP in Ex1e-4 are in the summer, where NPP is increased at all latitudes (Fig.4.1d,e). In January, increases in NPP in Ex1e-4 are found across the whole region of the SO, the strongest increases are just north of the sea ice edge, in the Argentine Basin and north of the STF (Fig.4.1e). The difference in NPP between Ex1e-5 and Ex1e-4 is small during winter south of the Antarctic Circumpolar Current (ACC), as there are very low phytoplankton productivity in both experimental runs (Fig.4.1d). In May (Austral late autumn/ winter) while most of the SO has minimal changes in NPP, again regions north of the STF and in the Argentine Basin have an increase in productivity in Ex1e-4 (Fig.4.1f). By September (Austral spring) a region of increased NPP occurs in Ex1e-4 along the edge of the spring sea ice. Productivity also increases north of the STF and north of 40°S in the Pacific Ocean. In September there are small areas where Ex1e-4 has lower NPP than Ex1e-5, reasons for this will be discussed in subsequent sections. As well as seasonal variations in the changes observed between the two experiments, the difference in NPP between Ex1e-5 and Ex1e-4 varies slightly throughout the six years of the experiment. The greatest increase in productivity north of the STF occurs in the summer of 2018. However, the summertime increase in NPP south of 60°S is greatest in 2014.

4.4.2 Changes to Phytoplankton Types

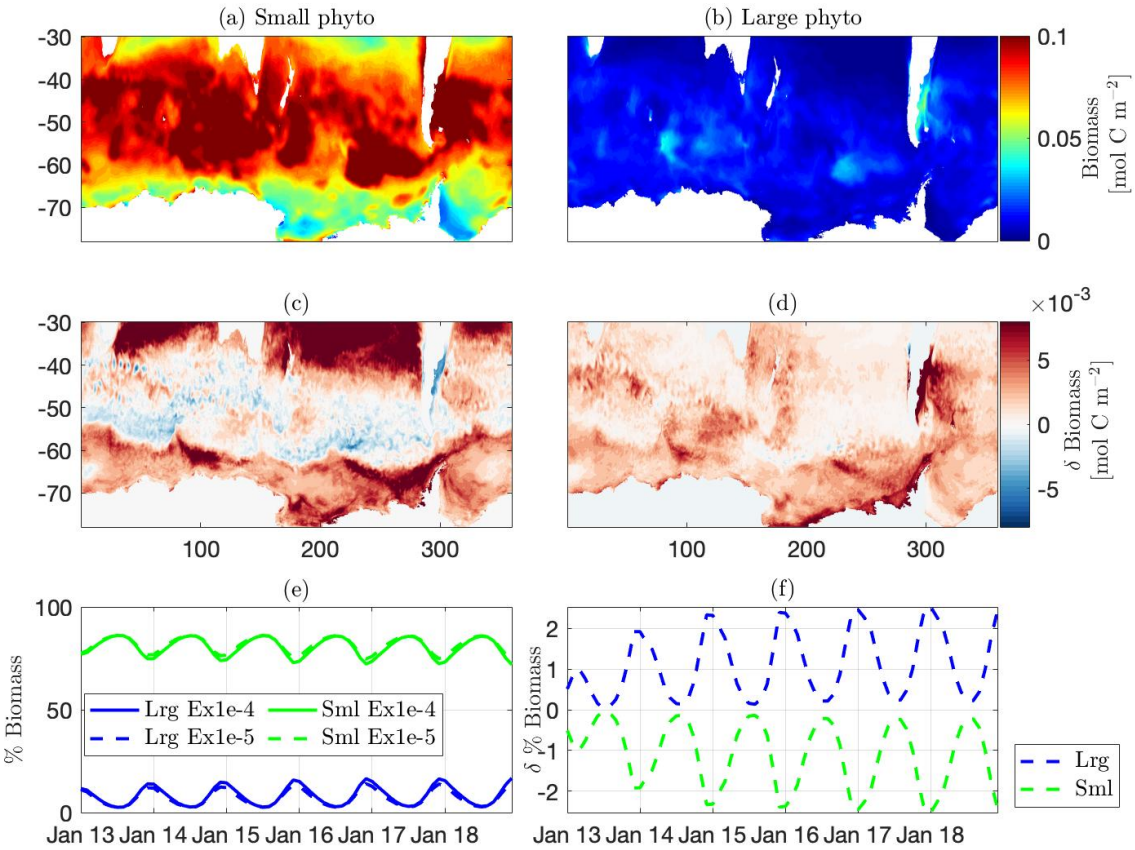


Figure 4.2: Phytoplankton types and changes in phytoplankton types. Ex1e-5 water column integrated six year mean in a) small phytoplankton biomass and b) large phytoplankton biomass 2013 to 2018. Ex1e-4 - Ex1e-5 change in six year c) small phytoplankton d) large phytoplankton biomass. e) Percentage of total SO Biomass for small (green) and large (blue) phytoplankton for Ex1e-4 (solid lines) and Ex1e-5 (dashed lines) from Jan 2013 to Dec 2018. f) Change in percentage of total biomass made up of small (green) and large (blue) phytoplankton from Ex1e-4 to Ex1e-5.

Phytoplankton productivity is made up of small phytoplankton and large phytoplankton. The contribution of each to the total biomass varies in time and space (Fig.4.2). Small phytoplankton have the highest annual mean total water column integrated biomass, with the highest levels found between 40°S and 60°S. Low levels of small phytoplankton occur south of 60°S. Large phytoplankton have far lower total biomass than small phytoplankton. Their biomass peaks between 50°S and 60°S, around the latitudes of the PF. A relatively high biomass of large phytoplankton is found in the Argentine Basin (Fig.4.2a,b).

The annual mean water column integrated biomass of each individual phytoplankton type is

altered with increased background diapycnal diffusivity in Ex1e-4. Small phytoplankton experiences spatially varying changes in biomass between Ex1e-5 and Ex1e-4 (Fig.4.2c). Increases in small phytoplankton biomass occur north of the STF, and south of 60°S in Ex1e-4. In other regions small phytoplankton biomass decreases in Ex1e-4, especially in the Argentine Basin, and between latitudes of 40°S and 60°S (Fig.4.2c). Large phytoplankton biomass increases in all regions of the SO with increased mixing. Large phytoplankton experience the greatest increase in biomass along the coast of Antarctica and in the Argentine Basin (Fig.4.2d).

Small phytoplankton makes up over 70% of the total biomass in Ex1e-4 and Ex1e-5 at all times of year (Fig.4.2e). The percentage contribution by small phytoplankton peaks in the winter and is at a minimum in the summer. Large phytoplankton make up almost none of the biomass during the winter months, but up to around 10% in the summer months. With an increase in mixing, the percentage biomass of large phytoplankton is increased in the summer, by 2% and remains unchanged in the winter (Fig.4.2f). The percentage of total biomass made up of small phytoplankton is decreased in Ex1e4 by 2% and is also unchanged in the winter. The changes to percentages of biomass are smaller in the first two years of the experiment when changes in the percentage of mean biomass for each phytoplankton type are closer to 1% (Fig.4.2e,f).

Herein, we aim to understand the dominant mechanisms responsible for these changes in NPP and phytoplankton types.

4.4.3 Changes to Nutrient Concentrations and Availability

Phytoplankton nutrient availability is set by nutrient concentrations of Fe, NO_3 and Phosphate (PO_4), following the minimum limiting term of Eq.3.1 (Fig.4.3a). A value close to 0 represents low nutrient availability, meaning phytoplankton NPP is limited by nutrients. The regions with the lowest nutrient availability in Ex1e-5 include the northern SO in the Pacific and Indian basins (Fig.4.3a). Regions with higher nutrient availability tend to be closer to land masses, including the Argentine Basin, the south coast of Australia, off the western tip of Africa and along the Antarctic continent. The waters further north have lower nutrient availability than waters further south. In this model, for almost all of the SO, Fe is the limiting nutrient. NO_3 is

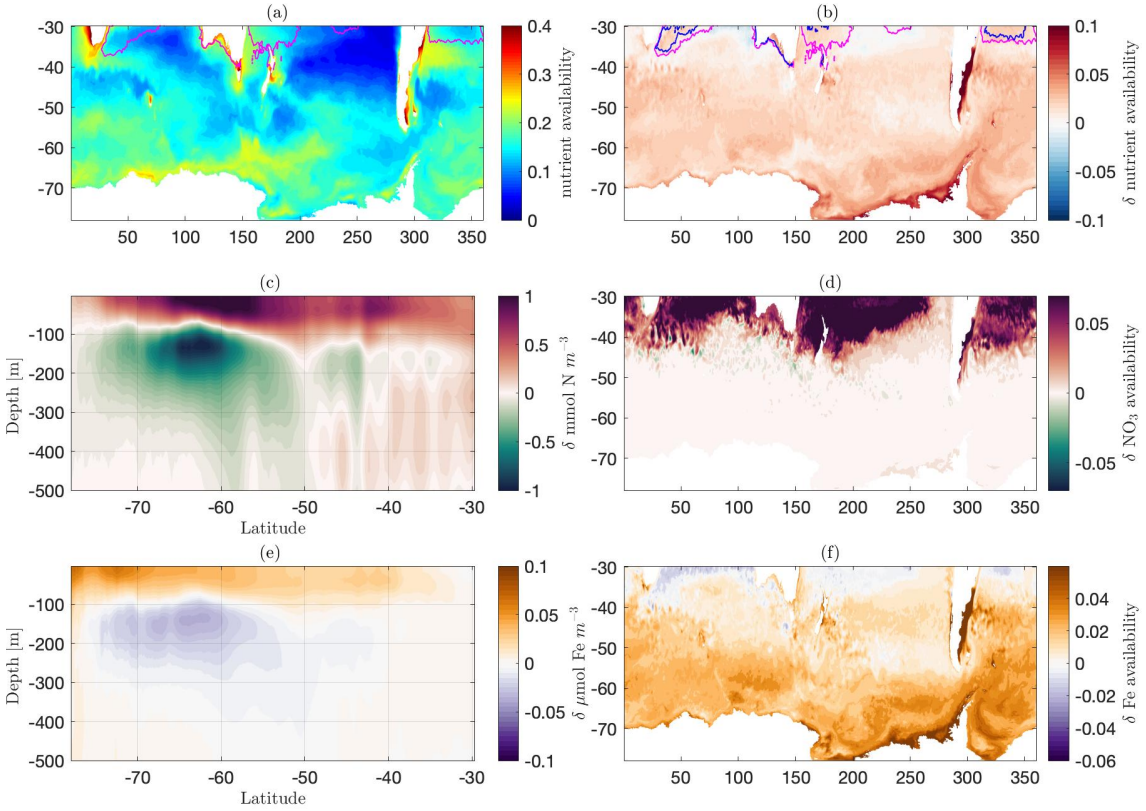


Figure 4.3: Changes in nutrient concentrations and nutrient availability. a) Annual mean surface nutrient availability ($min(Fe_{lim}, No_{3lim}, PO_{4lim})$) of Ex1e-5 (0=no nutrient available, 1= no limitation by nutrients). The pink line encloses NO_3 limitation, all other regions are Fe limited. b) Change in nutrient availability (Ex1e-4 - Ex1e-5). The pink line again surrounds the regions of NO_3 limitation for Ex1e-5, and the blue line encloses the same for Ex1e-4. Again, all other areas are Fe limited. c) Zonal average change in NO_3 concentration (Ex1e-4 - Ex1e-5). d) Change in surface NO_3 availability (Ex1e-4 - Ex1e-5). e) Zonal average change in Fe concentration (Ex1e-4 - Ex1e-5). f) Change in surface Fe availability (Ex1e-4 - Ex1e-5).

the limiting nutrient in small regions of the northern SO, and NO_3 limited regions are outlined in pink in Figure 4.3a. No region of the SO is PO_4 limited.

SO nutrient distributions and thus associated phytoplankton nutrient availability are altered from Ex1e-5 to Ex1e-4. Nutrient availability in surface waters across the SO increases with increased diapycnal mixing in all areas (Fig.4.3b). This increase appears not to vary significantly with the season, therefore annual mean changes are analysed. Regions with the greatest increase in nutrient availability include the Argentine Basin and the coast of Antarctica. Given that SO nutrient availability generally varies between 0 and 0.4, a change of 0.1 represents a significant increase in nutrient availability. The region with NO_3 limitation rather than Fe limitation is reduced in Ex1e-4 (blue vs pink lines), meaning Fe is the limiting nutrient over an even greater area in Ex1e-4 than in Ex1e-5.

The diapycnal flux for a given tracer is typically approximated by

$$\kappa \times \frac{\delta C}{\delta z}$$

where $\mathcal{K}$ is the diapycnal diffusivity rate and $\frac{\delta C}{\delta z}$ is the vertical tracer gradient. An increase in diapycnal mixing causes more tracer to mix down gradient, resulting in enhanced nutrient concentrations in Ex1e-4 above the nutraclines. The regions which experience the strongest change as a result of enhanced diapycnal mixing are regions with very strong vertical gradients in tracer concentrations. The concentration changes in NO_3 show a generalised pattern of an increase in concentration in the upper 100 m and a decrease in concentration from 100 m to 500 m, with some latitudinal variations (Fig.4.3c). South of 50°S, NO_3 concentration increases in waters above approximately 100 m while subsurface water NO_3 concentration decrease in Ex1e-4. The strongest changes occur around 64°S, where vertical gradients of NO_3 are the strongest. North of 50°S a deeper nutracline and less steep vertical gradients cause NO_3 concentrations to increase above depths of around 120 m with weaker increases in concentration below this depth. The concentration of surface Fe increases with a higher mixing value in waters above depths of around 100 m (where the vertical gradient of Fe is the strongest), and decreases below 100 m, from 75°S to around 45°S (Fig.4.3e). Further north of 45°S, surface waters still increase in

Fe concentration, but to a lesser extent than in the very south, and subsurface waters do not experience such a strong reduction in Fe concentration. This is due to weaker vertical gradients in Fe concentration occurring in waters further north.

The changes to nutrient concentrations cause changes to Fe and NO_3 availability (Fig.4.3e,h). Increases to surface NO_3 availability in Ex1e-4 are only seen in the north of the STF, whilst NO_3 availability is unchanged between the two experiments south of the STF. South of the STF, NO_3 availability is already at the maximum value of 1, hence the extra NO_3 fluxed up into the surface waters make no changes to the NO_3 availability. Therefore, changes in NO_3 phytoplankton availability do not resemble the redistribution of NO_3. Almost all surface waters of the SO have increased Fe availability in Ex1e-4 due to increased Fe concentration. Strong increases in Fe availability occur in the Argentine Basin, off the coast of Antarctica, and in waters south of 60°S. Surface waters from 55°S to 45°S have slightly increased Fe availability. In areas where Fe is the most limiting nutrient, an increase in Fe availability results in increased phytoplankton biomass. These large increases in the availability of Fe and NO_3 are able to relieve the nutrient limitation on SO phytoplankton productivity, enhancing NPP rates. Surface waters experience a decrease in Fe availability in the very northern SO from Ex1e-5 to Ex1e-4, especially in the Indian basin. This is likely due to increased biological productivity driven by increased NO_3 availability, increasing the Fe drawdown.

4.4.4 Changes to Mixed Layer Depth

The B-SOSE diagnosed MLD varies spatially and seasonally, extending down to maximum depths of around 200 m. The zonal average MLD is at its deepest in late winter/spring, before shallowing through spring (Fig.4.4a). The entrainment of nutrients into the mixed layer is driven by the deepening of the MLD, which occurs between April and Aug in Ex1e-5 (Fig.4.4a). During spring as the MLD shallows, nutrients are lost from the mixed layer via detrainment.

The increased background mixing of Ex1e-4 results in a deepened MLD (Fig.4.4b,e,f blue regions), but the changes vary seasonally and with latitude. Zonal average changes in the modelled MLD are greatest in the winter, with the MLD deepening in Ex1e-4 by up to 50 m. In the

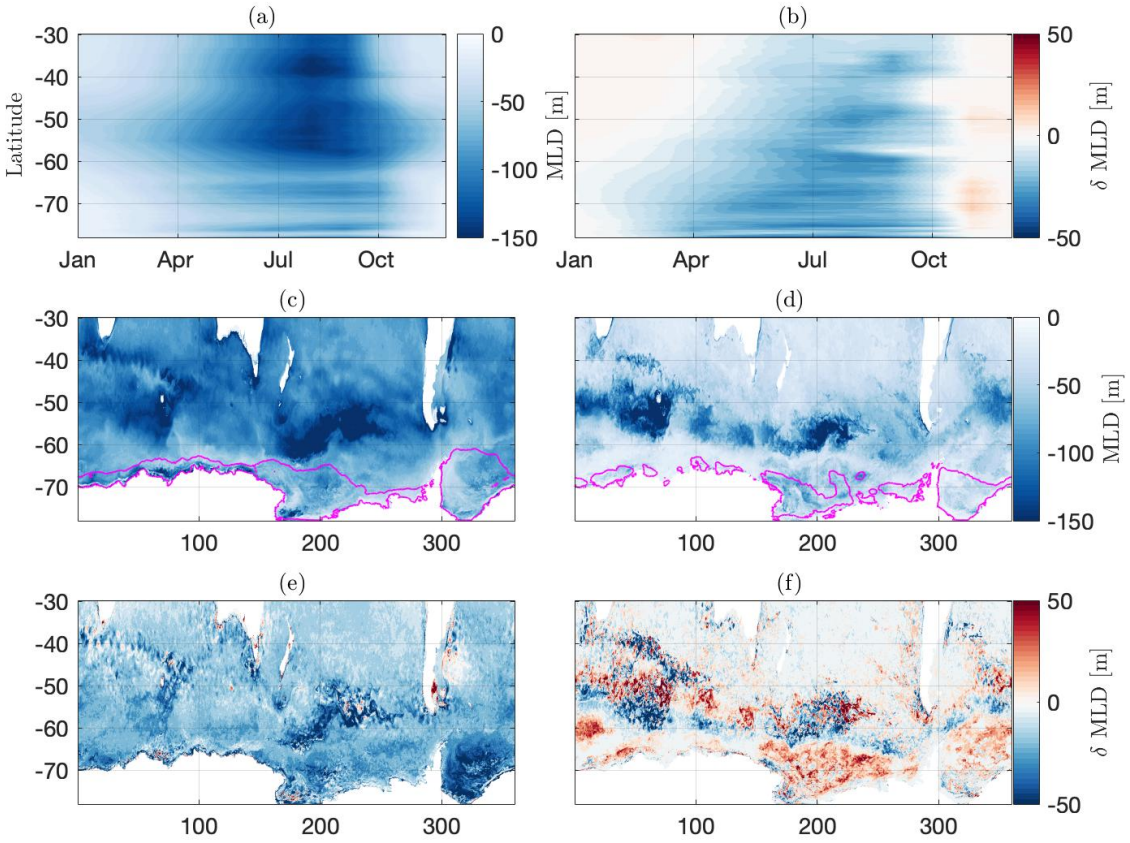


Figure 4.4: Changes in Mixed Layer Depth (MLD) averaged from 2013-2018. a) Seasonal cycle of zonal average MLD for Ex1e-5. b) Seasonal cycle of the zonal average change in MLD, Ex1e-4 - Ex1e-5, blue is the deepening of the mixed layer in Ex1e-4, while red is shallowing. c) June mean MLD for Ex1e-5. d) November mean MLD for Ex1e-5. The Magenta line shows ice extent. e) June mean change in MLD, Ex1e-4 - Ex1e-5. f) November mean change in MLD, Ex1e-4 - Ex1e-5. Blue is the deepening of the mixed layer in Ex1e-4.

summer, a slight mean shallowing of the MLD occurs south of 50°S in Ex1e-4, whilst the MLD north of 50°S is relatively unchanged. In June (Austral winter), there is a deepening of the MLD everywhere in Ex1e-4, especially along the PF under the winter storm tracks (Fig.4.4e). Surface Fe concentrations are set more by the winter MLD than the summer MLD (P. W. e. a. Boyd, 2000), making these changes in winter MLD highly significant. The weak vertical stratification found in the upper water column in winter means that an increase in diapycnal mixing can alter the background state, and cause the breakdown of this stratification and a deepening of the MLD. In November (Austral summer), some regions have a shallowing of the MLD with enhanced background mixing (Fig.4.4f). This is due to an increase in freshwater inputs due to increased sea ice melt with enhanced background mixing (this is discussed in a later section of this chapter). The increased freshwater inputs increase stratification and result in a shallower MLD as surface-generated mixing does not penetrate as deep. Meanwhile, regions that have lower levels of ice cover in Ex1e-4 than Ex1e-5 experience stronger wind-driven mixing and therefore have a deepened MLD.

4.4.5 Changes to Surface Iron Supply

The ferrocline, defined as the maximum vertical gradient in Fe concentration, shows a similar seasonal trend to the MLD, and is deepest in the winter and shallowest in the summer (Fig.4.5a-e). The ferrocline is the deepest in the STZ, north of the STF, reaching almost 150 m in Ex1e-5. With enhanced mixing, the depth of the winter ferrocline is deepened in all frontal zones except the SAZ, by 50 m or more in the STZ, the AZ and the PFZ. In these zones, the winter ferrocline is deepened by more than the MLD with enhanced diapycnal mixing (Fig.4.5a-e). Despite the deepening ferrocline, in the STZ, the SAZ and the PFZ, the upper 200 m of the water column have a year-round increase in Fe concentration in Ex1e-4. However in the AZ and the SIZ, between 100 m and 200 m depth, there is a decrease in Fe concentration in Ex1e-4.

Although the deepened winter MLD of Ex1e-4 would have extended below the ferrocline depth of Ex1e-5, in the STZ, the AZ and the SIZ, it doesn't reach the deepened ferrocline of Ex1e-4 (Fig.4.5a-e). Despite this, the combination of deeper MLD and the altered subsurface diapycnal

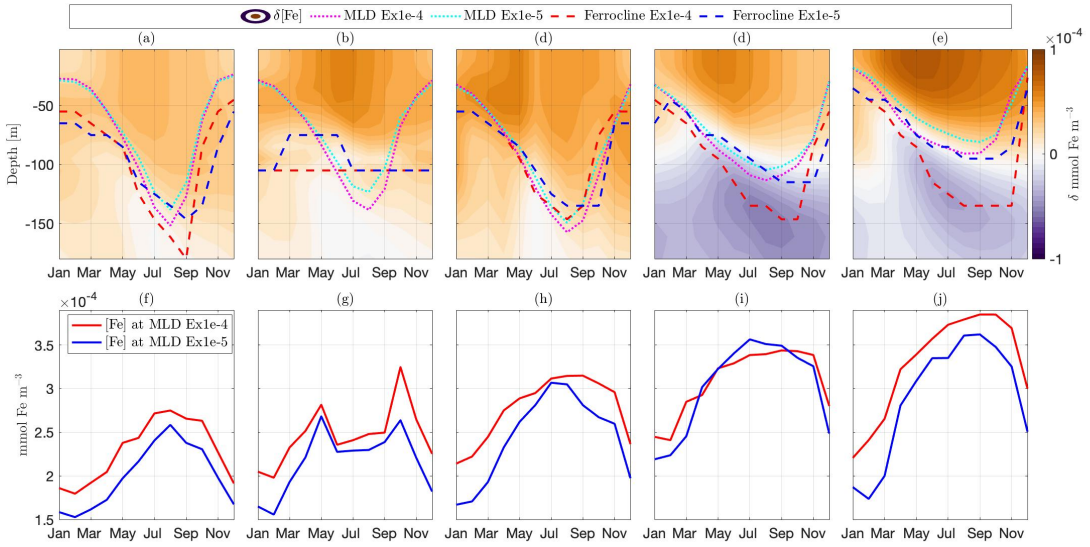


Figure 4.5: Changes to the mixed layer depth and ferrocline depths both result in altered Fe concentrations at the base of the mixed layer with enhanced mixing. a-e) The seasonal cycle of change in Fe concentration is given by the background colour (Ex1e-4 - Ex1e-5). The MLD for Ex1e-5 (light blue line) and Ex1e-4 (pink line) and the depth of the ferrocline for Ex1e-4 (red line) and Ex1e-5 (dark blue line). The ferrocline is defined as the maximum vertical gradient in Fe concentration in a) the Sub tropical zone (STZ), b) the Sub Antarctic Zone (SAZ), c) the Polar frontal zone (PFZ), d) the Antarctic zone (AZ) and e) the Seasonal Ice Zone (SIZ). f-j) Seasonal cycle of Fe concentration at the base of the MLD for Ex1e-4 (red) and Ex1e-5 (blue) in f) the STZ, g) the SAZ, h) the PFZ, i) the AZ and j) the SIZ. Fronts as defined in Gray et al. (2018) and shown in Figure 4.1.a

mixing and down gradient diapycnal fluxes of Fe both result in higher Fe concentrations at the base of the MLD (Fig.4.5f-h,j). In the AZ, there is a lower Fe concentration at the base of the MLD in the winter in Ex1e-4 as subsurface waters are depleted in Fe due to an increased upward diapycnal flux and a deepening of the ferrocline (Fig.4.5i), and the subsurface depletion depth corresponds to the MLD (Fig.4.5d).

The depth of the mixed layer relative to the nutracline will determine the nutrient supply resulting from a change in MLD. The key controls on winter nutrient entrainment are the extent of MLD deepening and the concentration of nutrients in waters at the MLD base which are entrained into the mixed layer. This concentration depends highly on whether the MLD extends below the nutracline or not. As discussed in the previous section, the MLD of the SO in all frontal regions is deepened in the SO winter in Ex1e-4 compared to Ex1e-5, whilst it is unchanged in the summer and shows a shallowing of some regions in spring (Fig.4.4). The higher mixing rates below the MLD in Ex1e-4 increase nutrient concentrations at the MLD base. This allows for a higher flux into the mixed layer, where mixing rates are orders of magnitude stronger than background mixing rates. The increase in surface nutrient concentrations are due to both the direct impact of a higher diapycnal flux, via increased localised diapycnal fluxes, and the indirect impact due to altered stratification and MLD, altering entrainment.

4.4.6 Changes to Light Limitation

Levels of light availability are known to have a key control over SO phytoplankton productivity. The light available to phytoplankton is altered between Ex1e-4 and Ex1e-5 (Fig.4.6a,b), while the incoming solar radiation is unchanged between the two model runs. Over most of the SO, light availability is reduced in Ex1e-4 compared to Ex1e-5 at all times of the year. Given that SO phytoplankton light availability varies between 0 and 0.8 in Ex1e-5, with 0 representing highly light-limited conditions, changes of up to 0.02 between Ex1e-4 and Ex1e-5 represent a significant change in light availability. The reduced light availability in most of the SO in Ex1e-4 is the result of two effects: an increase in biomass and a deeper MLD. A deeper MLD reduces the irr_{mix}, the instantaneous irradiance field averaged throughout the mixed layer, as

phytoplankton within the mixed layer spend more time at greater depths where light levels are lower. Higher water column biomass due to increased NPP increases the attenuation of incoming solar radiation through the water column, reducing light availability via self-shielding mechanisms. In summer, the regions with the strongest reduction in light availability are the Argentine Basin, and north of the STF, both areas experiencing a strong increase in NPP (Fig.4.6a). In spring (September), the strongest reductions in light availability occur around latitudes of 40°S in the Pacific, in the Argentine Basin, and in the Indian Ocean between latitudes of 40°S and 50°S.

Despite most areas having decreased light availability in Ex1e-4, around areas of sea ice, the light availability is increased (Fig.4.6). This increase in light availability occurs in the very south in January, and at latitudes of around 60°S in September, and leads to strong increases in NPP in regions with increased light (Fig.4.1e,g). The increased light availability in these regions is due to reduced sea ice cover in Ex1e-4 (Fig.4.6c,d). Sea ice extends over vast regions of the SO during winter but melts during the spring and summer as air and surface water temperatures increase. In January, the sea ice is almost at its minimum and is mostly confined south of 65°S. During September, the sea ice is melting back from its winter maximum, extending out as far north as 50°S. The surface waters around the sea ice edge in Ex1e-4 are warmer than in Ex1e-5 (Fig.4.6 e,f), increasing the rate of the spring and summer ice sheet melt. Therefore, ice cover in Ex1e-4 is reduced, and the light availability increases. The edge of the ice sheet becomes a region with highly increased light availability and NPP in Ex1e-4. A reduction in sea ice cover can increase wind stress acting on the ocean, deepening the MLD, as seen around the latitudes of the sea ice extent (Fig.4.4d). However, the increased freshwater melt can cause an increase in stratification, shallowing the MLD, which can also be seen in some areas (Fig.4.4d). It is also worth noting that a large polynya is formed in the Weddell Sea in 2018, but that this feature was only observed in the lower mixing case of Ex1e-5. Though this observation is highly interesting in its own right, it is a small scale feature, and therefore is not further discussed in this work.

Sea ice cover is changed between the experiments as altered mixing causes changes to the surface temperature (Fig.4.6e,f). Temperatures in the southern SO are as low as -2°C, rendering a

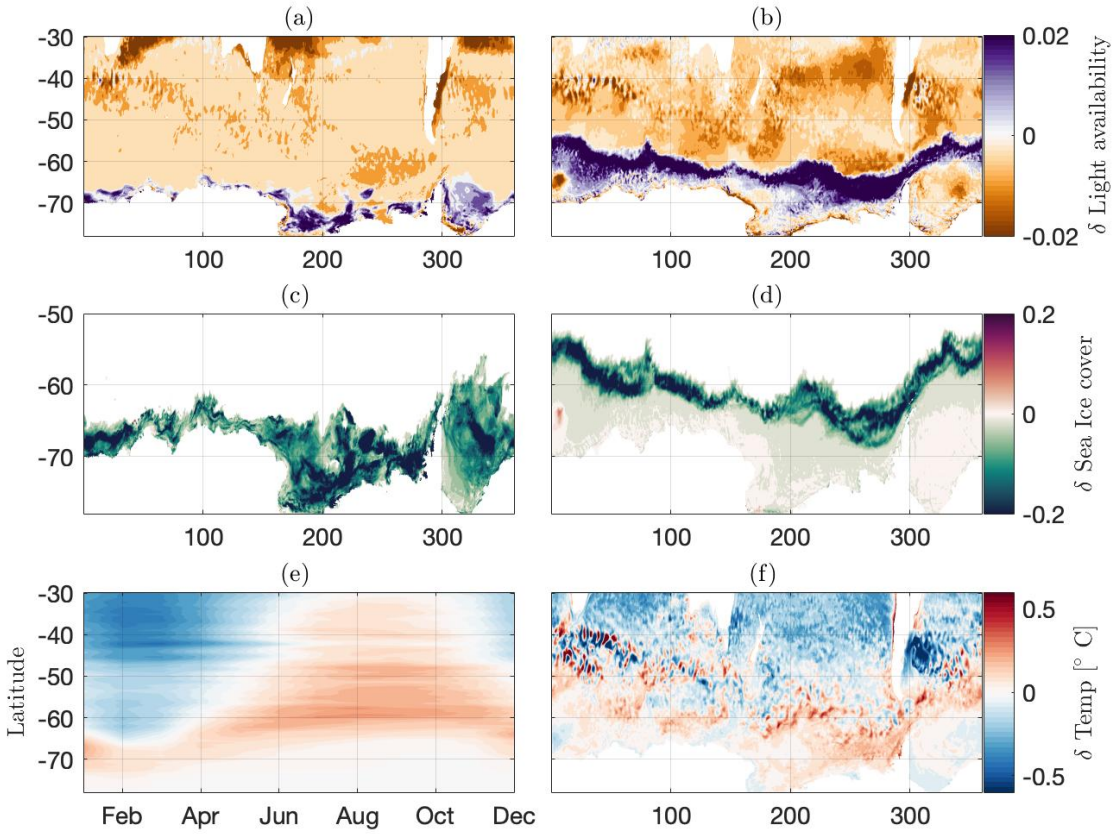


Figure 4.6: Increased surface water temperatures lead to reduced sea ice and increased light availability. The surface here is defined as the upper 25m of the water column. a) January change in surface light availability. b) September change in light availability. c) January change in sea ice cover. d) September change in sea ice cover. e) Seasonal cycle of the zonal average change in surface temperature (Ex1e-4 - Ex1e-5). f) Annual mean change in surface water temperature (Ex1e-4 - Ex1e-5).

change of 0.5°C significant. Annual mean surface temperatures generally increase south of the PF in Ex1e-4, whilst further north, temperatures of the surface waters decrease with increased diapycnal mixing (Fig.4.6.e). In the summer months, the zonal average temperature at most latitudes decreases with enhanced mixing. During the winter months, the zonal average surface temperature of the whole SO is increased in Ex1e-4. The latitudinal and seasonal variation in the effect of increased mixing is due to the difference in the vertical structure of the thermocline at different latitudes.

In the summer months, incoming solar radiation warms surface waters, and temperatures decrease with depth. Enhanced mixing results in more heat being mixed down from the surface, cooling surface waters at almost all latitudes. South of around 65°S, year-round cold temperatures mean that the water temperature increases with depth and enhanced diapycnal mixing allows more heat to be upwelled towards the surface. Equally, at all latitudes south of 30°S in the winter water temperatures increase with depth below the mixed layer. Therefore, increased diapycnal mixing mixes more heat into the surface layers. It is interesting to note that increased mixing is able to simultaneously increase surface water temperatures throughout the winter whilst also increasing the mixed layer depth. These two effects are typically counteractive, with a warmer surface temperature increasing the stratification of the upper water column and shoaling the mixed layer depth.

4.4.7 Changes to Export

The total integrated export at 100 m depth from 80°S to 30°S in this study (2.26 Gt C year^{-1} in Ex1e-5 to 2.74 Gt C year^{-1} in Ex1e-4) fall within the 1.99 Gt C year^{-1} to 3.66 Gt C year^{-1} estimated from previous studies (Su et al., 2022, and references within). During summer, the highest levels of export occur south of the STF, especially around the coast of Antarctica and in the Argentine Basin (Fig.4.7.b). In winter, south of 60°S, export is decreased to almost 0, while export around the PF and in the Argentine Basin is less than half of the magnitudes in the summer (Fig.4.7.c). Enhanced mixing in Ex1e-4 increases export, occurring at times and in locations with the strongest increases in water column integrated NPP (Fig.4.1 and Fig.4.7).

The biggest increases in export (over 10% in some areas) occur during the summer. In summer export increases across all regions of the SO (Fig.4.7.e).

In winter, while export is strongly increased in Ex1e-4 north of the STF, through the rest of the SO the export was slightly reduced in localised areas (Fig.4.7.f). Surface water temperatures are warmed in Ex1e-4, especially during the winter months, increasing the temperature-dependent mortality term (Eqs.3.5,3.6), increasing remineralisation rates, and decreasing export. Changes in phytoplankton NPP during the winter south of the STF are very minimal (Fig.4.1), with slight decreases shown in a few areas. Coupled together, the net effect is a decline in export with enhanced mixing in Ex1e-4.

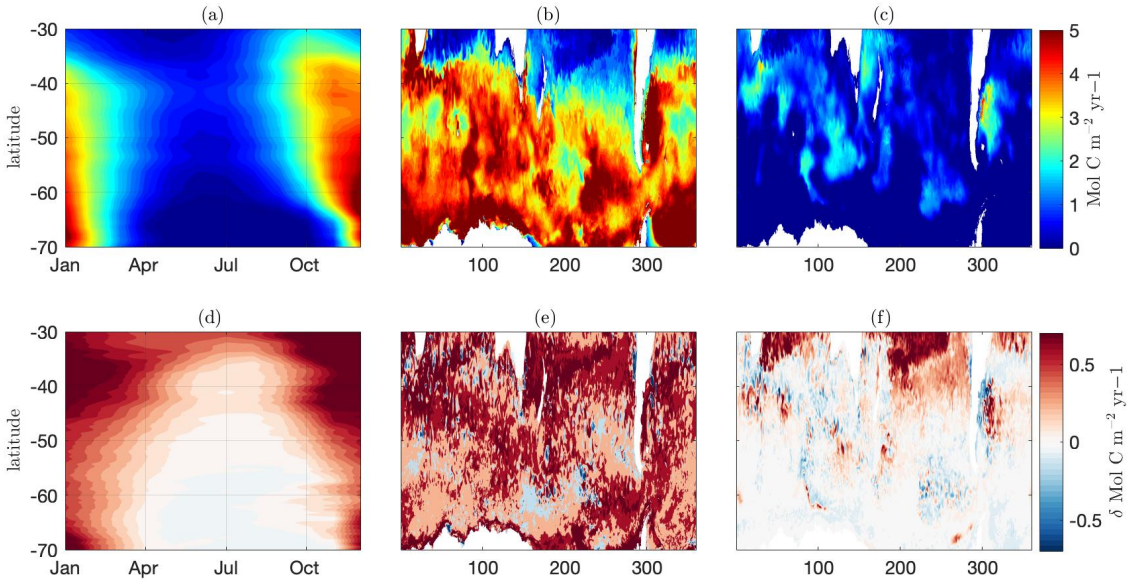


Figure 4.7: B-SOSE Carbon export at 100m depth. a) Zonal average seasonal cycle for Ex1e-5. b) January export in Ex1e-5. c) July export Ex1e-5. d) Change in the zonal average seasonal cycle (Ex1e-4 -Ex1e-5). e) Change in January export (Ex1e-4 -Ex1e-5). f) Change in July export (Ex1e-4 -Ex1e-5).

4.5 Discussion

In this work, we have shown that an increase in SO background diapycnal mixing alters biological productivity through the interplay of a range of competing and compounding mechanisms. Although altered background diapycnal mixing impacts physical and biogeochemical factors,

changes in nutrient supply dominate the changes to NPP. Despite a deeper MLD in Ex1e-4 which increases the light limitation for phytoplankton in the mixed layer, NPP still increases in almost all of the SO in all seasons with enhanced mixing. We have demonstrated the importance of allowing a full range of physical and biogeochemical parameters to change in response to altered background mixing. This is due to the feedback in the ocean system between the physical processes that supply nutrients, primary production, phytoplankton abundance, light penetration and the nitracline depth.

The net change in Fe supply is due to the deepened MLD as well as increased subsurface down gradient diapycnal fluxes. This indicates the importance of allowing both direct tracer fluxes and the indirect changes in background state to be allowed to realistically change in models to understand the impacts of altered diapycnal mixing. Surface nutrient concentrations were increased despite the increase in primary productivity. This suggests that the proportional change in nutrient uptake rate was smaller than the proportional change in nutrient supply rate, resulting in increased preformed nutrient concentrations, and associated outgassing of carbon. Changes to carbon fluxes are discussed in Chapter 5, and indeed show increased carbon outgassing with stronger background mixing.

The greatest increase in NPP and export due to enhanced mixing was during the summer. Whilst in winter, entrainment can supply more Fe to the surface waters than diapycnal diffusion (Tagliabue, Williams, et al., 2014), higher subsurface mixing appears to be most important in the summer to replenish Fe below the MLD. Our work agrees with the findings of Nicholson et al. (2016) that vertical mixing of $\mathcal{O}$ (10^{-4}) $m^2 s^{-1}$ is needed to maintain increased summer productivity. While this is higher than the average mixing experienced through much of the SO, localised and temporally sporadic areas with higher turbulent mixing well over this value are known to occur (Watson et al., 2013). Only biomass which is exported across the winter maximum MLD is likely to escape re-entrainment and thus be separated from the atmosphere over long timescales. Our use of the constant 100 m horizon for evaluating export flux is associated with errors, as the winter MLD is frequently well below the 100 m depth horizon. Previously studies have found reductions in estimated carbon export by as much as 24% when using the winter MLD as the export depth horizon rather than 100 m (Su et al., 2022). The

deeper winter MLD in Ex1e-4 is likely to allow for more remineralisation of organic matter in the mixed layer, meaning less organic carbon is exported below the seasonal maximum mixed layer for long-term sequestration.

Some responses to background mixing are likely to be dampened, while others are exaggerated in B-SOSE due to model limitations. Reduced nutrient limitation due to enhanced mixing causes a slight shift in phytoplankton assemblages. Higher background mixing rates caused a higher percentage of large phytoplankton, which on short timescales, have been suggested to cause more efficient carbon export (Henson et al., 2019). Phytoplankton types in B-SOSE are limited to small and large, while the assemblages in SO are more diverse, with silica requiring diatoms being the dominant phytoplankton group in the Antarctic zone (Swan et al., 2016). This model does not contain silica, known to be a key limiting nutrient on diazotroph productivity (Nelson, 1992). As a result, Fe is the limiting nutrient year-round in our simulations. Within coastal areas, Fe availability is very strongly increased by enhanced diapycnal mixing in B-SOSE. We do not resolve any bottom layer mixing processes: this makes the model overly sensitive to alterations in the background mixing value, as this alters the flux of Fe from their source, which in coastal areas is in the sediment. The impact of enhanced ice sheet melt is dampened in B-SOSE, as this process is not parameterised to release Fe, but is known to be a major source of Fe within the SO (Tagliabue, Williams, et al., 2014).

This work suggests that despite being orders of magnitude smaller than surface mixing, the representation of background diapycnal mixing has significant control over SO NPP, with the potential to alter the strength of the BCP. On long timescales, this could result in alterations to the distribution of remineralised DIC within the MOC, affecting carbon fluxes via the solubility pump (Chen et al., 2022). Alterations to the concentration of nutrients in waters which leave the SO via subduction can cause alterations to biological productivity throughout the global pycnocline and to preformed nutrient concentrations and deep ocean carbon sequestration (Sarmiento et al., 2004; Marinov et al., 2006; Marinov, Gnanadesikan, et al., 2008). Therefore, the parameterisation of diapycnal mixing in the SO is key to modelling biogeochemical cycles globally.

Chapter 5: Carbon Fluxes

Hypersensitivity of Southern Ocean Air-Sea Carbon Fluxes to Background Turbulent Diapycnal Mixing

A revised version (with minor revisions) has been submitted, to be published as E. Ellison, A. Mashayek, M. Mazloff, "Hypersensitivity of Southern Ocean air-sea carbon fluxes to turbulent diapycnal mixing", JGR Oceans.

5.1 Abstract

The Southern Ocean (SO) connects major ocean basins and hosts large air-sea carbon fluxes due to the resurfacing of deep nutrient and carbon-rich waters. While wind-induced turbulent mixing in the SO mixed layer is significant for air-sea fluxes, the importance of the orders-of-magnitude weaker background mixing below is less well understood. The direct impact of altering background mixing on tracers, as opposed to the response due to a longer-term change in large-scale ocean circulation, is also poorly studied. Here, we show that abruptly altering the background mixing in the SO over a range of values typically used in climate models ($\mathcal{O}(10^{-4})$ m^2 s^{-1}- $\mathcal{O}(10^{-5})$ m^2 s^{-1}) can lead to a $\sim$70% change in annual SO air-sea CO_2 fluxes in the first year of perturbations, and around a $\sim$40% change in annual SO air-sea CO_2 fluxes over the six-year duration of the experiment, with even greater changes

on a seasonal timescale. This is primarily through altering the temperature and the dissolved inorganic carbon and alkalinity distribution in the surface water. Given the high spatiotemporal variability of processes that induce small-scale background mixing, this work demonstrates the importance of their representation in climate models for accurate simulation of global biogeochemical cycles.

5.2 Introduction

The Southern Ocean (SO) is a key region for the global cycling of natural and anthropogenic carbon (Sabine, 2004; Takahashi et al., 2009). The SO connects the vast reservoirs of carbon in the deep ocean to the mixed layer and the surface ocean. Here, exchange with the atmosphere can occur, and the formation of abyssal waters which fill the deep ocean basins takes place (Marshall & Speer, 2012; L. Talley et al., 2016). Despite the importance of the SO in the climate system, there is still significant uncertainty in resolving the SO carbon budget, with problems in modelling the system often due to a lack of good parameterisations for unresolved yet highly important physical processes, such as small-scale turbulence (Tatebe et al., 2018).

The air-sea flux of CO_2 primarily depends on the difference in the Partial Pressures of CO_2 (pCO_2) between the atmosphere and the ocean. The pCO_2 is a function of Dissolved Inorganic Carbon (DIC), alkalinity (ALK), temperature and salinity, the distribution or concentration of which are set by physical and biological processes. These physical processes include; advective transport of tracers, vertical diffusion across the base of the mixed layer, entrainment of water from below the mixed layer, air-sea fluxes, evaporation, sea ice growth and the dilution of tracers due to precipitation, runoff and sea ice melting. The biological processes include; organic and inorganic matter formations via photosynthesis and calcification, the subsequent sinking of biomass, and finally the remineralisation of organic matter (Mahadevan et al., 2011; Rosso et al., 2017).

While the carbon fluxes in the northern SO, around the Subtropical Front (STF) are predominately temperature controlled, further south in the Seasonal Ice Zone (SIZ) the magnitude

of carbon fluxes are primarily biologically controlled (Prend et al., 2022). SO air-sea carbon fluxes are especially complex, due to strong seasonality in temperatures, wind regimes, ice/water conditions and biological activity (Takahashi et al., 2012). The balance between temperature-driven solubility, biological productivity and export, and the physical processes of large-scale upwelling and winter entrainment of carbon to the surface waters, cause high variability in time and space of the CO_2 fluxes in the SO (Takahashi et al., 2009, 2012; Rosso et al., 2017; Gray et al., 2018).

On centennial to millennial timescales diapycnal mixing in the global ocean interior is known to be an important factor in setting atmospheric carbon levels via alterations in ocean circulation (Sigman et al., 2010; Marinov & Gnanadesikan, 2011), as shown in Chapter 2. Enhanced mixing increases deep ocean ventilation, increasing the supply of carbon to the SO surface and reducing ocean carbon storage through the biological and solubility carbon pumps (Marinov, Gnanadesikan, et al., 2008; Marinov & Gnanadesikan, 2011). The influence of altering background diapycnal mixing on ocean carbon fluxes on shorter timescales is complex to predict. This is due to spatiotemporal variability in biological and physical responses to variations in mixing (Dutreuil et al., 2009), and the coupled multivariate dependency of ocean pCO_2 to temperature, salinity, ALK and DIC. The biological response to altered background mixing is discussed in Chapter 4. Previous studies have examined the impact of changes to subsurface mixing on SO carbon fluxes, but have not allowed Mixed Layer Depth (MLD) and vertical profiles of the key tracers in setting carbonate chemistry to be altered (Mahadevan et al., 2011). Other studies have examined the effect of surface intensified storm-driven mixing only (Song et al., 2020; Nicholson et al., 2022), rather than assessing changes to carbon fluxes from alterations to the mean background diffusivity.

In this chapter, we are concerned with the short-term response of the air-sea carbon fluxes to altered mixing below the surface mixed layer. It is the immediate response of the system to altered background mixing that is our focus, not a longer-term equilibrated state. We also solely focus on mixing in the SO which has been assumed to be of secondary importance for the global ocean circulation (Nikurashin & Ferrari, 2013) but significant for setting global tracer distributions (Ellison et al., 2022). Given the strong wind-driven isopycnal upwelling in the

SO, and the intense diapycnal mixing within the mixed layer induced by strong winds during storms, one may imagine that the modest changes in the background mixing below the mixed layer would be inconsequential for setting the air-sea fluxes of CO_2 on short timescales. We show the contrary, that modest perturbation of the background mixing strongly alters the SO-integrated air-sea CO_2 fluxes on seasonal, annual, and inter-annual timescales. We demonstrate that the major changes in air-sea carbon fluxes observed in this study are not due to alterations in biological productivity, which are described in Chapter 4.

5.3 Methods

In this chapter we use B-SOSE, as described in Chapter 3, to investigate how alterations to SO background mixing impact air-sea carbon fluxes. We use the experimental cases Ex1e-4, Ex1e-5 and ExVar to compare the carbon fluxes of B-SOSE when using a constantly high, low and spatially variable background mixing rate. The changes in carbon fluxes over the six year duration of these three state estimates are examined on a seasonal to annual timescale.

5.4 Results

5.4.1 Carbon Fluxes

The SO is a net sink of atmospheric CO_2, with most of the uptake occurring between 50°S and 30°S, with a peak at 40°S, where around 0.007 Pg C/yr is taken up (Fig.5.1A). 40°S is the average latitude of the STF, separating the subtropical waters from the subantarctic mode waters, thus hosting rich mesoscale and submesoscale frontal dynamics and enhanced air-sea exchange of tracers. This strong uptake generally occurs in regions with strong biological productivity, such as near topography and in the subpolar gyres. Uptake is also driven by the cooling of the surface waters as they are transported northwards, increasing the capacity to hold CO_2 (Gruber et al., 2009; Takahashi et al., 2002, 2009). To the south of the Polar Front (PF),

on the other hand, the upwelling of deep carbon-rich waters causes carbon outgassing (Fig.5.1E, shown in red). Locations of deep water upwelling lead to strong outgassing of natural carbon in the ACC south of the PF (Landschützer et al., 2015; Verdy & Mazloff, 2017). These waters are rich in carbon due to the sinking and remineralisation of biogenic carbon. Additional carbon uptake occurs further south around Antarctica due to downwelling (induced by a change in the wind direction from westerly to easterly) and deep water formation. Thus, SO fronts, which mark sharp gradients in temperature and carbon chemistry, separate regions of net uptake from regions of outgassing. Higher latitudes show very low mean annual carbon fluxes, partly due to seasonal ice cover.

Carbon uptake varies year-on-year during the six years of the state estimate run by almost 0.002 Pg C/yr at some latitudes, with especially high inter-annual variability at 60°S and 40°S (Fig.5.1A). We do not attempt to remove any linear drift which may be part of a natural change in the ocean carbon system, as this is not the focus of this work, and any trends should be present in all experimental runs. The inter-annual range of carbon fluxes for Ex1e-5 is non-monotonic, as the sign of the changes from year to year varies. The inter-annual variations are due to varying oceanic conditions each year.

Alterations to background diapycnal mixing alter SO carbon fluxes, with ExVar showing smaller differences from Ex1e-5 than Ex1e-4 (Fig.5.1B dashed vs solid lines). The sensitivity to altered diapycnal mixing is variable throughout the six years (Fig.5.1 B). This inter-annual range in sensitivity of around $1\text{x}10^{-5}$ Pg C/yr is well within the inter-annual variability of zonally integrated carbon fluxes in Ex1e-5, which has a mean standard deviation of $2.5\text{x}10^{-4}$ Pg C/yr over all latitudes for 2013 to 2018 (Fig.5.1A,B). A higher difference between Ex1e-5 and Ex1e-4, and to a lesser extent between Ex1e-5 and ExVar occurs in the first three years (2013 to 2015) than in the last three years (2016 to 2018) (Fig.5.1B). As upper ocean mixing is never in an equilibrium state due to constantly changing winds, eddies and buoyancy fluxes, the response to the mixing perturbation over the first three years of this experiment do not seem unrealistically exaggerated.

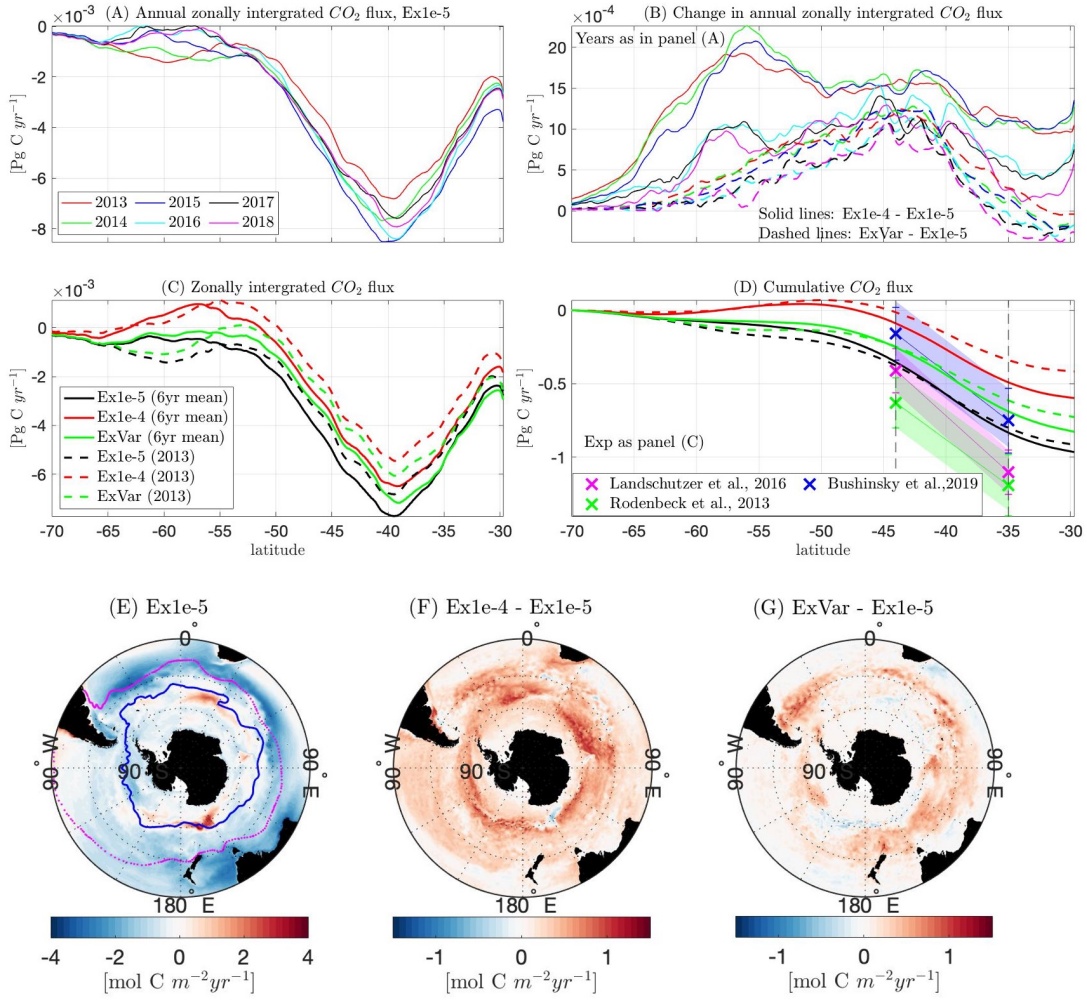


Figure 5.1: (A) Zonally integrated flux of Carbon for each year of Ex1e-5 (negative = Carbon flux from atmosphere to ocean). (B) The difference in the zonally integrated flux of Carbon between Ex1e-4 and Ex1e-5 (solid lines) and ExVar and Ex1e-5 (dashed lines) for each year of the experiment. (C) Zonally integrated annual mean Carbon flux for Ex1e-4, Ex1e-5 and ExVar over the 6-year period (2013 to 2018) and for the first year of the experiment (2013). (D) Annual mean (averaged over 2013 to 2018) cumulative integral of carbon fluxes from 70°S northward to 30°S (legend same as the previous panel). Observational markers are included for comparison (Landschützer et al., 2016; Bushinsky et al., 2019; Rödenbeck et al., 2013). The Landschützer et al. (2016) estimate utilised the Surface Ocean CO_2 Atlas (SOCAT) Version 2 database (D. C. Bakker et al., 2016), while the Rödenbeck et al. (2013) estimate used SOCAT Version 1.5 database. The Bushinsky et al. (2019) estimate utilised data from floats deployed by the Southern Ocean Carbon and Climate Observations and Modeling (SOCCOM) project (Johnson et al., 2017) as well as the SOCAT database. (E) Average annual carbon flux for Ex1e-5, the blue line shows the Polar Front, the magenta line shows Sub-tropical Front as defined by Orsi et al. (1995). (F) Annual mean change in Carbon flux (Ex1e-4 – Ex1e-5). (G) Annual mean change in Carbon flux (ExVar – Ex1e-5). Positive values imply reduced carbon uptake or increased outgassing.

Increasing the background mixing from Ex1e-5 to Ex1e-4 leads to a reduction in annual mean zonally integrated carbon uptake at all latitudes (Fig.5.1C,F). The most significant reduction is around 55°S (Fig.5.1C,F). Minor changes occur south of 65°S due to the ice cover. In ExVar, the most significant changes from Ex1e-5 occur further north, between 39°S and 53°S. South of 60°S, the difference between ExVar and Ex1e-5 is insignificant (Fig.5.1C,G). Large areas of ExVar have carbon fluxes unchanged from those in Ex1e-5 (Fig.5.1G). In Ex1e-5, the mean annual cumulative net flux of carbon into the ocean, integrated from 75°S northward to 30°S, is 1 Pg C/yr (Fig.5.1D). In Ex1e-4 only 0.6 Pg C/yr is taken up, a reduction of 0.4 Pg C yr^{-1}. The annual uptake of ExVar falls between the other two experiments at around 0.8 Pg C/yr. These numbers are for the six-year mean, and as panel B shows, the reductions from Ex1e-5 are much higher over the first three years (almost double).

The cumulative carbon fluxes are compared to other estimates of the integrated SO carbon flux from 75°S northward to up to 45°S and 35°S for the period 2015-2017 (Fig.5.1D; Bushinsky et al. (2019); Landschützer et al. (2016); Rödenbeck et al. (2013)). At 45°S, the Ex1e-5 cumulative flux lies between the three observationally inferred estimates, while the ExVar flux is slightly lower, with Ex1e-4 being the lowest of all three, well below the estimates of the other studies. At 35°S, there is a larger range in carbon uptake between the three model runs. Ex1e-5 is the only experiment that lies within the bounds of the three observational estimates, whilst the lower carbon uptake of ExVar and Ex1e-4 are outside the range of previous estimates. The difference between the cumulative carbon fluxes at 45°S of the three experiments is similar to the uncertainty associated with prior estimates. All experiments fall within the uncertain range of the Bushinsky et al. estimate at 35°S, but ExVar and Ex1e-5 are also within the Landschützer et al. estimate. At 45°S ExVar and Ex1e-5 are within the uncertainty range of the Bushinsky et al. estimate but are lower than the other estimates available for this period. This comparison to previous estimates suggests that Ex1e-4 underestimates the annual mean SO carbon uptake.

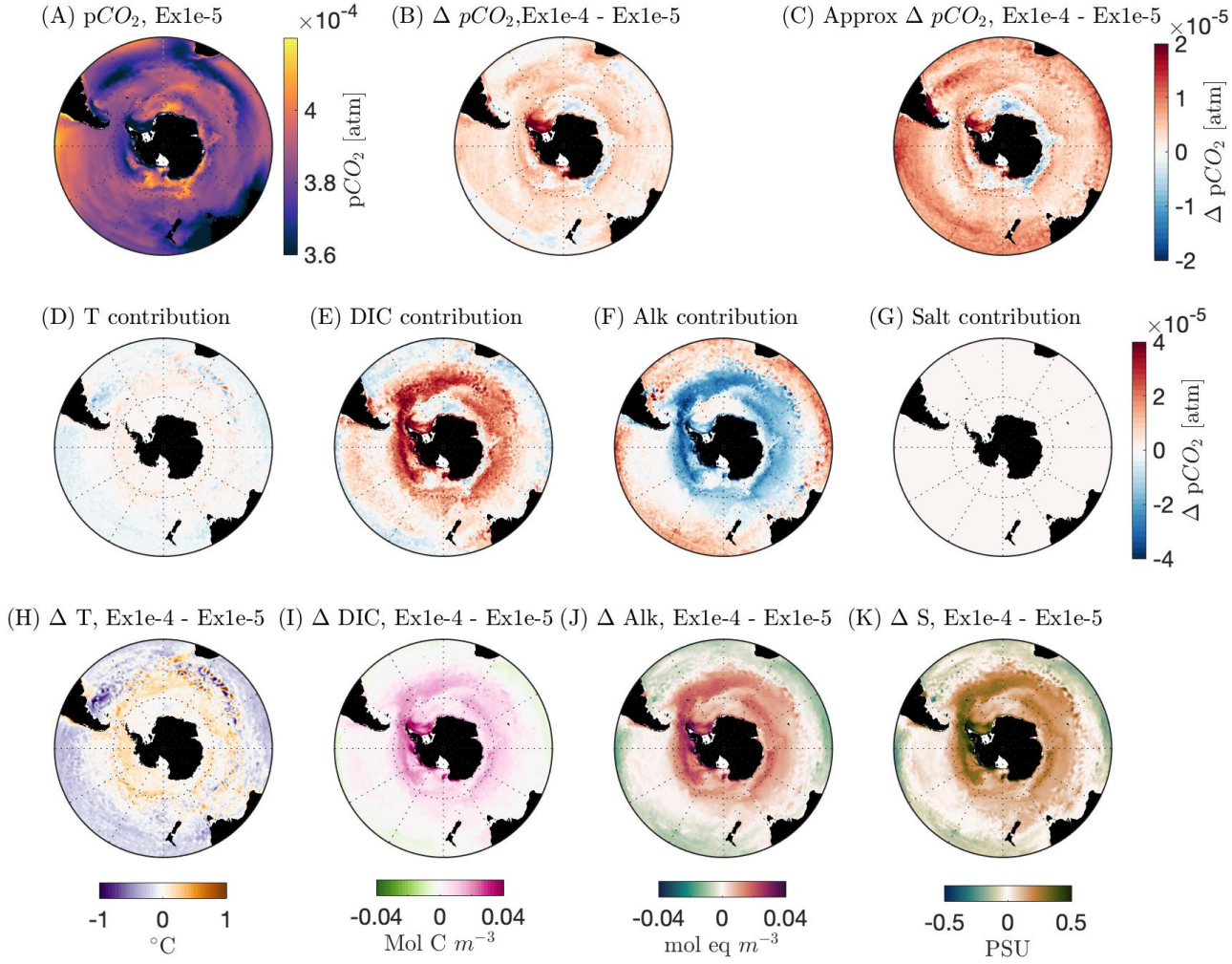


Figure 5.2: Changes to surface ocean partial pressure. (A) Annual mean surface ocean $p\mathrm{CO}_2$ in Ex1e-5. (B) Change in $p\mathrm{CO}_2$ between Ex1e-4 and Ex1e-5. (C) Same as panel B, but this time changes to $p\mathrm{CO}_2$ approximated based on the methodology of Takahashi et al. (2014) that breaks down the change into various contributions as per Eqs.5.1-5.5. The various contributions are shown in panels D-G. (H-K) Changes in annual mean Dissolved Inorganic Carbon (DIC), alkalinity (ALK), potential temperature and salinity.

5.4.2 Changes to Surface Ocean $p\mathrm{CO}_2$

Air-sea carbon fluxes exist due to the difference in $p\mathrm{CO}_2$ between the atmosphere and the surface ocean. The high (low) surface ocean $p\mathrm{CO}_2$ values result in regions of low (high) oceanic uptake or even outgassing of CO_2 from the atmosphere (Fig.5.2A). A region of exception is under sea ice, where the diffusive flux of gases is prevented. The changes in carbon fluxes due to altered mixing, as in Figure 5.1, are due to changes in surface ocean $p\mathrm{CO}_2$, as atmospheric conditions are constant across experiments.

The annual mean $p\mathrm{CO}_2$ of the surface ocean is higher in Ex1e-4 than in Ex1e-5 in almost all regions, reducing the $p\mathrm{CO}_2$ gradient and carbon uptake (Fig.5.2B). The areas of greatest increase in $p\mathrm{CO}_2$ include the south of South Africa and the waters east of the West Antarctic Peninsula. Small regions where the annual mean $p\mathrm{CO}_2$ is reduced in Ex1e-4 include latitudes of around 30°S, especially to the east of Australia, the Argentine Basin, and a few small bands just off the coast of Antarctica in the south.

Using the methodology set out by Takahashi et al. (2014), we break down the $p\mathrm{CO}_2$ change to contributions from changes in the upper ocean content of salinity, temperature, DIC and ALK (Eq.5.1). The change in $p\mathrm{CO}_2$ as a contribution from each of the four tracers is calculated using Eqs.5.2-5.5, where $\bar{p}CO_2$ is the mean $p\mathrm{CO}_2$, $\bar{A}lk$ is the mean ALK, γ_{CO_2} is the Revelle factor for CO_2 (value used = 11), and γ_{ALK} is the Revelle factor for ALK (value used = -10).

$$\Delta pCO_2 = (\frac{\delta pCO_2}{\delta T})\Delta T + (\frac{\delta pCO_2}{\delta DIC})\Delta DIC + (\frac{\delta pCO_2}{\delta Alk})\Delta Alk + (\frac{\delta pCO_2}{\delta S})\Delta S \quad (5.1)$$

$$\frac{\delta pCO_2}{\delta T}\Delta T = 2(\bar{p}CO_2)[Exp(0.0423(\pm 0.0002)\Delta T/2) - 1] \quad (5.2)$$

$$(\frac{\delta pCO_2}{\delta DIC}) = \gamma_{CO_2}(\bar{p}CO_2/\bar{T}CO_2) \quad (5.3)$$

$$\frac{\delta pCO_2}{\delta Alk} = \gamma_{ALK}(\frac{\bar{p}CO_2}{\bar{A}lk}) \quad (5.4)$$

$$(\frac{\delta pCO_2}{\delta S}) = 0.026(\pm 0.002) \cdot \bar{p}CO_2 \quad (5.5)$$

The four individual contributions, shown in Fig.5.2D-G, can be summed together to give the annual mean approximated change in pCO_2 (Fig.5.2C). This calculated change agrees satisfactorily with the changes in pCO_2 between the two experiments (Fig.5.2B). This verifies the assumptions made in Eqs.5.2-5.5, and confirms that changes to the distribution of these tracers are key in causing changes to carbon fluxes (Fig.5.2B,C). The only region where the Takahashi et al. method does not capture the changes is in the north of the SO, west of New Zealand and east of South America in the Argentine Basin. This is likely due to enhanced water mass mixing occurring in these regions, making changes in this area complex to approximate with simple assumptions. While the calculations shown in Fig.5.2 use the upper 2.6 m of the water column, they are not sensitive to depth and similar results are found down to ∼55 m.

On an annual basis, contributions from changes in DIC and ALK concentrations are the main drivers of changes in pCO_2 (Fig.5.2E,F), with the contributions from salinity and temperature being secondary (Fig.5.2D,G). An increase in the ALK content decreases pCO_2, whilst an increase in salinity or DIC increases pCO_2. Where the temperature increases, pCO_2 increases due to modulation of the equilibrium DIC. The increase in the DIC content of the surface waters of the southern SO in Ex1e-4 increases pCO_2, whilst in the north the decrease in DIC concentration decreases pCO_2. On the contrary, the increase in ALK concentration in the south decreases pCO_2, while the decrease in ALK in the north increases pCO_2. Changes in salinity concentrations act to slightly increase the pCO_2 in Ex1e-4. Temperature changes with enhanced mixing cause a slight decrease in pCO_2 in the north and an increase in pCO_2 in the south in Ex1e-4.

The initial changes in the upper ocean temperature, salinity, DIC and ALK are due to alterations to the diapycnal flux of these tracers. The diapycnal flux for a tracer with concentration C may be approximated by $/kappa \times \frac{\partial C}{\partial z}$. Therefore, if vertical diapycnal mixing $\mathcal{K}$ is increased, more tracer, e.g. DIC, is mixed downgradient (upward into the surface waters). This increase in upward flux is the strongest where the vertical gradients are the strongest. Therefore, strong correlations develop between locations with sharp vertical gradients and locations with significantly altered tracer content with enhanced mixing (Fig.5.3A-D). This correlation is especially clear when examining changes to tracer distributions in the first month of the perturbation

experiments, as shown in Figure 5.3. Over time, the carbonate chemistry of the surface waters is altered by indirect changes, such as the horizontal advection of tracers, causing the correlation between vertical gradients and changes in tracer concentrations to become less pronounced (Fig.5.4).

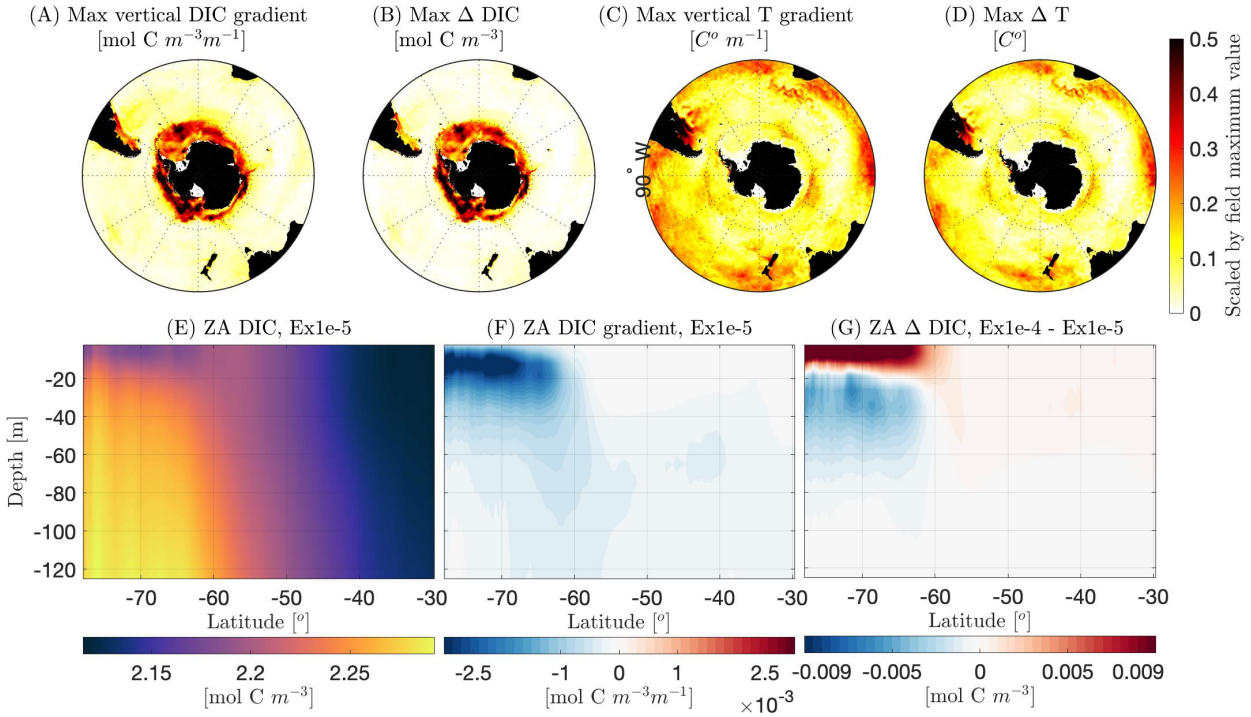


Figure 5.3: (A) Maximum vertical DIC gradient in the water column for Ex1e-5, scaled by the maximum DIC vertical gradient of the field (B) Maximum change in DIC between Ex1e-4 and Ex1e-5, scaled by the maximum difference in DIC of the field. (C,D) Same as A and B but for temperature. The maximum change in DIC (temperature) is defined as the greatest difference in DIC (temperature) concentration between the two experiments at any depth above 200 m at each latitude and longitude in the domain. All values are scaled by the maximum value of the field, with the colour bar ranging from 0 to 0.5. (E) Zonal Average (ZA) DIC concentration in Ex1e-5. (F) Zonal average DIC vertical gradient in Ex1e-5; blue indicates a decrease in concentration towards the surface. (G) ZA change in DIC concentration (Ex1e-4 - Ex1e-5). All are shown for December 2012, the first month of all experiments.

Regions that experience high changes in DIC concentration with enhanced mixing are around the coast of Antarctica, south of 60°S and above depths of 40 m. In these areas, surface waters are fed by wind-induced upwelling of deep waters rich in DIC due to the respiration of organic material. Further to the north, the upper 120 m of the water column has weak vertical gradients of DIC concentration (Fig.5.3E,F). The dipole pattern shown when looking in a zonal average

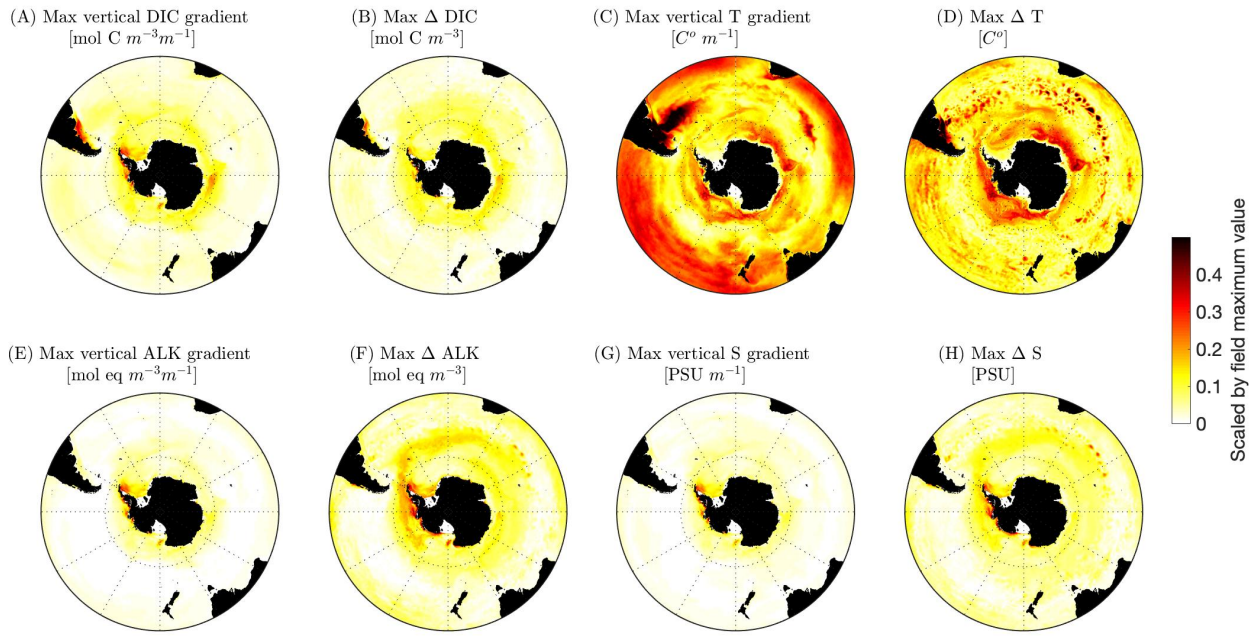


Figure 5.4: (A) Maximum vertical DIC gradient in the water column for Ex1e-5, scaled by the maximum vertical DIC gradient of the field. (B) The maximum change in DIC between Ex1e-4 and Ex1e-5, scaled by the maximum difference in DIC of the field. (C,D) Same as A and B but for temperature. (E,F) Same as A and B but for ALK. (G,H) Same as A and B but for salinity. The maximum change in each tracer is defined as the greatest difference in concentration between the two experiments at any depth above 200 m at each latitude and longitude in the domain. Shown as an average of January 2013 to December 2018.

sense implies the erosion of the sharp gradient by enhanced mixing. The DIC concentration increases with increased mixing in the upper surface waters (shown in red), while concentrations decrease between 40 m and 20 m depth (shown in blue) due to a flux divergence, as more of this carbon has been mixed upwards into the surface waters (Fig.5.3G). There is a clear divide at around 20 m; this depth corresponds to the depth of the maximum vertical gradient. Changes in ALK and salinity roughly follow a pattern similar to DIC and are therefore not shown. The greatest changes in temperature occur in different regions, mainly in the northern SO, especially at around 90°E, in the Argentine Basin, and in the waters surrounding New Zealand.

5.4.3 Temporal and Seasonal Variability of Changes in pCO_2

Carbon fluxes show strong seasonal and spatial variations (Fig.5.5), as discussed in Rosso et al. (2017). In the Austral summer (December to February), the SO from 60°S to 30°S is a net source of CO_2 outgassing (Fig.5.5A,B dashed lines). Some outgassing also occurs at the upwelling zone of the PF, especially in the Atlantic basin (Fig.5.5C). South of ∼60°S, the SO acts as a slight carbon sink even in summer. Austral winter (June to August) has much higher carbon uptake than summer, with the net uptake occurring in almost all regions of the SO, except beneath sea ice (Fig.5.5A,B,F). Small outgassing regions exist around the PF and at the upwelling region off the west coast of South America in the Argentine Basin (Fig.5.5F).

While Figure 5.1 and 5.2 show the changes to carbon fluxes between model runs in an annual mean sense, there are also significant temporal patterns in how mixing perturbation alters carbon fluxes (as will be shown in Fig.5.8). Figures 5.5 and 5.6 examine the dominant mechanisms for seasonal differences observed in the changes to pCO_2 between Ex1e-4, ExVar and Ex1e-5. The changes in carbon fluxes between experiments are greater in winter than in summer (Fig.5.5). An exception is in the very south, where ice cover during winter reduces gas exchange in all experiments. In winter, Ex1e-4 has a reduced carbon uptake compared to Ex1e-5, while ExVar has a similar carbon uptake to Ex1e-5. Cumulatively integrated winter carbon fluxes are reduced from almost 2 Pg C/yr in Ex1e-5 to 1.2 Pg C/yr in Ex1e-4. The greatest decreases

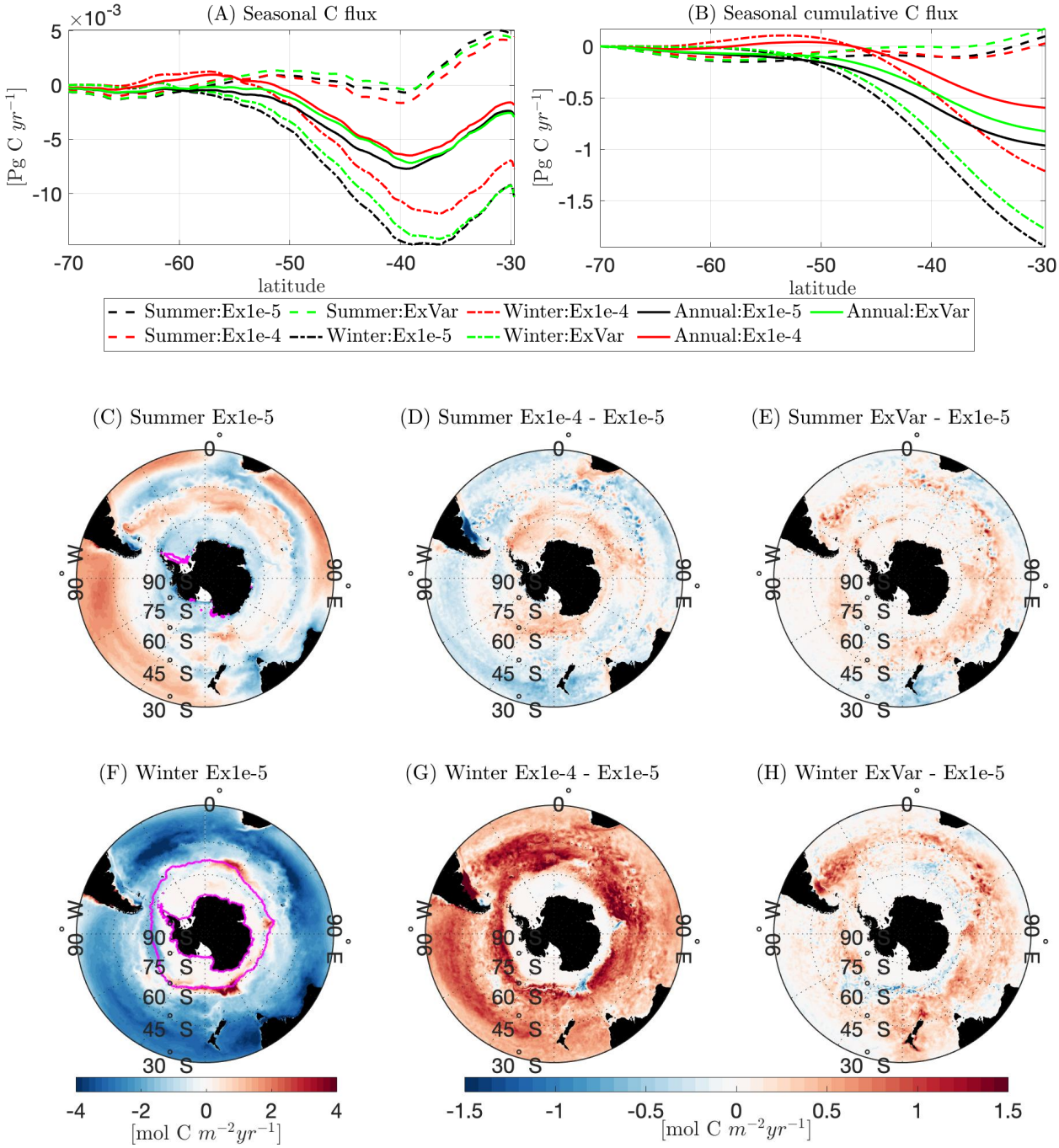


Figure 5.5: (A) Zonally integrated Carbon flux for Ex1e-4, Ex1e-5 and ExVar for summer (dashed), winter (Dotted), and annual mean (solid line). (B) The cumulative sum of carbon fluxes from 70°S northward to 30°S (legend same as the previous panel). (C) Average summer carbon flux for Ex1e-5; magenta lines show the minimum summer ice extent. (D) Mean change in summer Carbon flux (Ex1e-4 –Ex1e-5). (E) Mean change in summer Carbon flux (ExVar –Ex1e-5). (F) Average winter carbon flux for Ex1e-5; magenta lines show the maximum winter ice extent. (G) Mean change in winter Carbon flux (Ex1e-4 –Ex1e-5). (H) Mean change in winter Carbon flux (ExVar –Ex1e-5). Positive values imply reduced carbon uptake or increased outgassing.

in uptake occur around 40°S. The Argentine Basin is also a region of pronounced diminished carbon uptake (Fig.5.5D). Three small areas on the edge of the winter ice extent experience increased carbon uptake in the winter due to reduced ice cover, which is explained subsequently (blue areas, Fig.5.5G). Summer changes to carbon fluxes are of a smaller magnitude and show more spatial variability than the winter months (Fig.5.5). In summer, the cumulative integrated outgassing of Ex1e-5 is higher than Ex1e-4, and ExVar is higher than both Ex1e-4 and Ex1e-5, though the difference between all three runs is less than 0.2 Pg C/yr. At lower latitudes where the SO is a net source of carbon to the atmosphere, outgassing is decreased in Ex1e-4. Further south, where the SO is a carbon sink, CO_2 uptake is reduced in Ex1e-4 (Fig.5.5D). Changes in flux occur as far south as the Antarctic continent due to diminished summer sea ice.

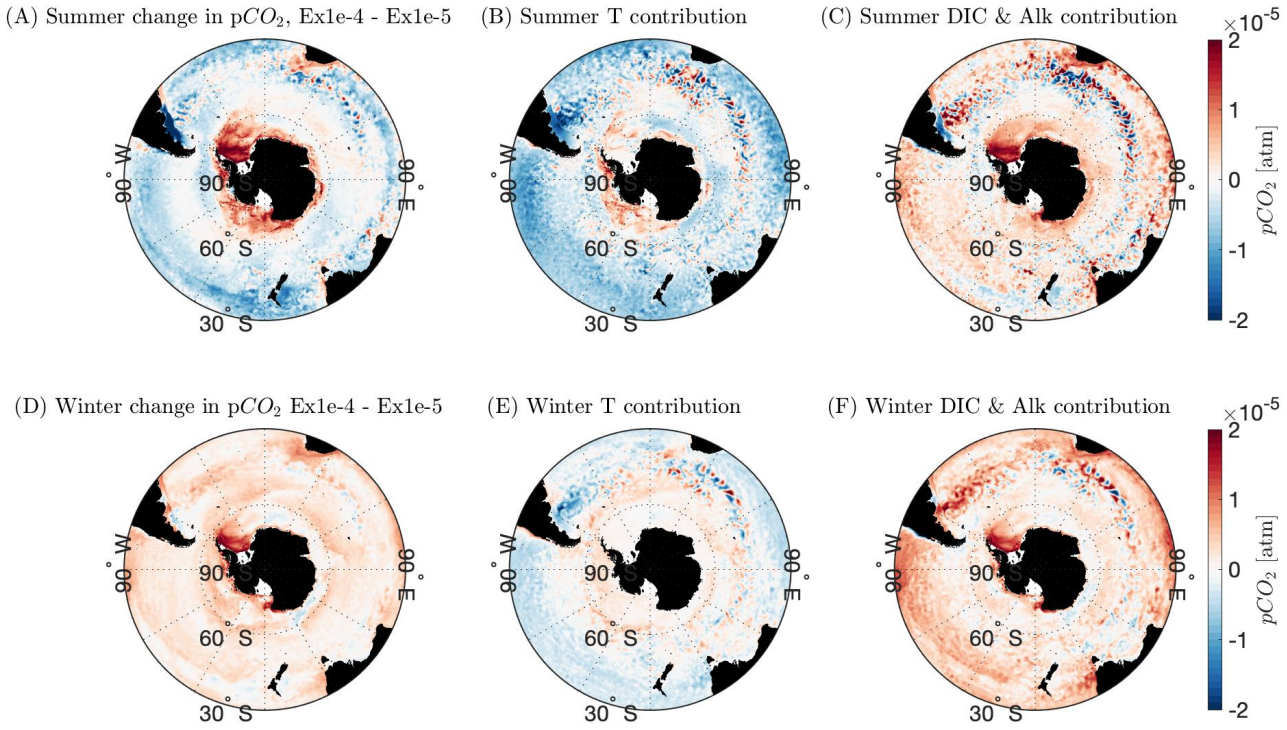


Figure 5.6: (A) January (summer) 2013-2018 mean change in $p\mathrm{CO}_2$ (Ex1e-4 - Ex1e-5) approximated by the method of Takahashi et al. (2014). (B) The contribution is due to changes in temperature. (C) The contribution is due to changes in carbon chemistry (DIC and ALK). (D-F) Same as A-C but for July (winter) mean.

Using Eqs.5.1-5.5 and Fig.5.2, we next use the Takahashi *et al*. methodology to examine seasonal changes to tracer contributions and their implications for the $p\mathrm{CO}_2$ and carbon fluxes. The

outcome is shown in Fig.5.6. Salinity contributions to changes to pCO_2 are not shown as they are negligible compared to DIC, ALK, and temperature contributions. The temperature contribution varies greatly between seasons, being stronger in January than in July (Fig.5.6B,E). Closer to Antarctica, changes in temperature increase the pCO_2 of Ex1e-4 surface waters in both seasons. In July, this positive contribution extends further north. In January, the change in temperature causes very strong reductions in pCO_2, especially in the subtropical gyres. Because the change in surface temperature and associated change to pCO_2 vary with season, the annual mean change in temperature and its contribution to change in pCO_2 appear much smaller (Fig.5.2D). They are nevertheless key to driving the seasonal response of changing SO carbon fluxes in response to altered diapycnal mixing.

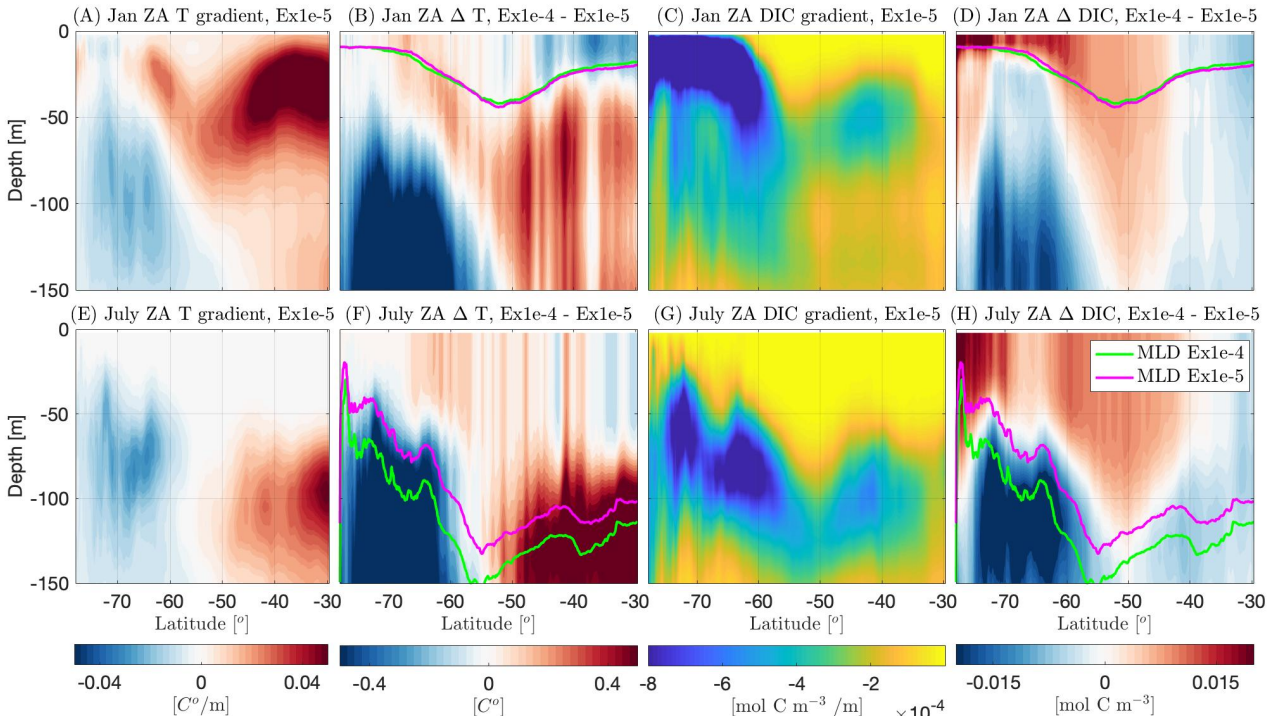


Figure 5.7: (A) January (2013 to 2018) Zonally Averaged (ZA) temperature vertical gradient (red implies an increase in temperature towards the surface). (B) January change in temperature (Ex1e-4 - Ex1e-5). Mixed layer depth (MLD) for Ex1e-5 (pink) and Ex1e-4 (green) overlain. (C) January zonally averaged DIC vertical gradient. (D) Change in DIC concentration (Ex1e-4 - Ex1e-5). (E-H) As in A-D but for July (2013 to 2018) mean.

The vertical structure of the thermocline and the associated change in surface temperature with enhanced mixing have seasonal trends (Fig.5.7B,F). In January, surface waters are warm,

and the temperature declines rapidly with depth down to 100 m, especially north of 60°S (Fig.5.7A). South of 60°S and below 100 m, water temperature increases with depth due to the upwelling of deep warm waters of North-Atlantic origin through Ekman transport. In Ex1e-4, subsurface cooler waters are mixed more strongly towards the surface, cooling the surface waters and warming the subsurface waters relative to Ex1e-5 (Fig.5.7B). This surface cooling reduces the pCO_2 (Fig.5.6A). In July the surface waters are well mixed and there is no temperature gradient in the upper 100 m (Fig.5.7E). Below the winter mixed layer, the temperature rises with depth south of 60°S, and decreases with depth north of 60°S. Enhanced mixing warms surface waters, increasing the pCO_2 (Fig.5.6E,F). This increase in surface temperature also increases the rate of sea ice melt, reducing the sea ice cover toward the end of winter/ spring in Ex1e-4 (fig.4.6d). This results in small regions of increased carbon uptake around the sea ice edge in winter (Fig.5.5F). North of 60°S and below the mixed layer, waters still decrease in temperature with depth (Fig.5.7E,F). Increased mixing cools the surface waters north of 45°S, while between 60°S and 45°S the changes in water temperature appear to be patchy. This is due to the interconnection of vertical mixing and horizontal advection by the meandering currents and eddies that lead to northward intrusion of warmer waters coming from south of 60°S. The vertical gradients of DIC and ALK are relatively constant regardless of season (Fig.5.7C,G). Changes in DIC and ALK concentrations have opposing effects on pCO_2 (Fig.5.2E,F), but together act to increase pCO_2 at all latitudes in summer and winter in Ex1e-4 (Fig.5.6C,F). The increase to pCO_2 in Ex1e-4 from combined carbonate chemistry changes is stronger in the winter than in summer, especially north of 40°S (Fig.5.6C,F).

Though all six years of the model run exhibit a similar seasonal cycle of changes to carbon fluxes with enhanced mixing in Ex1e-4, important inter-annual differences exist (Fig.5.8). Some differences in carbon fluxes between the two experiments become more pronounced over time, while other changes become less. North of 40°S, Ex1e-4 has an increase in carbon uptake (or reduced outgassing) during the summer. This becomes more pronounced and extends further south down to 50°S in subsequent summers as the model run progresses. While the winter time reductions in uptake in Ex1e-4 compared to Ex1e-5 around 45°S become stronger through the six years, the reductions in carbon uptake south of 60°S become weaker. The SO yearly mean

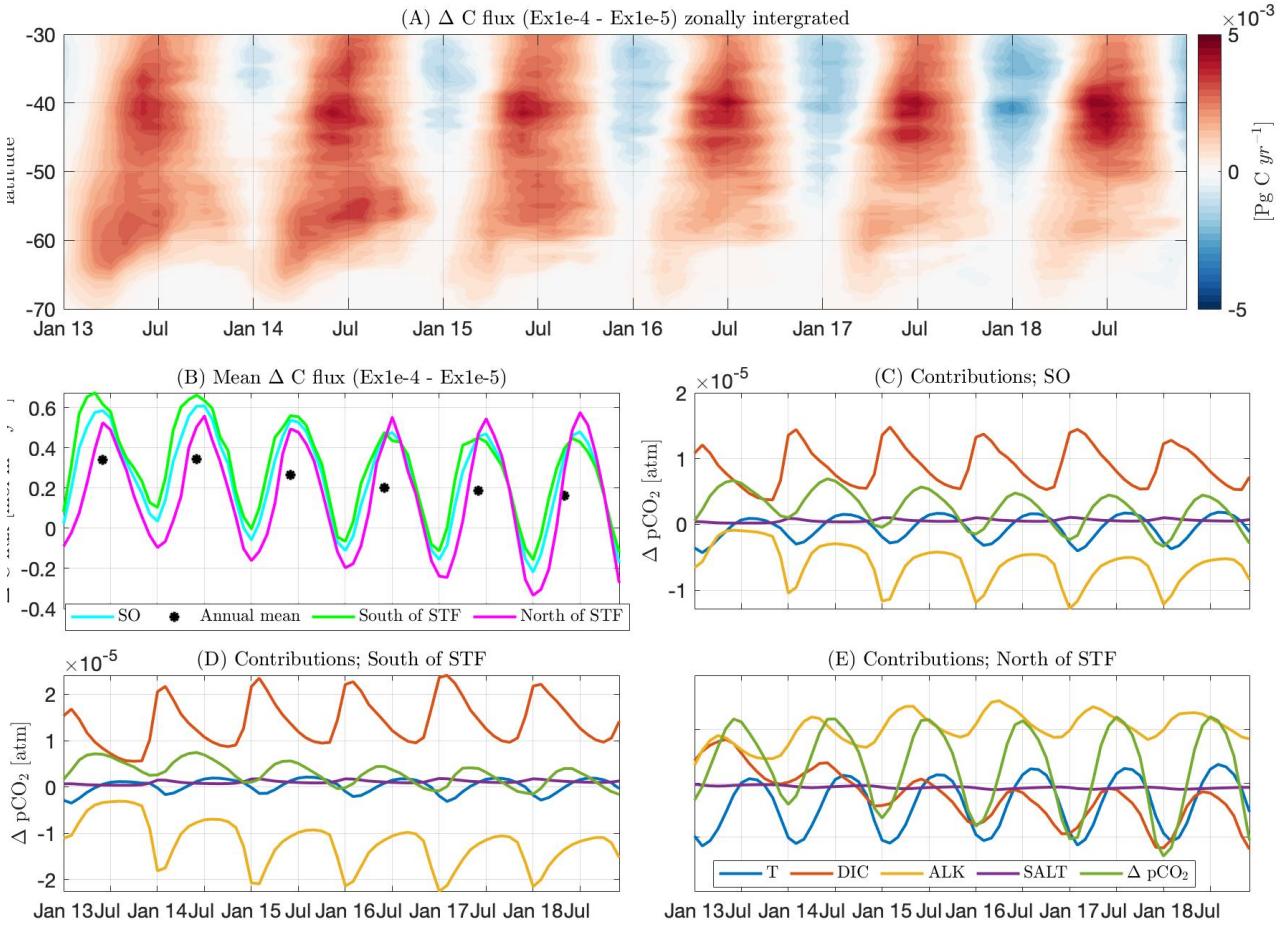


Figure 5.8: (A) Change in zonally integrated carbon flux between Ex1e-4 and Ex1e-5 over the six-year time period of Jan 2013 to Dec 2018 (red shows reduced uptake or increased outgassing in Ex1e-4). (B) Change in the mean carbon flux across the whole SO (blue), the SO North of the Subtropical Front (STF, pink) and South of the STF (green) for the same time period. The annual mean change for the whole SO for each year is shown (red star). Using the methodology of Takahashi et al. (2014) as discussed previously, the differences in carbon flux between the two model runs over time can be attributed to changes in surface ocean pCO_2 (green) from alterations to temperature (blue), DIC (red), ALK (yellow) and salinity (purple). These contributions are shown for; the whole SO in panel (C), the SO south of the STF in panel (D), and the SO north of the STF in panel (E). The STF is defined according to the frontal definitions of Gray et al. (2018).

change in C flux (red stars, Fig.5.8B) between Ex1e-4 and Ex1e-5 is the greatest in the first two years and decreases over the subsequent four years. The reduced carbon fluxes in Ex1e-4 summer are primarily responsible for the smaller annual mean change observed between Ex1e-4 and Ex1e-5 in later years.

40°S approximately corresponds to the mean latitude of the STF and marks a regime in terms of the leading mechanisms responsible for changes in pCO_2 and carbon fluxes. This marks the boundary between the nutrient deplete sub-tropical waters to the north and the nutrient and DIC rich waters to the south (Chapman et al., 2020). Regions to the north of this divide are responsible for the summer increases in carbon uptake in Ex1e-4 in the later years of the run. In contrast, regions to the south are responsible for the strong response of reduced carbon uptake in Ex1e-4.

The contributions to the total change in pCO_2 are drastically different across the STF (Fig.5.8C-E). To its south, opposite changes in pCO_2 due to ALK and DIC nearly balance, with the latter being slightly larger (Fig.5.8D). As before, salinity contributions remain negligible at all times. Over the first two years of the perturbation, the total change in pCO_2 is positive, meaning pCO_2 is higher in Ex1e-4 than in Ex1e-5. The magnitude of the reduction in pCO_2 due to ALK increases over time. The magnitude of total pCO_2 change decreases over time and becomes negative in the summer months, allowing for increased carbon uptake.

North of the STF, DIC and ALK do not balance each other out (Fig.5.8E) and changes in temperature between the two model runs are more dominant. ALK increases pCO_2 north of the STF, while changes in DIC initially also increase the pCO_2 in Ex1e-4. By the summer of the third year of the run, changes in DIC begin to reduce the pCO_2, causing the net total change in pCO_2 to be negative in summer. This causes an increase in carbon uptake in the summer north of the STF in Ex1e-4.

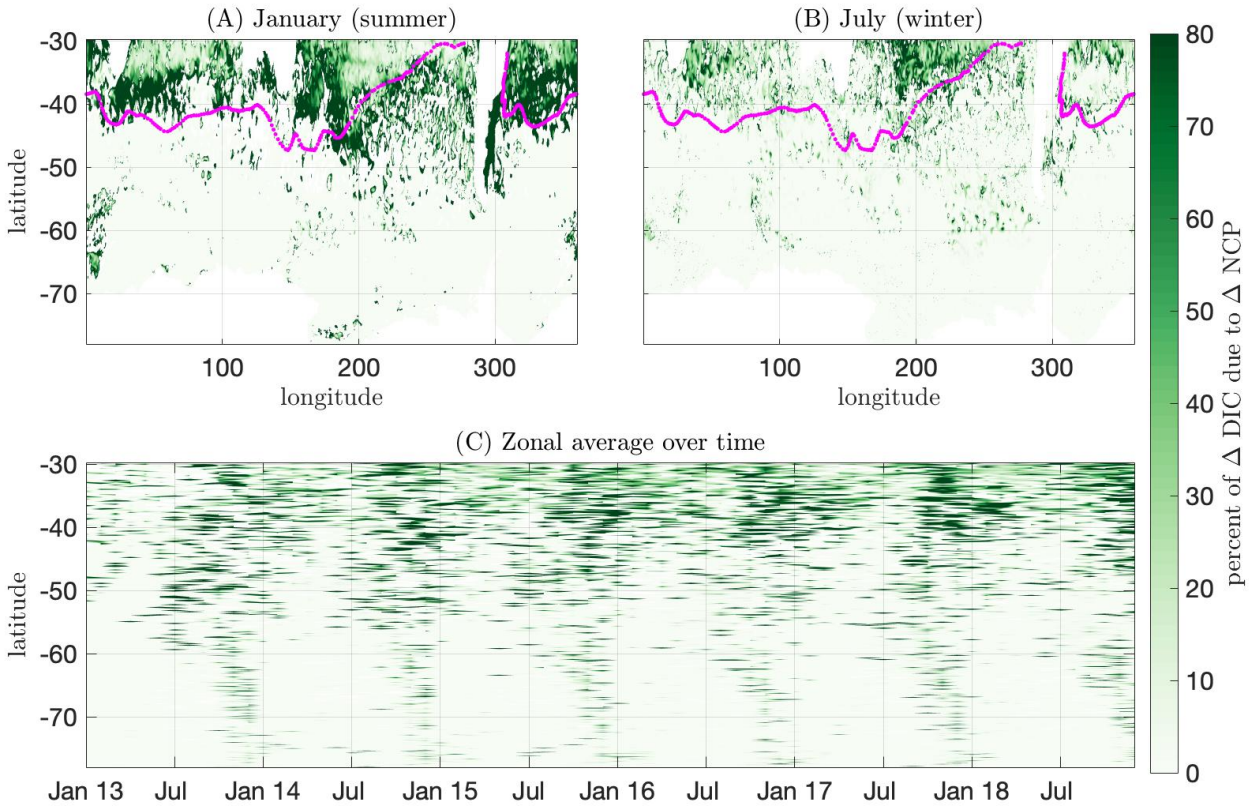


Figure 5.9: The percentage change of surface water DIC concentration due to changes in biological Net Community Productivity (NCP). Surface water is defined here as waters down to a depth of 55 m. Shown as a vertically integrated mean for (A) January (summer) and (B) July (winter). The mean location of the subtropical front (STF), as defined by Orsi et al. (1995), is also shown in pink. (C) The zonal mean of the vertically integrated percentage change due to altered NCP is shown over time.

5.4.4 Contribution of Altered Phytoplankton Productivity to Altered Carbon Fluxes

We assess if the changes to biological productivity as discussed in Chapter 4 are a significant cause of altered surface water DIC concentrations. Almost all changes in DIC between Ex1e-4 and Ex1e-5 are due to the direct impact of altered diapycnal fluxes of DIC due to enhanced background mixing, rather than due to indirect impacts via changes in biological productivity (Fig5.9). However, north of the STF the reduced surface water DIC concentrations which contribute towards a decreased surface $p\mathrm{CO}_2$, are due to increased productivity in the nutrient-depleted waters of the subtropical gyre, especially in the summer. While an increase in productivity occurs with higher mixing across almost the whole SO region (Fig.4.1), it is only in the north, roughly north of the STF where increased phytoplankton production and DIC uptake is the dominant mechanism in altering DIC concentrations. This increase in productivity does not occur instantaneously, but instead takes around 6 months to begin decreasing the DIC contribution to surface water $p\mathrm{CO}_2$ (red line, Fig.5.8E and Fig.5.9C). In the context of this chapter, we consider the STF as the lower boundary of the biologically-dominated change in $p\mathrm{CO}_2$ north of the SO.

5.5 Discussion

The relevance of diapycnal mixing in setting global air-sea carbon fluxes has previously been considered to be through changes to the underlying stratification and of regional and global overturning circulation and ventilation patterns on centennial to millennial timescales, as shown in Chapter 2. Although true on centennial or longer timescales, we show that on faster timescales (less than one year) non-equilibrated changes in mixing also lead to a significant change in air-sea carbon fluxes. SO background mixing is known to vary by over two orders of magnitude (from $10^{-5}\ m^2s^{-1}$ to $10^{-3}\ m^2s^{-1}$) over these timescales or shorter in the real ocean. The high correlation found between vertical gradients and strong changes in tracer distributions with

altered mixing in this work demonstrates that on a timescale of months to years, the direct changes in diapycnal mixing fluxes of tracers are the predominant drivers of the pCO_2 response in the SO. On longer timescales, from months to years, further feed-backs involving changes to biological productivity begin to cause further changes to the surface ocean pCO_2.

This work demonstrates the importance of considering the changes in the full suite of parameters which set surface ocean pCO_2 to understand the changes to carbon fluxes with altered mixing. The strong seasonality of the changes in carbon fluxes with altered mixing occurs due to the range of physical, chemical and biological processes which are altered. This in turn causes alterations to the distributions of temperature, DIC, ALK and salinity, which can enhance or oppose each other to alter the surface ocean pCO_2. The changes in surface water temperature with enhanced mixing, and the changes in biological productivity due to an enhanced nutrient supply are the predominant drivers of the seasonal response to enhanced mixing.

Ex1e-5 gives carbon fluxes more consistent with our current best estimates from previous studies (Landschützer et al., 2016; Bushinsky et al., 2019; Rödenbeck et al., 2013) than Ex1e-4 or ExVar. We would expect the spatially variable mixing map of ExVar to better match previous observation-based estimates and possible reasons why this is not the case are discussed in Chapter 6. The difference in cumulative carbon fluxes between the experiments of around 0.4 pg C /year is highly significant, given that estimates of total SO carbon uptake range from 0.5 to 1.8 pg C /year (Nevison et al., 2016, and references within). A caveat is that though B-SOSE inputs are optimised to bring it into consistency with observations, biases do still exist with regard to the true ocean state (Mazloff et al., 2023). For example, Swierczek et al. (2021) showed a weaker upper-ocean DIC gradient in B-SOSE than in the GLODAPv2 and BGC-Argo observations in the Argentine Basin. These may impact the details of the perturbation response presented here. However, the relatively rapid and large-scale change in carbon flux in response to changing mixing is likely to be a robust signal.

A latitudinal divide exists at roughly the location of the STF, generally considered as the boundary between the nutrient-depleted sub-tropical waters to the north of the STF and the nutrient and DIC rich waters to the south (Chapman et al., 2020). Altered DIC concentrations

due to directly altered vertical carbon fluxes dominate changes in surface DIC concentration with altered mixing to the south of the STF. Conversely, changes in biological productivity dominate the trends in DIC surface concentrations with altered mixing north of the STF, especially during the summer months. The biologically dominated control north of the STF is surprising, as the seasonal cycle of CO_2 fluxes in the SO is considered as biologically controlled south of the STF, but thermally controlled north of the STF (Prend et al., 2022; Gray et al., 2018).

Climate models on long timescales are sensitive to the intensity and distribution of global diapycnal mixing (Gnanadesikan et al., 2003; Wunsch & Ferrari, 2004; Ross et al., 2012), accounting for about 25% of the uncertainty in the estimated range of atmospheric CO_2 concentrations by 2100 in some studies (Schmittner et al., 2009). With climate change, we can expect an increase in surface ocean temperatures and increased vertical gradients in temperature (Li et al., 2020), increasing the sensitivity of surface temperature to diapycnal mixing. By contrast, as shown in Global Ocean Data Analysis Project (GLODAP) data, surface ocean anthropogenic carbon accumulation will diminish the large natural surface-to-deep DIC gradient, making DIC-driven changes to pCO_2 less sensitive to spatial variations in diapycnal mixing (Monteiro et al., 2010; Körtzinger et al., 2001). This work highlights the absolute necessity for climate models to resolve the spatiotemporal variability of small-scale turbulent mixing, or to skillfully parameterise the processes responsible for generating them.

Chapter 6:

Can Biogeochemical Tracer Observations Constrain SO Diapycnal Mixing Rates?

6.1 Abstract

Direct observations of background diapycnal mixing rates in the Southern Ocean (SO) are limited spatially and temporally, making the choice of an appropriate value to parameterise this mixing in Earth system models a challenge. However, the deployment of ARGO floats throughout the SO has provided an extensive range of observations of both physical and biogeochemical parameters. We use an ocean state estimate run with various background diapycnal mixing parameterisations to assess if biogeochemical tracer observations can be used to better constrain SO diapycnal mixing rates. We find that vertical tracer distributions in the SO are highly sensitive to the rate of background diapycnal mixing and can provide an upper limit on background mixing rates. Using a spatially variable mixing map, representative of our current best estimate of SO diapycnal mixing does not improve the match of a state estimate to biogeochemical observations compared to using a constant background mixing rate. This suggests that current mixing maps do not represent many key processes important in the generation of background mixing. To improve the match of ocean state estimates to observations mixing maps which vary both spatially and temporally are required.

6.2 Introduction

Observations of turbulent vertical mixing rates obtained through tracer release experiments and microstructure measurements are sparse in the SO, covering small spatial regions over limited time periods (Ledwell et al., 1993; Naveira Garabato et al., 2004; Waterhouse et al., 2014). Physical and biogeochemical tracer distributions are sensitive to diapycnal mixing rates, and to ocean circulation and ventilation over centennial to millennial timescales (Doney et al., 2004; Gnanadesikan et al., 2004; Matsumoto et al., 2004). They therefore could provide a way to validate and constrain diapycnal mixing rates.

Biogeochemical cycles and tracer distributions can be an especially useful indicator for physical ocean parameters such as diapycnal mixing rates, as models with different physics can produce oceans with a similar physical structure, but very different nutrient cycles (Gnanadesikan et al., 2001). Measurements of nutrient cycling and biological productivity can therefore give information about weaknesses in ocean models, complementing that provided by the large-scale density structure and transient tracers (Gnanadesikan et al., 2001). Some tracers are influenced by physical processes only, whereas biogeochemical tracer distributions in models are also strongly affected by the choice of biogeochemical parameters. For example, oxygen vertical gradients are strongly dependent on mixing across and along isopycnals and on deep wintertime convection, whilst alkalinity is sensitive to fresh and saltwater perturbations and phosphate vertical gradients are a function of its supply and utilisation rates. Biogeochemical tracers have shown that high background mixing values result in an ocean that is too vigorously ventilated and too young by comparing the apparent oxygen utilisation, Dissolved Inorganic Carbon (DIC) concentrations, preformed nutrient concentrations and C_{14} tracer distributions in models to observations (Schmittner et al., 2009). Vertical fluxes are key in setting surface DIC concentrations over mixing hot spots, including meandering fronts, continental shelves and downstream of topographic features (Rosso et al., 2017), and are likely to be key in setting the distribution of other biogeochemical tracers. While biogeochemical cycling estimates are clear markers about when the circulation is getting something wrong, they do not provide an

unambiguous picture of how such problems may be fixed (Gnanadesikan et al., 2004).

Values of diapycnal mixing can be derived from fine-scale observations of temperature, salinity and pressure using a strain-based fine-scale parameterisation (Whalen et al., 2012). The values for diapycnal mixing obtained using this method compare well with microstructure measurements of mixing (Whalen et al., 2015). The extensive observations of ocean stratification obtained from ARGO floats have improved estimates of turbulent mixing rates in the upper 2000 m of the ocean, and have reduced the model error between physical and biogeochemical observations (Forget, Ferreira, & Liang, 2015; Zhu et al., 2020). This suggests that it is possible to partly observe regional turbulent transport rates from observations of physical tracers. Attempts to constrain mixing rates with in situ observation of biogeochemical tracers have also been made (Schmittner et al., 2009; Trossman et al., 2020, 2021). Although observations such as atmospheric CO_2 concentration and global mean surface temperature poorly constrain mixing, the analysis of model misfits between multiple physical, geochemical and biogeochemical tracer observations at high spatial resolution can provide a constraint on diffusivity rates (Schmittner et al., 2009). O_2 vertical gradients have shown particular promise as a method to improve estimates of diapycnal mixing, with a less clear correlation between mixing rates and the vertical gradients of DIC and phosphate observed (Trossman et al., 2021).

In the past, observations of biogeochemical and physical tracers in the SO have been limited spatially and temporally. This contributes to the high disagreements between the carbon fluxes in models and observations (Gruber et al., 2019) and prevents being able to attribute specific processes to explain the misfit to observations. In recent decades, core-Argo (temperature and salinity only measuring) and Biogeochemical-Argo (BGC-Argo) profiling floats have provided an incredible increase in the spatial and temporal coverage of tracer observations in the top 2000 m of the SO (Johnson et al., 2017). The Southern Ocean Carbon and Climate Observations and Modelling (SOCCOM) project has released over 250 BGC Argo floats into the SO, measuring O_2, pH, Nitrate (NO_3), and fitted with bio-optical sensors (Johnson et al., 2017; L. D. Talley et al., 2019). These have provided unprecedented, year-round biogeochemical observations, including under sea ice. The advances in the availability of SO biogeochemical observations provide a new opportunity to validate and constrain diapycnal mixing rates using

tracer observations.

In ocean state estimates, the diapycnal mixing rate influences the model fit to observational data of both physical and biogeochemical tracers (Forget, Campin, et al., 2015; Forget, Ferreira, & Liang, 2015). In this chapter, we use the model outputs from the three experimental runs of B-SOSE as described in Chapter 3 (Ex1e-5, Ex1e-4 and ExVar), and a range of ship, seal and float observations of physical and biogeochemical tracers to compare the model-observation misfits. This allows us to see where and for which tracers B-SOSE is most sensitive to changes in background mixing rates.

Firstly using observations of tracers through the water column and of surface carbon fluxes obtained from the Surface Ocean CO_2 Atlas (SOCAT, D. C. E. Bakker et al. (2014)) we assess if the spatially variable mixing map, ExVar, can improve the fit of biogeochemical observations to model outputs compared to the homogeneous mixing in Ex1e-4 and Ex1e-5. Secondly, we investigate if it could be possible to constrain the diapycnal mixing rates using observations of tracer vertical gradients. The focus of this work is not on the misfit of the model outputs when compared to observational data, but is instead focused on how the misfits to observational data for each experiment compare to each other.

6.3 Methods

6.3.1 Data Sources

The observational data is obtained from Core and BGC Argo floats, ships and seals (Table 6.1). While our focus remains on constraining diapycnal mixing rates using biogeochemical tracers, given the sparsity of biogeochemistry observations compared to the availability of temperature and salinity, we include both physical and biogeochemical tracer data in the analysis of this chapter. Over 10,000 Core Argo floats have been deployed globally since 1999, which gives far greater coverage in the SO that the BGC Argo deployment of the SOCCOM project. BGC Argo floats provide direct observations of depth, temperature, salinity, NO_3 and dissolved oxygen.

DIC values are obtained indirectly via measurements of alkalinity and pH, and chlorophyll concentrations are inferred from float measurements of fluorescence. Core and BGC Argo floats drift with ocean currents at 1000 m, then descend to 2000 m after around 10 days and ascend to the surface, profiling the water column. The vertical resolution of this data is as high as 10 m in the upper 100 m of the water column and decreases with depth to a resolution of 50 m from 400 m to 2000 m. All data used was collected during the period January 2013 to December 2018.

Measurement type	Variable(s)	Year(s)	Data Source
BGC Argo Float (SOCCOM)	Salt, Temp, NO_3, pH, Alk, O_2	2014 - 2018	http://www.usgodae.org/
BGC Argo Float (UW)	Temp, Salt, O_2	2013 - 2015	http://runt.ocean.washington.edu/O_2/
Ship (GLODAPv2)	Temp, Salt, O_2, NO_3, pH, Alk	2019	http://cdiac.ornl.gov/oceans/GLODAPv2/
Ship (HDO)	Temp, Salt, O_2	2013 - 2017	http://cchdo.ucsd.edu/
Ship (XBT)	Temp, Salt	2013 - 2016	http://www-hrx.ucsd.edu/
Seals	Temp, Salt	2013 - 2015	Meo http://www.meop.net/
Argo Float	Salt, Temp	2013 - 2017	http://www.usgodae.org/
SOCATv4	pCO_2	2013 - 2018	http://cdiac.ornl.gov/ftp/oceans/SOCATv4/

Table 6.1: Ocean physical and biogeochemical observations used to assess model-observations misfits.

6.3.2 Data Coverage

The spatial and temporal coverage of available observations is shown in Figure 6.1 (except the spatial distribution of SOCAT data, which is shown in Figure 6.5). The greatest coverage of data is obtained from floats (dark blue, Fig.6.1a), while ship data and seal data are more spatially constrained (green, Fig.6.1a). Seals are able to overcome the challenges of sea ice by emerging from small holes in the ice to transmit data and have provided year-round observations of temperature and salinity within the Seasonal Ice Zone (SIZ). Ship data is strongly biased towards the summer months, with a low number of profiles in winter, SOCAT data is also highly seasonal (Fig.6.1b). Biogeochemical observations have much lower spatial and temporal

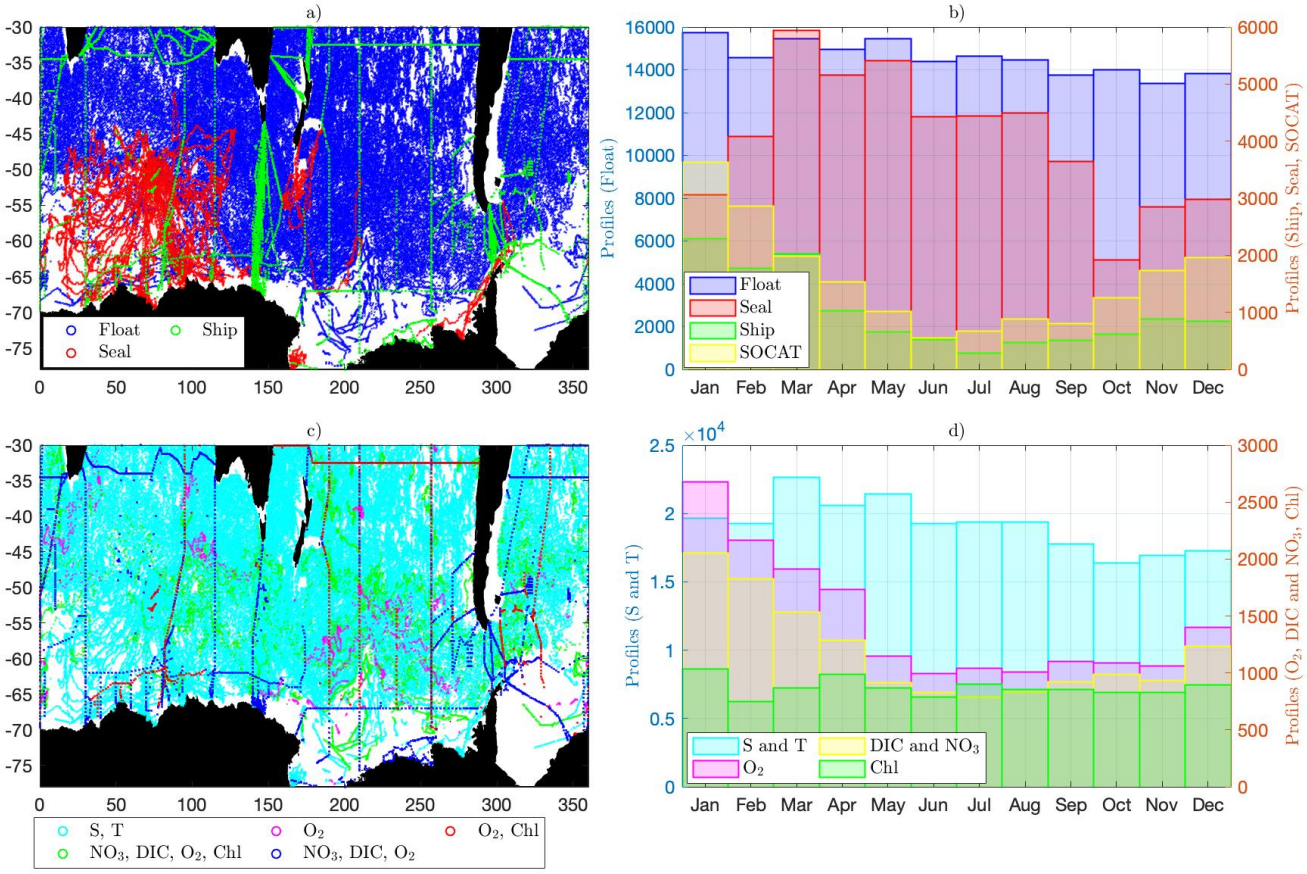


Figure 6.1: a) The location of data profiles collected using floats (blue), seals (red) and ships (green) between 2013 to 2018. Locations of SOCAT observations are not shown here, and are instead shown in Figure 6.5. b) The number of profiles collected in each month of the year for 2013 to 2018 for floats (red), seals (blue) ship (green) and SOCAT (yellow). c) The location of data profiles and the variables observed. d) The number of profiles collected in each month of the year from 2013 to 2018 for each of the variables, salt and temperature (blue), O_2 (pink) and NO_3 and DIC (yellow) and chlorophyll (green).

coverage than temperature and salinity data (Fig.6.1c,d). There is a large coverage of temperature and salinity data, as these variables are measured by seals, ships, core and BCG Argo floats. Ship data is especially important for the collection of biogeochemical data (Fig.6.1c). Because of this, biogeochemical observations are still strongly biased towards summer for all biogeochemical observations used in this study (Fig.6.1d). Chlorophyll data is mainly from floats, and therefore does not show this seasonal bias, but has a smaller number of observations than temperature or salinity.

6.3.3 Comparison of B-SOSE Outputs to Observational Data Profiles

In this chapter, we use B-SOSE as described in Chapter 3 to asses how alterations to SO background mixing impact the match to available observational data. We use the experimental cases Ex1e-4, Ex1e-5 and ExVar in this work.

All observational profiles are linearly interpolated vertically to give values at the same depth levels. To find the model output to compare to each observational profile, the model is interpolated linearly in-depth and bilinear in the horizontal, and the nearest time interval is used. The cost function indicates the misfit of the data to observations, using all data profiles collected between January 2013 and December 2018. The cost function is calculated for each tracer to give a value for model misfit which takes into account the uncertainty associated with observational data and model outputs. This is calculated as $cost = \sum(model - obs)^2 * weight$ where weight is $uncertainty^2$ of the model output and the observational instrument used for each variable.

6.4 Results

6.4.1 Does a Spatially Variable Mixing Map Improve the Model Output Fit to Observations?

The cost function for DIC, NO_3, O_2, temperature and salinity for each experiment are compared in Figure 6.2. The cost functions for Ex1e-5 and ExVar are normalised by the cost function of Ex1e-4 allowing for the comparison of cost functions for each experiment relative to each other. Altering the parameterisation of background mixing in B-SOSE alters the cost function for all tracers examined (Fig.6.2). For DIC, NO_3 and O_2, Ex1e-4 has the highest cost function. For DIC, ExVar outperforms Ex1e-5 and has the lowest cost function, whereas, for NO_3 and O_2, Ex1e-5 has the lowest cost function, though the cost functions of ExVar and Ex1e-5 are very similar, differing by less than 1%. It is worth noting that there many more float observations than ship observations for all tracers, indicating that these results are more reliable.

The difference in cost functions between experiments is much larger for physical than biochemical tracers (Fig.6.2). For biogeochemical tracers, the biggest change in cost function was between Ex1e-4 and Ex1e-5 for shipboard NO_3 observations, where Ex1e-5 reduced the cost function by 17% relative to Ex1e-4. The cost function of salinity in Ex1e-5 relative to Ex1e-4 is increased by 50% for ship profiles, by almost 20% for float observations and by over 70% for seal observations. This strong signal from a high number of observations with good spatial and temporal distribution suggests an improvement in the match of the model output to observations for salinity when using a high background diapycnal mixing value. The trends for the cost functions between experiments were less consistent for temperature. ExVar has the lowest cost function when using ship observations of temperature, while float observations best matched the output from Ex1e-5, and seal data was best matched to Ex1e-4. The strongest differences were in the float data, which is the data set with the most observations. It is interesting to note that in the temperature and salinity data collected from seals, Ex1e-4 shows the best fit to the data. Seal data has less spatial coverage than the ship and float data, making analysis

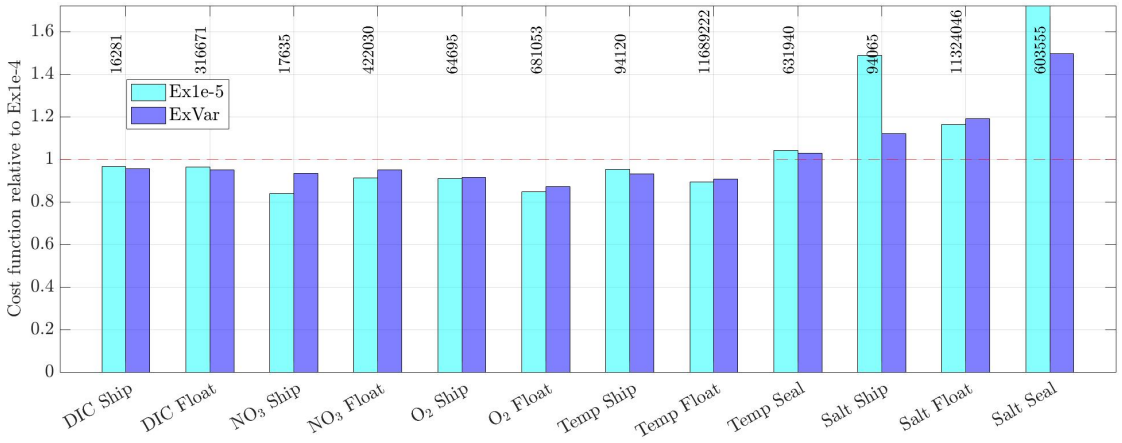


Figure 6.2: The cost function of B-SOSE model outputs for ExVar and Ex1e-5, normalised relative to the cost function of Ex1e-4. The cost functions shown are for DIC, NO_3, O_2, temperature and salinity. A cost function lower (higher) than 1 means Ex1e-5 or ExVar has a lower (higher) misfit to observations than Ex1e-4 for the available profiles. The numbers shown in black indicate the total number of profiles used in each data set.

of seal data applicable to specific regions, rather than the whole SO.

Below depths of 500 m, the difference in tracer distributions between experiments becomes insignificant (not shown). Therefore we focus our subsequent analysis on the upper 500 m of the water column. As chlorophyll concentrations below 150 m depth are very low and unchanged between experiments, we use 150 m as the cut-off depth in this analysis for chlorophyll. To calculate the mean Root Mean Squared Error (RMSE), a mean of the RMSE over the depth range of interest is taken to give one value for each location.

The mean RMSE reveals the spatial trends and broad patterns of where Ex1e-4, Ex1e-5 or ExVar is best matched to observations in the upper 500 m of the water column (Fig.6.3). We compared Ex1e-4 with Ex1e-5 (Fig.6.3 left column), and Ex1e-5 with ExVar (Fig.6.3 right column) for physical and biogeochemical tracers. For NO_3 and DIC, the largest difference in RMSE between models are in the energetic frontal regions of the Subantarctic Front (SAF) and the Polar Front (PF), while for O_2 they are south of the PF, and for chlorophyll are widespread from the edge of the Seasonal Ice Zone (SIZ) up to the Subtropical Front (STF).

For NO_3, Ex1e-4 has a lower RMSE than Ex1e-5 south of the PF, indicating a better match to observations, the opposite occurs north of the PF where Ex1e-5 better matches observations

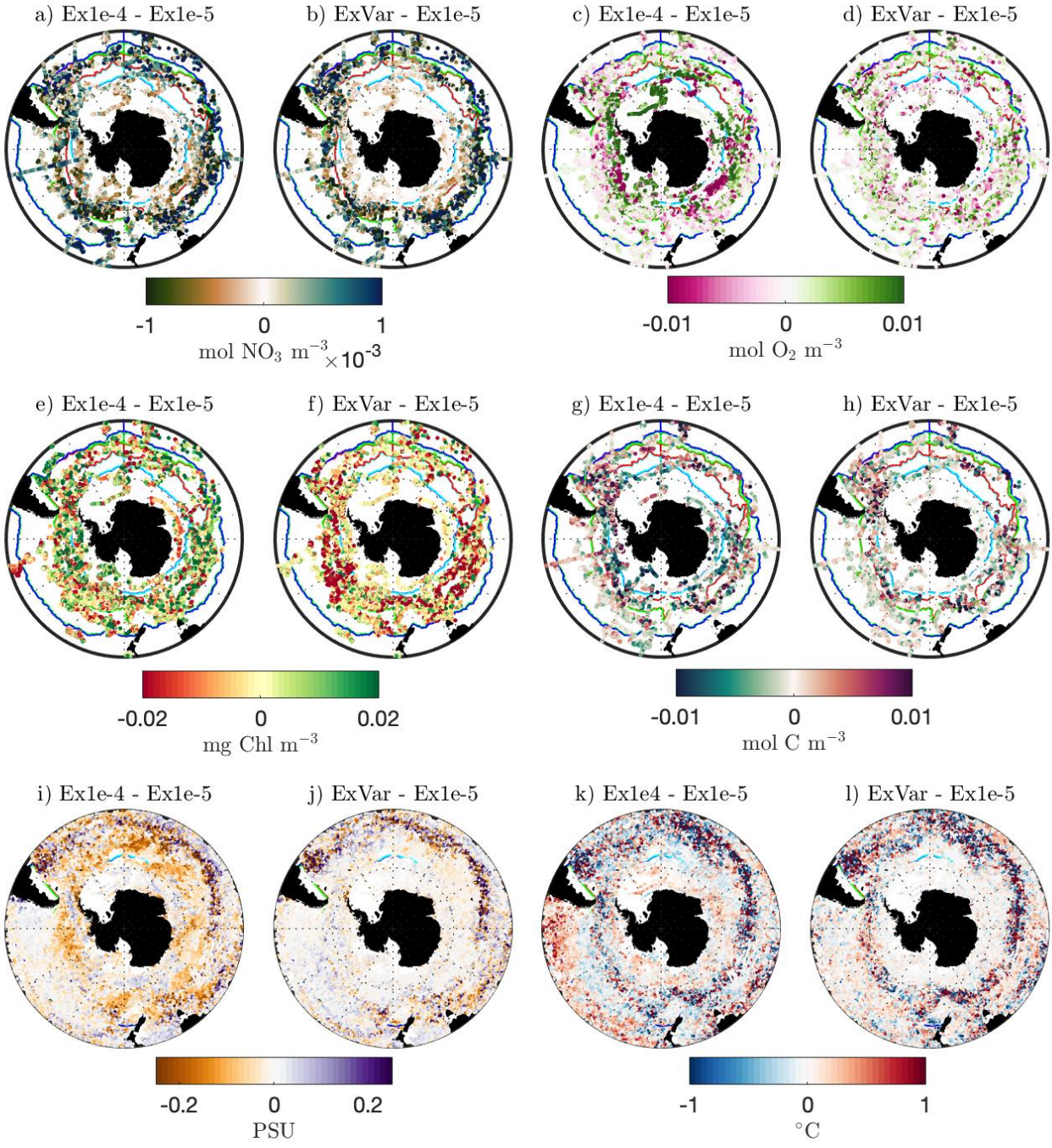


Figure 6.3: The mean difference in root mean squared error (RMSE) for the upper 500 m (150 m for chlorophyll) between experiments for; a&b) NO_3, c&d) O_2, e&f) chlorophyll, g&h) DIC, i&j) salinity and k&l) temperature. The left column compares the RMSE of Ex1e-4 and Ex1e-5, where positive (negative) values occur in regions where Ex1e-5 (Ex1e-4) has a lower RMSE. The right column compares the RMSE for Ex1e-5 with ExVar, where positive (negative) values occur in regions where Ex1e-5 (ExVar) has a lower RMSE. Coloured lines show the outline of the fronts of Gray et al. (2018). From north to south, they are the Subtropical Front (STF, blue), Subantarctic Front (SAF, green), Polar Front (PF, red), and the northern extent of the Seasonal Ice Zone (SIZ, light blue).

(Fig.6.3a,b). The mean RMSE between ExVar and Ex1e-5 for NO_3 south of the SIZ is the same. North of the SIZ Ex1e-5 has a lower RMSE than ExVar. For O_2 the RMSE of Ex1e-4 and Ex1e-5 are the same north of the PF, but in the SIZ Ex1e-5 has a lower RSME than Ex1e-4, especially in the Drake Passage and Weddel Gyre (Fig.6.3c,d). There are no major differences in the RMSE of ExVar compared to Ex1e-5 for O_2 in any region of the SO. For chlorophyll the RMSE of Ex1e-5 is smaller than Ex1e-4 over most of the SO, especially in the Indian basin of the SO (Fig.6.3e,f). ExVar has a lower RMSE than Ex1e-5 north of the SIZ especially in the Pacific basin of the SO. There are no clear regions where Ex1e-5 has a lower RMSE than ExVar. The difference in RMSE of DIC between Ex1e-4 and Ex1e-5 is greatest south of the PF (Fig.6.3g,h). South of the PF Ex1e-4 has a lower RMSE. East of the Drake Passage and up along the east coast of South America, the RMSE of Ex1e-5 is smaller than that of Ex1e-4. Differences in RMSE between Ex1e-5 and ExVar for DIC are concentrated around the PF and SAF, though it is unclear which experiment has a lower RMSE, except west of the Drake Passage where Ex1e-5 shows a lower RMSE than ExVar.

More observations of physical tracers make trends in the RMSE between experiments clearer than for biogeochemical tracers. For salinity, around the PF and SAF, Ex1e-4 has a lower RMSE than Ex1e-5 (Fig.6.3i,j). However, north of the STF and south of the SIZ Ex1e-5 appears to have a lower RMSE. The strongest differences in RMSE between Ex1e-5 and Ex1e-4, and also between ExVar and Ex1e-5 are along the STF below the tip of South Africa, and off the east coast of South America, though in these regions it is unclear which experiment has a generally lower RMSE. South of the SIZ, differences in RMSE between Ex1e-5 and Ex1e-4 are minimal. Over most of the SO, the RMSE for salinity is the same in ExVar as in Ex1e-5. In regions where there are high magnitudes of difference, there is no clear trend as to which experiment has the lowest RMSE out of Ex1e-5 and ExVar.

For temperature, the biggest difference in RMSE between experiments occurs in bands along roughly the STF (Fig.6.3k,l). Within this band, the RMSE difference between experiments is highly variable, with neither of the three experiments clearly having a lower or higher RMSE. Around the SAF Ex1e-4 has a lower RMSE than Ex1e-5, while Ex1e-5 has a lower RMSE than ExVar. In the Pacific SO around the STF Ex1e-5 has a lower RMSE than Ex1e-4. South of the

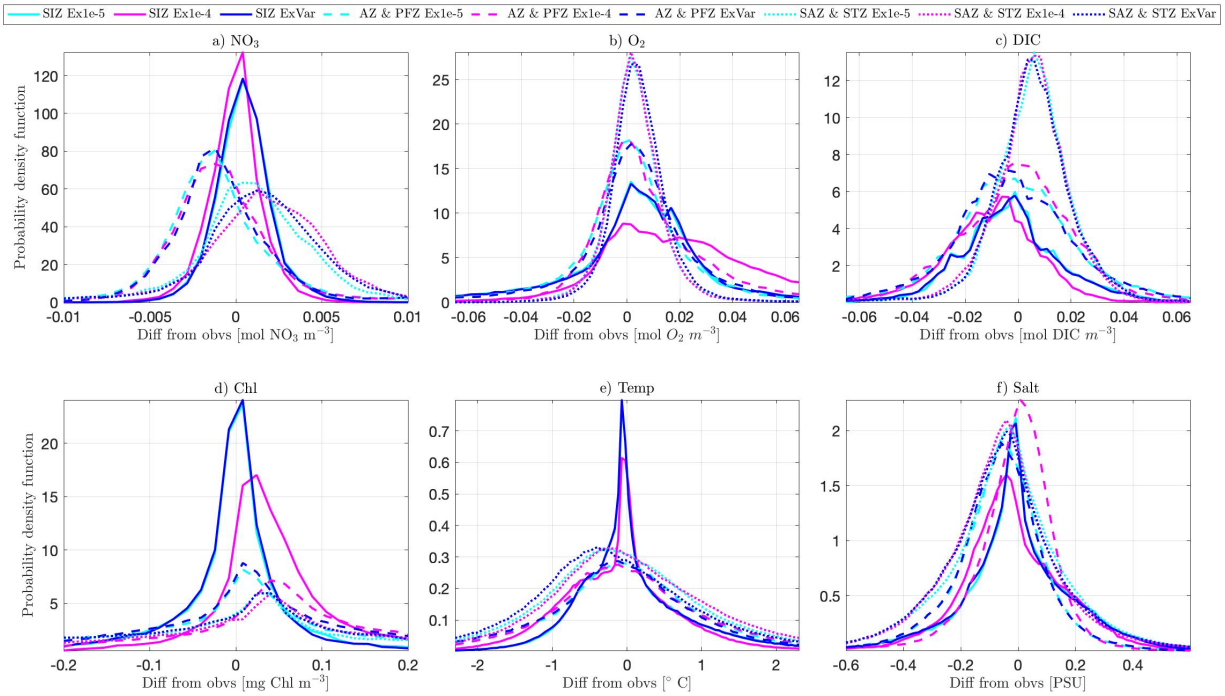


Figure 6.4: Probability density function (PDF) showing the misfit between observed tracer concentrations (obvs) and the B-SOSE model outputs for; a) NO_3, b) O_2, c) DIC, d) chlorophyll, e) temperature, and f) salinity in the upper 500 m (150 m for chlorophyll). This is shown for Ex1e-5 (light blue), Ex1e-4 (pink), and ExVar (dark blue). Differences are grouped by the frontal zones of Gray et al. (2018) showing the PDF in the SIZ (solid lines), the AZ and PFZ datasets combined (dashed lines) and the SAZ and STZ data combined (dotted lines). Peaks at negative (positive) values indicate that the B-SOSE outputs are underestimating (overestimating) a tracer value.

PF the difference in RMSE between Ex1e-5 and ExVar is minimal, while Ex1e-5 has a generally lower RMSE than Ex1e-4.

The Probability Density Function (PDF) for the difference between observations and B-SOSE outputs for the three experiments is broken down by frontal zones and tracers (Fig.6.4). Peaks close to zero indicate a good match between model outputs and observations. In all cases ExVar shows an almost identical PDF to Ex1e-5, so in the subsequent text, we will refer only to Ex1e-5.

For NO_3, in the SIZ Ex1e-4 best matches the observations, while Ex1e-5 is positively skewed relative to observations. In the AZ & PFZ, all model outputs are negatively skewed. In the SAZ & STZ Ex1e-5 has a modal peak closest to 0, and a smaller standard deviation than Ex1e-4. O_2 in the SIZ has large differences between the three model outputs, and Ex1e-4 has a

more positive skew and a larger standard deviation than Ex1e-5, though the standard deviation for all experiments is large in this zone. There are no major differences in the distribution in the SAZ & STZ, or the AZ & PFZ. DIC in the SIZ has a large standard deviation in all experiments. Ex1e-4 shows more of a negative bias to the observations than Ex1e-5. In the AZ & PFZ, Ex1e-4 has a mode closer to zero than Ex1e-5, which is more negatively skewed. In the SAZ & STZ the background mixing rate in B-SOSE makes a minimal impact on the fit to observations. For chlorophyll in the SIZ and the AZ & PFZ, Ex1e-5 has a modal value close to 0, while Ex1e-4 is positively skewed.

We also compare the distribution for physical tracers. Temperature is best constrained in the SIZ in all experiments, with Ex1e-5 having a mode value closest to 0, as well as a lower standard deviation. In the AZ & PFZ and the SAZ & STF all experiments have a similar distribution, and are very negatively skewed. Salt observations in the SIZ are best matched to Ex1e-5, while Ex1e-4 has a more negative skew. In the AZ & PFZ Ex1e-4 has a mode closer to zero than Ex1e-5, and Ex1e-5 has a negative bias. In the SAZ & STF all experiments have a very similar distribution and have a slight negative skew.

6.4.2 Comparison to pCO_2 Observational Data

The pCO_2 values from the Surface Ocean CO_2 Atlas (SOCAT, D. C. Bakker et al. (2016)) observations from 2013 to 2018 can be compared to B-SOSE outputs for Ex1e-4, Ex1e-5 and ExVar (Fig.6.5). Neither experiment clearly matches SOCAT observations better than the other. Regional trends are also unclear, although, from the limited data available, Ex1e-5 appears to better match observations than Ex1e-4 in the northern Pacific Ocean, as well as off the coast of South Africa and Tasmania, where Ex1e-4 has a larger RMSE. Meanwhile estimates from Ex1e-4 are better matched to observations in the western Atlantic and the northern Indian Oceans (Fig.6.5a). The difference in RMSE between Ex1e-5 and ExVar is smaller than the differences between Ex1e-5 and Ex1e-4. Ex1e-5 has a lower RMSE than ExVar in the Atlantic SO west of the Drake Passage, while ExVar has a lower RMSE in regions north of the STF.

The probability density function for the difference between SOCAT and B-SOSE for the three

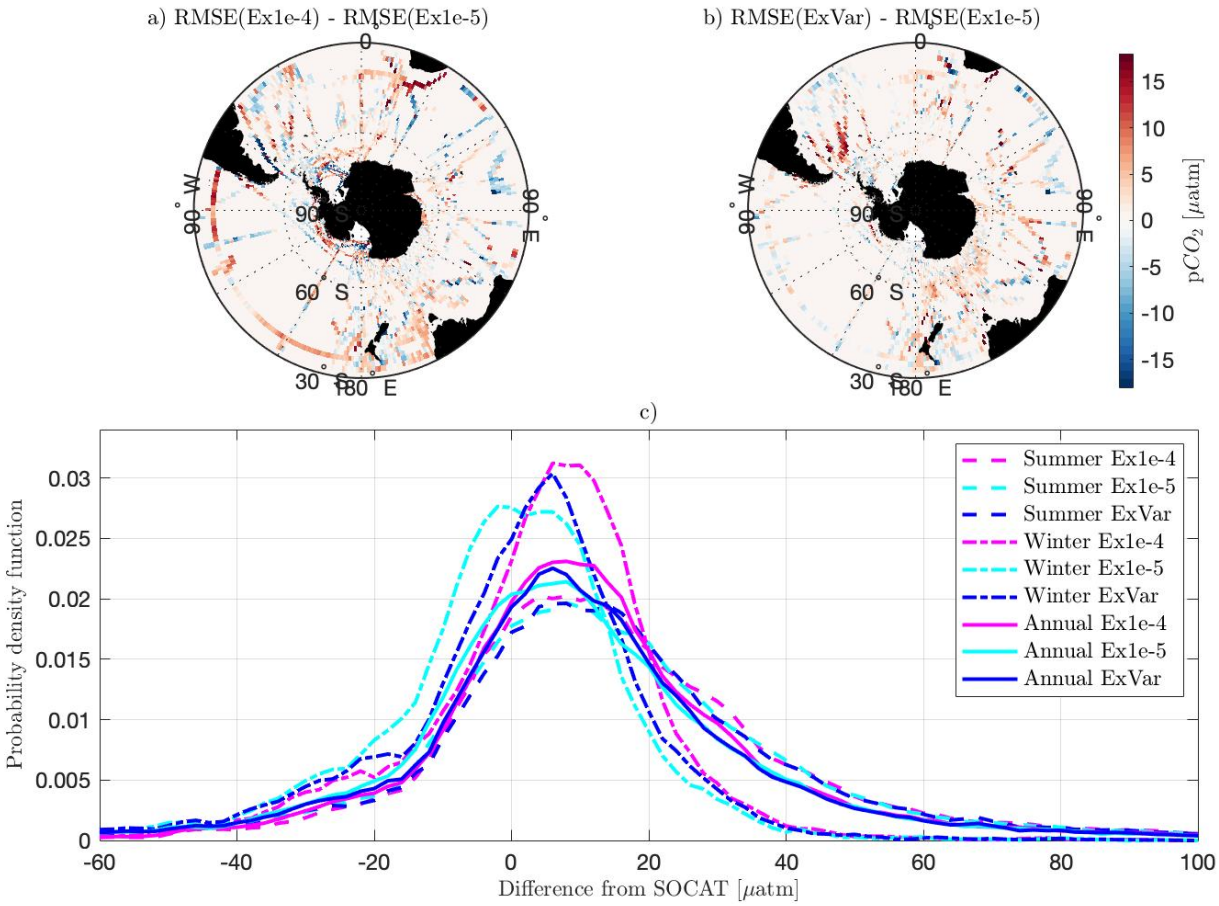


Figure 6.5: Comparison of modelled $p\mathrm{CO}_2$ to observations from Surface Ocean CO_2 Atlas (SOCAT) between 2012 and 2018 (D. C. Bakker et al., 2016). a) Comparison of the root mean squared error between Ex1e-4 and Ex1e-5. Red/blue shows regions where Ex1e-5/Ex1e-4 is closer to the observations. b) Comparison of the root mean squared error between Ex1Var and Ex1e-5. Red/blue shows regions where Ex1e-5/ExVar is closer to the observations. c) Probability density function showing the misfit between observed carbon fluxes from SOCAT and the model outputs for $p\mathrm{CO}_2$ in Ex1e-5 (black), Ex1e-4 (red), and ExVar (green). Summer is defined as November to April, and Winter as May to October.

experiments is broken down over seasons (Fig.6.5b). In summer the standard deviation of differences between ExVar and data is much larger than those for Ex1e-4 and Ex1e-5. The mean difference of 15.5 μatm for Ex1e-5 is lower than 17.46 μatm for Ex1e-4, whilst ExVar has the lowest mean difference from observations. The high-end tails of the distributions are more skewed than the lower ends, implying a systematic over-estimate of pCO_2 by B-SOSE. In winter, Ex1e-5 has the smallest mean difference from SOCAT at -0.94 atm. The mean differences in winter were not all positive, suggesting the model was not overestimating winter pCO_2 as much as summer. B-SOSE overestimates the flux of carbon from the ocean to the atmosphere or underestimates the SO carbon uptake from the atmosphere, particularly in the summer.

SOCAT data is heavily biased towards summer data due to limitations on data collection in the winter (Fig.6.1b). The mean difference between SOCAT and B-SOSE is lower for the winter mean than for the summer in all experiments. In the winter, ExVar has the largest mean difference from observations but also the largest standard deviation. In an annual mean sense, ExVar better matches SOCAT observations, though with a much higher standard deviation. Despite the large differences in modelled pCO_2 between these experiments (as shown in Chapter 5), both are fairly equally consistent with the SOCAT data available. This suggests that we do not have enough observational data on SO pCO_2, especially in the winter, and in remote regions such as the Pacific. The positive skew in B-SOSE pCO_2 outputs compared to observations could be due to systematic under-sampling of the strong outgassing in the SO during winter, meaning SOCAT does not have adequate measurements of these high pCO_2 waters (Gray et al., 2018). It is possible that different trends between SOCAT and each of the B-SOSE experiments would be seen in un-sampled regions including much of the central Pacific, or with a more complete data set.

6.4.3 Can Observations of Vertical Gradients be used to Constrain Mixing Rates

We examine the vertical gradient of tracers from observations and compare these to the vertical tracer gradients from the model outputs of each experiment. The vertical gradients of biogeochemical tracers have significant variability between the tracer and frontal zone (Fig.6.6). Altering the background mixing rate alters tracer vertical distributions, and for all tracers (except chlorophyll) the B-SOSE outputs in Ex1e-4 do not reproduce vertical gradients as strong as those in observations.

For NO_3 in the STZ, SAZ and PFZ no model experiments are able to reproduce the high vertical gradients present in observations (Fig.6.6 first row), but ExVar is the closest. In the upper 200 m of the AZ, Ex1e-5 and ExVar have a higher vertical gradient than observations, while Ex1e-4 has a lower gradient. In the SIZ, Ex1e-4 has a significantly lower vertical gradient than the observations and does not match the vertical gradient profiles well.

In all regions of the SO, the vertical gradient of O_2 in Ex1e-4 is of a lower magnitude than in observations (Fig.6.6 second row). Minimal differences are seen between the vertical gradients of Ex1e-5 and ExVar, and both these experiments seem to capture the general patterns seen in O_2 vertical gradients of observations across frontal zones, although the depth of the maximum vertical gradient in the AZ and SIZ is deeper in observations than in B-SOSE experiments. Major differences between Ex1e-5 and ExVar vertical gradients and observations occur below 200 m in the SAZ, where B-SOSE overestimates the gradient relative to the observations.

No major differences in vertical gradients of chlorophyll between experiments are observable (Fig.6.6 third row). Observations of chlorophyll show a large standard deviation in all frontal zones, so the mean value used to compare to B-SOSE outputs may not be a very representative value. B-SOSE outputs generally capture the patterns in vertical chlorophyll gradients seen in observations, except in the PFZ.

DIC vertical gradients vary highly between each experiment in the SAZ, PFZ, AZ and SIZ

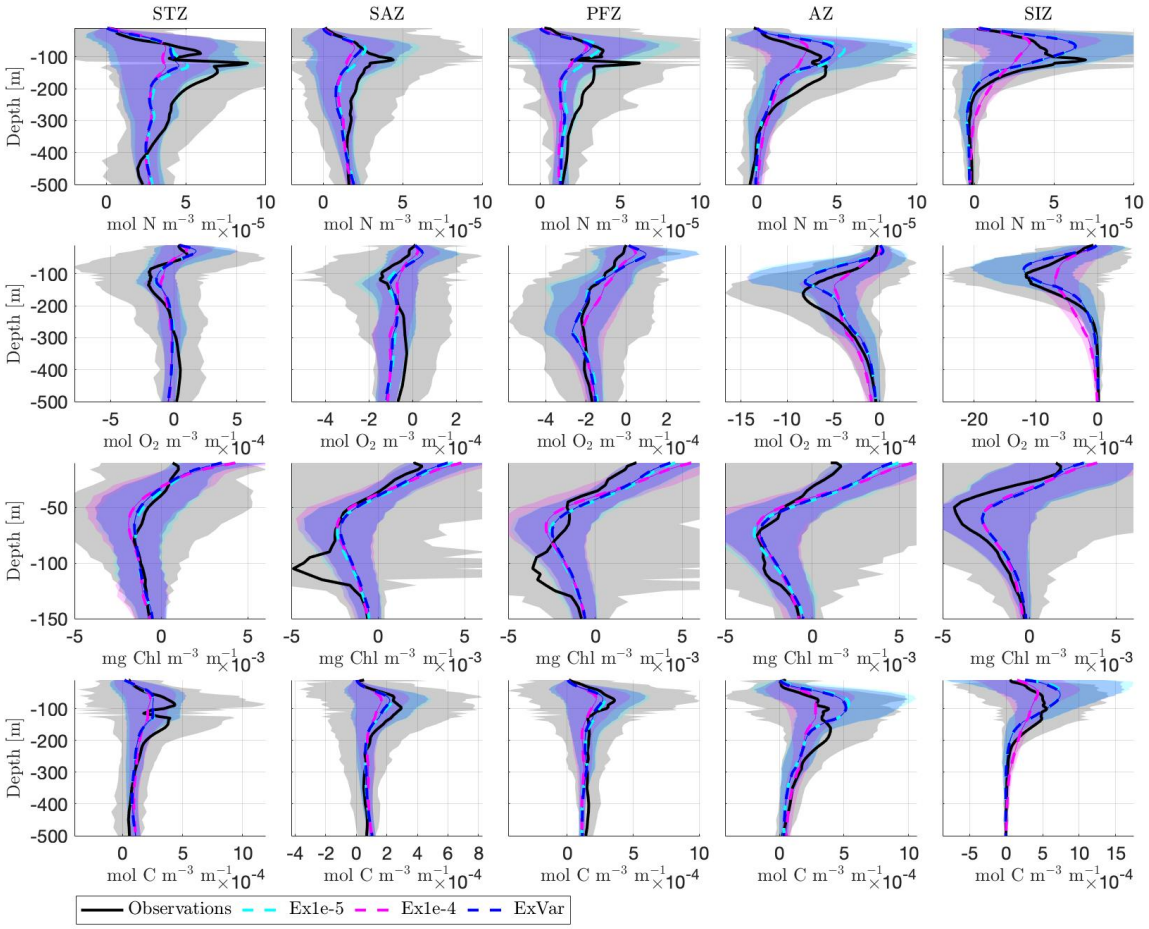


Figure 6.6: The vertical gradients of biogeochemical tracers within the SO for the upper 500 m of the water column (upper 150 m for chlorophyll). The mean vertical gradients for a tracer profile and the standard deviation within each frontal zone for observations (black), Ex1e-5 (dark blue), Ex1e-4 (pink) and ExVar (light blue) are shown. The biogeochemical tracers shown are NO_3 (top row), O_2 (second row), chlorophyll (third row) and DIC (bottom row). The SO frontal zones used in this analysis are the STZ (first column), the SAZ (second column), the PFZ (third column), the AZ (fourth column) and the SIZ (fifth column).

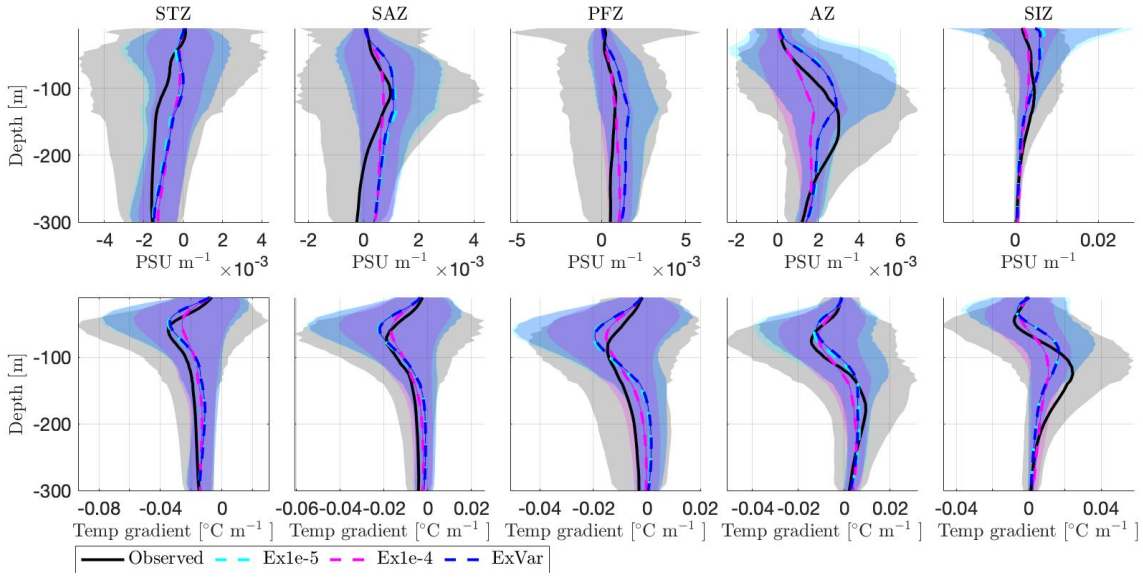


Figure 6.7: The vertical gradient of physical tracers within the SO for the upper 500 m of the water column. The mean vertical gradient and the standard deviation within each frontal zone for observations (black), Ex1e-5 (dark blue), Ex1e-4 (pink) and ExVar (light blue) are shown. The tracers shown are salinity (top row) and temperature (bottom row). The SO frontal zones used in this analysis are the STZ (first column), the SAZ (second column), the PFZ (third column), the AZ (fourth column) and the SIZ (fifth column).

(Fig.6.6 fourth row). In the STZ, DIC observations are poorly matched to any B-SOSE outputs. In the SAZ and PFZ, the vertical gradient of DIC in Ex1e-5 and ExVar is closest to observations, while in Ex1e-4 the vertical gradients are too low. In the AZ and SIZ Ex1e-5 and ExVar have a maximum vertical gradient similar in magnitude to the observations, though it occurs at too shallow a depth. Ex1e-4 does not reproduce the high vertical gradient present in observations.

The vertical gradient of physical tracers are also compared in each experiment (Fig.6.7). Vertical gradients in temperature are better reproduced by B-SOSE than the vertical gradients in salinity. No major inter-experiment differences are observed in the salinity gradients of the STZ. In the SAZ, Ex1e-5 and ExVar have a high vertical gradient at around 200 m which Ex1e-4 does not. None of the experiments replicates observations below 150 m, where B-SOSE produces a positive vertical salinity gradient yet observations show a slightly negative one. In the PFZ Ex1e-4 has a vertical gradient closest to observations in the upper 150 m and Ex1e-5 and ExVar have a vertical gradient higher than in observations. Below 150 m again B-SOSE overestimates the vertical gradient in all experiments. In the AZ Ex1e-5 and ExVar have a maximum vertical gradient of a similar magnitude to observations, but it is too shallow, while

Ex1e-4 does not have the high vertical gradient present in observations. In the SIZ, the greatest difference in vertical gradients between experiments is in the upper 100 m, where Ex1e-4 best matches the observations and Ex1e-5 and ExVar overestimate the gradient.

In the STZ and SAZ, the vertical gradient of temperature in Ex1e-5 and ExVar best match those in observations while Ex1e-4 has too low a vertical gradient. In the PFZ Ex1e-4 better matches the observations, as Ex1e-5 and ExVar have vertical gradients greater than those seen in observations. In the AZ ExVar and Ex1e-5 better match observations than Ex1e-4. Ex1e-4 does not have the high vertical gradients at 175 m and just above 100 m which occur in observations. In the SIZ, again Ex1e-4 has vertical gradients which are low compared to observations, while even Ex1e-5 and ExVar have a maximum vertical gradient which is lower than that of observations.

We find that Ex1e-4 performs significantly better than Ex1e-5 for salinity south of the PF. In these regions where sea water is especially cold, sea water density is predominantly set by the salinity of the ocean. Conversely north of the PF, where waters are warmer and density is more temperature controlled, Ex1e-5 is able to better match observations of temperature.

The mean difference in absolute tracer gradients between model outputs for Ex1e-5 and Ex1e-4 and observations over the upper 500 m of the water column can indicate where model outputs have vertical gradients lower than those seen in observations (Fig.6.8). We do not carry out this analysis for ExVar, as the results are similar to those seen for Ex1e-5. A high value in Figure 6.8 indicates that there is a lower vertical tracer gradient in the model output than in observations, and could indicate that the model has an overly high mixing rate.

For NO_3 Ex1e-5 has some regions where the model output has a higher vertical gradient than observations (suggesting model vertical mixing rates are too low) and some regions where the vertical gradient in the model output is lower than observations (suggesting model vertical mixing rates are too high) (Fig.6.8a). For Ex1e-4, the model output results in a lower mean vertical gradient than observations over the entire SO (Fig.6.8b). This analysis could suggest that in regions with a negative value in Ex1e-5 but a positive value in Ex1e-4 the actual mixing rate is between the value of 10^{-4} $m^2 s^{-1}$ and 10^{-5} $m^2 s^{-1}$. These regions include areas south

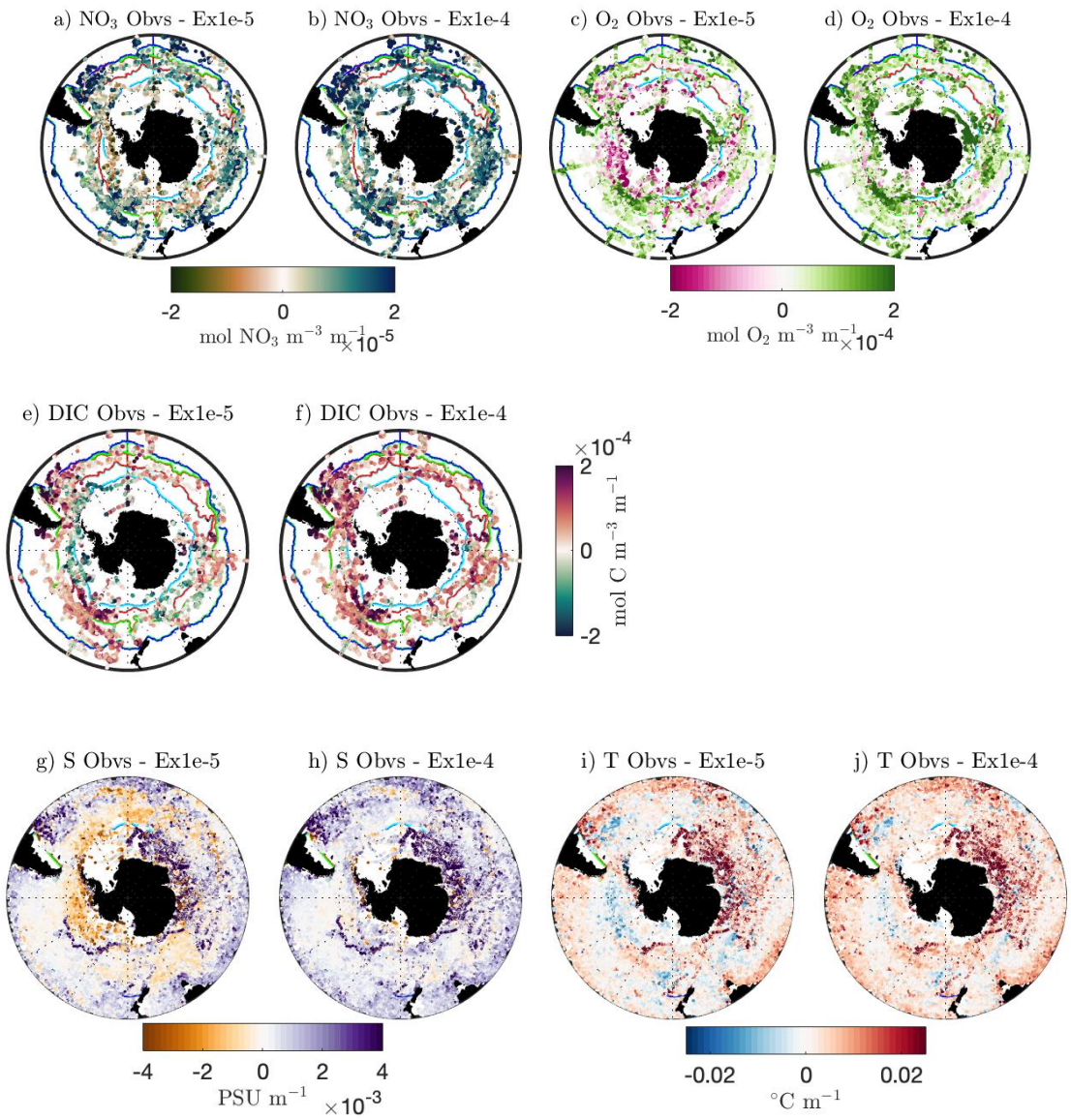


Figure 6.8: The mean of the difference in absolute vertical gradient over the upper 500 m of the water column between model outputs and observations for a,b) NO_3, c,d) O_2 and e,f) DIC g,h) salinity i,j) temperature. A positive value indicates that the mean vertical gradient is higher in observational profiles than the B-SOSE output for Ex1e-5 (left column) and Ex1e-4 (right column).

of the SIZ and a few points within the AZ south of Australia. For O_2 and DIC, in Ex1e-5 and Ex1e-4 the mean difference in tracer gradient is generally positive, indicating higher tracer gradients in observations than in the model outputs (Fig.6.8c-f). Ex1e-5 has a higher mean DIC and O_2 gradient than observations in the Pacific SO south of the PF, and south of the STF below Australia, suggesting the model-generated vertical mixing in these regions is too low. In the SAZ south of Australia, and along the SAF in the Pacific basin, the mean absolute difference in vertical O_2 gradients is negative between observations and both Ex1e-5 and Ex1e-4. These regions also show a very slightly lower DIC gradient in Ex1e-4 than in observations.

For both temperature and salinity in Ex1e-4 and Ex1e-5 over most of the SO the mean vertical gradient in observational data is higher than in B-SOSE output data (Fig.6.8g-j). In Ex1e-5, the model output has a mean higher vertical physical tracer gradient than observations south of the PF in the east of the Pacific SO and through the Drake Passage, into the AZ and PFZ of the Atlantic basin, as well as off the west coast of South Africa, and though the SAZ and PFZ. In Ex1e-4 these same areas also show a negative value, though the value is less negative than in Ex1e-5.

6.5 Discussion

The diapycnal mixing rate used in B-SOSE alters the misfit between model outputs and observations, with regional and temporal variability in the sensitivity to the mixing rates used. Using the spatially variable mixing map in ExVar, constructed from our current best estimates of SO mixing, did not clearly improve the model fit to observations of biogeochemical tracers or SOCAT pCO_2 data compared to using the spatially constant value of 10^{-5} $m^2 s^{-1}$. Despite the B-SOSE initial conditions being determined using the adjoint method with 10^{-4} $m^2 s^{-1}$ as the background diffusivity, our results suggest that a better match to physical and biogeochemical tracer observations occurs in Ex1e-5 and ExVar than Ex1e-4. An exception to this is salinity, where model outputs appeared better matched to observations in Ex1e-4 than Ex1e-5 or ExVar. We did not rerun the adjoint method to determine the idealised initial conditions

for each background mixing rate. Therefore an even closer model fit to observations is likely to be achieved in Ex1e-5 and ExVar through the optimisation of the initial conditions for each experiment.

It is worth noting that while all models are equally well constrained to pCO_2 observations, we find that the distribution of other biogeochemical tracers are best represented by the lower mixing rates of Ex1e-5 and ExVar. pCO_2 is a surface only measurement, whereas for other biogeochemical tracers, we have compared model outputs to observations from a vertical profile in the upper ocean. The vertical gradient of tracers are rapidly eroded in high mixing experiments, resulting in the large model - observation mismatch seen for most tracers. The impacts of altered mixing on surface water pCO_2 are less linear than the distribution of other tracers, making this a less useful measurement for constraining diapycnal mixing rates

Only minor differences in cost function and RMSE occurred between the spatially variable ExVar and the spatially constant Ex1e-5. Previous works have demonstrated that using spatially variable mixing rates in models significantly alters the distribution of biogeochemical tracers compared to using a constant mixing rate (Gnanadesikan et al., 2001, 2004; Schmittner et al., 2005; Marinov, Gnanadesikan, et al., 2008; Friedrich et al., 2011). These previous works compared using spatially variable mixing maps throughout the global ocean, rather than being SO focused. They also utilised models or state estimates run over timescales long enough to allow changes in circulation to occur as a result of altered mixing parameterisations, unlike the work presented here. It is possible that the ExVar mixing map does not result in an improved fit of model outputs to observations as the enhanced mixing in ExVar is predominantly in the deep ocean close to topographic features. Therefore this mixing map has a lower impact on tracer distributions in the upper ocean which are key for biogeochemical processes on the short time scales used in this study. The vertical gradients in tracer distributions found in the deep ocean are significantly lower than those found in the surface waters. On longer time scales, changes to large scale circulation may occur as a result of using the ExVar mixing map compared to using the spatially constant Ex1e-5 mixing map, causing an improvement in the fit of the model output to observations. However, on the time scales of this study, the tracer distributions in Ex1e-5 and ExVar are similar to each other.

Direct observations of diapycnal mixing in the SO have suggested that current maps such as that used in ExVar are unlikely to be representative of the mixing process in the SO for two main reasons;

- Firstly, key processes that result in higher turbulence in upper surface waters are not represented, as current parameterisations of mixing primarily take into account mixing in storm tracks over the SO. The lee wave contributions to the ExVar mixing map are potentially significantly underestimated, as turbulence has been shown to exist under the sea ice due to bottom-generated lee waves penetrating all the way to the top boundary where they can induce large vertical velocities (Baker & Mashayek, 2021). Recent work has shown that contrary to the conventional assumption that the lee waves contribute to mixing in the close vicinity of the topography (Nikurashin & Ferrari, 2013) in the SO, a significant portion of their energy can travel to the upper ocean and interact with the mixed layer dynamics (Lavergne et al., 2020). Unaccounted for sub-mesoscale instabilities as well as changes to the efficiency of transfer of energy from the kinetic energy of oceanic flows to small-scale mixing (Mashayek, Salehipour, et al., 2017; Cimoli et al., 2019) can both contribute to mixing in ways that are both absent in model parameterisations and in the ExVar mixing map.

- Secondly, ExVar is constant in time, while observations within the SO show mixing to vary by orders of magnitude over timescales ranging from hourly to seasonally as well as varying spatially (Naveira Garabato et al., 2004; Sloyan, 2005; Damerell et al., 2012; Sheen et al., 2014). Storm-driven ocean physics is a key part of the SO carbon cycle (Nicholson et al., 2022) and 30% of the SO has synoptic (1-10 day) variance that is greater or equal in magnitude to the summer mean inter-annual variance of pCO_2 (Nicholson et al., 2022). Diffusive processes have also been shown to be a key control on SO surface DIC concentration variability on timescales of under 45 days (Rosso et al., 2017). ExVar employed our best estimate of a time-mean spatially variable mixing map, resulting in carbon fluxes and tracer distributions similar to that obtained in Ex1e-5, suggesting the importance of representing temporal variability. Thus, using a temporally-constant

spatially variable map of mixing is inherently incapable of capturing tracer distributions correctly. It is possible that we can achieve a more accurate ocean state estimate if we calculate a time-dependent, dynamically active diapycnal diffusivity field using a suite of parameterisations instead of allowing the diapycnal diffusivity to be treated as a control parameter.

The vertical gradients of biogeochemical tracers are lower than observations in Ex1e-4 throughout the upper 500 m of the SO. This finding agrees with the suggestion that in the original SOSE model which used a background mixing rate of $10^{-4}\ m^2 s^{-1}$, the mixing regime used may have been overestimating the degree of mixing (Mazloff et al., 2010). Sensitivity studies examining model observation misfits of salinity, C_{14}, CFC-11, PO_4, apparent oxygen utilisation and alkalinity have also concluded that the distribution of these tracers provides a firm upper limit on the rate of diapycnal diffusivity at around 3e-5 $m^2\ s^{-1}$, whilst no lower limit on the mixing rate can be clearly defined (Schmittner et al., 2009). For physical tracer gradients, B-SOSE has a higher vertical gradient than observational data in some regions, indicating that the mixing rate experienced by these tracers in the ocean may have been higher than the mixing of Ex1e-4. This is observed in regions known to be highly energetic, including the Agulhas current, the Argentine Basin (for temperature only) and through the PFZ where SO storm tracks are known to be at their most intense (Nicholson et al., 2022).

The use of biogeochemical tracers poses two major issues; Firstly, the altered cost functions and RMSE in each experiment could be due to direct changes in the physical transport of the biogeochemical tracer, or due to indirect effects from alterations to other physical variables which impact biogeochemistry. The fact that the RMSE and cost functions of each biogeochemical tracer varied differently with altered mixing suggests that the model data misfit is at least in part influenced by downstream effects and the choices we made in regard to other parameters. While chlorophyll concentration outputs from B-SOSE were altered between experiments, the vertical gradients of chlorophyll were unchanged, demonstrating that the changes in chlorophyll were likely due to indirect effects of altered mixing altering other tracer distributions. Secondly, although biogeochemical models are fundamentally dependent on the underlying physical cir-

culation, there are also several unconstrained biogeochemical parameters which are responsible for some of the mismatch (Verdy & Mazloff, 2017). Using a tracer such as pre-formed oxygen concentrations can alleviate both of these issues and allow a biogeochemical tracer to become a passive tracer, meaning changes in distribution with altered background mixing can be considered purely physical.

Despite the significant investments in observations such as SOCAT and SOCCOM, Fig.6.5 and Fig.6.1 show the sparsity of the available observational data. This sparseness of surface ocean pCO_2 data and wind speeds, essential for estimating air-sea carbon fluxes due to the nonlinear interaction between gas exchange and wind speed, contributes to difficulties in modelling air-sea carbon fluxes (Bushinsky et al., 2019). From a statistical perspective, this coverage is insufficient to discern which background mixing value better represents the real ocean despite the strong impact of these choices on pCO_2. This issue can be resolved only through sustained observations. Despite this, the year-round SO biogeochemical observations obtained through the SOCCOM project since 2014 (Johnson et al., 2017) have helped to significantly improve our knowledge of the seasonal cycle of SO air-sea carbon fluxes (Gray et al., 2018; Prend et al., 2022). Observations are predominately in the upper 2000 m of the water column, due to the current range of BGC and Core Argo floats. The deep Argo program is beginning to provide observations down to depths of 6000 m, allowing for better constraints of turbulence at these depths (Roemmich et al., 2019). More physical and biogeochemical observations with spatial and temporal resolution can provide much stronger constraints on the diapycnal ocean diffusivity, reducing the uncertainty of this parameter and therefore reducing levels of error in future climate projections.

Chapter 7

Conclusion

7.1 Summary of Contributions

This thesis has presented the results of an investigation into the role of Southern Ocean (SO) diapycnal mixing rates on biogeochemical cycles and biogeochemical tracer distributions. As laid out in Chapter 1, the parameterisation of turbulent diapycnal mixing in the ocean interior poses a significant uncertainty in current Earth System Models (ESM). Measurements have demonstrated the extreme spatial and temporal variability of diapycnal mixing rates within the SO. While interior diapycnal mixing rates are understood to be a key control on the strength of the Meridional Overturning Circulation (MOC), ocean ventilation and biogeochemical cycles, the importance of SO interior diapycnal mixing processes on biogeochemical cycles has been poorly studied. In this thesis, we demonstrated the importance of correctly parameterising SO mixing rates for biogeochemical cycles by addressing three key aims:

1. *Examine the sensitivity of biogeochemical cycles and tracer distributions to diapycnal mixing rates in the SO below the mixed layer on both long and short timescales due to altered advection and direct tracer mixing.*

   Using a highly idealised single basin model, we show that on sub-decadal timescales, altered diapycnal mixing alters tracer distributions within the SO and in the surface waters of the Atlantic, by directly altering vertical tracer fluxes. High mixing rates,

representative of mixing hot spots in the SO allow for tracer movement independent of the water mass movement. This can result in the short circulating of the MOC, and alterations to the subsequent fate of carbon and nutrients as a result of the SO biogeochemical divide.

On longer timescales changes to the vertical buoyancy fluxes alter the large scale structure of the ocean and the MOC. This alters tracer advection and distributions within the SO and Atlantic, altering atmospheric CO_2 levels.

2. *Demonstrate the sensitivity of biogeochemical tracer distributions to diapycnal mixing rates on short timescales and understand the mechanisms behind the sensitivity of SO carbon fluxes and SO biological productivity to alter diapycnal mixing rates on short timescales.*

   We have illustrated how slight modifications in background mixing rates can significantly impact air-sea carbon fluxes and biological productivity in the SO. Enhanced background mixing leads to an overall increase in biological productivity across most of the SO, but it simultaneously diminishes the annual carbon uptake. These alterations in background mixing produce pronounced seasonal and regional variations in both biological productivity and carbon fluxes, reflecting the diverse physical and biogeochemical conditions found at different locations and times of the year.

   The sensitivity of both carbon fluxes and biological productivity to background mixing rates occurs despite surface-generated mixing from the GGL90 parameterisation (Gaspar et al., 1990) being orders of magnitude greater than the background mixing rate. Numerical mixing from horizontal diffusion operators and advection schemes acting across large isopycnal slopes are potentially more impactful to vertical exchange in the model than the explicit vertical diffusion (Ilicak et al., 2012). For this reason, one may hypothesize that changing background mixing from $10^{-5}\ m^2 s^{-1}$ to $10^{-4}\ m^2 s^{-1}$ would have a negligible impact in B-SOSE. Nevertheless, the impact of this change is significant, suggesting this spurious diapycnal mixing must have an effective value of less than $10^{-5}\ m^2 s^{-1}$ over large regions of the model domain.

Enhanced biological productivity with increased background mixing is due to an enhanced supply of nutrients to the mixed layer. An increase in iron (Fe) supply reduces phytoplankton nutrient limitation over most of the SO, however, north of the Subtropical Front (STF) it is an enhanced supply of nitrate (NO_3) to the surface layer which increases productivity. Surface water temperatures are increased with enhanced mixing around the seasonal ice zone, reducing the sea ice cover and increasing the light availability to phytoplankton, which also increases phytoplankton productivity. The increased nutrient supply is due to the indirect impacts of enhanced mixing increasing the winter mixed layer depth, and due to directly enhanced vertical diapycnal fluxes.

Changes to carbon fluxes are due to enhanced down gradient diapycnal fluxes of Dissolved Inorganic Carbon (DIC) and alkalinity, and changes to surface temperatures, which alter the surface ocean pCO_2. The sensitivity of these tracers to diapycnal mixing is due to the strong vertical gradients found in regions of the SO. The overall changes to carbon fluxes depend on the interactive effects of changes to DIC, temperature, and alkalinity, which can compensate for or reinforce each other, and the predominant driver varies regionally, seasonally and temporally.

Although the equilibrium between physical and biological processes typically governs SO carbon fluxes, our findings demonstrate that changes in carbon fluxes due to altered mixing are independent of changes to phytoplankton productivity. The exception to this is during the summer months north of the STF, where the altered biological productivity is the primary mechanism which alters surface DIC concentrations.

3. *Investigate whether biogeochemical tracer observations can be used to constrain SO diapycnal mixing rates.*

   Using a spatially variable mixing map, which represents our current best estimate of diapycnal mixing rates, does not improve the model's ability to accurately reproduce biogeochemical tracer observations compared to employing a spatially constant value. Moreover, the introduction of this variable mixing map does not result in improved alignment between SO carbon fluxes and observed data. Model outputs obtained using a

spatially variable mixing map or a lower mixing rate exhibit comparable agreement with tracer observations, while using a higher mixing rate results in poorly constrained model outputs when compared to biogeochemical observations. Model outputs using a high mixing rate had significantly lower vertical tracer gradients than observations, placing a clear upper limit on the mean SO diapycnal mixing rate experienced by tracers. The limited availability of year-round biogeochemical observations hampers our ability to more precisely constrain diapycnal mixing rates using observations.

Actual background mixing rates show variations of even greater orders of magnitude than examined in this thesis, demonstrating the importance of implementing an appropriate diapycnal mixing scheme in ocean general circulation models.

7.2 Future Directions

The work carried out in this thesis could be extended in several ways to improve our understanding of how biogeochemical cycles respond to altered SO background mixing.

The work presented in Chapter 2 could be extended from a single-basin model of the Atlantic into a three-basin coupled model. This would demonstrate if results obtained in the Atlantic basin are also seen in the Pacific and Indian basins. It would also demonstrate the scale of the changes in ocean-atmosphere carbon partitioning over the global system. When considering the full three-basin circulation of the oceans, the nutrient content of the Upper Circumpolar Deep Waters (UCDW) and Lower Circumpolar Deep Waters (LCDW) differ due to the different origins of each of these water masses. UCDW originate from the low latitudes of the Indian and Pacific oceans, and are relatively 'old' water masses, meaning they are rich in remineralised nutrients and DIC. LCDW originate from NADW, are nutrient and DIC depleted relative to UCDW, as they are younger water masses, and organic matter within them has not been fully remineralised (Palter et al., 2013). The DIC concentration gradients between UCDW and LCDW are therefore likely to be greater in the real ocean than in this Atlantic basin-only model. This idealized single basin framework therefore likely significantly underestimates the

sensitivity of the global budgets to the SO mixing. The biogeochemical model in this work could also be modified to include nutrient limitation by Fe, as we have demonstrated that changes to Fe cycling are key to altered SO productivity.

The results in Chapters 4 & 5 could be extended through improvements to the B-SOSE model.

The biogeochemistry model could be altered to represent silicifying diatoms. The addition of silicifying diatoms would allow for changes in important biogeochemical cycles in the SO to be observed, as diatoms make up a majority proportion of the SO phytoplankton community (Swan et al., 2016). Unlike other phytoplankton types, diatoms require silicic acid to produce and maintain their silica frustules. Deep old waters that upwell at the Polar Front (PF) are silica-rich, but become increasingly depleted in silica as they flow north in mode and intermediate waters due to diatom productivity. Diatom blooms in the SO are believed to terminate in the summer as a result of silica limitation. As seen with other nutrients, silica limitation would most likely be reduced with enhanced background mixing, meaning summer diatom blooms could be elongated, further increasing SO biological productivity. It is also possible that with enhanced mixing, more silica would be exported out of the SO in mode and intermediate waters, allowing an increase in diatom productivity at low latitudes. Diatoms have a higher Fe requirement than other phytoplankton types, and SO regions with lower light but higher Fe availability favour the growth of diatoms over small phytoplankton (Krumhardt et al., 2022). Therefore diatoms would likely be favoured with higher background mixing. This could further improve export, as diatoms show high export efficiency due to the ballasting effect of their inorganic skeletons (Arteaga et al., 2019). More efficient export and therefore deep remineralisation within the SO can trap nutrients in the SO, preventing them from entering the low latitude pycnocline (Primeau et al., 2013). The level of silicification of diatoms is heavily altered by the availability of Fe, with more Fe lowering silicification (Tréguer, 2014). Therefore increased Fe supply has been hypothesised to cause less silicate to be exported from the SO relative to nitrate, allowing low latitude waters to become enriched in silicate, and resulting in a community shift towards more diatoms in low latitudes. This demonstrates the significance of silicifying diatoms and the global nutrient and biogeochemical cycle.

The physical model in B-SOSE could also be improved. Currently, the bottom boundary layers are not resolved due to the low vertical resolution of the model grid in the deep ocean. Thus, there are diapycnal mixing processes in the abyssal ocean responsible for significant water mass transformation of AABW that are not represented here (Nikurashin & Ferrari, 2013; Waterhouse et al., 2014). The inclusion of these processes could be key in understanding diapycnal transformations of water masses which occur. The model does not include any mesoscale eddy parameterisation and thus under represents mesoscale structures. Altered background mixing and the associated altered SO stratification is likely to have an impact on these mesoscale and sub-mesoscale processes, which would further alter biogeochemical cycles. B-SOSE does not currently account for double diffusive processes. It is possible that if double diffusivity was included in B-SOSE, the impacts of altering the background diapycnal mixing rates on biogeochemistry would be dampened, as a higher background mixing rate could erode the unstable salinity and temperature stratification, and result in less mixing driven by double diffusive processes. However, the impacts of altered background mixing on biogeochemical processes are highly nonlinear, making predictions hard to make.

Finally, future work should attempt to assess the sensitivity of SO biogeochemical tracer distributions and cycles in B-SOSE to temporally variable diapycnal mixing rates. Regions of the SO have been shown diapycnal mixing rates that vary temporally by a factor of up to 100 (Damerell et al., 2012). The driving mechanisms behind the strong temporal variability in the SO are likely to vary regionally depending on topography and local atmospheric and oceanic settings. Atmospheric storms, ocean eddy activity, strong currents, the movement of fronts, and tidal cycles can all contribute to the temporal variability of SO mixing on timescales ranging from hourly to decadal (Damerell et al., 2012; Whalen et al., 2012; Sheen et al., 2014). There is a clear need for a more direct connection between the processes that cause background mixing and model parameterisations.

7.3 Thesis Implications

In this thesis, we have demonstrated the importance of the parameterisation of SO background diapycnal mixing rates for biogeochemical cycles on a range of timescales. While the work in this thesis is based on the use of two ocean models (SAMBUCA and B-SOSE), we believe that these results are applicable to any ocean model or state estimate which requires the parameterisation of SO diapycnal mixing. While this work assessed the sensitivity of biogeochemistry to SO background diapycnal mixing, it is likely that the ocean biogeochemistry in many other regions will exhibit high sensitivity to diapycnal mixing rates. This is likely to be especially true in other regions which have high vertical gradients in tracer concentrations, such as in regions of upwelling, or in regions particularly limited by nutrients, including low latitude gyres.

We have shown that the impact of altering SO background diapycnal mixing on biogeochemistry highly depends on the time scale considered, with tracer distributions altered directly by changes in background mixing rates far faster than they are altered indirectly via changes in the background oceanographic state induced by changes in the underlying turbulence. On sub decadal time scales, the impacts of altered background mixing are predominantly on local biogeochemical cycles as a direct impact of altered vertical fluxes. Given that mixing is induced by turbulent events that are highly intermittent in time and space, this highlights the absolute necessity for climate models to resolve the spatiotemporal variability of SO small-scale turbulent mixing, or to skillfully parameterise the processes responsible for generating them. Currently, explicit parameterisations of small-scale diapycnal mixing below the mixed layer in the SO are uncommon, if not nonexistent. Over longer timescales, the impacts of altered mixing on ocean biogeochemistry are likely to be further reaching due to the advection of tracers. Finally, over time scales greater than centennial, changes in biogeochemistry can occur as a result of altered large scale ocean circulation patterns due to changes in background turbulence acting on physical tracers. This work suggests that we need a better understanding of how background mixing rates in the ocean have varied over long time scales. Changes in continental configuration and sea level on climatic time scales cause changes to the processes responsible

for generating background turbulence, such as tidal flows, meaning that diapycnal mixing rates are not constant on long timescales. Regions of high turbulence today may not have had such high turbulence in the past, or may not have such high turbulence in the future. Accounting for this difference in the state of background mixing in ocean models will provide a more accurate representation of the ocean system at the time of interest.

We have demonstrated the sensitivity of sea ice cover to background diapycnal mixing rates. We have shown that higher rates of background mixing result in an earlier retreat of spring sea ice. This demonstrates the importance of gaining a better understanding of the processes responsible for the generation of turbulence beneath sea ice or within the ocean sea-ice interface. It is also important that we better understand how background mixing rates near the ocean sea-ice interface and beneath sea-ice will be altered with climate change as global temperatures warm and ice cover is reduced. It is possible that as ice cover is reduced, wind generated turbulence will increase, resulting in further sea ice loss.

The SO is a key region for the control of global productivity and the cycling of anthropogenic and natural carbon. The air-sea carbon balance is determined by the carbon and preformed nutrient concentrations in regions of Antarctic Bottom Water (AABW) formation, as well as the strength of bottom water formation. Global productivity north of the SO is influenced by the nutrient concentrations in waters at the site of Antarctic Intermediate Waters (AAIW) and Sub Antarctic Mode Water (SAMW) formation (Palter et al., 2013; Ito & Follows, 2005; Archer et al., 2000; Marinov, Gnanadesikan, et al., 2008; Marinov et al., 2006).

We have demonstrated that changes to SO mixing significantly alter SO biological productivity and carbon fluxes. Over longer timescales these mechanisms have the potential to alter atmospheric carbon concentration, alluding to the importance of accurate representation of diapycnal mixing in climate models. The increase in surface nutrient concentrations with higher background mixing would increase the export of preformed nutrients to the lower latitude ocean via mode and intermediate waters. The extra biomass produced within the SO as a result of increased nutrient supply and productivity could be predominately remineralised within the MLD of the SO, causing nutrient trapping and an increase in SO nutrient retention, or be

exported to the deeper ocean to form part of the regenerated nutrient pool. Assessing which mechanism predominantly occurs is beyond the scope of this work, but would be necessary to understand whether enhanced mixing results in an increase in the nutrients retained by the SO or an increase in nutrient export.

A more complete understanding of the physical processes which cause the spatial and temporal variability of turbulent mixing in the SO is required to develop more realistic parameterisations for ESM. Until these mixing processes are accurately represented, they will cause inaccuracies in our representation of the MOC and ocean biogeochemical cycles, limiting our ability to predict future climate change.

References

Afkar, E. (2012). Localization of the Dissimilatory Arsenate Reductase in Sulfurospirillum Barnesi Strain SeS-3. *American Journal of Agricultural and Biological Sciences*. doi: 10.3844/ajabssp.2012.97.105

Alford, M. H. (2020, 10). Global Calculations of Local and Remote Near-Inertial-Wave Dissipation. *Journal of Physical Oceanography*, *50*(11), 3157–3164. Retrieved from `https://journals.ametsoc.org/view/journals/phoc/50/11/JPO-D-20-0106.1.xml` doi: 10.1175/JPO-D-20-0106.1

Archer, D. E., Eshel, G., Winguth, A., Broecker, W., Pierrehumbert, R., Tobis, M., & Jacob, R. (2000, 12). Atmospheric pCO2 sensitivity to the biological pump in the ocean. *Global Biogeochemical Cycles*, *14*(4), 1219–1230. Retrieved from `https://onlinelibrary.wiley.com/doi/full/10.1029/1999GB001216https://onlinelibrary.wiley.com/doi/abs/10.1029/1999GB001216https://agupubs.onlinelibrary.wiley.com/doi/10.1029/1999GB001216` doi: 10.1029/1999GB001216

Arteaga, L. A., Pahlow, M., Bushinsky, S. M., & Sarmiento, J. L. (2019, 8). Nutrient Controls on Export Production in the Southern Ocean. *Global Biogeochemical Cycles*, *33*(8), 942–956. doi: 10.1029/2019GB006236

Badin, G., Williams, R. G., Jing, Z., & Wu, L. (2013). Water mass transformations in the southern ocean diagnosed from observations: Contrasting effects of air-sea fluxes and diapycnal mixing. *Journal of Physical Oceanography*. doi: 10.1175/JPO-D-12-0216.1

Baker, L. E., & Mashayek, A. (2021, 10). Surface reflection of bottom generated oceanic lee waves. *Journal of Fluid Mechanics*, *924*, A17. doi: 10.1017/jfm.2021.627

Bakker, D. C., Bozec, Y., Nightingale, P. D., Goldson, L., Messias, M. J., De Baar, H. J., ... Watson, A. J. (2005). Iron and mixing affect biological carbon uptake in SOIREE and

EisenEx, two Southern Ocean iron fertilisation experiments. *Deep-Sea Research Part I: Oceanographic Research Papers*. doi: 10.1016/j.dsr.2004.11.015

Bakker, D. C., Pfeil, B., Landa, C. S., Metzl, N., O'Brien, K. M., Olsen, A., ... Xu, S. (2016, 9). *A multi-decade record of high-quality fCO2 data in version 3 of the Surface Ocean CO2 Atlas (SOCAT)* (Vol. 8) (No. 2). Retrieved from `https://essd.copernicus.org/articles/8/383/2016/` doi: 10.5194/essd-8-383-2016

Bakker, D. C. E., Pfeil, B., Smith, K., Hankin, S., Olsen, A., Alin, S. R., ... Watson, A. J. (2014, 3). An update to the Surface Ocean CO₂ Atlas (SOCAT version 2). *Earth System Science Data*, *6*(1), 69–90. Retrieved from `https://essd.copernicus.org/articles/6/69/2014/` doi: 10.5194/essd-6-69-2014

Bianchi, D., Galbraith, E. D., Carozza, D. A., Mislan, K. A., & Stock, C. A. (2013, 7). Intensification of open-ocean oxygen depletion by vertically migrating animals. *Nature Geoscience*, *6*(7), 545–548. Retrieved from `http://www.nature.com/articles/ngeo1837` doi: 10.1038/ngeo1837

Boyd, P. W. (2002, 1). The role of iron in the biogeochemistry of the Southern Ocean and equatorial Pacific: A comparison of in situ iron enrichments. *Deep-Sea Research Part II: Topical Studies in Oceanography*, *49*(9-10), 1803–1821. Retrieved from `https://www.sciencedirect.com/science/article/pii/S0967064502000139` doi: 10.1016/S0967-0645(02)00013-9

Boyd, P. W., Doney, S. C., Strzepek, R., Dusenberry, J., Lindsay, K., & Fung, I. (2008, 5). Climate-mediated changes to mixed-layer properties in the Southern Ocean: assessing the phytoplankton response. *Biogeosciences*, *5*(3), 847–864. Retrieved from `https://bg.copernicus.org/articles/5/847/2008/` doi: 10.5194/bg-5-847-2008

Boyd, P. W. e. a. (2000). *A mesoscale phytoplankton bloom in the polar Southern Ocean stimulated by iron fertilization.*

Bryan, F. (1987). Parameter sensitivity of primitive equation ocean general circulation models. *J. PHYS. OCEANOGR.*. doi: 10.1175/1520-0485(1987)017⟨0970:psopeo⟩2.0.co;2

Bryan, K., & Lewis, L. J. (1980, 5). A water mass model of the world ocean. *Journal of Geophysical Research*, *85*(C5), 2503–2518. Retrieved from `http://doi.wiley.com/`

10.1029/JC084iC05p02503 doi: 10.1029/jc084ic05p02503

Bushinsky, S. M., Landschützer, P., Rödenbeck, C., Gray, A. R., Baker, D., Mazloff, M. R., ... Sarmiento, J. L. (2019, 11). Reassessing Southern Ocean Air-Sea CO2 Flux Estimates With the Addition of Biogeochemical Float Observations. *Global Biogeochemical Cycles*, *33*(11), 1370–1388. Retrieved from https://onlinelibrary.wiley.com/doi/abs/10.1029/2019GB006176 doi: 10.1029/2019GB006176

Cessi, P. (2019, 1). *The global overturning circulation* (Vol. 11) (No. 1). Annual Reviews. Retrieved from https://www.annualreviews.org/doi/10.1146/annurev-marine-010318-095241 doi: 10.1146/annurev-marine-010318-095241

Chapman, C. C., Lea, M. A., Meyer, A., Sallée, J. B., & Hindell, M. (2020). Defining Southern Ocean fronts and their influence on biological and physical processes in a changing climate. *Nature Climate Change*. doi: 10.1038/s41558-020-0705-4

Chen, H., Haumann, F. A., Talley, L. D., Johnson, K. S., & Sarmiento, J. L. (2022, 7). The Deep Ocean's Carbon Exhaust. *Global Biogeochemical Cycles*, *36*(7). doi: 10.1029/2021GB007156

Cimoli, L., Caulfield, C. c. P., Johnson, H. L., Marshall, D. P., Mashayek, A., Naveira Garabato, A. C., & Vic, C. (2019, 12). Sensitivity of Deep Ocean Mixing to Local Internal Tide Breaking and Mixing Efficiency. *Geophysical Research Letters*, *46*(24), 14622–14633. Retrieved from https://onlinelibrary.wiley.com/doi/full/10.1029/2019GL085056https://onlinelibrary.wiley.com/doi/abs/10.1029/2019GL085056https://agupubs.onlinelibrary.wiley.com/doi/10.1029/2019GL085056 doi: 10.1029/2019GL085056

Damerell, G. M., Heywood, K. J., Stevens, D. P., & Naveira Garabato, A. C. (2012, 3). Temporal Variability of Diapycnal Mixing in Shag Rocks Passage. *Journal of Physical Oceanography*, *42*(3), 370–385. doi: 10.1175/2011JPO4573.1

Dee, D. P., Uppala, S. M., Simmons, A. J., Berrisford, P., Poli, P., Kobayashi, S., ... Vitart, F. (2011, 4). The ERA-Interim reanalysis: configuration and performance of the data assimilation system. *Quarterly Journal of the Royal Meteorological Society*, *137*(656), 553–597. Retrieved from https://onlinelibrary.wiley.com/doi/full/10.1002/

qj.828https://onlinelibrary.wiley.com/doi/abs/10.1002/qj.828https://rmets.onlinelibrary.wiley.com/doi/10.1002/qj.828 doi: 10.1002/QJ.828

De Lavergne, C., Madec, G., Le Sommer, J., Nurser, A. J., & Naveira Garabato, A. C. (2016). On the consumption of Antarctic Bottom Water in the abyssal ocean. *Journal of Physical Oceanography*, *46*(2), 635–661. Retrieved from https://journals.ametsoc.org/doi/pdf/10.1175/JPO-D-14-0201.1 doi: 10.1175/JPO-D-14-0201.1

DeVries, T., & Primeau, F. (2011, 12). Dynamically and Observationally Constrained Estimates of Water-Mass Distributions and Ages in the Global Ocean. *Journal of Physical Oceanography*, *41*(12), 2381–2401. Retrieved from https://journals.ametsoc.org/jpo/article/41/12/2381/11258/Dynamically-and-Observationally-Constrainedhttp://journals.ametsoc.org/doi/10.1175/JPO-D-10-05011.1 doi: 10.1175/JPO-D-10-05011.1

Doney, S. C., Lindsay, K., Caldeira, K., Campin, J. M., Drange, H., Dutay, J. C., ... Yool, A. (2004). Evaluating global ocean carbon models: The importance of realistic physics. *Global Biogeochemical Cycles*. doi: 10.1029/2003GB002150

Dove, L. A., Thompson, A. F., Balwada, D., & Gray, A. R. (2021, 7). Observational Evidence of Ventilation Hotspots in the Southern Ocean. *Journal of Geophysical Research: Oceans*, *126*(7). doi: 10.1029/2021JC017178

Dufour, C. O., Sommer, J. L., Gehlen, M., Orr, J. C., Molines, J., Simeon, J., & Barnier, B. (2013, 9). Eddy compensation and controls of the enhanced sea-to-air CO ¡sub¿2¡/sub¿ flux during positive phases of the Southern Annular Mode. *Global Biogeochemical Cycles*, *27*(3), 950–961. Retrieved from https://onlinelibrary.wiley.com/doi/10.1002/gbc.20090 doi: 10.1002/gbc.20090

Dunne, J. P., Armstrong, R. A., Gnnadesikan, A., & Sarmiento, J. L. (2005, 12). Empirical and mechanistic models for the particle export ratio. *Global Biogeochemical Cycles*, *19*(4), n/a-n/a. Retrieved from http://doi.wiley.com/10.1029/2004GB002390 doi: 10.1029/2004GB002390

Dutkiewicz, S., Follows, M. J., Heimbach, P., & Marshall, J. (2006, 1). Controls on ocean productivity and air-sea carbon flux: An adjoint model sensitivity study. *Geophysi-*

cal Research Letters, *33*(2), L02603. Retrieved from http://doi.wiley.com/10.1029/2005GL024987 doi: 10.1029/2005GL024987

Dutkiewicz, S., Sokolov, A., Scott, J., & Stone, P. (2005). A three-dimensional ocean-seaice-carbon cycle model and its coupling to a two- .... *Joint Program on the Science and Policy of Global ...*. Retrieved from http://web.mit.edu/globalchange/www/MITJPSPGC_Rpt122.pdfhttp://scholar.google.com/scholar?start=100&hl=en&cites=642048877832323420#0

Dutreuil, S., Bopp, L., & Tagliabue, A. (2009). Impact of enhanced vertical mixing on marine biogeochemistry: Lessons for geo-engineering and natural variability. *Biogeosciences*, *6*(5), 901–912. Retrieved from www.biogeosciences.net/6/901/2009/ doi: 10.5194/bg-6-901-2009

Ellison, E., Cimoli, L., & Mashayek, A. (2022, 5). Multi-time scale control of Southern Ocean diapycnal mixing over Atlantic tracer budgets. *Climate Dynamics*, *60*(9), 3039–3050. Retrieved from https://link.springer.com/article/10.1007/s00382-022-06428-5 doi: 10.1007/S00382-022-06428-5/TABLES/1

Fauchereau, N., Tagliabue, A., Bopp, L., & Monteiro, P. M. (2011, 9). The response of phytoplankton biomass to transient mixing events in the Southern Ocean. *Geophysical Research Letters*, *38*(17), n/a-n/a. Retrieved from http://doi.wiley.com/10.1029/2011GL048498 doi: 10.1029/2011GL048498

Fenty, I., & Heimbach, P. (2013, 5). Coupled Sea Ice–Ocean-State Estimation in the Labrador Sea and Baffin Bay. *Journal of Physical Oceanography*, *43*(5), 884–904. Retrieved from https://journals.ametsoc.org/view/journals/phoc/43/5/jpo-d-12-065.1.xml doi: 10.1175/JPO-D-12-065.1

Ferrari, R. (2014). *Oceanography: What goes down must come up.* doi: 10.1038/513179a

Ferrari, R., Jansen, M. F., Adkins, J. F., Burke, A., Stewart, A. L., & Thompson, A. F. (2014). Antarctic sea ice control on ocean circulation in present and glacial climates. *Proceedings of the National Academy of Sciences of the United States of America*, *111*(24), 8753–8758. Retrieved from www.pnas.org/cgi/doi/10.1073/pnas.1323922111 doi: 10.1073/pnas.1323922111

Ferrari, R., Mashayek, A., McDougall, T. J., Nikurashin, M., & Campin, J.-M. (2016). Turning Ocean Mixing Upside Down. *Journal of Physical Oceanography*, *46*(7), 2239–2261. Retrieved from https://journals.ametsoc.org/doi/pdf/10.1175/JPO-D-15-0244.1 doi: 10.1175/jpo-d-15-0244.1

Follows, M. J., Ito, T., Dutkiewicz, S., & Michael, J. F. T. I. S. D. (2006, 1). On the solution of the carbonate chemistry system in ocean biogeochemistry models. *Ocean Modelling*, *12*(3-4), 290–301. Retrieved from https://www.sciencedirect.com/science/article/abs/pii/S1463500305000533 doi: 10.1016/j.ocemod.2005.05.004

Forget, G., Campin, J.-M., Heimbach, P., Hill, C. N., Ponte, R. M., & Wunsch, C. (2015, 10). ECCO version 4: an integrated framework for non-linear inverse modeling and global ocean state estimation. *Geoscientific Model Development*, *8*(10), 3071–3104. doi: 10.5194/gmd-8-3071-2015

Forget, G., Ferreira, D., & Liang, X. (2015, 10). On the observability of turbulent transport rates by Argo: supporting evidence from an inversion experiment. *Ocean Science*, *11*(5), 839–853. doi: 10.5194/os-11-839-2015

Fox-Kemper, B., Johnson, L., & Qiao, F. (2022, 1). Ocean near-surface layers. *Ocean Mixing*, 65–94. doi: 10.1016/B978-0-12-821512-8.00011-6

Freilich, M. A., & Mahadevan, A. (2019, 6). Decomposition of Vertical Velocity for Nutrient Transport in the Upper Ocean. *Journal of Physical Oceanography*, *49*(6), 1561–1575. Retrieved from https://journals.ametsoc.org/view/journals/phoc/49/6/jpo-d-19-0002.1.xml doi: 10.1175/JPO-D-19-0002.1

Friedrich, T., Timmermann, A., Decloedt, T., Luther, D. S., & Mouchet, A. (2011, 1). The effect of topography-enhanced diapycnal mixing on ocean and atmospheric circulation and marine biogeochemistry. *Ocean Modelling*, *39*(3-4), 262–274. doi: 10.1016/J.OCEMOD.2011.04.012

Galbraith, E. D., Dunne, J. P., Gnanadesikan, A., Slater, R. D., Sarmiento, J. L., Dufour, C. O., ... Marvasti, S. S. (2015). Complex functionality with minimal computation: Promise and pitfalls of reduced-tracer ocean biogeochemistry models. *Journal of Advances in Modeling Earth Systems*, *7*(4), 2012–2028. Retrieved from https://earthsystemdynamics

.org/wp-content/uploads/2019/11/Galbraith-JAMES-2015.pdf doi: 10.1002/2015MS000463

Galbraith, E. D., Gnanadesikan, A., Dunne, J. P., & Hiscock, M. R. (2010). Regional impacts of iron-light colimitation in a global biogeochemical model. *Biogeosciences*, *7*(3), 1043–1064. Retrieved from www.biogeosciences.net/7/1043/2010/ doi: 10.5194/bg-7-1043-2010

Garabato, A. C., Stevens, D. P., Watson, A. J., & Roether, W. (2007, 5). Short-circuiting of the overturning circulation in the Antarctic Circumpolar Current. *Nature*, *447*(7141), 194–197. Retrieved from https://www.nature.com/articles/nature05832.pdfhttp://www.nature.com/articles/nature05832 doi: 10.1038/nature05832

Garcia, H. E., Boyer, T. P., Locarnini, R. A., Antonov, J. I., Mishonov, A. V., Baranova, O. K., ... Levitus, S. (2013). *World ocean atlas 2013. Volume 3, Dissolved oxygen, apparent oxygen utilization, and oxygen saturation* (Tech. Rep.). Retrieved from https://repository.library.noaa.gov/view/noaa/14849 doi: 10.7289/V5XG9P2W

Garcia, H. E., Locarnini, R. A., Boyer, T. P., Antonov, J. I., Baranova, O. K., Zweng, M. M., ... Johnson, D. R. (2013). *World Ocean Atlas 2013, Volume 4 : Dissolved Inorganic Nutrients (phosphate, nitrate, silicate)* (Vol. 4) (No. September). Retrieved from https://repository.library.noaa.gov/view/noaa/14850 doi: 10.7289/V5J67DWD

Gaspar, P., Grégoris, Y., & Lefevre, J.-M. (1990, 9). A simple eddy kinetic energy model for simulations of the oceanic vertical mixing: Tests at station Papa and long-term upper ocean study site. *Journal of Geophysical Research*, *95*(C9), 16179. Retrieved from http://doi.wiley.com/10.1029/JC095iC09p16179 doi: 10.1029/JC095iC09p16179

Gille, S. T., Sheen, K. L., Swart, S., & Thompson, A. F. (2022, 1). Mixing in the Southern Ocean. *Ocean Mixing: Drivers, Mechanisms and Impacts*, 301–327. doi: 10.1016/B978-0-12-821512-8.00019-0

Gnanadesikan, A. (1999, 3). A simple predictive model for the structure of the oceanic pycnocline. *Science*, *283*(5410), 2077–2079. doi: 10.1126/science.283.5410.2077

Gnanadesikan, A., Dunne, J. P., Key, R. M., Matsumoto, K., Sarmiento, J. L., Slater, R. D., & Swathi, P. S. (2004). Oceanic ventilation and biogeochemical cycling: Understanding the physical mechanisms that produce realistic distributions of tracers

and productivity. *Global Biogeochemical Cycles*, *18*(4), 1–17. Retrieved from https://agupubs.onlinelibrary.wiley.com/doi/pdf/10.1029/2003GB002097https://pdfs.semanticscholar.org/09bf/eb7e7728fb8ad30f253e13e72adf20992330.pdf doi: 10.1029/2003GB002097

Gnanadesikan, A., Sarmiento, J. L., & Slater, R. D. (2003, 6). Effects of patchy ocean fertilization on atmospheric carbon dioxide and biological production. *Global Biogeochemical Cycles*, *17*(2), n/a-n/a. Retrieved from http://doi.wiley.com/10.1029/2002GB001940 doi: 10.1029/2002GB001940

Gnanadesikan, A., Slater, R. D., Gruber, N., & Sarmiento, J. L. (2001). Oceanic vertical exchange and new production: A comparison between models and observations. *Deep-Sea Research Part II: Topical Studies in Oceanography*. doi: 10.1016/S0967-0645(01)00107-2

Gouretski, V., & Koltermann, K. P. (2004). WOCE global hydrographic climatology. *Berichte des BSH 35*, 1–52.

Gray, A. R., Johnson, K. S., Bushinsky, S. M., Riser, S. C., Russell, J. L., Talley, L. D., ... Sarmiento, J. L. (2018). Autonomous Biogeochemical Floats Detect Significant Carbon Dioxide Outgassing in the High-Latitude Southern Ocean. *Geophysical Research Letters*, *45*(17), 9049–9057. doi: 10.1029/2018GL078013

Groeskamp, S., Griffies, S. M., Iudicone, D., Marsh, R., Nurser, A. J., & Zika, J. D. (2019). *The water mass transformation framework for ocean physics and biogeochemistry* (Vol. 11). Retrieved from https://doi.org/10.1146/annurev-marine-010318- doi: 10.1146/annurev-marine-010318-095421

Gruber, N., Gloor, M., Mikaloff Fletcher, S. E., Doney, S. C., Dutkiewicz, S., Follows, M. J., ... Takahashi, T. (2009, 3). Oceanic sources, sinks, and transport of atmospheric CO ¡sub¿2¡/sub¿. *Global Biogeochemical Cycles*, *23*(1), n/a-n/a. Retrieved from http://doi.wiley.com/10.1029/2008GB003349 doi: 10.1029/2008GB003349

Gruber, N., Landschützer, P., & Lovenduski, N. S. (2019, 1). The Variable Southern Ocean Carbon Sink. *https://doi.org/10.1146/annurev-marine-121916-063407*, *11*, 159–186. Retrieved from https://www.annualreviews.org/doi/abs/10.1146/annurev-marine-121916-063407 doi: 10.1146/ANNUREV-MARINE-121916-063407

Henson, S., Le Moigne, F., & Giering, S. (2019, 7). Drivers of Carbon Export Efficiency in the Global Ocean. *Global Biogeochemical Cycles*, *33*(7), 891–903. doi: 10.1029/2018GB006158

Hieronymus, M., Nycander, J., Nilsson, J., Döös, K., & Hallberg, R. (2019, 2). Oceanic Overturning and Heat Transport: The Role of Background Diffusivity. *Journal of Climate*, *32*(3), 701–716. Retrieved from https://journals.ametsoc.org/view/journals/clim/32/3/jcli-d-18-0438.1.xml doi: 10.1175/JCLI-D-18-0438.1

Ilicak, M., Adcroft, A. J., Griffies, S. M., & Hallberg, R. W. (2012, 1). Spurious dianeutral mixing and the role of momentum closure. *Ocean Modelling*, *45-46*, 37–58. doi: 10.1016/J.OCEMOD.2011.10.003

Ito, T., & Follows, M. J. (2005). Preformed phosphate, soft tissue pump and atmospheric CO 2. *Journal of Marine Research*. Retrieved from http://ocean.mit.edu/~mick/Papers/ItoFollows-preformed-JMR2005.pdf doi: 10.1357/0022240054663231

Ito, T., & Marshall, J. (2008). Control of lower-limb overturning circulation in the Southern Ocean by diapycnal mixing and mesoscale eddy transfer. *Journal of Physical Oceanography*, *38*(12), 2832–2845. Retrieved from https://journals.ametsoc.org/doi/pdf/10.1175/2008JPO3878.1 doi: 10.1175/2008JPO3878.1

Jackett, D. R., & McDougall, T. J. (1997, 2). A Neutral Density Variable for the World's Oceans. *Journal of Physical Oceanography*, *27*(2), 237–263. Retrieved from http://journals.ametsoc.org/doi/10.1175/1520-0485(1997)027<0237:ANDVFT>2.0.CO;2 doi: 10.1175/1520-0485(1997)027⟨0237:ANDVFT⟩2.0.CO;2

Jansen, M. F., & Nadeau, L.-P. (2016). The Effect of Southern Ocean Surface Buoyancy Loss on the Deep-Ocean Circulation and Stratification. *Journal of Physical Oceanography*, *46*(11), 3455–3470. doi: 10.1175/jpo-d-16-0084.1

Jayne, S. R. (2009). The impact of abyssal mixing parameterizations in an ocean general circulation model. *Journal of Physical Oceanography*. doi: 10.1175/2009JPO4085.1

Jayne, S. R., & St. Laurent, L. C. (2001, 3). Parameterizing tidal dissipation over rough topography. *Geophysical Research Letters*, *28*(5), 811–814. Retrieved from

https://onlinelibrary.wiley.com/doi/full/10.1029/2000GL012044https://onlinelibrary.wiley.com/doi/abs/10.1029/2000GL012044https://agupubs.onlinelibrary.wiley.com/doi/10.1029/2000GL012044 doi: 10.1029/2000GL012044

Johnson, K. S., Plant, J. N., Coletti, L. J., Jannasch, H. W., Sakamoto, C. M., Riser, S. C., ... Sarmiento, J. L. (2017, 8). Biogeochemical sensor performance in the SOCCOM profiling float array. *Journal of Geophysical Research: Oceans*, *122*(8), 6416–6436. Retrieved from https://onlinelibrary.wiley.com/doi/abs/10.1002/2017JC012838 doi: 10.1002/2017JC012838

Key, R. M., Olsen, A., Van Heuven, S., Lauvset, S. K., Velo, A., Lin, X., ... Suzuki, T. (2015). GLOBAL OCEAN DATA ANALYSIS PROJECT, VERSION 2 (GLODAPv2). *Earth System Science Data*.

Khatiwala, S., Primeau, F., & Hall, T. (2009). Reconstruction of the history of anthropogenic CO2 concentrations in the ocean. *Nature*, *462*(7271), 346–349. Retrieved from www.nature.com/nature. doi: 10.1038/nature08526

Klocker, A. (2018). Opening the window to the Southern Ocean: The role of jet dynamics. *Science Advances*. doi: 10.1126/sciadv.aao4719

Körtzinger, A., Hedges, J. I., & Quay, P. D. (2001, 6). Redfield ratios revisited: Removing the biasing effect of anthropogenic CO2. *Limnology and Oceanography*, *46*(4), 964–970. Retrieved from http://doi.wiley.com/10.4319/lo.2001.46.4.0964 doi: 10.4319/lo.2001.46.4.0964

Krumhardt, K. M., Long, M. C., Sylvester, Z. T., & Petrik, C. M. (2022, 8). Climate drivers of Southern Ocean phytoplankton community composition and potential impacts on higher trophic levels. *Frontiers in Marine Science*, *9*, 1466. doi: 10.3389/FMARS.2022.916140/BIBTEX

Landschützer, P., Gruber, N., & Bakker, D. C. E. (2016, 10). Decadal variations and trends of the global ocean carbon sink. *Global Biogeochemical Cycles*, *30*(10), 1396–1417. Retrieved from http://doi.wiley.com/10.1002/2015GB005359 doi: 10.1002/2015GB005359

Landschützer, P., Gruber, N., Haumann, F. A., Rödenbeck, C., Bakker, D. C. E., van Heuven,

S., ... Wanninkhof, R. (2015, 9). The reinvigoration of the Southern Ocean carbon sink. *Science*, *349*(6253), 1221–1224. Retrieved from https://www.sciencemag.org/lookup/doi/10.1126/science.aab2620http://science.sciencemag.org/ doi: 10.1126/science.aab2620

Large, W. G., McWilliams, J. C., & Doney, S. C. (1994, 11). Oceanic vertical mixing: A review and a model with a nonlocal boundary layer parameterization. *Reviews of Geophysics*, *32*(4), 363. Retrieved from http://doi.wiley.com/10.1029/94RG01872 doi: 10.1029/94RG01872

Large, W. G., & Yeager, S. G. (2009, 8). The global climatology of an interannually varying air - Sea flux data set. *Climate Dynamics*, *33*(2-3), 341–364. Retrieved from http://link.springer.com/10.1007/s00382-008-0441-3 doi: 10.1007/s00382-008-0441-3

Lauderdale, J. M., Naveira Garabato, A. C., Oliver, K. I. C., Follows, M. J., Williams, R. G., Garabato, A. C., ... Williams, R. G. (2013). Wind-driven changes in Southern Ocean residual circulation, ocean carbon reservoirs and atmospheric CO 2. *Climate Dynamics*. Retrieved from https://link.springer.com/content/pdf/10.1007%2Fs00382-012-1650-3.pdf doi: 10.1007/s00382-012-1650-3

Lauvset, S. K., Key, R. M., Olsen, A., van Heuven, S., Velo, A., Lin, X., ... Watelet, S. (2016, 8). A new global interior ocean mapped climatology. *Earth System Science Data*, *8*(2), 325–340. Retrieved from www.earth-syst-sci-data.net/8/325/2016/https://essd.copernicus.org/articles/8/325/2016/ doi: 10.5194/essd-8-325-2016

Lavergne, C., Vic, C., Madec, G., Roquet, F., Waterhouse, A. F., Whalen, C. B., ... Hibiya, T. (2020, 5). A Parameterization of Local and Remote Tidal Mixing. *Journal of Advances in Modeling Earth Systems*, *12*(5). doi: 10.1029/2020MS002065

Law, C. S., Abraham, E. R., Watson, A. J., & Liddicoat, M. I. (2003). Vertical eddy diffusion and nutrient supply to the surface mixed layer of the Antarctic Circumpolar Current. *Journal of Geophysical Research C: Oceans*. doi: 10.1029/2002jc001604

Ledwell, J. R., Montgomery, E. T., Polzin, K. L., Laurent, L. C. S., Schmitt, R. W., & Toole, J. M. (2000). Evidence for enhanced mixing over rough topography in the abyssal ocean. *Nature*. doi: 10.1038/35003164

Ledwell, J. R., St. Laurent, L. C., Girton, J. B., & Toole, J. M. (2011). Diapycnal mixing in the antarctic circumpolar current. *Journal of Physical Oceanography*, *41*(1), 241–246. Retrieved from http://www.rocklandscientific.com doi: 10.1175/2010JPO4557.1

Ledwell, J. R., Watson, A. J., & Law, C. S. (1993, 8). Evidence for slow mixing across the pycnocline from an open-ocean tracer-release experiment. *Nature*, *364*(6439), 701–703. Retrieved from http://www.nature.com/articles/364701a0 doi: 10.1038/364701a0

Li, G., Cheng, L., Zhu, J., Trenberth, K. E., Mann, M. E., & Abraham, J. P. (2020, 12). Increasing ocean stratification over the past half-century. *Nature Climate Change*, *10*(12), 1116–1123. Retrieved from http://www.nature.com/articles/s41558-020-00918-2 doi: 10.1038/s41558-020-00918-2

Llort, J., Lévy, M., Sallée, J. B., & Tagliabue, A. (2019, 3). Nonmonotonic Response of Primary Production and Export to Changes in Mixed-Layer Depth in the Southern Ocean. *Geophysical Research Letters*, *46*(6), 3368–3377. Retrieved from https://onlinelibrary.wiley.com/doi/abs/10.1029/2018GL081788 doi: 10.1029/2018GL081788

Losch, M., Menemenlis, D., Campin, J. M., Heimbach, P., & Hill, C. (2010, 1). On the formulation of sea-ice models. Part 1: Effects of different solver implementations and parameterizations. *Ocean Modelling*, *33*(1-2), 129–144. Retrieved from https://www.sciencedirect.com/science/article/abs/pii/S1463500309002418 doi: 10.1016/j.ocemod.2009.12.008

Lumpkin, R., & Speer, K. (2007). Global ocean meridional overturning. *Journal of Physical Oceanography*, *37*(10), 2550–2562. Retrieved from https://journals.ametsoc.org/doi/pdf/10.1175/JPO3130.1 doi: 10.1175/JPO3130.1

MacKinnon, J., St Laurent, L., & Naveira Garabato, A. C. (2013). Diapycnal mixing processes in the ocean interior. In *International geophysics* (Vol. 103, pp. 159–183). doi: 10.1016/B978-0-12-391851-2.00007-6

MacKinnon, J. A., Zhao, Z., Whalen, C. B., Waterhouse, A. F., Trossman, D. S., Sun, O. M., ... Alford, M. H. (2017, 11). Climate process team on internal wave-driven ocean mixing. *Bulletin of the American Meteorological Society*, *98*(11), 2429–2454. Retrieved from https://journals.ametsoc.org/doi/10.1175/BAMS-D-16-0030.1 doi: 10.1175/

BAMS-D-16-0030.1

Mahadevan, A. (2016, 1). The Impact of Submesoscale Physics on Primary Productivity of Plankton. *Annual Review of Marine Science*, *8*(1), 161–184. Retrieved from https://www.annualreviews.org/doi/10.1146/annurev-marine-010814-015912 doi: 10.1146/annurev-marine-010814-015912

Mahadevan, A., Tagliabue, A., Bopp, L., Lenton, A., Mémery, L., & Lévy, M. (2011, 5). Impact of episodic vertical fluxes on sea surface pCO ¡sub¿2¡/sub¿. *Philosophical Transactions of the Royal Society A: Mathematical, Physical and Engineering Sciences*, *369*(1943), 2009–2025. Retrieved from https://royalsocietypublishing.org/doi/10.1098/rsta.2010.0340 doi: 10.1098/rsta.2010.0340

Mahowald, N. M., Baker, A. R., Bergametti, G., Brooks, N., Duce, R. A., Jickells, T. D., ... Tegen, I. (2005, 12). Atmospheric global dust cycle and iron inputs to the ocean. *Global Biogeochemical Cycles*, *19*(4). Retrieved from https://onlinelibrary.wiley.com/doi/full/10.1029/2004GB002402https://onlinelibrary.wiley.com/doi/abs/10.1029/2004GB002402https://agupubs.onlinelibrary.wiley.com/doi/10.1029/2004GB002402 doi: 10.1029/2004GB002402

Manizza, M., Quéré, C. L., Watson, A. J., & Buitenhuis, E. T. (2005, 3). Bio-optical feedbacks among phytoplankton, upper ocean physics and sea-ice in a global model. *Geophysical Research Letters*, *32*(5), L05603. Retrieved from http://doi.wiley.com/10.1029/2004GL020778 doi: 10.1029/2004GL020778

Marinov, I., Follows, M. J., Gnanadesikan, A., Sarmiento, J. L., & Slater, R. D. (2008, 7). How does ocean biology affect atmospheric pCO2? Theory and models. *Journal of Geophysical Research: Oceans*, *113*(7). doi: 10.1029/2007JC004598

Marinov, I., & Gnanadesikan, A. (2011). Changes in ocean circulation and carbon storage are decoupled from air-sea CO2 fluxes. *Biogeosciences*, *8*(2), 505–513. Retrieved from www.biogeosciences.net/8/505/2011/ doi: 10.5194/bg-8-505-2011

Marinov, I., Gnanadesikan, A., Sarmiento, J. L., Toggweiler, J. R., Follows, M., & Mignone, B. K. (2008). Impact of oceanic circulation on biological carbon storage in the ocean and atmospheric pCO2. *Global Biogeochemical Cycles*. doi: 10.1029/2007GB002958

Marinov, I., Gnanadesikan, A., Toggweiler, J. R., & Sarmiento, J. L. (2006, 6). The Southern Ocean biogeochemical divide. *Nature*, *441*(7096), 964–967. Retrieved from http://www.nature.com/articles/nature04883 doi: 10.1038/nature04883

Marshall, J., Adcroft, A., Hill, C., Perelman, L., & Heisey, C. (1997). A finite-volume, incompressible navier stokes model for, studies of the ocean on parallel computers. *Journal of Geophysical Research C: Oceans*. doi: 10.1029/96JC02775

Marshall, J., & Radko, T. (2003). Residual-mean solutions for the Antarctic Circumpolar Current and its associated overturning circulation. *Journal of Physical Oceanography*. doi: 10.1175/1520-0485(2003)033⟨2341:RSFTAC⟩2.0.CO;2

Marshall, J., & Speer, K. (2012). *Closure of the meridional overturning circulation through Southern Ocean upwelling* (Vol. 5) (No. 3). Retrieved from www.nature.com/naturegeoscience doi: 10.1038/ngeo1391

Martin, J. H. (1990, 2). Glacial-interglacial CO 2 change: The Iron Hypothesis. *Paleoceanography*, *5*(1), 1–13. Retrieved from http://doi.wiley.com/10.1029/PA005i001p00001 doi: 10.1029/PA005i001p00001

Mashayek, A., Ferrari, R., Merrifield, S., Ledwell, J. R., St Laurent, L., & Garabato, A. N. (2017). Topographic enhancement of vertical turbulent mixing in the Southern Ocean. *Nature Communications*, *8*. Retrieved from http://dimes.ucsd.edu/en/ doi: 10.1038/ncomms14197

Mashayek, A., Ferrari, R., Vettoretti, G., & Peltier, W. R. (2013, 6). The role of the geothermal heat flux in driving the abyssal ocean circulation. *Geophysical Research Letters*, *40*(12), 3144–3149. Retrieved from http://doi.wiley.com/10.1002/grl.50640 doi: 10.1002/grl.50640

Mashayek, A., Salehipour, H., Bouffard, D., Caulfield, C. P., Ferrari, R., Nikurashin, M., ... Smyth, W. D. (2017, 6). Efficiency of turbulent mixing in the abyssal ocean circulation. *Geophysical Research Letters*, *44*(12), 6296–6306. doi: 10.1002/2016GL072452

Matsumoto, K., Sarmiento, J. L., Key, R. M., Aumont, O., Bullister, J. L., Caldeira, K., ... Orr, J. C. (2004). Evaluation of ocean carbon cycle models with data-based metrics. *Geophysical Research Letters*. doi: 10.1029/2003GL018970

Mazloff, M. R., Heimbach, P., & Wunsch, C. (2010). An eddy-permitting Southern Ocean state estimate. *Journal of Physical Oceanography*, *40*(5), 880–899. Retrieved from https://journals.ametsoc.org/view/journals/phoc/40/5/2009jpo4236.1.xml doi: 10.1175/2009JPO4236.1

Mazloff, M. R., Verdy, A., Gille, S. T., Johnson, K. S., Cornuelle, B. D., & Sarmiento, J. (2023, 5). Southern Ocean Acidification Revealed by Biogeochemical-Argo Floats. *Journal of Geophysical Research: Oceans*, *128*(5), e2022JC019530. Retrieved from https://onlinelibrary.wiley.com/doi/full/10.1029/2022JC019530https://onlinelibrary.wiley.com/doi/abs/10.1029/2022JC019530https://agupubs.onlinelibrary.wiley.com/doi/10.1029/2022JC019530 doi: 10.1029/2022JC019530

Melet, A., Hallberg, R., Legg, S., & Nikurashin, M. (2014, 3). Sensitivity of the Ocean State to Lee Wave–Driven Mixing. *Journal of Physical Oceanography*, *44*(3), 900–921. Retrieved from https://journals.ametsoc.org/view/journals/phoc/44/3/jpo-d-13-072.1.xml doi: 10.1175/JPO-D-13-072.1

Melet, A., Legg, S., & Hallberg, R. (2016, 5). Climatic Impacts of Parameterized Local and Remote Tidal Mixing. *Journal of Climate*, *29*(10), 3473–3500. Retrieved from https://journals.ametsoc.org/view/journals/clim/29/10/jcli-d-15-0153.1.xml doi: 10.1175/JCLI-D-15-0153.1

Melet, A. V., Hallberg, R., & Marshall, D. P. (2022, 1). The role of ocean mixing in the climate system. *Ocean Mixing: Drivers, Mechanisms and Impacts*, 5–34. doi: 10.1016/B978-0-12-821512-8.00009-8

Mitchell, B. G., Brody, E. A., Holm-Hansen, O., McClain, C., & Bishop, J. (1991). Light limitation of phytoplankton biomass and macronutrient utilization in the Southern Ocean. *Limnology and Oceanography*. doi: 10.4319/lo.1991.36.8.1662

Monteiro, P. M., Monteiro, P. M., Monteiro, P. M., Monteiro, P. M., Monteiro, P. M., Monteiro, P. M., ... Monteiro, P. M. (2010, 12). A Global Sea Surface Carbon Observing System: Assessment of Changing Sea Surface CO2 and Air-Sea CO2 Fluxes. In *Proceedings of oceanobs'09: Sustained ocean observations and information for society* (pp. 702–714).

European Space Agency. Retrieved from http://www.oceanobs09.net/proceedings/cwp/cwp64 doi: 10.5270/oceanobs09.cwp.64

Moore, C. M., Mills, M. M., Arrigo, K. R., Berman-Frank, I., Bopp, L., Boyd, P. W., ... Ulloa, O. (2013). *Processes and patterns of oceanic nutrient limitation.* doi: 10.1038/ngeo1765

Moore, J. K., Doney, S. C., & Lindsay, K. (2004, 12). Upper ocean ecosystem dynamics and iron cycling in a global three-dimensional model. *Global Biogeochemical Cycles*, *18*(4), n/a-n/a. Retrieved from http://doi.wiley.com/10.1029/2004GB002220 doi: 10.1029/2004GB002220

Munk, W., & Wunsch, C. (1998). Abyssal recipes II: Energetics of tidal and wind mixing. *Deep-Sea Research Part I: Oceanographic Research Papers*. doi: 10.1016/S0967-0637(98)00070-3

Munk, W. H. (1966, 8). Abyssal recipes. *Deep-Sea Research and Oceanographic Abstracts*, *13*(4), 707–730. Retrieved from https://linkinghub.elsevier.com/retrieve/pii/0011747166906024 doi: 10.1016/0011-7471(66)90602-4

Naveira Garabato, A. C., Frajka-Williams, E. E., Spingys, C. P., Legg, S., Polzin, K. L., Forryan, A., ... Meredith, M. P. (2019). Rapid mixing and exchange of deep-ocean waters in an abyssal boundary current. *Proceedings of the National Academy of Sciences of the United States of America*. doi: 10.1073/pnas.1904087116

Naveira Garabato, A. C., Polzin, K. L., King, B. A., Heywood, K. J., & Visbeck, M. (2004). Widespread Intense Turbulent Mixing in the Southern Ocean. *Science*, *303*(5655), 210–213. Retrieved from www.sciencemag.org doi: 10.1126/science.1090929

Nelson, D. M. (1992). Role of silicon as a limiting nutrient to Antarctic diatoms: evidence from kinetic studies in the Ross Sea ice-edge zone. *marine ecology progress series*, *80*, 255–264.

Nevison, C. D., Manizza, M., Keeling, R. F., Stephens, B. B., Bent, J. D., Dunne, J., ... Yukimoto, S. (2016, 3). Evaluating CMIP5 ocean biogeochemistry and Southern Ocean carbon uptake using atmospheric potential oxygen: Present-day performance and future projection. *Geophysical Research Letters*, *43*(5), 2077–2085. Retrieved from https://onlinelibrary.wiley.com/

doi/full/10.1002/2015GL067584https://onlinelibrary.wiley.com/doi/abs/10.1002/2015GL067584https://agupubs.onlinelibrary.wiley.com/doi/10.1002/2015GL067584 doi: 10.1002/2015GL067584

Nicholson, S. A., Lévy, M., Jouanno, J., Capet, X., Swart, S., & Monteiro, P. M. (2019, 12). Iron Supply Pathways Between the Surface and Subsurface Waters of the Southern Ocean: From Winter Entrainment to Summer Storms. *Geophysical Research Letters*, *46*(24), 14567–14575. doi: 10.1029/2019GL084657

Nicholson, S.-A., Lévy, M., Llort, J., Swart, S., & Monteiro, P. M. S. (2016, 9). Investigation into the impact of storms on sustaining summer primary productivity in the Sub-Antarctic Ocean. *Geophysical Research Letters*, *43*(17), 9192–9199. doi: 10.1002/2016GL069973

Nicholson, S.-A., Whitt, D. B., Fer, I., Du Plessis, M. D., Lebéhot, A. D., Swart, S., ... Monteiro, P. M. S. (2022). Storms drive outgassing of CO 2 in the subpolar Southern Ocean. *Nature Communications*. Retrieved from https://doi.org/10.1038/s41467-021-27780-w doi: 10.1038/s41467-021-27780-w

Nikurashin, M., & Ferrari, R. (2013). Overturning circulation driven by breaking internal waves in the deep ocean. *Geophysical Research Letters*. doi: 10.1002/grl.50542

Nikurashin, M., & Vallis, G. (2011). A theory of deep stratification and overturning circulation in the ocean. *Journal of Physical Oceanography*, *41*(3), 485–502. Retrieved from https://journals.ametsoc.org/doi/pdf/10.1175/2010JPO4529.1 doi: 10.1175/2010JPO4529.1

Nikurashin, M., & Vallis, G. (2012). A theory of the interhemispheric meridional overturning circulation and associated stratification. *Journal of Physical Oceanography*, *42*(10), 1652–1667. Retrieved from https://journals.ametsoc.org/doi/pdf/10.1175/JPO-D-11-0189.1 doi: 10.1175/JPO-D-11-0189.1

Oka, A., & Niwa, Y. (2013, 9). Pacific deep circulation and ventilation controlled by tidal mixing away from the sea bottom. *Nature Communications 2013 4:1*, *4*(1), 1–8. Retrieved from https://www.nature.com/articles/ncomms3419 doi: 10.1038/ncomms3419

Olsen, A., Lange, N., Key, R. M., Tanhua, T., Bittig, H. C., Kozyr, A., ... Woosley, R. J. (2020, 12). *An updated version of the global interior ocean biogeochemical data product,*

GLODAPv2.2020 (Vol. 12) (No. 4). doi: 10.5194/essd-12-3653-2020

Orsi, A. H., Whitworth, T., & Nowlin, W. D. (1995, 5). On the meridional extent and fronts of the Antarctic Circumpolar Current. *Deep Sea Research Part I: Oceanographic Research Papers*, *42*(5), 641–673. Retrieved from `https://www.sciencedirect.com/science/article/pii/096706379500021Whttps://linkinghub.elsevier.com/retrieve/pii/096706379500021W` doi: 10.1016/0967-0637(95)00021-W

Osborn, T. R. (1980, 1). Estimates of the Local Rate of Vertical Diffusion from Dissipation Measurements. *Journal of Physical Oceanography*, *10*(1), 83–89. doi: 10.1175/1520-0485(1980)010⟨0083:EOTLRO⟩2.0.CO;2

Palter, J. B., Marinov, I., Sarmiento, J. L., & Gruber, N. (2013). Large-Scale, Persistent Nutrient Fronts of the World Ocean: Impacts on Biogeochemistry. In *The handbook of environmental chemistry.* Springer. doi: 10.1007/698{_}2013{_}241

Palter, J. B., Sarmiento, J. L., Gnanadesikan, A., Simeon, J., & Slater, R. D. (2010). Fueling export production: Nutrient return pathways from the deep ocean and their dependence on the Meridional Overturning Circulation. *Biogeosciences*. doi: 10.5194/bg-7-3549-2010

Peters, W., Jacobson, A. R., Sweeney, C., Andrews, A. E., Conway, T. J., Masarie, K., ... Tans, P. P. (2007). An atmospheric perspective on North American carbon dioxide exchange: CarbonTracker. *Proceedings of the National Academy of Sciences of the United States of America*, *104*(48), 18925–18930. Retrieved from `www.pnas.org/cgi/content/full/` doi: 10.1073/pnas.0708986104

Polzin, K. L. (1999). A rough recipe for the energy balance of quasi-steady internal lee waves. *Aha Huliko'a: Dynamics of oceanic internal gravity waves II*.

Polzin, K. L., Toole, J. M., Ledwell, J. R., & Schmitt, R. W. (1997, 4). Spatial Variability of Turbulent Mixing in the Abyssal Ocean. *Science*, *276*(5309), 93–96. Retrieved from `https://www.science.org/doi/10.1126/science.276.5309.93` doi: 10.1126/SCIENCE.276.5309.93

Prend, C. J., Hunt, J. M., Mazloff, M. R., Gille, S. T., & Talley, L. D. (2022, 5). Controls on the Boundary Between Thermally and Non-Thermally Driven pCO2 Regimes in the South Pacific. *Geophysical Research Letters*, *49*(9),

e2021GL095797. Retrieved from https://onlinelibrary.wiley.com/doi/full/10.1029/2021GL095797https://onlinelibrary.wiley.com/doi/abs/10.1029/2021GL095797https://agupubs.onlinelibrary.wiley.com/doi/10.1029/2021GL095797 doi: 10.1029/2021GL095797

Prentice, I., Farquhar, G., Fasham, M., Goulden, M., Heimann, M., Jaramillo, V., ... Wallace, D. (2001). The carbon cycle and atmospheric carbon dioxide co-ordinating. In *Climate change 2001: The scientific basis. contribution of working group i to the third assessment report of the intergovernmental panel on climate change* (pp. 183–237). IPCC. Retrieved from https://www.ipcc.ch/site/assets/uploads/2018/02/TAR-03.pdf

Primeau, F. W., Holzer, M., & DeVries, T. (2013, 5). Southern Ocean nutrient trapping and the efficiency of the biological pump. *Journal of Geophysical Research: Oceans*, *118*(5), 2547–2564. doi: 10.1002/jgrc.20181

Rödenbeck, C., Keeling, R. F., Bakker, D. C., Metzl, N., Olsen, A., Sabine, C., & Heimann, M. (2013, 3). Global surface-ocean pCO2 and sea-Air CO2 flux variability from an observation-driven ocean mixed-layer scheme. *Ocean Science*, *9*(2), 193–216. doi: 10.5194/OS-9-193-2013

Roemmich, D., Alford, M. H., Claustre, H., Johnson, K. S., King, B., Moum, J., ... Yasuda, I. (2019, 1). On the future of Argo: A global, full-depth, multi-disciplinary array. *Frontiers in Marine Science*, *6*(JUL), 439. doi: 10.3389/FMARS.2019.00439/BIBTEX

Roemmich, D., Johnson, G., Riser, S., Davis, R., Gilson, J., Owens, W. B., ... Ignaszewski, M. (2009, 6). The Argo Program: Observing the Global Oceans with Profiling Floats. *Oceanography*, *22*(2), 34–43. doi: 10.5670/oceanog.2009.36

Ross, A., Matthews, H. D., Schmittner, A., & Kothavala, Z. (2012). Assessing the effects of ocean diffusivity and climate sensitivity on the rate of global climate change. *Tellus, Series B: Chemical and Physical Meteorology*, *64*(1), 17733. Retrieved from https://www.tandfonline.com/action/journalInformation?journalCode=zelb20 doi: 10.3402/tellusb.v64i0.17733

Rosso, I., Mazloff, M. R., Verdy, A., & Talley, L. D. (2017, 9). Space and time variability of the Southern Ocean carbon budget. *Journal of Geophysical Research: Oceans*, *122*(9), 7407–

7432. Retrieved from http://doi.wiley.com/10.1002/2016JC012646 doi: 10.1002/2016JC012646

Ruan, X., Thompson, A. F., Flexas, M. M., & Sprintall, J. (2017, 11). Contribution of topographically generated submesoscale turbulence to Southern Ocean overturning. *Nature Geoscience*, *10*(11), 840–845. doi: 10.1038/NGEO3053

Sabine, C. L. (2004, 7). The Oceanic Sink for Anthropogenic CO2. *Science*, *305*(5682), 367–371. Retrieved from https://www.sciencemag.org/lookup/doi/10.1126/science.1097403 doi: 10.1126/science.1097403

Saenko, O. A. (2006, 1). The Effect of Localized Mixing on the Ocean Circulation and Time-Dependent Climate Change. *Journal of Physical Oceanography*, *36*(1), 140–160. Retrieved from https://journals.ametsoc.org/view/journals/phoc/36/1/jpo2839.1.xml doi: 10.1175/JPO2839.1

Saenko, O. A. (2008, 5). Influence of the enhanced mixing within the Southern Ocean fronts on the overturning circulation. *Geophysical Research Letters*, *35*(9). doi: 10.1029/2008GL033565

Saenko, O. A., & Merryfield, W. J. (2005). On the effect of topographically enhanced mixing on the global ocean circulation. *Journal of Physical Oceanography*, *35*(5), 826–834. doi: 10.1175/JPO2722.1

Saenko, O. A., Zhai, X., Merryfield, W. J., & Lee, W. G. (2012). The combined effect of tidally and eddy-driven diapycnal mixing on the large-scale ocean circulation. *Journal of Physical Oceanography*, *42*(4), 526–538. Retrieved from https://journals.ametsoc.org/doi/pdf/10.1175/JPO-D-11-0122.1 doi: 10.1175/JPO-D-11-0122.1

Sallée, J. B., Speer, K. G., & Rintoul, S. R. (2010, 4). Zonally asymmetric response of the Southern Ocean mixed-layer depth to the Southern Annular Mode. *Nature Geoscience*, *3*(4), 273–279. Retrieved from http://www.nature.com/articles/ngeo812 doi: 10.1038/ngeo812

Sarmiento, J. L., Gruber, N., Brzezinski, M. A., & Dunne, J. P. (2004, 1). High-latitude controls of thermocline nutrients and low latitude biological productivity. *Nature*, *427*(6969), 56–60. Retrieved from http://www.nature.com/articles/nature02127 doi: 10.1038/

nature02127

Sarmiento, J. L., & Toggweiler, J. R. (1984, 4). A new model for the role of the oceans in determining atmospheric PCO 2. *Nature*, *308*(5960), 621–624. Retrieved from http://www.nature.com/articles/308621a0 doi: 10.1038/308621a0

Schlitzer, R. (2002). Carbon export fluxes in the Southern Ocean: results from inverse modeling and comparison with satellite based estimates. *EPIC3Deep-sea research ii, 49, pp. 1623-1644*.

Schmittner, A., Oschlies, A., Giraud, X., Eby, M., & Simmons, H. L. (2005). A global model of the marine ecosystem for long-term simulations: Sensitivity to ocean mixing, buoyancy forcing, particle sinking, and dissolved organic matter cycling. *Global Biogeochemical Cycles*, *19*(3), 1–17. doi: 10.1029/2004GB002283

Schmittner, A., Urban, N. M., Keller, K., & Matthews, D. (2009). Using tracer observations to reduce the uncertainty of ocean diapycnal mixing and climate-carbon cycle projections. *Global Biogeochemical Cycles*, *23*(4). Retrieved from http://www.nodc. doi: 10.1029/2008GB003421

Shakespeare, C. J. (2020, 3). Interdependence of Internal Tide and Lee Wave Generation at Abyssal Hills: Global Calculations. *Journal of Physical Oceanography*, *50*(3), 655–677. Retrieved from https://journals.ametsoc.org/view/journals/phoc/50/3/jpo-d-19-0179.1.xml doi: 10.1175/JPO-D-19-0179.1

Sheen, K. L., Naveira Garabato, A. C., Brearley, J. A., Meredith, M. P., Polzin, K. L., Smeed, D. A., ... Watson, A. J. (2014, 8). Eddy-induced variability in Southern Ocean abyssal mixing on climatic timescales. *Nature Geoscience*, *7*(8), 577–582. doi: 10.1038/ngeo2200

Sigman, D. M., Hain, M. P., & Haug, G. H. (2010). *The polar ocean and glacial cycles in atmospheric CO2 concentration* (Vol. 466) (No. 7302). doi: 10.1038/nature09149

Silvester, J. M., Lenn, Y. D., Polton, J. A., Rippeth, T. P., & Maqueda, M. M. (2014). Observations of a diapycnal shortcut to adiabatic upwelling of Antarctic Circumpolar Deep Water. *Geophysical Research Letters*. doi: 10.1002/2014GL061538

Simmons, H. L., Jayne, S. R., St Laurent, L. C., & Weaver, A. J. (2004). Tidally driven mixing in a numerical model of the ocean general circulation. *Ocean Modelling*. Retrieved from

www.elsevier.com/locate/omodol doi: 10.1016/S1463-5003(03)00011-8

Sloyan, B. M. (2005). Spatial variability of mixing in the Southern Ocean. *Geophysical Research Letters*. doi: 10.1029/2005GL023568

Sloyan, B. M., & Rintoul, S. R. (2001). Circulation, renewal, and modification of antarctic mode and intermediate water. *Journal of Physical Oceanography*. doi: 10.1175/1520-0485(2001)031⟨1005:CRAMOA⟩2.0.CO;2

Sokolov, S., & Rintoul, S. R. (2007, 7). On the relationship between fronts of the Antarctic Circumpolar Current and surface chlorophyll concentrations in the Southern Ocean. *Journal of Geophysical Research: Oceans*, *112*(7), C07030. Retrieved from http://doi.wiley.com/10.1029/2006JC004072 doi: 10.1029/2006JC004072

Song, H., Marshall, J., McGillicuddy, D. J., & Seo, H. (2020). Impact of Current-Wind Interaction on Vertical Processes in the Southern Ocean. *Journal of Geophysical Research: Oceans*, *125*(4). Retrieved from https://doi.org/10.1029/2020JC016046 doi: 10.1029/2020JC016046

Speer, K., Rintoul, S. R., & Sloyan, B. (2002). The Diabatic Deacon Cell*. *Journal of Physical Oceanography*. doi: 10.1175/1520-0485(2000)030⟨3212:tddc⟩2.0.co;2

Stewart, A. L., Ferrari, R., & Thompson, A. F. (2014, 3). On the importance of surface forcing in conceptual models of the deep ocean. *Journal of Physical Oceanography*, *44*(3), 891–899. Retrieved from http://journals.ametsoc.org/doi/10.1175/JPO-D-13-0206.1 doi: 10.1175/JPO-D-13-0206.1

St. Laurent, L., Naveira Garabato, A. C., Ledwell, J. R., Thurnherr, A. M., Toole, J. M., & Watson, A. J. (2012). Turbulence and diapycnal mixing in drake passage. *Journal of Physical Oceanography*, *42*(12), 2143–2152. Retrieved from http://dimes. doi: 10.1175/JPO-D-12-027.1

Su, J., Schallenberg, C., Rohr, T., Strutton, P. G., & Phillips, H. E. (2022, 8). New Estimates of Southern Ocean Annual Net Community Production Revealed by BGC-Argo Floats. *Geophysical Research Letters*, *49*(15). doi: 10.1029/2021GL097372

Sun, S., Eisenman, I., & Stewart, A. L. (2018). Does Southern Ocean Surface Forcing Shape the Global Ocean Overturning Circulation? *Geophysical Research Letters*,

45(5), 2413–2423. Retrieved from https://doi.org/10.1002/2017GL076437 doi: 10.1002/2017GL076437

Swan, C. M., Vogt, M., Gruber, N., & Laufkoetter, C. (2016, 3). A global seasonal surface ocean climatology of phytoplankton types based on CHEMTAX analysis of HPLC pigments. *Deep Sea Research Part I: Oceanographic Research Papers*, *109*, 137–156. doi: 10.1016/J.DSR.2015.12.002

Swierczek, S., Mazloff, M. R., Morzfeld, M., & Russell, J. L. (2021, 7). The effect of resolution on vertical heat and carbon transports in a regional ocean circulation model of the Argentine Basin. *Journal of Geophysical Research: Oceans*, *126*(7), e2021JC017235. Retrieved from https://onlinelibrary.wiley.com/doi/10.1029/2021JC017235 doi: 10.1029/2021jc017235

Tagliabue, A., Sallée, J.-B., Bowie, A. R., Lévy, M., Swart, S., & Boyd, P. W. (2014, 4). Surface-water iron supplies in the Southern Ocean sustained by deep winter mixing. *Nature Geoscience*, *7*(4), 314–320. doi: 10.1038/ngeo2101

Tagliabue, A., Williams, R. G., Rogan, N., Achterberg, E. P., & Boyd, P. W. (2014, 10). A ventilation-based framework to explain the regeneration-scavenging balance of iron in the ocean. *Geophysical Research Letters*, *41*(20), 7227–7236. Retrieved from http://doi.wiley.com/10.1002/2014GL061066 doi: 10.1002/2014GL061066

Takahashi, T., Sutherland, S. C., Chipman, D. W., Goddard, J. G., & Ho, C. (2014). Climatological distributions of pH, pCO2, total CO2, alkalinity, and CaCO3 saturation in the global surface ocean, and temporal changes at selected locations. *Marine Chemistry*. doi: 10.1016/j.marchem.2014.06.004

Takahashi, T., Sutherland, S. C., Sweeney, C., Poisson, A., Metzl, N., Tilbrook, B., ... Nojiri, Y. (2002, 1). Global sea–air CO2 flux based on climatological surface ocean pCO2, and seasonal biological and temperature effects. *Deep Sea Research Part II: Topical Studies in Oceanography*, *49*(9-10), 1601–1622. Retrieved from https://linkinghub.elsevier.com/retrieve/pii/S0967064502000036 doi: 10.1016/S0967-0645(02)00003-6

Takahashi, T., Sutherland, S. C., Wanninkhof, R., Sweeney, C., Feely, R. A., Chipman, D. W., ... de Baar, H. J. (2009, 4). Climatological mean and decadal change in surface ocean

pCO2, and net sea–air CO2 flux over the global oceans. *Deep Sea Research Part II: Topical Studies in Oceanography*, *56*(8-10), 554–577. Retrieved from https://linkinghub.elsevier.com/retrieve/pii/S0967064508004311 doi: 10.1016/j.dsr2.2008.12.009

Takahashi, T., Sweeney, C., Hales, B., Chipman, D., Newberger, T., Goddard, J., ... Sutherland, S. (2012, 9). The Changing Carbon Cycle in the Southern Ocean. *Oceanography*, *25*(3), 26–37. Retrieved from https://tos.org/oceanography/article/the-changing-carbon-cycle-in-the-southern-ocean doi: 10.5670/oceanog.2012.71

Talley, L., Feely, R., Sloyan, B., Wanninkhof, R., Baringer, M., Bullister, J., ... Zhang, J.-Z. (2016, 1). Changes in Ocean Heat, Carbon Content, and Ventilation: A Review of the First Decade of GO-SHIP Global Repeat Hydrography. *Annual Review of Marine Science*, *8*(1), 185–215. Retrieved from http://www.annualreviews.org/doi/10.1146/annurev-marine-052915-100829 doi: 10.1146/annurev-marine-052915-100829

Talley, L. D. (2013). Closure of the Global Overturning Circulation Through the Indian, Pacific, and Southern Oceans: Schematics and Transports. *Oceanography*, *26*(1), 80–97. doi: 10.5670/OCEANOG.2013.07

Talley, L. D., Reid, J. L., & Robbins, P. E. (2003, 10). Data-Based Meridional Overturning Streamfunctions for the Global Ocean. *Journal of Climate*, *16*(19), 3213–3226. Retrieved from http://journals.ametsoc.org/doi/10.1175/1520-0442(2003)016<3213:DMOSFT>2.0.CO;2 doi: 10.1175/1520-0442(2003)016⟨3213:DMOSFT⟩2.0.CO;2

Talley, L. D., Rosso, I., Kamenkovich, I., Mazloff, M. R., Wang, J., Boss, E., ... Sarmiento, J. L. (2019, 1). Southern Ocean Biogeochemical Float Deployment Strategy, With Example From the Greenwich Meridian Line (GO-SHIP A12). *Journal of Geophysical Research: Oceans*, *124*(1), 403–431. doi: 10.1029/2018JC014059

Tamsitt, V., Drake, H. F., Morrison, A. K., Talley, L. D., Dufour, C. O., Gray, A. R., ... Weijer, W. (2017). Spiraling pathways of global deep waters to the surface of the Southern Ocean. *Nature Communications*, *8*(1). doi: 10.1038/s41467-017-00197-0

Tatebe, H., Tanaka, Y., Komuro, Y., & Hasumi, H. (2018, 12). Impact of deep ocean mixing on the climatic mean state in the Southern Ocean. *Scientific Reports*, *8*(1), 14479. Retrieved

from http://www.nature.com/articles/s41598-018-32768-6 doi: 10.1038/s41598-018-32768-6

Thompson, A. F., Gille, S. T., MacKinnon, J. A., & Sprintall, J. (2007). Spatial and temporal patterns of small-scale mixing in Drake Passage. *Journal of Physical Oceanography*, *37*(3), 572–592. doi: 10.1175/JPO3021.1

Thompson, A. F., & Sallée, J. B. (2012). Jets and Topography: Jet Transitions and the Impact on Transport in the Antarctic Circumpolar Current. *Journal of Physical Oceanography*. doi: 10.1175/JPO-D-11-0135.1

Toggweiler, J. R., Russell, J. L., & Carson, S. R. (2006). Midlatitude westerlies, atmospheric CO2, and climate change during the ice ages. *Paleoceanography*. doi: 10.1029/2005PA001154

Tréguer, P. J. (2014). The Southern Ocean silica cycle. *Comptes Rendus - Geoscience*. doi: 10.1016/j.crte.2014.07.003

Trossman, D., Whalen, C., Haine, T., Waterhouse, A., Bigdeli, A., Nguyen, A., ... Heimbach, P. (2020). Tracer Versus Observationally-Derived Constraints on Ocean Mixing Parameters in an Adjoint-Based Data Assimilation Framework. *Earth and Space Science Open Archive*, 0–45. Retrieved from https://www.essoar.org/doi/10.1002/essoar.10502123.2 doi: 10.1002/ESSOAR.10502123.2

Trossman, D., Whalen, C., Haine, T., Waterhouse, A., Nguyen, A., Bigdeli, A., ... Heimbach, P. (2021). Tracer and observationally-derived constraints on diapycnal diffusivities in an ocean state estimate. *Ocean Science Discussions*(September), 1–40. Retrieved from https://doi.org/10.5194/os-2021-87 doi: 10.5194/os-2021-87

Verdy, A., & Mazloff, M. R. (2017). A data assimilating model for estimating Southern Ocean biogeochemistry. *Journal of Geophysical Research: Oceans*, *122*(9), 6968–6988. Retrieved from http://hycom.org doi: 10.1002/2016JC012650

Volk, T., & Hoffert, M. I. (1985). Ocean Carbon Pumps: Analysis of Relative Strengths and Efficiencies in Ocean-Driven Atmospheric CO 2 Changes. In *he carbon cycle and atmospheric co2, natural variations archean to present.* Sundquist E. doi: 10.1029/gm032p0099

Wanninkhof, R. (1992, 5). Relationship between wind speed and gas exchange over the ocean. *Journal of Geophysical Research*, *97*(C5), 7373–7382. Retrieved from http://doi.wiley.com/10.1029/92JC00188 doi: 10.1029/92JC00188

Wanninkhof, R., Park, G. H., Takahashi, T., Sweeney, C., Feely, R., Nojiri, Y., ... Khatiwala, S. (2013, 3). Global ocean carbon uptake: magnitude, variability and trends. *Biogeosciences*, *10*(3), 1983–2000. Retrieved from https://bg.copernicus.org/articles/10/1983/2013/ doi: 10.5194/bg-10-1983-2013

Waterhouse, A. F., Mackinnon, J. A., Nash, J. D., Alford, M. H., Kunze, E., Simmons, H. L., ... Lee, C. M. (2014). Global patterns of diapycnal mixing from measurements of the turbulent dissipation rate. *Journal of Physical Oceanography*. doi: 10.1175/JPO-D-13-0104.1

Watson, A. J., Ledwell, J. R., Messias, M. J., King, B. A., Mackay, N., Meredith, M. P., ... Naveira Garabato, A. C. (2013, 9). Rapid cross-density ocean mixing at mid-depths in the Drake Passage measured by tracer release. *Nature*, *501*(7467), 408–411. Retrieved from http://www.nature.com/articles/nature12432 doi: 10.1038/nature12432

Watson, A. J., & Naveira Garabato, A. C. (2006). The role of Southern Ocean mixing and upwelling in glacial-interglacial atmospheric CO2 change. *Tellus, Series B: Chemical and Physical Meteorology*, *58*(1), 73–87. Retrieved from https://www.tandfonline.com/action/journalInformation?journalCode=zelb20 doi: 10.1111/j.1600-0889.2005.00167.x

Watson, A. J., Vallis, G. K., & Nikurashin, M. (2015). Southern Ocean buoyancy forcing of ocean ventilation and glacial atmospheric CO 2. *Nature Geoscience*. Retrieved from www.nature.com/naturegeoscience doi: 10.1038/NGEO2538

Whalen, C. B., de Lavergne, C., Naveira Garabato, A. C., Klymak, J. M., MacKinnon, J. A., & Sheen, K. L. (2020, 11). Internal wave-driven mixing: governing processes and consequences for climate. *Nature Reviews Earth and Environment*, *1*(11), 606–621. Retrieved from https://www.nature.com/articles/s43017-020-0097-z doi: 10.1038/s43017-020-0097-z

Whalen, C. B., MacKinnon, J. A., Talley, L. D., & Waterhouse, A. F. (2015, 4). Estimating

the Mean Diapycnal Mixing Using a Finescale Strain Parameterization. *Journal of Physical Oceanography*, *45*(4), 1174–1188. Retrieved from https://journals.ametsoc.org/view/journals/phoc/45/4/jpo-d-14-0167.1.xml doi: 10.1175/JPO-D-14-0167.1

Whalen, C. B., Talley, L. D., & MacKinnon, J. A. (2012). Spatial and temporal variability of global ocean mixing inferred from Argo profiles. *Geophysical Research Letters*. doi: 10.1029/2012GL053196

Wunsch, C., & Ferrari, R. (2004). VERTICAL MIXING, ENERGY, AND THE GENERAL CIRCULATION OF THE OCEANS. *Annual Review of Fluid Mechanics*. doi: 10.1146/annurev.fluid.36.050802.122121

Zhu, Y., Zhang, R.-H., & Sun, J. (2020, 9). North Pacific Upper-Ocean Cold Temperature Biases in CMIP6 Simulations and the Role of Regional Vertical Mixing. *Journal of Climate*, *33*(17), 7523–7538. doi: 10.1175/JCLI-D-19-0654.1